Origin of fluorescence and voltage sensitivity in microbial rhodopsin-based voltage sensors

Ursprung der Fluoreszenz und Spannungsempfindlichkeit in mikrobiellen Rhodopsin-basierten Spannungssensoren

Dissertation

zur Erlangung des akademischen Grades
Doctor rerum naturalium
(Dr. rer. nat.)
im Fach Biophysik

eingereicht an der
Lebenswissenschaftlichen Fakultät
der Humboldt Universität zu Berlin

von
Arita Silapetere, M. Sc.

Präsidentin der Humboldt-Universität zu Berlin:
Prof. Dr.-Ing. Dr. Sabine Kunst

Dekan der Lebenswissenschaftlichen Fakultät:
Prof. Dr. Dr. Christian Ulrichs

Gutachter/innen:
1. Prof. Dr. Peter Hegemann
2. Prof. Dr. Peter Hildebrandt
3. Prof. Dr. Franz Bartl

Tag der mündlichen Prüfung: 10.11.2021

„The unforgotten moments of my life are those rare ones which come after years of plodding work, when the veil over nature's secret seems suddenly to lift, and when what was dark and chaotic appears in a clear and beautiful light and pattern."

Gerty Cori

Abstract

Novel class of fluorescent membrane voltage sensors QuasArs, based on Archaerhodopsin-3, have been reported by Hochbaum et al. in 2014. The new constructs show unusually high fluorescence quantum yield for microbial rhodopsins. Furthermore the fluorescence is voltage-dependent, which is a desirable property for membrane voltage sensors. These tools would offer high spatiotemporal resolution allowing to track neuronal spiking. Although multiple constructs have been proposed, their fluorescence quantum yield is still too low (<1%) for applications in living rodents and requires further improvement for imaging applications. However, rational design of the next generation rhodopsin-based fluorescent sensors is restrained since the current constructs were found using random mutagenesis. To develop improved constructs it is essential to understand the functionality of the voltage-sensitive fluorescence and the role of the introduced mutations. In this thesis, the microbial rhodopsin based voltage sensors and the origin of their voltage-modulated fluorescence were studied. The photodynamics of microbial rhodopsin-based voltage sensors were studied with UV/Vis steady state and transient spectroscopy. The archaerhodopsin-3 variants undergo an unusual photocycle with extended excited state lifetime and inefficient photoisomerization. Pre-resonance Raman spectroscopy and high-pressure liquid chromatography allowed to directly study the chromophore composition in these peculiar rhodopsins. Molecular dynamics simulations, supported by spectroscopic studies, provide a model of protein dynamics taking place under different membrane voltage conditions. Protein engineering allowed to identify the residues needed for the increase of the fluorescence quantum yield and key residues involved in the voltage sensing. Promising constructs, with improved properties, were proposed and tested.

Zusammenfassung

QuasArs, eine neue Klasse von fluoreszierenden Membranspannungssensoren basierend auf Archaerhodopsin-3, wurde von Hochbaum et al. im Jahr 2014 beschrieben. Die neuen Konstrukte zeigen eine für mikrobielle Rhodopsine außergewöhnlich hohe Fluoreszenzquantenausbeute. Außerdem ist die Fluoreszenz spannungsabhängig, was für Membranspannungssensoren eine wünschenswerte Eigenschaft ist. Diese Sensoren bieten ein hohes räumliches und zeitliches Auflösungsvermögen, wodurch neuronale Aktivität verfolgt werden könnte. Obwohl mehrere Varianten vorgeschlagen wurden ist ihre Fluoreszenzquantenausbeute immer noch zu gering (<1%) für Anwendungen in lebenden Nagetieren und erfordert weitere Verbesserungen für bildgebende Anwendungen. Das rationale Design der Rhodopsin-basierten Fluoreszenzsensoren der nächsten Generation ist jedoch nur eingeschränkt möglich, da die derzeit verwendeten QuasArs mittels zufälliger Mutagenese gefunden wurden. Um verbesserte Konstrukte zu entwickeln, ist es wichtig die Funktionalität der spannungssensitiven Fluoreszenz und die Rolle der eingeführten Mutationen zu verstehen. In dieser Arbeit wurden die mikrobiellen Rhodopsin-basierten Spannungssensoren und der Ursprung ihrer spannungsmodulierten Fluoreszenz untersucht. Die Photodynamik dieser Spannungssensoren wurde mit UV/Vis-*Steady-State* und -transienter Spektroskopie untersucht. Die Archaerhodopsin-3 Varianten durchlaufen einen ungewöhnlichen Photozyklus mit verlängerter Lebensdauer des angeregten Zustands und ineffizienter Photoisomerisierung. Präresonanz-Raman-Spektroskopie und Hochdruckflüssigkeitschromatographie ermöglichten die direkte Untersuchung des Chromophors in diesen besonderen Rhodopsinen. Molekulardynamiksimulationen, unterstützt durch spektroskopische Studien, liefern ein Modell der Proteindynamik unter Einfluss der Membranspannung. Protein-*Engineering* ermöglichte die Identifizierung der Aminosäuren, die für die Erhöhung der Fluoreszenzquantenausbeute benötigt werden, und der Schlüsselreste, die an der Spannungsmessung beteiligt sind. Aussichtsreiche Konstrukte mit verbesserten Eigenschaften wurden vorgeschlagen und getestet.

Parts of this work have been already published in the following articles:

1. Penzkofer, A., Silapetere A., Hegemann P. (2019) Absorption and Emission Spectroscopic Investigation of the Thermal Dynamics of the Archaerhodopsin 3 Based Fluorescent Voltage Sensor QuasAr1 *International Journal of Molecular Sciences* **20**, 4086–0, https://doi.org/10.3390/ijms20174086

2. Penzkofer, A., Silapetere A., Hegemann P. (2019) Photocycle Dynamics of the Archaerhodopsin 3 Based Fluorescent Voltage Sensor QuasAr1 *International Journal of Molecular Sciences* **21**, 160–0, https://doi.org/10.3390/ijms21010160

3. Penzkofer, A., Silapetere A., Hegemann P. (2020) Absorption and Emission Spectroscopic Investigation of the Thermal Dynamics of the Archaerhodopsin 3 Based Fluorescent Voltage Sensor Archon2, *International Journal of Molecular Sciences* **21**, 6576–0, https://doi.org/10.3390/ijms21186576

4. Penzkofer, A., Silapetere, A., Hegemann, P. (2021) Photocycle dynamics of the Archaerhodopsin 3 based fluorescent voltage sensor Archon2 *Journal of Photochemistry and Photobiology B: Biology* **225**, 112331, https://doi.org/10.1016/j.jphotobiol.2021.112331

5. Silapetere, A., Hwang, S., Hontani, Y., Lahore, R. F., Balke, J., Escobar, F. V., Tros, M., Konold, P. E., Matis, R., Croce, R., Walla, P. J., Hildebrandt, P., Alexiev, U., Kennis, J. T. M., Sun, H., Utesch, T., Hegemann, P. (2022) QuasAr Odyssey: The Origin of voltage dependent fluorescence in rhodopsin-based sensors *Nature communication* **13**, 5501, https://doi.org/10.1038/s41467-022-33084-4

Additional publications during the thesis:

1. Hontani, Y., Broser, M., Silapetere, A., Krause, B. S., Hegemann, P., Kennis, J. T. M. (2017) The femtosecond-to-second photochemistry of red-shifted fast-closing anion channelrhodopsin ACR1 *Physical Chemistry Chemical Physics* **19**, 30402–

30409, https://doi.org/10.1039/C7CP06414D

2. Grimm, C., Silapetere A., Vogt, A., Sierra, Y. A. B., Hegemann, P. (2018) Electrical properties, substrate specificity and optogenetic potential of the engineered light-driven sodium pump eKR2 *Scientific Reports* **8**, 9316, https://doi.org/10.1038/s41598-018-27690-w

3. Vogt, A., Silapetere A., Grimm, C., Hegemann, P. (2019) Electrophysiology of the engineered light-driven sodium pump eKR2 and its conversion into a channel *Biophysical journal* **116**, 1941-1951, https://doi.org/10.1016/j.bpj.2019.04.001

4. Oppermann, J., Fischer, P., Silapetere, A., Liepe, B., Rodriguez-Rozada, S., Flores-Uribe, J., Peter, E., Keidel, A., Vierock, J., Kaufmann, J., Broser, M., Luck, M., Bartl, F., Hildebrandt, P., Wiegert, J. S., Béjà, O., Hegemann, P., Wietek, J. (2019). MerMAIDs: A novel family of metagenomically discovered marine anion-conducting and intensely desensitizing channelrhodopsins. *Nature Communications* **10,** 3315, https://doi.org/10.1038/s41467-019-11322-6

Conferences and meeting contributions:

1.“Modification of sensory photoreceptors by uncanonical amino acids”, BIG-NSE Annual Meeting , 15-16 June, 2017, Templin (Germany), *Talk.*

2.“Spectroscopic characterization of light-driven sodium pump KR2” Collaborative Research Center – SFB 1078 Annual Meeting, 4-5 October, 2017 Elstal (Germany), *Poster.*

3.“Spectroscopic characterization of light-driven sodium pump KR2” Biophysical Society 62nd Annual Meeting, February 17-21, 2018, San Francisco(United States of America), (original abstract control number - 18-L-5296-BPS), *Poster.*

4.“Spectroscopical characterization of voltage sensitive fluorescent sensors QuasArs”, BIG-NSE Annual Meeting, 17-18 May, 2018, Templin (Germany), *Talk.*

5.“Isomerization versus fluorescence: case study of voltage sensors QuasArs”, 18th International Conference on Retinal Proteins, 24-29 September, 2018, Hockley Valley Resort, Ontario (Canada), *Poster.*

6.“Isomerization versus fluorescence: case study of voltage sensors QuasArs”, World Congress on Life and Light (17th Congress of the International Union of Photobiology and 18th Congress of the European Society for Photobiology), 25-30 August, 2019, Barcelona (Spain), *Poster.*

7.“Spectroscopic odyssey: study of fluorescent voltage sensors QuasArs”, UniSysCat Annual Meeting, 10-12 February, 2020, Golm (Germany), *Talk.*

8.“Optogenetics, Time for the next paradigm shift”, contributing author for section “Why are some rhodopsins fluorescent and others are not?” the 8th NeuroTechnology Symposium: Optogenetics 2020, 27th May, 2020, online (hosted by New York University, USA), *Talk, presented by Prof. Dr. P. Hegemann.*

Acknowledgments

I would like to express my greatest gratitude to my supervisor Prof. Dr. Peter Hegemann for the guidance, support and encouragement during my work on this challenging project.

I would like to thank all of the people, who have made this project possible and have contributed in various ways. I would like to thank Prof. Dr. Peter Hildebrandt and Dr. Francisco Velazquez Escobar for introducing me to the FT-Raman spectroscopy. I would like to thank Prof. Dr. John T.M. Kennis, Dr. Yusaku Hontani and Dr. Patrick E. Konold for all of the support with ultrafast pump-probe spectroscopy. I am thankful to Dr. Tillmann Utesch, Dr. Han Sun and Dr. Songhwan Hwang for tremendous work invested in developing the MD simmulations models. I am grateful to Rodrigo Fernandez Lahore who supported me with the patch-clamp fluorescent voltage recordings. I am thankful to Dr. Prof. Ulrike Alexiev and Jens Balke for the successful FLIM measurements. I am appreciative for the Streak camera fluorescence kinetics recordings to Dr. Rainer Matis and Roberta Croce. I am thankful to Prof. Dr. Peter J. Walla and Dr. Rainer Matis for the investigation of the two-photon fluorescence excitation spectra. I would like to thank Prof. Dr. Martin Heck for providing facilities to carry out the HPLC measurements. I am thankful to student assistant Janosch Brandhorst for all the help in the lab.

I would like to thank all the colleagues in the group AG Hegemann, for welcoming me openly in their company, ensuring a positive work environment and all of the advice given. I am grateful to take part in international graduate school BIG-NSE. I would like to thank its managing director Dr. Jean-Philippe Lonjaret and the fellow PhD students for all the help through out the PhD period.

The work was supported by the Deutsche Forschungsgemeinschaft (DFG, German Research Foundation) under Germany´s Excellence Strategy – EXC 2008/1–390540038 “Unifying Systems in Catalysis”, and the Gottfried Wilhelm Leibniz Prize. The ultrafast pump-probe experiments carried out in Vrije Universiteit Amsterdam were supported by European Community – Access to Research Infrastructures action of the Improving Human Potential Program “LaserLab Europe” (Contract no. RII-CT-2003-506350).

I am truly grateful for all the emotional support, love, and encouragement

provided by my family and friends.

I am sincerely thankful for all the support I have been provided!

Table of Contents

Abbreviation

1799	-	2,6-dihydroxy-1,1,1,7,7,7-hexafluoro-2,6-bis(trifluoromethyl)heptane-4-one
6xHis-tag	-	Hexa-histidine-tag (polyhistidine-tag)
7TM	-	Seven transmembrane alpha helices
$A_{280}/A_{chromophore}$	-	Ratio between absorption maxima at 280 nm and chromophore absorption maxima (~585 nm) of the investigated microbial rhodopsin
AAV	-	Adeno-associated virus
ACRs	-	Anion-conducting channelrhodopsin
Ag, Bu	-	Spatial symmetry of the excited state: Ag – even (gerade), Bu - odd (ungerade)
AR1(2)	-	Archaerhodopsin-1(2) from *Halobacterium sp.*
Arch3	-	Archaerhodopsin-3 from *Halorubrum sodomense*
Arch5	-	Archaerhodopsin-3 with 5 point mutations introduced to improve the voltage sensitive fluorescence of the construct, as shown in MsIsaac et al. 2014[1]
Arch7	-	Archaerhodopsin-3 with 7 point mutations introduced to improve the voltage sensitive fluorescence of the construct, as shown in MsIsaac et al. 2014[1]
Archon1	-	Construct based on Arch3, with additional 13 point mutations introduced to improve the voltage sensitive fluorescence, as shown in Pietkevich et al. 2018[2]
Archon2	-	Constructs based on Arch3, with additional 10 point mutations introduced to improve the voltage sensitive fluorescence of the construct, as shown in Pietkevich et al. [2]
ATP	-	Adenosine triphosphate
ATR	-	all-*trans* retinal
BR	-	Bacteriorhodopsin from of *Halobacterium salinarium*
C1V1	-	Chimeric channelrhodopsin from CrChR1 and VcChR1
cAMP	-	Cyclic adenosine monophosphate
CCCP	-	Carbonyl cyanide m-chlorophenyl hydrazine

CCRs	-	Cation-conducting channelrhodopsin
CheRiff	-	Channelrhodopsin variant from *Scherffelia dubia*
ChR	-	Channelrhodopsin
ChR1(2)	-	Channelrhodopsin 1(2) of *Chlamydomonas reinhardtii*
CHS	-	Cholesteryl hemisuccinate
CI	-	Conical intersection
cm^{-1}	-	Wavenumber
D590/P580/P400 / D590'photoproducts	-	D590 - Dark state with absorption maximum at 590 nm; P580 – Photoproduct with absorption maximum at 580 nm, P400 – photoproduct absorption maximum at 400 nm, D590' – dark state-like photoproduct with recovered absorption maximum at 590 nm
DADS	-	Decay-associated difference spectra
DDM	-	Dodecyl-β-D-maltosid
DMSO	-	Dimethylsulfoxid Dimethyl sulfoxide
DNA	-	Deoxyribonucleic acid
E. coli	-	Escherichia coli
EADS	-	Evolution Associated Difference Spectra
ER	-	Endoplasmic reticulum
ESA	-	Excited state absorption
eYFP	-	enhanced Yellow Fluorescent Protein
FC	-	Franck-Condon region
FLIM	-	Fluorescence lifetime imaging microscopy
FP	-	Fluorescent protein
FRET	-	Förster resonance energy transfer
FTIR	-	Fourier-transform infrared spectroscopy
FWHM	-	Full width at half maximum
GECI	-	Genetically encoded calcium indicator
GEVI	-	Genetically encoded voltage indicator
GFP	-	Green fluorescent protein
GSB	-	Ground state bleach

HB	-	Hydrogen bond
HKR	-	Histidine kinase rhodopsins
HOOP	-	Hydrogen out of plane
HPLC	-	High-pressure liquid chromatography
HR	-	Halorhodopsin from halobacterium *Natronomonas pharaonis*
I640/I620 photointermediates	-	I640 – photointermediate with absorption maximum at 640 nm, I620 - photointermediate with absorption maximum at 620 nm
ICCD camera	-	Intensified charge-coupled device camera
IPTG	-	Isopropyl β-D-thiogalactopyranoside
IRF	-	Instrument response function
KR2	-	Sodium-pumping *Krokinobakter eikastus* rhodopsin-2
LB media	-	Lysogeny broth media
LED	-	Light-emitting diode
LOV domain	-	Light-oxygen-voltage domain
LV	-	Lentivirus
MD	-	Molecular dynamics
Nd:YAG laser	-	Neodymium-doped yttrium aluminum garnet
OD	-	Optical density
OPO	-	Optical parametric oscillator
PCR	-	Polymerase chain reaction
PeT	-	Photo induced electron transfer
PMSF	-	Phenylmethylsulfonyl fluoride
PMT	-	Photomultiplier tube
PR:MMAR	-	Proteorhodopsin with retinal analog 3-methylamino-16-nor-1,2,3,4-didehydroretinal
QM/MM	-	Quantum mechanics/molecular mechanics
QuasArs	-	(Quality superior to Arch) Arch3 based constructs with 5 point mutations to increase the voltage sensitive fluorescence as shown in Hochbaum et al. 2014[3]
QY	-	Quantum yield

RSB	-	Retinal Schiff base
$RSBH^+$	-	Protonated retinal Schiff base
S_0	-	Singlet ground state
S_1	-	First singlet excited state
SE	-	Stimulated emission
SMA	-	Styrene–maleic acid
SNR	-	Signal to noise ratio
SRI (II)	-	Sensory rhodopsin I (II) found in *Halobacterium salinarum*
TAS	-	Transient absorption spectra
TCSPC	-	Time-correlated single photon counting
UV/Vis spectroscopy	-	Ultraviolet–visible spectroscopy
VSD	-	Voltage sensing domain
VSFP	-	Voltage sensitive fluorescent proteins
Wat	-	Water molecule
$\Delta F/F$	-	Fluorescence change upon increase of membrane voltage
λ	-	Wavelength
τ	-	Time constant
Φ_{FL}	-	Fluorescence quantum yield

Amino acids are indicated with the common one letter code (example, D - aspartate). Mutations are also indicated with the one letter code and shown after the replaced residue.

1. Introduction

Light plays a crucial role for living organisms in their energy storage, orientation and development. Living organisms have adapted various ways to perceive light. As a result, an abundance of photoreceptor proteins have evolved, which mediate the response to the stimuli of light[4]. In this work, microbial rhodopsins are of particular interest. They are membrane-bound photoreceptors comprised of an opsin apoprotein and a retinal chromophore. Rhodopsins have attracted a broad scientific attention beyond their physiological role. Due to their properties, rhodopsins have become a desirable tool in optogenetics, allowing activation and suppression of neuronal signals, using light[5]. Our curiosity has been sparked from a novel application of microbial rhodopsins as fluorescent voltage indicators. For a long time the fluorescence of microbial rhodopsins has been considered negligible, designating this feature particularly astounding[3].

Properties of microbial rhodopsin based sensors are highly desirable for application in neuroscience research. These sensors would allow non-invasive, direct, real time and cell specific monitoring of changes in the membrane voltage. Mostly variants of the proton pump archaerhodopsin-3 (Arch3) are used for the development of rhodopsin-based fluorescent voltage sensors[3,6]. Although different variants have been established, the highest reported fluorescence quantum yield (QY) is only ~1.2%[1], which is significantly lower than fluorescent proteins commonly used in fluorescence imaging (e.g., 79% in GFP[7]). For applications in tissue, where strong light scattering is observed, it is necessary to improve the efficiency of these constructs, more precisely their QY. Additionally, red-shifted absorption maximum would be desirable, as it would provide lower scattering in the tissue. To develop improved constructs it is essential to understand their functionality and origin of the voltage sensitive fluorescence. This work aims to elucidate the underlying mechanism of these peculiar rhodopsins, in particular, the Arch3 variants – QuasArs and Archons[3,8].

In the following chapter the reader will be introduced to microbial rhodopsins, in particular the proton pumps bacteriorhodopsin (BR) and Arch3, optogenetics and fluorescent voltage sensors. In the closing section of this chapter, the outline of the objectives of this study will be described.

1. 1. Photoreceptors

Photoreceptor proteins mediate responses to light stimuli, converting the light signal into a cellular signal. A variety of photoreceptor proteins have been found with different chromophores and signaling concepts. The chromophores cover a broad spectral range, from UV to far red, with help of the spectral fine-tuning generated by the chromophore binding pocket of the proteins[4]. In the UV-B spectral region a protein, UVR8, exploits tryptophan side chain as a chromophore[9]. The blue and UV-A spectral region is covered by proteins binding flavin or *p*-coumaric acid as chromophore, such as BLUF (blue light sensors using flavin-adenine dinucleotide (FAD)), LOV (light-oxygen-voltage), cryptochromes, and xanthopsins[10,11]. Proteins that bind cobalamin as chromophore, such as coenzyme B12-based photoreceptor, absorb green to red light[12]. However, the broadest spectral region, from near UV to red light, is covered by the retinal and linear tetrapyrrole (bilin) chromophores[13–15].

Retinal-binding proteins, called Rhodopsins, are a special class of photoreceptors, because they are embedded in the cell membrane. Rhodopsins are, based on their structure, the bound retinal isomer, and the organism of origin, classified into two larger groups – animal and microbial rhodopsins. Animal rhodopsins are comprised of an opsin with a bound 11-*cis* retinal and are coupled to a G-protein. Light triggers retinal isomerization to all-*trans.* The light energy is used to activate heterotrimeric G-proteins, and initiate a downstream signal transduction cascade[16,17]. Microbial rhodopsins are comprised of an opsin and a covalently bound all-*trans* retinal. The light energy triggers retinal isomerization *to* 13-*cis* and enables ion translocation or activation of signal transducer.

In the following section microbial rhodopsins, and in particular BR and Arch3, will be discussed in more detail.

1. 2. Microbial rhodopsins

Microbial rhodospins are found in Eukaryotes (Fungi, Algae), Bacteria, Archaea[16,18]. They consist of seven transmembrane alpha helices (7TM) and an all-*trans* retinal cofactor bound via a Schiff base to helix G[17,18]. The energy of an absorbed photon induces retinal isomerization from all-*trans* to 13-*cis,* initiating conformational changes in the opsin domain. These conformational changes

facilitate diverse functions – active or passive ion transport, intracellular signalling or enzymatic activity (Figure 1)[16–25].

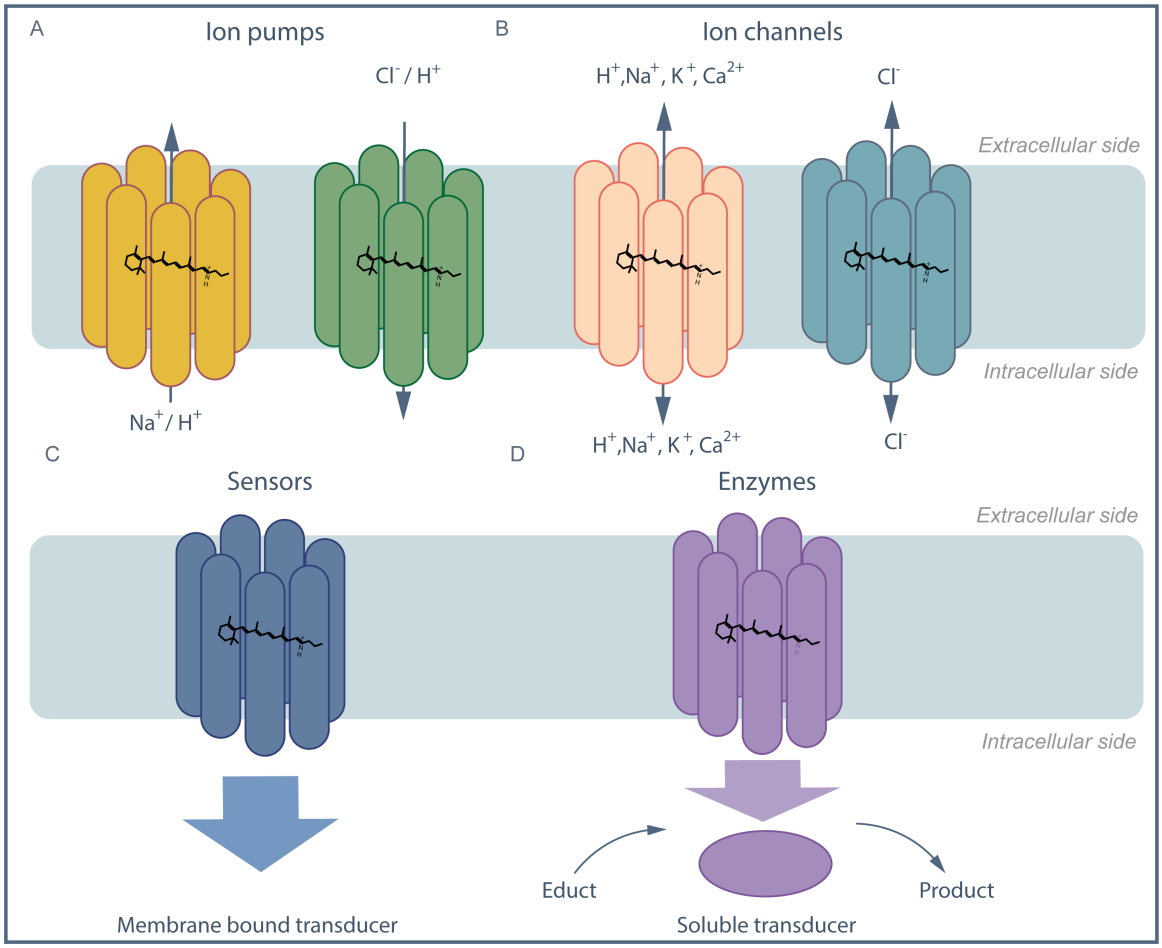

Figure 1. Different functions of microbial rhodopsins are depicted

Figure adapted from (Ernst et al. 2014; Kato et al. 2016; Mukherjee et al. 2019)[17,26,27]. Microbial rhodopsins can function as light-induced ion transporters. The arrows indicate direction of ion transport or flow. (A) Ion pumps actively transport ions against their electrochemical gradient. The pumping is either inward- or outward-directed. (B) Ion channels passively conduct cations or anions along an electrochemical gradient. (C) Sensory rhodopsins activate soluble or transmembrane transducer proteins. (D) Enzyme rhodopsins use the harvested light energy to catalyze a biochemical reaction.

Ion pumps (Figure 1 A) are using the harvested light energy for active ion transport against an electrochemical gradient. Based on the pump selectivity, there are four types of ion pumps. Inward-directed chloride (Cl^-) pumps, such as Halorhodopsin (HR)[28]. Outward-directed proton (H^+) pumps, such as BR and Arch3[19,29–32]. More recent additions are outward-directed sodium (Na^+) pumps, such

as *Krokinobakter eikastus* rhodopsin-2 (KR2), which were first reported in 2013[33]. And only in 2016 the first inward directed H^+ pump xenorhodopsin (PoXeR) was reported from a deep-ocean marine bacterium, *Parvularcula oceani*[34].

Light-gated ion channels (Figure 1 B), also referred to as channelrhodopsins (ChRs), passively transport ions along their electrochemical gradient. Based on their charge selectivity, ChRs can be categorized into two groups - anion channels and cation channels. Cation-conducting channelrhodopsins (CCRs), such as Channelrhodopsin-2 (ChR2) from the alga *Chlamydomonas reinhardtii*, transport competitively positively charged ions (H^+, Na^+, Ca^{2+}, Mg^{2+})[35]. Anion-conducting channelrhodopsins (ACRs), such as anion-conducting channelrhodopsin-1 from the alga *Guillardia theta* (*Gt*ACR1), transport Cl^- ions but also other anions[36].

Sensory rhodopsins (Figure 1 C) use the light energy to activate secondary signaling pathways, triggering photophobic or phototactic responses of the microorganism. The phototaxis response is mediated via protein-protein interaction with either a membrane-embedded transducer or a cytosolic transducer[17,24,37,38]. Sensory rhodopsin I and II (SRI and SRII), found in *Halobacterium salinarum*, were the first reported (1985) sensory rhodopsins. They act as positive and negative phototaxis sensors, respectively, by regulating a phosphorylation cascade, sending signals to the flagellar motor[37,39].

Enzyme rhodopsins (Figure 1 D) function as light-activated catalyzers of biochemical reactions. They are comprised of a membrane-bound light-sensing rhodopsin domain and an intracellular catalytical domain connected via linker[27]. Three types of enzyme rhodopsins have been reported. Histidine kinase rhodopsins (HKR) initiate a phosphorylation cascade[23]. Rhodopsin phosphodiesterase (RhoPDE) and rhodopsin guanylyl cyclase (RhGC) regulate hydrolysis or catalyze production of cyclic nucleotides [25,40–42].

1. 3. Bacteriorhodopsin and its photocycle

Bacteriorhodopsin (BR) is one of the most extensively studied microbial rhodopsins and has servred as a model protein. BR is a light-driven outward proton pump discovered in the halophilic archaea *Halobacterium salinarum* (1970s)[19]. BR, as other microbial rhodopsins, is comprised of seven transmembrane helices and a retinal chromophore, bound via Schiff base[17,43,44]. Absorption of a photon by retinal

drives a stepwise reaction chain – the photocycle – which ultimately returns to the initial dark state. The photocycle enables proton transport across the membrane. The resulting proton gradient drives production of adenosine triphosphate (ATP), which is serving as an energy source [29,30].

The photocycle consists of a sequence of spectroscopically distinguishable photointermediates– I, J, K, L, M, N, O -, as shown in Figure 2 A, B. The extensive study of BR with spectroscopic, crystallographic and other methods[45] has enabled thorough understanding of the protein transport and associated changes in BR. The active site of BR consists of a hydrogen-bonded network incorporating the positively charged retinal Schiff base ($RSBH^+$), negatively charged D85 and D212, and water molecule Wat402 (Figure 2)[46]. The counterions D85 and D212 aid to maintain the electrical neutrality. The active site is crucial for the proton transfer mechanism and will be in focus in discussing the following photointermediates.

The light adapted BR_{568} binds protonated 13-*trans*/15-*anti* (all-*trans*) retinal in the dark state[47]. The absorption of a photon drives isomerization of the conjugate double bond C_{13}=C_{14} resulting in a 13-*cis*/15-*syn* retinal isomer[48–51]. The excited state dynamics and the course of the retinal isomerization are shown in Figure 2 B, C. Ultrafast spectroscopy has allowed to determine and study the photointermeidates I, J and K[52–55]. Upon absorption of light, the BR_{568} is brought from the ground singlet state S_0 to Franck Condon region of the first singlet excited state S_1 (Figure 2 B)[56,57]. The excited molecules rapidly relax to the lowest vibrational level of the excited state S_1, denoting the I state (Figure 2 B, C)[53,56]. The I state is reached in ~200 fs and can be spectroscopically distinguished by rise of the absorption maximum at 460 nm and stimulated emission > 650 nm[53,57–61]. At the excited state the charges in the retinal are redistributed towards the β-ionone ring, changing the dipole moment and polarizing the retinal (Figure 2 C)[52,62]. The planar geometry of the retinal is distorted where changes in the bond lengths (extension of double bonds and contraction of single bonds) and torsion around the C_{13}=C_{14} bond take place[48,53,63]. Interaction between the adiabatic surfaces - S_1 and S_2, raises a small energy barrier for depopulation of the S_1 state[53,58,63]. The passage from the S_1 excited state back to S_0 occurs through the conical intersection (CI) where the potential energy surfaces intersect[64]. Within ~500 fs the J state is populated, giving rise to an absorption maximum at 625 nm[53,59,65]. The J state is the primary ground state

photointermediate, which initiates the retinal isomerization, resulting in the K state (λ_{MAX} = 590 nm)[53–55]. The quantum efficiency of the retinal photoisomerization is 0.64. The K state is reached within ~ 3 ps after photoexcitation and has a 13-*cis* retinal (Figure 2 B, C)[55,66]. The interaction between the retinal chromophore and the chromophore-binding pocket of the protein play a crucial role in the stereo selectivity of retinal isomerization[48,64]. Series of structural snapshots recorded with X-ray laser allowed identifying aspartic acids D85 and D212 and functional water molecule (Wat402) in the retinal Schiff base (RSB) proximity as guides for highly efficient *trans*-to-*cis* isomerization[48,67]. In particular, the loss of the hydrogen bond between $RSBH^+$ and Wat402 lowers energy barrier particularly for C_{13}=C_{14} isomerization[66], as indicated by the high isomerization quantum efficiency[55,66]. Additionally, quantumchemical calculations showed that energy barrier for other isomerization pathways are considerably higher, designating C_{13}=C_{14} isomerization the most energetically favourable[68].

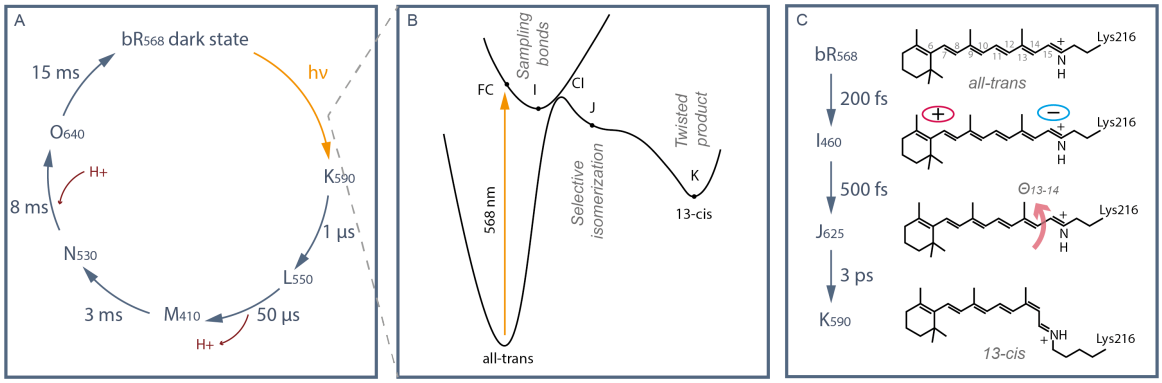

Figure 2. Retinal isomerization and photocycle of bacteriorhodopsin

Panel (A) shows a photocycle of light adapted BR_{568} [69,70]. The reaction coordinate of BR excitation and isomerization is shown in panel (B)[48]. The photointermediates leading to photoisomerization of BR_{568} is shown panel (C).

The energy accumulated in the K state with torsion of the polyene chain drives the photocycle (Figure 2, Figure 3) and the vectorial proton transport[69,71,72]. The L state rises in ~ 1 µs and it is denoted by a blue shift of the absorption maximum to 550 nm[73]. The helix C bends towards the helix G and $RSBH^+$ moves towards hydrophobic pocket on the cytoplasmic side[73,74]. Additionally, slight perturbation of R82 and E194 is observed. The movement of the residues affects the hydrogen-

bonding network in their proximity[74]. Furthermore, hydrogen bond between $RSBH^+$ and Wat 402 is reestablished and interaction between $RSBH^+$ and proton acceptor D85 is increased[74–76]. The alterations taking place affect the local pK_a values of the residues in the active site[77]. Reports of the structural changes taking place in the L state are ambiguous, but it is recognized that these changes accommodate the transfer of the Schiff base proton to the counterion D85, during the formation of subsequent M state[74].

The M state is denoted by a further blue-shifted absorption maximum (λ_{MAX} = 410 nm) and is populated in ~50 μs[78,79]. The M state differentiates in two substates M_1 and M_2. The M_1 state is in equilibrium with the L state and maintains accessibility to the extracellular side, whereas M_2 state is in equilibrium with N state and switches accessibility to the intracellular side[17,80–85]. In the transition L to M_1 state, the proton from $RSBH^+$ is transferred to D85 via T89[86]. With the rise of M_2 state the proton, from proton release complex on the extracellular side (E194 and E204), is released[87]. The proton release is facilitated through R82. Upon D85 protonation, the positively charged R82 flips away, towards the extracellular side (E194 and E204), repelling the bound proton[88–90]. The rise of N state take place in 3 ms and is accompanied by rise of absorption maximum at 530 nm[91]. Upon rise of the N state, D96 donates a proton to the RSB via water molecule chain[92]. The rearrangement of hydrogen bonds between helix F and helix G allows formation of proton conducting pathway through the water molecules, and aids transient decrease of D96 pK_a value from 11 to 7.5[90,93,94]. The O state is accompanied by the rise of the absorption at 640 nm at ~8 ms[70]. Charged residues on the cytoplasmic side capture the proton as an "antenna"[95–97]. A second water chain allows the proton transfer to D96[69,98]. Simultaneously, back isomerization of retinal from 13-*cis* to all-*trans* takes place[99]. With the dark state recovery the proton from the D85 is donated to the proton release group (E194, E204)[100]. The changes in pK_as (D85 pK_a ~3.5 and proton release complex pK_a ~ 11) are believed to be the incentive for the proton transfer. The D85 remains protonated until the last step of the photocycle, insuring one directional charge transfer[69,101,102].

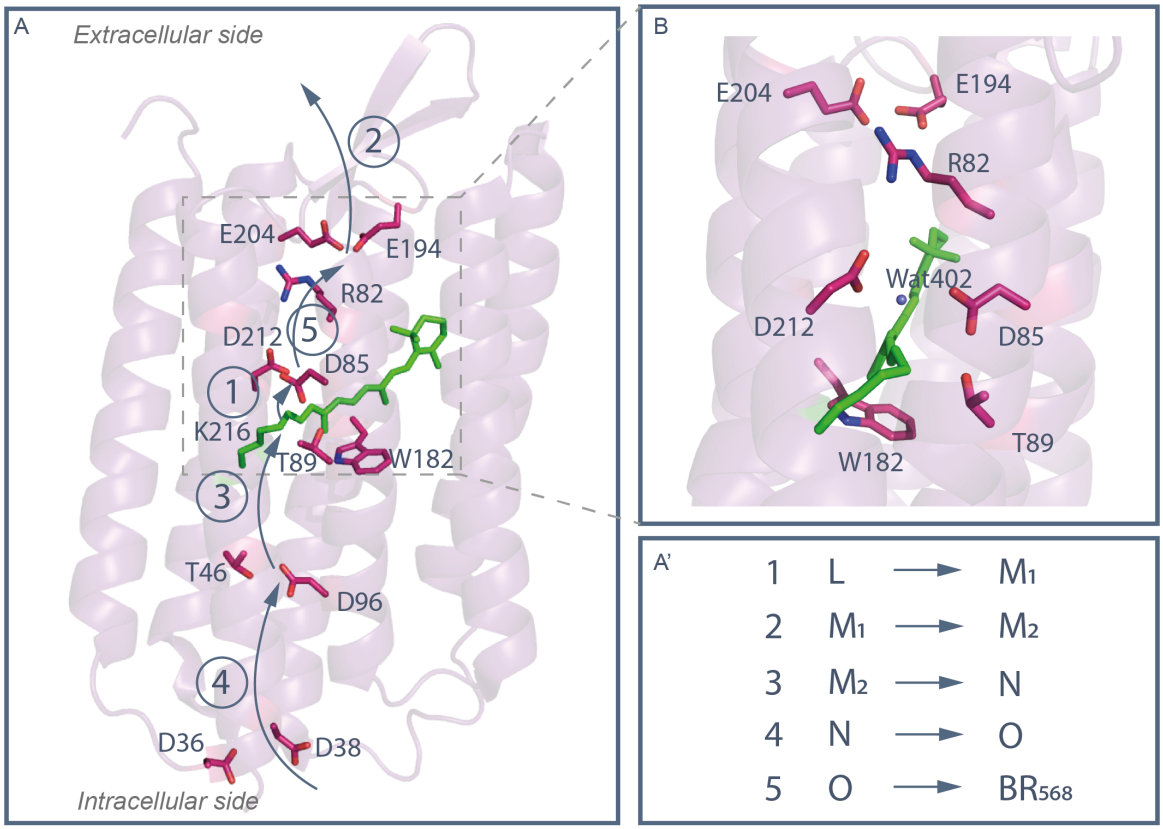

Figure 3. Ion transport in BR

Panel (A) shows the steps involved in BR proton transport overlayed on the crystal structure (PDB ID: 5ZIM[103]). A close-up of the active site is shown in panel (B) indicated in the crystal structure of BR. Image is adapted from (Bondar et al. 2004, Ernst et al. 2014)[17,86].

1. 4. Fluorescence studies of bacteriorhodopsin

The initially reported values of fluorescence quantum yield (QY) of BR showed inconsistencies. The reported QY ranged between 0.0025% - 0.027%[104–106]. Additionally, three fluorescent decay components had been observed – sub ps, ~9 ps and ~62 ps[107]. The discrepancies arise from intensity dependent accumulation of different photointermediates throughout the photocycle of BR_{568}, under continuous illumination.

Picosecond fluorescence studies of BR have revealed the O and the Q as the fluorescent states, in contrast to the N state and the dark state[107–110]. However, the O and Q states yield fluorescence as multi photon process. Single photon-triggered fluorescence emerges from the dark state of BR_{568}. The low emission arises from the excited state (I_{460}), which is short-lived (~0.5 ps)[110–112].

The fluorescence of the O state is a two-photon process with a QY = 0.1% and decay of ~9 ps (Figure 4)[110]. The emission spectrum of the O state is similar to that of deionized purple membrane BR_{605}, with maximum at 750 nm[109]. Interestingly, the observed photoproduct of the O state, along with the photoproduct of deionized purple membrane BR_{605}, are reported to comprise a 9-*cis* retinal[113,114].

The Q state has the highest reported QY = 0.7% (estimated from radiative lifetime) and the slowest decay of ~ 62 ps[110]. The fluorescence emission spectrum of the Q state is similar to that of the dark state BR_{568}, with maximum at 720 nm[109]. But the Q state fluorescence arises from a three photon process. The Q state can be populated only through photo-branching from the N state in alkaline conditions (pH > 9.3) (Figure 4)[108]. Alkaline conditions shift the quasi-equilibrium between N and O states, towards the N state, increasing likelihood of photo-branching[107,109]. The Q state is not thermally stable and ultimately converts to the dark state BR_{568} within 1.7 ms[108,109]. Although the Q state absorption overlaps with the O state absorption (~630 nm), the states differ in their kinetics. Furthermore, the Q state kinetics are independent of the pH[108].

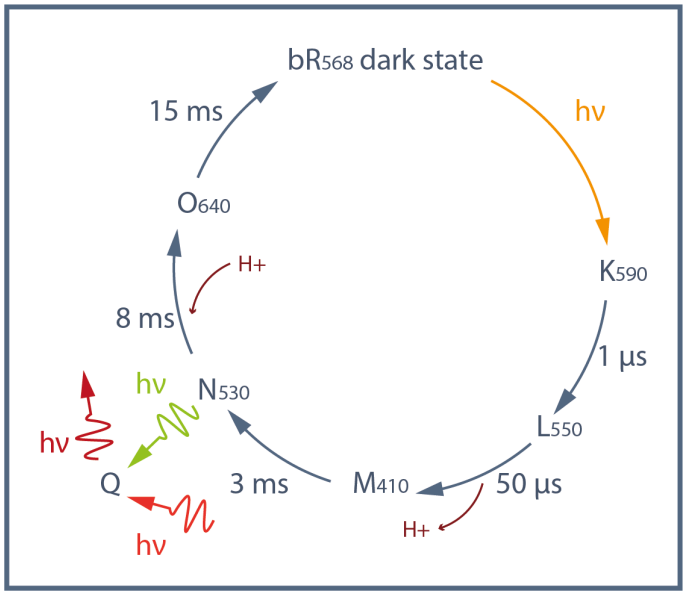

Figure 4. Bacteriorhodopsin photocycle with indicated fluorescent state

The fluorescence of BR arises through a three-photon process, where the first photon (558nm) initiates the photocycle. The second photon (530 nm) induces branching form the N state. The third photon (red) absorbed by the fluorescent Q state is reemitted (> 650 nm).

1. 5. Archaerhodopsin 3

Archaerhodopsin-3 (Arch3) is a microbial rhodopsin that shows high similarity to BR (~ 75% sequence homology)[31,115]. It has attracted interest due to its applications in neuroscience research. Primarily, Arch3 is used in optogenetics to inhibit action potential firing. Upon light-activation Arch3 hyperpolarizes the cell membrane[32]. Secondarily, Arch3 allows optical recoding of neuronal signaling operating as fluorescent voltage sensor[6].

Arch3 was found in *Halorubrum sodomense* and functions as a light-driven outward-directed proton pump[31,32]. The key residues involved in proton transport are conserved in Arch3 compared to BR. For example, residues located in the active site (Arch3-D95, D222; BR- D85, D212), the proton release complex (Arch3-E204, E214; BR- E194, E204) and the proton donor (Arch3-D106; BR-D96) are equivalent[31,115]. The mechanism of Arch3 proton-pumping has been studied with transient absorption spectroscopy[116], Fourier-transform infrared (FTIR) spectroscopy[115], and Raman spectroscopy[117]. Additional insights into Arch3 mechanism have been obtained from resolved X-ray crystal structures of highly homologous proton pumps archaerhodopsin-1 (AR1) and archaerhodopsin-2 (AR2) (~90% sequence homology)[31,118].

The reported photocycle of Arch3 is similar to that of BR (Figure 5)[115,116]. The FTIR and Raman spectroscopic studies[115,117] provided evidence of similar retinal isomers and conformational changes taking place during the proton transport. Correspondingly, after absorption of a photon (550 nm) Arch3 undergoes retinal isomerization from all-*trans* to 13-*cis*, designating population of the K state[115,117]. The transient absorption spectral recordings (from 10^{-5} to 10^{-1} s) revealed kinetics of the subsequent states (M, N and O)[116]. Although the provided temporal window is too slow to resolve the L state, it is postulated that it is formed prior to the M state in analogy to BR [115,116]. L state corresponds to conformational changes taking place in the rhodopsin to facilitate proton transfer from the $RSBH^+$ to proton acceptor[74]. Blue-shifted ($\lambda_{MAX} =$ 400 nm) M state arises in 50 μs. The proton from the $RSBH^+$ is transferred to adjacent negatively charged D95. The M state decay is fit with single exponential of 390 μs. The N state is barely spectroscopically evident, due to its absorption overlapping with the ground state. During the N state, a proton is released from the negatively charged residues on the extracellular side (E204,

E214), and the RSB is reprotonated from D106. The fit of the red-shifted O state (640 nm) rise is bi-exponential, revealing two time constants - 390 µs and 4.1 ms. The O state designates retinal backisomerization to all-*trans* and reprotonation of D106 from the intracellular side. The O state decays within 14 ms back to the dark state, indicating proton transfer from proton acceptor D95 to proton release complex E204 and E214[45,115–117].

Besides the photocycle, also the fluorescence properties are conserved between the two rhodopsins. However, the fluorescence properties of Arch3 have not been studies as thoroughly as for BR. Fluorescence studies with multi-photon excitation revealed an intermediate with 6-fold increased fluorescence intensity compared to the dark state (estimated QY ~0.01%[1]). The analogous Q state is reached with a three-photon process (Figure 5). The first photon (550 nm; dark state absorption maximum) triggers the photocycle, the second photon (560 nm; 10 nm blue-shifted compared to the dark state absorption) initiates photo-branching to the Q state and the third photon (570 nm) gives rise to fluorescence[116]. The emission maxima was observed at 710 nm[116], however no reports are available on estimated quantum yield.

Moreover, Arch3 fluorescence studies with HEK293T cell assay revealed that fluorescence attained through multi-photon process (likely Q state) is voltage sensitive. Whereas, the fluorescence generated through dark state was not. Interestingly, the excitation wavelength titration, to attain the largest change of fluorescence intensity depending on the voltage change, peaked at 590 nm. Although, the highest fluorescence intensity was obtained with excitation at 570 nm[6,116].

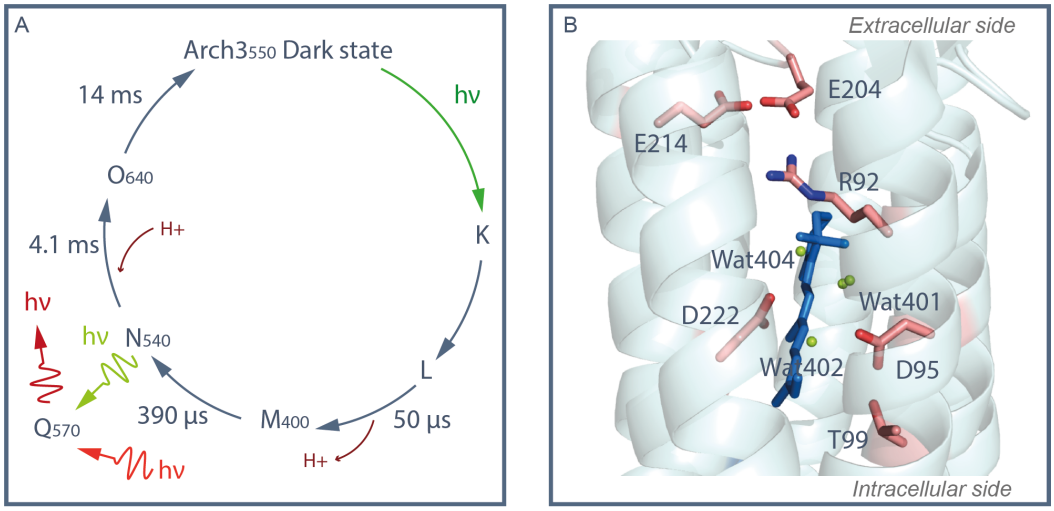

Figure 5. Photocycle of Arch3

The photocycle of Arch3 is adapted from[116] *and shown in panel (A). The proposed photocycle is similar to BR. Upon photoexcitation and ion transport the protein goes stepwise through the following intermediates K, L, M, N and O. Fluorescence of Arch3 is expected to arise from photobranching of the N state, consequently requiring three photons. The retinal-binding pocket of Arch3 with indicated counterion complex and proton release complex are shown in panel (B). The source of the crystal structure: RCSB PDB 6S63* [119].

1. 6. Optogenetics

Optogenetics employs the light-dependent nature of photoreceptor proteins to optically control the activity of cells/neurons[120–124]. Although, the proposal of controlling cell activity with light dates back to 1980s[125,126], there were many obstacles to overcome. For this field to develop, advancements in suitable photoreceptors, genetic targeting strategies and optics were needed[120].

A big stepping-stone was discovery of ChRs[35,127]. ChR2 had sufficiently high photocurrents and expression levels to enable the early experiments for light-triggered neuron activation[123,128,129]. This prompted microbial rhodopsins to become a crucial part of optogenetic toolbox. Microbial rhodopsins provide “on”- and “off”-switches for neuron activity. ChR2, which is a passive cation channel, depolarize the cell membrane, triggering action potential in neurons (Figure 6 C). Whereas ion pumps, such as HR and Arch3, hyperpolarize cell membrane, inhibiting action potential transmission in neurons (Figure 6 D)[120,121,130].

The requirements for neuronal studies contributed to new quests in microbial rhodopsin research. Search of new microbial rhodopsins, and engineering of custom

properties of the available variants accelerated to meet the demand in particular kinetics, wavelength sensitivity, and ion selectivity[118,119]. For example, engineering of ChR variants like ChETA (ChR2 variants with point mutation of E123T) with faster kinetics[131], or C1V1 (chimeric channelrhodopsin from CrChR1 and VcChR1) with red-shifted absorption maximum[132]. Further applications of rhodopsins were introduced by enzyme rhodopsins, which allow optical control of signaling cascades through secondary messengers (cAMP - cyclic adenosine monophosphate)[27,42]. The discovery of Na^+ pump KR2 introduced additional inhibitory tool, which would not affect the local H^+ or Cl^- gradient[33,133]. KR2 showed also potential as engineered K^+ channel, which would also serve as a highly desirable inhibitory tool[134].

Crucial aspect of optogenetics is targeting specific cell types. Cell targeting can be achieved using viral (frequently used Lentivirus (LV) or Adeno-associated virus (AAV)) delivery of microbial rhodopsin with cell type specific promoter (Figure 6 A). However, in some cases the specific promoter sequences become too long to introduce into viral sequences or are unknown. In these cases recombinase-dependent rhodopsin expression is used[121,135]. To achieve cell-specificity in complex neuronal networks in this manner, viral injection of opsin (recombinase-dependent expression) is combined with either injection of second virus expressing recombinase, or transgenic animal line (which expresses recombinase in specific cell types)[121,136–138].

The activation of microbial rhodopsins with high precision is achieved through illumination. Dependent on the experimental setup different illumination strategies are employed. Light from high-intensity LEDs (Light-emitting diodes), which are controlled with a shutter, is delivered through optical fibers directly to freely moving animals. Optical fibers can be simultaneously used for input and output of optical signals (Figure 6 A)[139]. Laser-scanning one-photon microscopy[135], or highly specific two-photon microscopy[140] is frequently used for static samples. Holographic light patterns enable the monitoring of changes with high spatial precision up to nanometer-scale[141].

Effects initiated by optogenetic tools can be observed either as changes in animal behaviour or readout of cellular signals[121]. To monitor the changes in cells either electrodes or fluorescent sensors are used. Patch-clamp electrophysiology is used for monitoring changes in single-cell membrane potential and to track action potentials

(Figure 6 B)[142–144]. Genetically encoded calcium indicators (GECIs) give fluorescent signals once bound to calcium ion indicating neuronal synaptic transmission. Imaging of fluorescent signals from GECIs provides immediate information of many genetically defined neurons[145,146]. Although GECIs show advantage over patch-clamp for multicellular monitoring of neuronal signal transmission, GECIs provide only indirect measurement of neuronal activity. Genetically encoded voltage indicators (GEVIs) are able to overcome this limitation and provide simultaneous multicellular information of direct neuronal activity[147,148]. Function and application of GEVIs will be discussed in more detail in the following paragraph.

Optogenetics has become an essential tool in neuroscience, proving high temporal and spatial resolution for study of neuron activity. It has provided understanding in animal behaviour[142,143] and neurodegenerative disease development[149], and shows high potential in application for treatments, such as vision restoration[150,151]. The field of optogenetics continues to grow, providing further advancements and novelties in application[121]

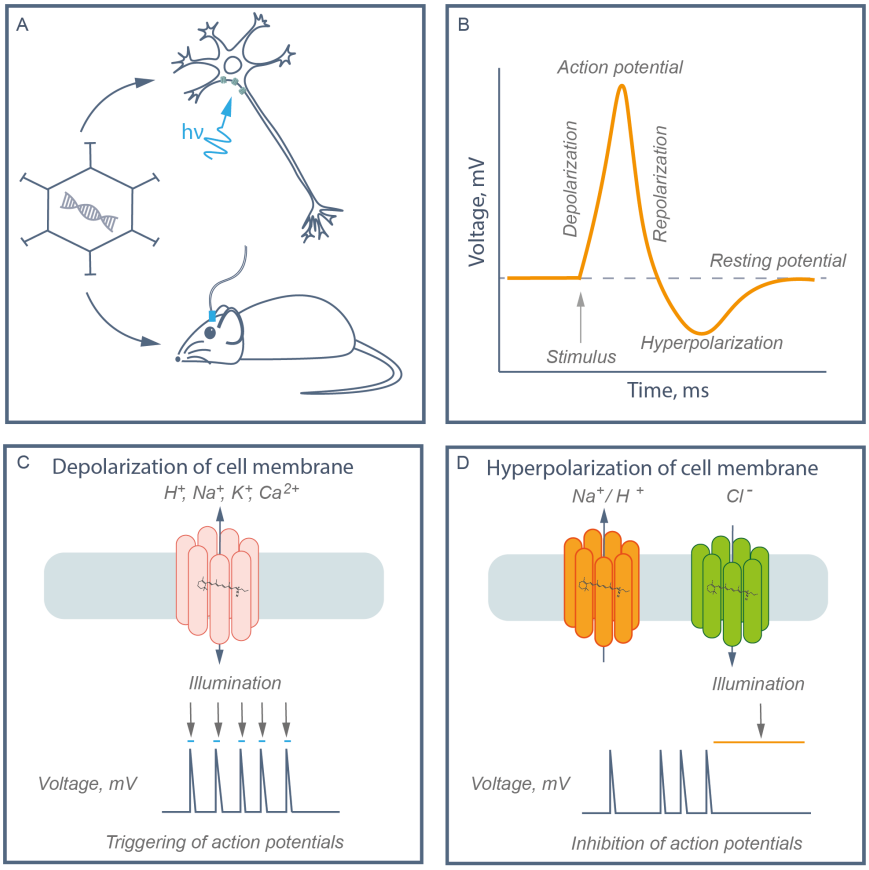

Figure 6. Optogenetics

The panel (A) shows schematic representation of viral opsin gene injection in neuron cultures or animal models. The panel (B) shows a representation of action potential. The panel (C) displays a cation-conducting channelrhodopsin used for membrane depolarization and a schematic representation of activation of action potentials. The panel (D) displays a cation outward pump and anion inward pump used for cell membrane hyperpolarization. And a schematic representation of inhibition of action potentials. Images adapted from (Deisseroth et al. 2015; Lodish et al. 2013)[120,152].

1. 7. Genetically encoded voltage indicators (GEVIs)

The primary goal in neuroscience is to study the brain function and understand how emotions, memories, behaviour, and perception are formed. Essential part of understanding the fundamentals is to study how the neuronal electrical signals translate in different brain activity. The direct monitoring of neuronal circuit dynamics, firing of action potentials, and membrane voltage are facilitated using genetically encoded voltage indicators (GEVIs). Only recently, breakthroughs in imaging techniques and design of suitable GEVIs opened the way for its applications in neuroscience[153,154].

To study the mechanism of complex neuronal networks, it is essential to have high spatial resolution and target specific neuron types. As introduced in the previous section, also expression of GEVIs can be regulated with cell specific promoters. And additional selection parameters can be provided with illumination patterns. GEVIs are expressed and localized in the cell membrane, enabling direct observations of the cell membrane potential. GEVIs are fluorescent voltage sensors, that is, their fluorescence intensity depends on the membrane voltage. The response in fluorescence change must be fast enough (≤ms) to resolve processes taking place in neuronal networks. Optical recordings of the fluorescence fluctuations provide readouts of brain electrical activity across different spatial scales – ranging from single neuron up to interaction between multiple neurons in large neuronal networks[153].

Based on GEVI conformation they can be divided into three groups (Figure 7). The first group (Figure 7 A) of GEVIs (also called voltage sensitive fluorescent proteins (VSFPs)) entails fusion constructs comprised of voltage-sensing domains (VSD) and fluorescent protein (FP)[155]. Two subtypes are in this group – FP-FP- Förster resonance energy transfer (FRET) and Monochromatic FP. In case of FP-FP-FRET, two FPs (commonly GFP (green fluorescent protein) variants) are attached to voltage-sensing four-transmembrane domain (commonly used potassium channel Kv3.1). The membrane potential change results in conformational changes of VSD, affecting interaction between the pair of attached FPs and the efficiency of FRET (VSFP 2.3[156]). Mechanism of monochromatic FP (also called single FP) GEVIs is based on sensitizing the FP domain through circular permutation, however further studies need to be carried out for complete explanation of the processes taking place[153,157] (cpFP VSFP3[158]).

Second group (Figure 7 B) are opsin-based GEVIs. Here, an opsin mutant is a single component GEVI, which simultaneously serves as voltage-sensing and fluorescent domain (Arch3-D95N[6], QuasArs[3], Archons[157]). As the current constructs are limited with low fluorescence QY, FRET based pairs have been developed, which are comprised of opsin as voltage-sensing domain and an FP (QuasAr2-mOrange2[159])[153] .

The third group comprises hybrid GEVIs (Figure 7 C). This group of GEVIs requires a synthetic compound that needs to be invasively added to the cells. These

constructs rely either on FRET or photo-induced electron transfer (PeT). Here, different combinations have been explored with opsin-dye pair, FP-dye and combination of PeT dyes with membrane protein (VoltageSpy)[160].

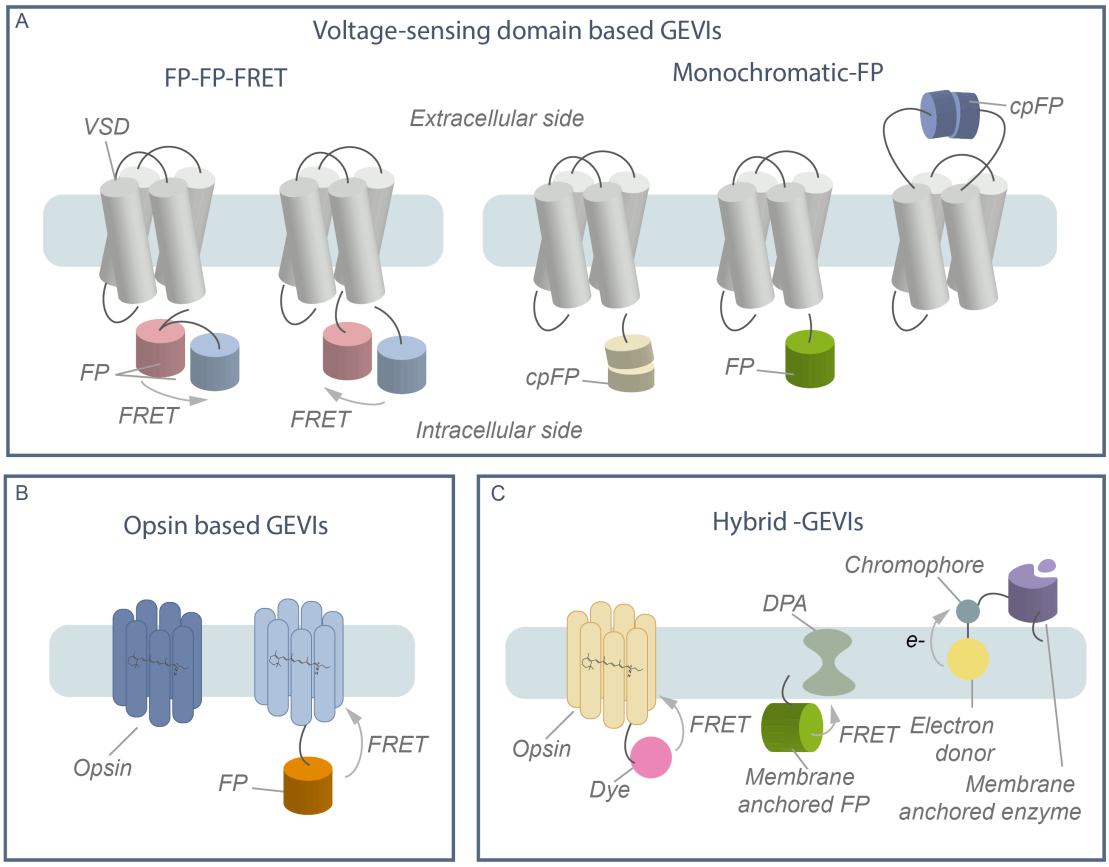

Figure 7. Classification of GEVIs

The image is adapted from Knöpfel et al. 2019[153]. The upper panel (A) displays fluorescent sensors, which are based on voltage-sensing domain (four transmembrane segment) and fluorescent protein. Based on the mechanism, this category can be subdivided in two groups. First, FRET based sensors with two fluorescent proteins. Second, monochromatic fluorescent sensors, where one fluorescent protein is attached and fluorescence is modulated by voltage-dependent conformational changes. In the lower left panel (B) the opsin-based sensors are designated. Opsin-based GEVIs can be classified in stand-alone tools (left) and fusion constructs (right). The stand-alone opsin based GEVIs are simultaneously the voltage-sensing and the florescent domain. Whereas in the fusion constructs, opsin serves as the voltage-sensing domain and fluorescence of attached fluorescent protein is modulated by FRET. In the lower right panel (C) the hybrid sensors are shown. These constructs are fusion between a protein and a synthetic dye. Two main mechanisms for functionality have been established. First, fluorescence intensity modulated via FRET. Second, fluorescence intensity is modulated via photo-induced electron transfer (PeT).

The compatibility of the different developed GEVI variants to the experimental setup is characterized by following properties: fluorescence QY and brightness (depends on expression level), photo-bleaching (loss of fluorescent signal with longer illumination), voltage-dependent change of fluorescence intensity (described as ΔF/F), response time, molecular signal-to-noise ratio (SNR) (depends on the brightness), sensitivity (depends on membrane localization) and photo-toxicity[153].

Using GEVIs, in contrast to patch-clamp electrophysiology, allows scaling up the number of measured neurons and measuring membrane voltage in freely moving animals. Recordings of fluorescent signal from living animals can be achieved with optical fibers[161,162]. For static samples, techniques with higher spatial resolution can be used, such as microscope setups and two-photon excitation[163]. As mentioned in previous paragraph, optogenetic tools can be used in combination with GEVIs, provided sufficient spectral separation between the constructs. This method allows all-optical electrophysiology in large neuronal networks with high temporal and spatial resolution and is very powerful tool in neuroscience research[3,153,164].

1. 8. Opsin-based GEVIs

In this study, the opsin based fluorescent voltage sensors are of particular interest. When compared to other types of GEVIs, rhodopsin based sensors have the following advantages: high cell specificity, fast response and low photo-toxicity[6,153]. However, for long time, microbial rhodopsin fluorescent quantum yield was considered too low ($2.5 \cdot 10^{-3}$ % – $2.7 \cdot 10^{-2}$ %) for imaging application[104–106]. The reports of peculiar constructs, showing voltage-sensitive fluorescence, and increased fluorescence QY, changed this paradigm[2,3,6,165]. Rhodopsin-based constructs serve as both, the voltage-sensing and the fluorescent domain[6,153].

Since Arch3 was demonstrated as fluorescent voltage sensor in 2012[6], many Arch3-based constructs have been published (Table S1). From these the most prominent ones are QuasArs[3], Archons[2] and Arch5/7[1] and will be introduced in the following paragraphs.

Arch3 is a desirable construct for development of voltage sensors, due to high membrane-targeting and early findings of its membrane potential-dependent fluorescence. Inspired by BR-D85N construct[166], transfer of counterion mutation in

Arch3 (D95N) inhibits proton pumping[6]. This was a favorable mutant for further development of Arch3-based fluorescent voltage sensor. The fluorescence QY of Arch3-D95N is rather low (0.04%)[6] and comparable to the wild-type (~0.01%)[1]. Notably, this mutation increases the voltage sensitivity 1.5-fold, yet it slows down the voltage response kinetics from sub-milliseconds ($\tau_{response}$~0.5 ms) to tens of milliseconds ($\tau_{response}$~40 ms)[6]. Nonetheless, Arch3-D95N was a suitable candidate for development of new fluorescent voltage sensors.

Studies on Arch3 and Arch3-D95N hypothesized that membrane potential regulates the protonation of RSB[6,116,117]. Raman spectra recordings of Arch3-D95N chromophore provided some additional insights into the possible voltage-sensing mechanism. *Escherichia coli* (*E. coli*) cell solution with overexpressed Arch3-D95N was measured before and after addition of protonophore carbonyl cyanide m-chlorophenyl hydrazine (CCCP) to abolish the resting membrane potential. Comparison of the two spectra indicated voltage-sensitive 13-*cis* retinal isomer. 13-*cis* retinal contributions to the spectra increased upon more positive membrane voltage. This observation was interpreted as protonation and deprotonation of 13-*cis* retinal Schiff base upon change in membrane voltage[117]. However, more studies need to be carried out to explain the voltage-sensing mechanism.

1. 8. 1. QuasArs

In 2014 Hochbaum et al.[3] reported two constructs, QuasAr1 and QuasAr2 (QuasAr– quality superior to Arch), which showed more than ~10-fold increase in fluorescence QY compared to the wild-type Arch3[1,3,167]. The two constructs were discovered using random mutagenesis of Arch3 and high-throughput screening of variants for fluorescent voltage sensitivity[3].

The two constructs carry five mutations, respectively, compared to the wild-type as indicated in Figure 8. But they differ from one another with a critical mutation at the counterion position D95Q/H. QuasAr1 holds exchange of the negative charge to a positive charge (D95H). This mutation contributes to its higher fluorescence QY (0.8%), faster response to the voltage change (τ_1=0.05 ms, τ_2=3.2 ms, measured at 23 °C), but lower voltage sensitivity (ΔF/F=33% per 100mV). In QuasAr2, a neutral residue replaces the negatively charged residue (D95Q). This mutation results in

comparably lower fluorescence QY (0.04%) and slower response to the voltage change (τ_1=1.2 ms, τ_2=11.8 ms, measured at 23°C). Despite these minor drawbacks, QuasAr2 is a desirable construct due to its high voltage sensitivity, presenting increase of fluorescence by ΔF/F=90% per 100mV voltage step. Both constructs displayed linear increase in fluorescence intensity dependent on increase in membrane voltage (measured with 640 nm excitation). Excitation maxima of QuasArs were reported to be 590nm, whereas emission maxima were at 715 nm. The fluorescence intensity showed linear dependence on the excitation intensity, suggesting one-photon induced fluorescence. Characterization of QuasArs was performed in HEK cells with 637nm laser excitation (300 W/cm^2). Neither of the constructs produces photocurrents, making them desirable voltage reporters[3].

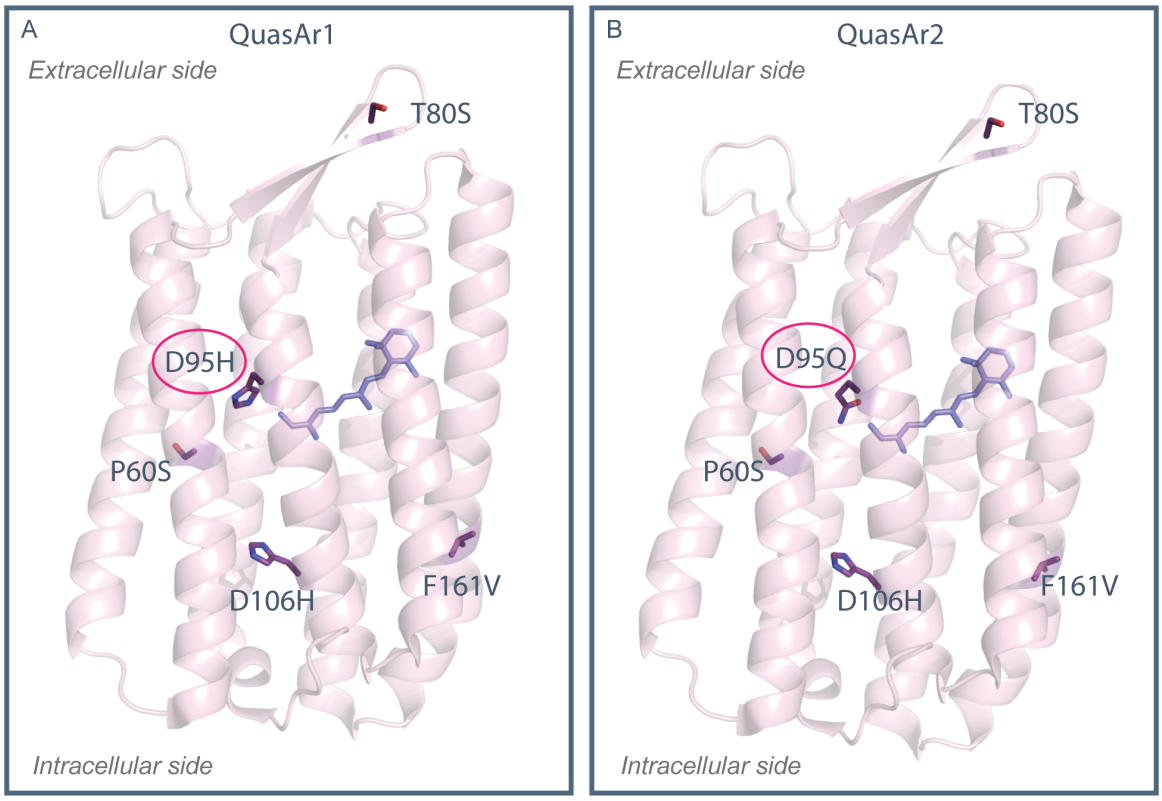

Figure 8. Mutations introduced to create QuasArs

QuasAr1 and QuasAr2 mutations[3] represented in crystal structure of Arch3 (RCSB PDB 6S63[119]).

QuasArs were tested in combination with the channelrhodopsin CheRiff (Optopatch[3] – coexpressed pair) to establish all-optical electrophysiology. The neuronal actuator and the fluorescent sensors were spectrally well distinguished to

eliminate cross-talk. The excitation of QuasArs was achieved using 640 nm while CheRiff was excited with 488 nm. Optopatch was shown to be suitable construct for triggering and reporting neuronal action potentials in neuron cell cultures and brain slices. The voltage sensors were sufficient to resolve even subthreshold events. However, averaging over 100-400 recorded temporal signals were required to improve the signal-to-noise ratio[3].

1. 8. 2. Archons

In 2018 Pietkevich et al.[2] published two new promising constructs Archon1 and Archon2 (Figure 9). The constructs were discovered using high-throughput screening. The group from Media Lab, Massachusetts Institute of Technology (MIT) developed robotic multidimensional directed evolution technique to pursuit improved fluorescent voltage sensors. The high-throughput screening allowed automated microscopy-guided selection of mammalian cell cultures with preselected desirable properties – increased brightness and improved membrane localization. This method allows screening of hundreds of thousands of proteins in just few hours[2].

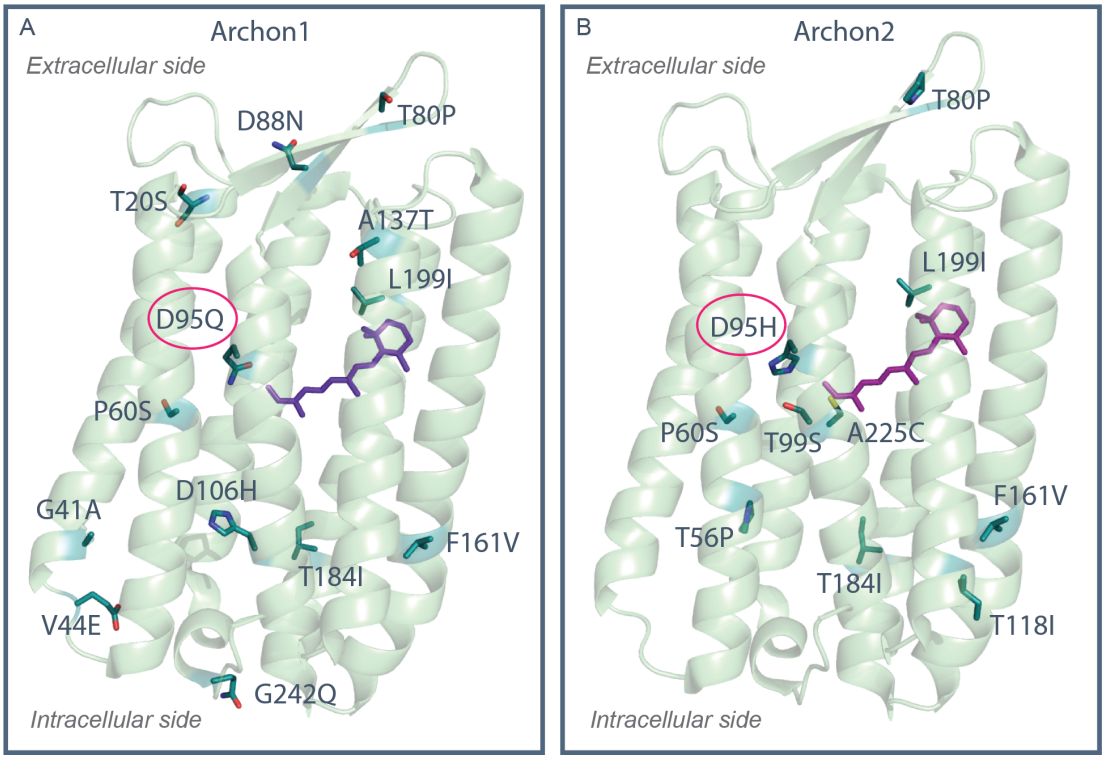

Figure 9. Mutations introduced to create Archons

Archon1 and Archon2[2] *mutations in Arch3 crystal structure (PDB 6S63*[119]*). The mutations at the counterion positions are conserved from QuasArs. Additionally, P60S, T80P, D106H and F161V originate from the first-generation QuasArs.*

The most prominent candidate was found to be Archon1, with introduced 13 point mutations compared to wild-type Arch3 (Figure 9 A). Also, Archon1 holds D95Q mutation as QuasAr2. But with the additional mutations, the construct outperformed the previous generation QuasAr2 with improved membrane localization, SNR, stability, and brightness (2.4-fold). Archon1 response to the voltage change is biexponetial τ_1=0.61 ms, τ_2=8.1 ms (measured at 34°C) and results in increase of fluorescence by ΔF/F=81% per 100mV. The second promising construct Archon2 has 10 point mutations compared to the wild-type Arch3 (Figure 9 B). The counterion mutation D95H is resembling QuasAr1. Archon2 possesses faster voltage change (τ_1=0.06 ms, τ_2=6.7 ms, measured at 34°C), but lower voltage response (ΔF/F=20% per 100mV). However, Archon2 shows 6.8-fold increase in brightness compared to QuasAr2. Analogous to QuasArs, it was demonstrated that fluorescence of Archons is a one-photon process, fluorescence intensity linearly depends on membrane voltage and Archons do not produce any photocurrents.

Characterization was carried out in HEK cells with 637 nm laser excitation (800 mW/mm^2)[2].

Performance of Archons was tested in neuronal cell cultures, brain slices, and *in vivo* in zebra fish. The experiments verified capability of Archons to record the synaptic activity[2].

1. 8. 3. Arch5 and Arch7

Alternative study of directed evolution of fluorescent voltage sensors was reported in 2014 by MsIsaac et al.[1]. Error-prone PCR (polymerase chain reaction) mutagenesis and screening identified mutations in the retinal-binding pocket that result in increased fluorescence intensity. The two constructs with the highest fluorescence QY were Arch5 (0.87) and Arch7 (1.2%) The QY of Arch7 is still the highest reported up to date. Arch5 has 5 point mutation compared to the wild-type Arch3, whereas Arch7 has 7 point mutations (Figure 10). In difference to QuasArs and Archons, the Arch5 and Arch7 constructs retain a negative charge at the counterion position with the replacement D95E, but carry additional mutation in the Schiff base proximity T99C. Interestingly the double mutation D95E-T99C results in a strong red shift (70 nm) of the absorption maximum compared to the wild-type Arch3. The constructs were tested in *E.coli* cell assay upon external pH exchange to predict the voltage-sensing capability. In these experiments, Arch5 fluorescence intensity would strongly depend on the external pH, whereas Arch7 would display only minor change[1].

Additionally, MsIsaac et al. 2014[1] proposes the role of the RSB pK_a in voltage-sensing mechanism. Both Arch5 (7.6) and Arch7 (8.4) have lower pK_a than the wild-type (>10). Arch5 has the pK_a value closest to neutral, allegedly aiding better voltage sensing properties[1].

There are no reported studies on Arch5 and Arch7 voltage-dependent fluorescence in mammalian cells. Nonetheless, the parental construct Archer1 with the key mutations D95E and T99C has been studied in neuron cell cultures. Archer1 is bifunctional depending on the excitation wavelength. Excitation with red light (655 nm) provides voltage-sensitive fluorescence, whereas excitation with green light (560 nm) produces photocurrents[1]. It displayed high voltage sensitivity ΔF/ F =85% per 100mV and comparable kinetics to Arch3 ($\tau_{response}$~0.5 ms)[1,6].

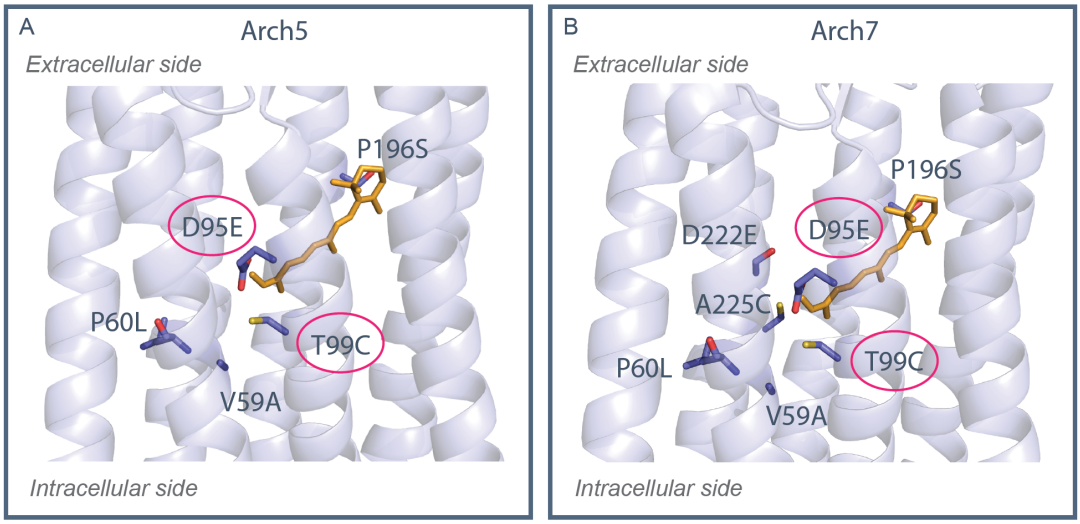

Figure 10. Mutations introduced to create Arch5 and Arch7

Arch5 and Arch7 [1] *mutations indicated in Arch3 structure (RCSB PDB 6S63*[119]*). Compared to QuasArs, the Arch5 and Arch7 conserve a negative charge at the counterion position with the replacement D95E, but carry additional mutation in the active site T99C.*

1. 9. Objectives

Availability of suitable tools for monitoring neuronal activity is critical to aid development in neuroscience research. Microbial rhodopsin-based neuronal actuators and fluorescent voltage sensors can be combined to establish all-optical electrophysiology. These advances result in cell-specific non-invasive imaging and modulation of membrane voltage in large neuronal networks[120,121,153].

It has been shown that Arch3 based fluorescent sensors are a promising tool for monitoring of neuronal activity. Extensive high throughput mutant library screenings have been carried out in pursuit of improved sensor features[1–3]. Despite multiple studies of directed evolution of Arch3-based sensors and their applications, there is lack of biophysical studies, which report the underlying mechanism of these sensors. Understanding of the functionality of these sensors is crucial for rational design of next-generation rhodopsin-based fluorescent sensors. Improved properties, in particular, fluorescence QY is necessary for applications in living animals.

In this work, my aim is to resolve three focal questions: (1) how the fluorescence arises in Arch3-based sensors, (2) how the membrane voltage generates change in fluorescence intensity and (3) whether it is possible to further increase the fluorescence QY of the most recent constructs. To tackle the manifold questions, variety of methods have been used - spectroscopy, imaging and molecular dynamics (MD) simulations. From the various mutants (Table S1), QuasAr1[3], QuasAr2[3], and Archon1[2] have been selected as suitable candidates for this study. For the simplicity, in the further text they will be referred to as one group – QuasArs.

In the first part of this work, steady-state and time-resolved UV/Vis spectroscopy (Ultraviolet–visible spectroscopy), fluorometry, and Raman spectroscopy have been applied to study the origin of fluorescence of QuasArs. Spectroscopy allowed to investigate the dynamics and photocycle of the contrustcs. Here, QuasAr1 and QuasAr2[3] have been chosen as suitable candidates for spectroscopic studies. These constructs provide evident differences in fluorescence QY and voltage-sensing, while just differing in one mutation. The distinctive properties allow correlation of spectroscopic characteristics to their functionality.

The second part of this work focuses on the study of voltage-sensing mechanism. Here, Archon1[2] has been chosen as a model protein. Archon1 shows properties

desirable for this study - high expression, membrane-targeting and voltage sensitivity. MD simulation is a powerful tool, providing insights in the voltage-sensitive conformational and hydrogen-bonding changes. In addition, *E. coli* cell assay for spectroscopic measurements was established. The cell assay allowed to study protein dynamics at different voltage conditions. Here, two spectroscopic methods were chosen -fluorescence lifetime imaging microscopy (FLIM) to specify alterations in fluorescence lifetime, and Raman spectroscopy to detect changes in the retinal chromophore composition.

Third part of this work is dedicated to Archon1 mutant studies to identify the key residues essential for increase in fluorescence QY and voltage-sensing. Mutant studies also aided the quest of finding novel voltage sensors with improved properties. To determine capability for applications, preliminary tests of most promising mutants were carried out in neuronal cell cultures.

In the following chapters the reader will be introduced to the methods used in this study, the results obtained in different phases of this project, leading to a discussion of the results and the outlook for future prospective.

2. Methods

2. 1. Molecular Biology

2. 1. 2. DNA preparation for *E.coli* expression

To express the constructs in E.coli cultures, E.coli codon-optimized genes were ordered from GenScript (Piscataway, NJ, USA). Genes encoding for Arch3 variants (listed below) with TEV protease cleavage site at the C-terminus (ENLYFQSL) were cloned into pET21a(+) vector between the NdeI and SalI restriction sites. Additionally, the pET21a(+) vector introduced hexa-histidine-tag (6xHis-tag) at the C-terminus of the gene encoding for Arch3 variants. The 6xHis tag is crucial for further purification steps of the expressed protein. The Arch3 sequence (UniProtKB - P96787, amino acids 1–253) was modified according to the published constructs: Archon1/Archon2[2], Arch5[1]. Further site-directed mutagenesis, if necessary, were carried out using polymerase chain reaction (PCR).

Genes encoding for Arch3 variants with QuasAr1/QuasAr2[3] mutations were a gift from Adam Cohen. pBAD-His-B-QuasAr1 (AddGene catalogue #64135[3]) and pBAD-His-B-QuasAr1 (AddGene catalogue #64134[3]) were also sub-cloned into pET21a(+) vector between the NdeI and SalI restriction sites.

Gene encoding for the wild-type Arch3 (sequence as listed in UniProtKB - P96787, amino acids 1–253) was subcloned in pET28b(+) between NcoI and EcoRI. The polyhistidine-tag (6xHis-tag) is provided by the vector at the C-terminus of the Arch3 gene. The construct was a gift from Prof. Dr. Adam Cohen.

2. 1. 2. DNA preparation for ND7/23 expression

To express the constructs in ND7/23 (PEG-mediated fusion of mouse neuroblastoma and rat dorsal root ganglia) cell line, mammalian codon-optimized gene pCAG-Archon1-KGC-EGFP-ER2-WPRE was ordered from AddGene (catalogue #108423). Using restriction enzyme-free Gibson cloning, the sequence encoding for Archon1 was sub-cloned into pEYFP-C1[133,168] in frame with eYFP (enhanced Yellow Fluorescent Protein) fluorophore[133]. The new vector[133] carries modifications at the N- and C- terminus to improve membrane trafficking and targeting of the construct

(C2C1-Archon1-TS-eYFP-ER). The N-terminus holds fusion of CrChR2 and CrChR1 sequences to enhance protein expression (MDYGGALSAVGLFQTSY-TLENNGSVICIPNNGQCFCLAWLKSNG)[133,168,169]. The C-terminus consists of fluorophore (eYFP), which is flanked by two sequences TS and ER. TS (KSRITSEGEYIPLDQIDINV) enhances membrane trafficking[133,136,168], whereas ER (FCEYENEV) prevents aggregation in the endoplasmic reticulum[133,168,170]. To enhance the membrane trafficking even further Kir2.1 Golgi trafficking signal (RSRFVKKDGHCNVQFINV)[136] was introduced at the N-terminus following the C2C1 sequence (final construct: pEYFP-C1-C2C1-GE-Archon1-TS-eYFP-ER).

2. 1. 3. Site-directed mutagenesis PCR

For mutant studies, the site-directed mutations were introduced with PCR[171]. Software GENtle v1.9.4 was used for primer design. A set of forward and reverse primers were designed to be roughly 30 base pairs (bp) long with annealing temperature (T_A) of ~55°C. The central part of the primer encodes for the desired mutation and overhang of at least 10 bp to each side overlap with the original sequence. The primers were synthesized by Integrated DNA Technologies (Leuven, Belgium).

The PCR mix was prepared as listed in Table 1. The PCR solutions were inserted in Thermal cycler (T100 Thermal Cycler, Bio-Rad Laboratories GmbH, München, Germany, or peqSTAR 96X Universal gradient, VWR Peqlab, Erlangen, Germany) and underwent temperature cycles as listed in Table 2. The PCR product was supplemented with 0.5 µL of DpnI enzyme to cleave methylated template plasmid DNA. The digestion reaction was run for 40 min at 37°C.

Gel electrophoresis[172,173] was used for initial estimate of the success of the PCR reaction. Samples (mixed with DNA Gel Loading Dye (6X), Thermo Fisher Scientific, Waltham, Massachusetts, USA) are transferred into the pockets of 1% w/v agarose gel (TAE buffer; SYBR Green gel stain, Thermo Fisher Scientific, Waltham, Massachusetts, United States) and subjected to an electric field. The negatively charged DNA moves towards the positively charged anode. The longer fragments move more slowly, and the shorter fragments move more rapidly, resulting in band separation by size. To assess the size (kbp) of the DNA, the band height is compared to the marks of GeneRuler DNA Ladder Mix (Thermo Fisher Scientific, Waltham,

Massachusetts, United States). The gel images are recorded using ChemiDoc MP Imaging System (Bio-Rad Laboratories GmbH Deutschland, München, Germany).

The PCR product (2 µL to 25 µL) are transformed into chemocompetent *E.coli* cells (DH5α, XL1-Blue or DH10B) and grown overnight on LB (Lysogeny broth) agar plates (at 37°C). The grown colonies are picked for overnight growth in liquid culture (at 37°C). On the following day, the plasmid DNA is purified from the liquid cell cultures using NucleoSpin Plasmid EasyPure Kit (Macherey-Nagel, Düren, Germany). The presence of the mutation is confirmed with sequencing by LGC Genomics GmbH (Berlin, Germany).

Table 1. PCR reaction mix

PCR MIX	
Template DNA	30 ng
5x PhusionHF buffer	1x/ 6 µL
dNTP-Mix (10 mM)	200 µM/ 0.6 µL
DMSO	3% v/v / 0.9 µL
Phusion Polymerase (2 U/µL)	0.02 U/µL / 0.3 µL
Forward primer (10 µM)	0.5 µM / 1.5 µL
Reverse primer (10 µM)	0.5 µM / 1.5 µL
ddH_2O	Fill up to 30 µL
Total volume	30 µL

Table 2. PCR temperature cycles.

PCR program (pET21a(+) vector)				**PCR program (pEYFP-C1 vector)**			
Step	Repeat	Temperature	Time	Step	Repeat	Temperature	Time
1	1	98 °C	2 min	1	1	98 °C	30 s
2	25	98 °C	30 s	2	25	98 °C	10 s
3		Gradient 50°C – 55 °C	30 s	3		Gradient 55°C – 60 °C	15 s
4		72 °C	3.5 min	4		72 °C	5 min
5	1	72 °C	3.5 min	5	1	72 °C	10 min

2. 1. 4. Subcloning - Restriction enzyme digestion and ligation

Subcloning is used to transfer the DNA encoding for protein of interest into a new desired vector[174]. The standard way of subcloning is using restriction enzymes. The most straight forward technique can be carried out if two unique restriction enzyme sites exist in parent and destination vector. The two vectors are digested with the two restriction enzymes (Table 3 left). The destination vector undergoes additional step of dephosphorylation to reduce the chance of self-ligated vectors. After completion of the step, the digestion products are loaded on agarose gel (2%w/v) for size based separation. The DNA is extracted from the gel using NucleoSpin Gel and PCR clean-up (Macherey-Nagel, Düren, Germany). The purified DNA fragments are ligated using T4 ligase (Thermo Fisher Scientific, Waltham, Massachusetts, USA) as described in Table 3 (right side). The ligation product is transformed into competent *E.coli*, and the resulting colonies are screened for the desired final construct.

If the restriction enzymes are not present in the donor vector, the DNA fragment with newly introduced restriction sites can be amplified using PCR with specifically designed primers.

Table 3. Digestion and Ligation

Digestion		**Ligation**	
Reaction mix		Reaction mix	
DNA	1.5 µg	DNA vector	150 ng
10x FastDigest reaction buffer	3 µL	DNA insert (3:1)	50 ng
Restriction enzyme 1	1 µL	10 x Ligase Buffer	2 µL
Restriction enzyme 2	1 µL	T4 Ligase	1 µL
ddH_2O	~ 23µL	ddH_2O	~ 15µL
Final Volume	30 µL	Final Volume	20 µL
The specific enzymes define reaction incubation duration and temperature.		Reaction is carried out for 1h at 22 °C, and inactivated by incubation at 70 °C for 5 min	

2. 1. 5. Gibson cloning

Gibson assembly can be used to seamlessly compile longer fragments of DNA[175]. Primers to introduce overlap sequence with adjacent DNA fragments are designed

using NEBuilder v2.1.0 (New England Biolabs Inc., Ipswich, MA) and synthesized by Integrated DNA Technologies (Leuven, Belgium). DNA fragments with overhang sequence were then amplified using PCR (Table 4 and Table 5. Amplification of DNA fragment). DpnI (0.5 µL) was added to the PCR product to remove methylated template plasmid DNA (40 min, 37°C). The resulting DNA fragments are loaded on agarose gel (2%w/v) for size-based separation. The DNA of expected size is extracted from the gel using NucleoSpin Gel and PCR clean-up (Macherey-Nagel, Düren, Germany). To join the DNAs, the purified gene fragments are mixed with three enzymes and other buffer components (Table 6) and incubate for 20 min at 50°C. The Gibson assembly product is then transformed into competent *E.coli*, and the resulting colonies are screened for the desired final construct.

Table 4 and Table 5. Amplification of DNA fragment

PCR MIX	
Component	Amount
Template DNA	80 ng
5x PhusionHF buffer	1x/ 5 µL
dNTP-Mix (10 mM)	200 µM/ 2.5 µL
DMSO	3% v/v / 0.75 µL
Phusion Polymerase (2 U/ µL)	0.02 U/µL / 0.25 µL
Forward primer (10 µM)	1 µM / 2.5 µL
Reverse primer (10 µM)	1 µM / 2.5 µL
ddH_2O	Fill up to 25 µL
Total volume	25 µL

PCR program		
Repeat	Temperature	Time
1	98 °C	5 min
29	98 °C	1 min
	60 °C	45 s
	72 °C	5 min
1	72 °C	10 min

Table 6. Gibson assembly

Gibson assembly reaction mix	
DNA vector	50 ng
DNA insert (1:4)	200 ng
10 x ISO Buffer	320 µL
T5 exonucelase (10 U/ µL)	0.64 µL
Phusion Polymerase (2 U/µL)	20 µL

Taq ligase (40 U/µL)	160 µL
ddH_2O	~ 700 µL
Final Volume	1.2 mL
Reaction is carried out for 20 min at 50°C	

2. 1. 6. *E. coli* Transformation and DNA Purification

DNA is transformed into chemocompetent *E.coli* (DH5α, XL1-Blue or DH10B) using a heat shock. 100 ng of the DNA is mixed with 50 µL of cell suspension (freshly thawed) and kept on ice (0°C) for 15 min. After the cold temperature incubation, the mixture undergoes a heat shock and is kept at 42°C for 45 s. After this step, the cells are transferred back on ice for 2 min. Afterwards, cell suspension is supplemented with 900 µL of LB (Lysogeny broth) media and grown for 1h, rigorously shaking (650 rpm) at 37°C. Subsequently, 100 µL of the solution is transferred onto LB agar plate, which contains appropriate antibiotics (pET21a(+) – 100 µg/mL Ampicillin, pEYFP-C1 - 50 µg/mL Kanamycin). The cell colonies are grown overnight (12-18h) at 37 °C.

The cell colonies are picked with sterile toothpick and transferred into liquid LB media (5 mL) with appropriate antibiotics. The cells are incubated shaking (190 rpm) at 37°C overnight. On the following day, the plasmid DNA is purified from the liquid cell cultures using NucleoSpin Plasmid EasyPure Kit (Macherey-Nagel, Düren, Germany). The correct sequence of the gene of interest is confirmed by sequencing (LGC Genomics GmbH, Berlin, Germany).

2. 2. Microbiology

2. 2. 1. Cell cultures

The expression plasmid (pET21a (+)) was chosen for high expression yield in *E.coli* cell cultures. The plasmid with the fluorescent rhodopsin variant (QuasAr1/2 Archon1 (and its mutants)/ Archon2/ Arch5) was transformed into C41 (DE3) *E. coli* cells as described above. The cell colonies, with transfected gene of interest, are picked from LB agar plate and inoculated into LB media pre-culture (50 mL, 100 µg/mL Ampicillin). The cell culture is grown shaking (190 rpm) at 37°C overnight. After incubation, a cloudy haze in the media indicates the cell growth. The cell suspension

is then transferred to a larger Erlenmeyer flask; 8 mL of the pre-culture is dispersed into 800 mL LB media (1:100). The cells are grown further, shaking (190 rpm) at 37°C, for ~2h until optical density of the cell culture reaches OD_{600} ≈0.6. Once the cell culture is ready, the protein expression is induced by addition of 0.5 mM isopropyl β-D-thiogalactopyranoside (IPTG; Carl Roth GmbH, Karlsruhe, Germany) and 5 μM all-*trans* retinal (ATR; Sigma-Aldrich, St. Louis, USA). The cells are incubated shaking (190 rpm) at 37 ° C, for 4h. Once the protein is expressed the following steps are carried out under blue light (~470 nm) to avoid bleaching of the rhodopsin samples. The cells are harvested by centrifugation (6000g, 10 min, 4°C). The supernatant can be discarded and the cells are resuspended into ~30 mL (10 mL/g cells) Buffer A (with additional 0.1 mM phenylmethylsulfonyl fluoride (PMSF; Sigma-Aldrich, St. Louis, USA)). Steps of sample preparation for *E.coli* cell assay measurements with FLIM or Raman spectroscopy are described further below. If stored, the cells are frozen in liquid nitrogen, wrapped into aluminium foil and transferred into freezer (–80°C). The following procedures for protein purification are described in the next paragraph.

Similar steps are followed for pET28b (+) vector containing Arch3. For this plasmid it was found that BL21 (DE3) *E.coli* strain was more compatible. And the protein expression step was prolonged to 5h.

2. 2. 2. Cell lysis

The harvested cells are supplemented with 0.01 mg/mL Deoxyribonuclease I (DNaseI, Sigma-Aldrich, St. Louis, USA) recombinant enzyme. DNaseI is needed to cleave the released DNA during cell lysis to avoid unwanted cell clumping. The cells are disrupted with high pressure (4 passages under 1100-1300 bar pressure) using an EmulsiFlex-C3 Homogenizer (AVESTIN Inc., Ottawa, Canada). The lysed cells are centrifuged in two steps. The first centrifugation (10 000 rpm, Type 45 Ti; Beckman Inc., Indianapolis, USA) step is done at 4°C for 10 min to remove the cell debris. In the second centrifugation step (45 000 rpm, 1h, 4°C) the cell membrane fragments are separated from the cytosolic part. As rhodopsins are membrane bound protein, the membrane fractions need to be collected (the pellet) and the supernatant is discarded.

2. 2. 3. Protein purification

The fluorescent microbial rhodopsins are extracted from the membrane fraction by one of two solubilisation methods – detergent solubilisation or styrene–maleic acid (SMA, Polyscope Polymers BV, Geleen, Netherlands) copolymer solubilisation.

In the first approach, the membrane pallet is resuspended in Buffer A with additional 0.1 mM PMSF and detergent - 1.5% n-dodecyl-β-D-maltoside (DDM, GLYCON Biochemicals GmbH, Luckenwalde, Germany), and 0.3% cholesteryl hemisuccinate (CHS, Sigma-Aldrich, St. Louis, USA) using Dounce homogenizer. The suspension is incubated overnight (4°C) under slow nutation.

In the second approach, the membrane pallet is resuspended in Buffer A with additional 2.5% (w/v) SMA copolymer (2:1) using Dounce homogenizer. SMA (2:1) was a gift from Polyscope Polymers B.V. (Geleen, Netherlands). For SMA nanodisc preparation it is crucial to keep the pH of the buffer above 8 and adjust the final wet membrane concentration to 10 mg/mL. The suspension is incubated overnight (4°C) under slow nutation.

After overnight solubilisation the sample is centrifuged (45 000 rpm, 1h, 4°C) to separate the solubilized protein from the membrane fragments. The supernatant carries the protein in detergent micelles (or SMA nanodiscs) and the pellet is discarded.

The protein is purified in two-step chromatography using ÄKTAxpress protein purification system (GE Healthcare Life Science, Chicago, USA) configured with a HisTrap HP Ni-NTA column and a HiPrep 26/10 Desalting column. The sample is loaded onto HisTrap HP Ni-NTA column with binding Buffer B. The unbound sample is removed with wash Buffer C. The sample is eluted with Buffer D containing high imidazole concentration. The desalt column is equilibrated with Buffer E to ensure sample collection in Buffer E free from imidazole. A preview of different purified Arch3 variants are shown in Figure 11.

UV/Vis spectrum (Cary 300Bio) was measured of the sample to verify successful purification of the protein and estimate the concentration by the optical density.

If other buffer conditions were required for experiments, rapid buffer exchange was carried out using PD-10 Desalting Columns with Sephadex G-25 resin (GE Healthcare Life Science, Chicago, USA).

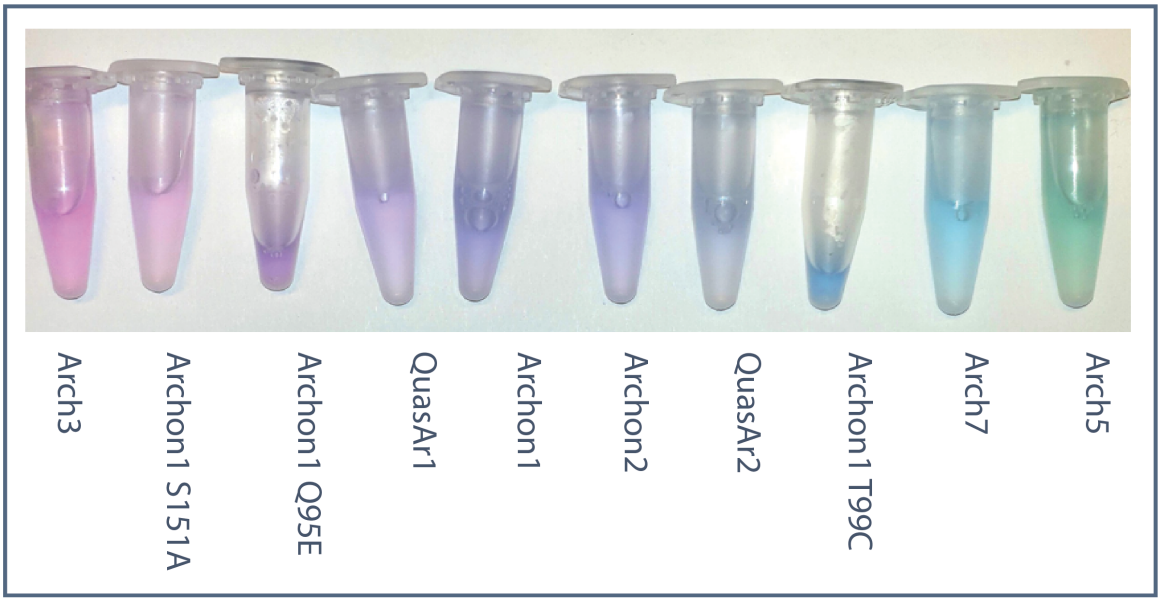

Figure 11. Purified Arch3 variants

Purified and solubilized Arch3 and its mutants – Archon1-S151A, Archon1-Q95E, QuasAr1 and Archon1, Archon2, QuasAr2, Archon1-T99C, Arch7, and Arch5. Due to their different absorption properties the constructs display a broad range of color.

2. 2. 4. *E. coli* cell assay sample preparation

To prepare *E. coli* cell suspension with overexpressed Archon1 for spectroscopic studies, similar protocol was used as described above. Also for these experiments C41 (DE3) *E. coli* strain was chosen. To prepare the *E. coli* cell assay sample, the expression time and temperature were adjusted to ensure fresh cell before measurements. After expression induction with 0.5 mM IPTG and 5 μM all-*trans* retinal. The cells were grown overnight (20h) at 28°C, shaking (180 rpm). The following steps are done under blue light (~470 nm) to avoid bleaching of the sample. The cells are harvested by centrifugation (6000g, 10 min, room temperature ~22°C). The cell pellet is resuspended in buffer comprised of 50 mM Tris-HCl (pH 8.0), 75 mM NaCl, 75 mM KCl.

2. 2. 5. Mammalian cell culture

The ND7/23 cell line is a hybrid of mouse neuroblastoma and rat neuronal cells[168,176] (Sigma-Aldrich, St. Louis, MO, USA).The cells are cultured in Dulbecco's Modified Eagle Medium (DMEM, Biochrom GmbH, Berlin, Germany) supplemented with 5% (v/v) fetal bovine serum (FBS, Sigma-Aldrich, St. Louis, MO, USA) and 1 μg/

ml penicillin/streptomycin (Sigma-Aldrich, St. Louis, MO, USA) and incubated at 37°C under a 5% CO_2 atmosphere. To prepare the cells for fluorescence recordings with a patch-clamp voltage control, the ND7/23 cells were seeded into 35mm petri dishes enclosing three round glass cover slips coated with poly-D-Lysine (PDL). The following day, the cells were transfected using the FuGENE® HD Transfection Reagent (Promega, Madison, WI, USA) and the Archon1 variant (pEYFP-C1-Archon1-X) with ratio 6 µl FuGENE/2 µg DNA per dish. The cell medium was supplemented with 2.5 µM all-*trans* retinal. The cells were grown for 48h, expressing the protein and measured as described below.

2. 2. 6. Solutions

LB (Lysogeny broth) media

The LB media contains: 1% w/v sodium chloride (NaCl) (Carl Roth GmbH, Karlsruhe, Germany); 1% w/v tryptone (Carl Roth GmbH, Karlsruhe, Germany); 0.5% w/v yeast extract (Carl Roth GmbH, Karlsruhe, Germany); ddH2O.

LB (Lysogeny broth) agar

The LB agar contains: 1% w/v sodium chloride (NaCl) (Carl Roth GmbH, Karlsruhe, Germany); 1% w/v tryptone (Carl Roth GmbH, Karlsruhe, Germany); 0.5% w/v yeast extract (Carl Roth GmbH, Karlsruhe, Germany); 2% w/v agar (Carl Roth gmbH, Karlsruhe, Germany); ddH_2O (double distilled water).

IPTG Stock solution (1M)

A 10 mL stock solution of isopropyl β-D-thiogalactopyranoside (IPTG; Carl Roth GmbH, Karlsruhe, Germany) is prepared by dissolving 2.38 g of IPTG in 10 mL of ddH_2O. The solution is sterilized by filtration (0.22 µm pore size). The stock solution is stored at – 20°C.

PMSF Stock solution (0.1M)

A 10 mL stock solution of phenylmethylsulfonyl fluoride (PMSF; Sigma-Aldrich, St. Louis, USA) is prepared by dissolving 0.1742 g of PMSF in 10 mL dimethyl sulfoxide (DMSO, Carl Roth GmbH, Karlsruhe, Germany). The stock solution is stored at –20°C.

10% w/v DDM and 2% w/v CHS stock solution

A 50 mL stock solution of detergent mixture is comprised of 5g of DDM (GLYCON Biochemicals GmbH, Luckenwalde, Germany), 1g of CHS (Sigma-Aldrich, St. Louis, USA) and ~50 mL Buffer (200mM Tris-HCl pH 8 (Carl Roth GmbH, Karlsruhe, Germany)). Continuous ultrasonication (~6h) is used to aid complete dissolving of the detergent. Sonication is done until the solution becomes translucent. The stock solution is stored at –20°C.

SMA (2:1) 5% w/v

Styrene maleic acid (SMA 2:1, 25% w/v) was a gift from Polyscope Polymers B.V. (Geleen, Netherlands). The stock solution of SMA is prepared with final concentration of 5% w/v. The 25 mL of SMA (25% w/v) is dissolved in 75 mL Buffer (ddH_2O, 300 mM NaCl, 50 mM Tris-HCl, pH8.0). It is crucial to keep the solution pH above 8.0, otherwise SMA is destabilized and aggregates. The stock solution is kept at 4°C.

Buffers used for protein purification

Buffer A (lysis buffer) is comprised of: 50 mM Tris-HCl pH 8.0 (Carl Roth GmbH, Karlsruhe, Germany), 300mM NaCl (Carl Roth GmbH, Karlsruhe, Germany), 0.1 mM PMSF and ddH_2O.

Buffer B (Binding buffer) is comprised of: 50 mM Tris-HCl pH 8.0, 300mM NaCl, 20mM imidazole (Sigma-Aldrich, St. Louis, USA), 0.1 mM PMSF and ddH_2O. If samples are solubilized in detergent micelles, the buffer is supplemented with 0.02% DDM and 0.004% CHS detergent mixture. If sample is solubilized in SMA nanodiscs, no additional compounds are needed.

Buffer C (Wash buffer) is comprised of : 50 mM Tris-HCl pH 8.0, 150mM NaCl, 0.1 mM PMSF and ddH_2O. If samples are solubilized in detergent micelles, the buffer is supplemented with 0.02% DDM and 0.004% CHS detergent mixture.

Buffer D (Elution buffer) is comprised of: 50 mM Tris-HCl pH 8.0, 150mM NaCl, 500mM imidazole, 0.1 mM PMSF and ddH_2O. If samples are solubilized in detergent micelles, the buffer is supplemented with 0.02% DDM and 0.004% CHS detergent mixture.

Buffer E (Desalt buffer) is comprised of: 50 mM Tris-HCl pH 8.0, 150mM NaCl, 0.1 mM PMSF and ddH_2O. If samples are solubilized in detergent micelles, the buffer is supplemented with 0.02% DDM and 0.004% CHS detergent mixture.

Additional buffer conditions used for spectroscopic studies

To study QuasArs at alkaline conditions, rapid buffer exchange was carried out with PD-10 Desalting Columns with Sephadex G-25 resin (GE Healthcare Life Science, Chicago, USA). The final buffer was comprised of: 150 mM NaCl, 50 mM CAPS (3-(Cyclohexylamino)-1-propanesulfonic acid, Sigma-Aldrich, St. Louis, USA) and final pH 11.0 adjusted with NaOH.

For pH titration the buffers were prepared in the following sets. Citric Acid – Na2HPO4 Buffer Solutions were used to obtain acidic conditions (pH 2.6, 2.8, 3.2, 3.6, 4.2, 4.6). Buffer with slightly acidic conditions (pH 5.0., 5.5, 6.0) was prepared with 50 mM MES-NaOH (2-Morpholinoethanesulfonic acid monohydrate, Sigma-Aldrich, St. Louis, USA). Buffers with pH close to neutral value (pH 6.5, 7.0, 7.5) were prepared with 50 mM HEPES-NaOH (4-(2-Hydroxyethyl)piperazine-1-ethanesulfonic acid, N-(2-Hydroxyethyl)piperazine-N′-(2-ethanesulfonic acid), Sigma-Aldrich, St. Louis, USA). Slightly alkaline buffers (pH 9.0, 9.5) were prepared using CHES-NaOH (2-(Cyclohexylamino)ethanesulfonic acid, Sigma-Aldrich, St. Louis, USA). Alkaline buffers (pH 10.0, 10.3, 10.6 and 11.0) were prepared using 50 mM CAPS-NaOH.

All of the buffers were supplemented with 150 mM NaCl and 0.02% DDM and 0.004% CHS detergent mixture.

2. 3. Spectroscopy

2. 3. 1. UV/Vis steady state

The steady state Ultraviolet-visible (UV/Vis) absorption spectra were recorded with Cary 300 spectrophotometer (Varian Inc., Palo Alto, USA) at room temperature (~22°C). The spectral resolution is 1.6 nm. To monitor spectral changes of the absorption spectra after short (10s) and prolonged (1 min) illumination, LEDs were placed facing the sample holder. The sample was illuminated with a red light 625 nm LED (0.11W, Luxeon Star LEDs, Alberta, Canada) to accumulate the P580/P400

species. Whereas, blue light (400 nm) LED (0.12W, Luxeon Star LEDs, Alberta, Canada) was used to recover the dark-like D590' state. After varied light illumination steps, spectra were recorded of the same sample and compared using Microsoft Excel 2016 and Origin 9.0.

2. 3. 2. UV/Vis flash photolysis

Modified LKS.60 flash photolysis system (Applied Photohysics Ltd., Leatherhead, UK) was used, as previously reported[133], to record transient absorption spectra in time range between 10 ns up to 10 s (Figure 12). Multi-wavelength datasets (350 – 700 nm) with resolution of 0.4 nm are recorded as one point per decade in nanosecond-to-second time range. The sample was excited with 10 ns laser pulse (5 mJ/shot). Third harmonic of a Nd:YAG (neodymium-doped yttrium aluminium garnet) laser (BrilliantB, Quantel, Les Ulis, France) is tuned with an optical parametric oscillator (OPO MagicPrism, Opotek Inc., Carlsbad, CA, USA). To observe the spectral changes after laser excitation a 150 W Xenon lamp (Osram, München, Germany) was used as monitoring light. The light collected with an optical fibre is delivered to Shamrock 303i spectrometer (Andor Technology Ltd, Belfast, Ireland), and split by a grating into its component wavelengths. The spectra are recorded with an Andor iStar ICCD (intensified charge-coupled device) camera (DH734; Andor Technology Ltd, Belfast, Ireland) at 46 different time points between 10 ns and 10 s (5 points per decade, isologarithmically). Each recording delivers one spectra per decade point and a pause of 60 s is taken before commencing the next measurement. The measurements were carried out at room temperature (~22 °C). The data analysis is carried out using MATLAB R2016b (The MathWorks, Natick, MA) and Glotaran 1.5.1 (Joris Snellenburg, VU University Amsterdam).

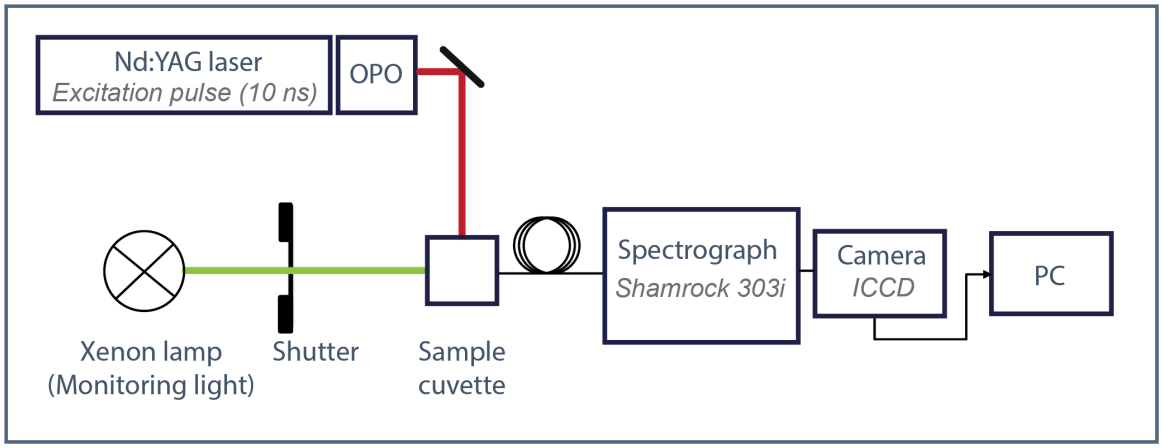

Figure 12. Schematic drawing of flash photolysis setup

Flash photolysis spectroscopy was used to measure the transient absorption difference spectra of QuasArs. The third harmonic of a Nd:YAG pump pulse wavelength is tuned via optical parametric oscillator (OPO). The excitation pulse is aligned with a mirror to propagate through the sample holder. Xenon lamp (350nm-700nm) is used to monitor the changes in absorption spectra. The probe light is collected and delivered to spectrometer (Shamrock 303i) via an optical fiber. The light is spectrally dispersed with a grating and projected onto a fast gating camera (Andor iStar ICCD).

2. 3. 3. Femto- to microsecond transient absorption spectroscopy (TAS)

Ultrafast pump-probe spectrometer was used to record transient absorption spectra in time range between -50 fs to 1 μs (Figure 13). Ultrafast pump-probe spectroscopy is carried out with two femtosecond (fs) laser pulses and allows monitoring of the excited state dynamics of the protein. The pump pulse excites the molecule and triggers photoreaction. The probe pulse with specific time delay propagates through the sample and projects on a detector, carrying the information of the sample absorption changes[177–179].

Seed pulse from Ti:Sapphire oscillator (Vitesse, Coherent, Santa Clara, California, USA) is split into two beam lines (pump and probe) and amplified separately by two Ti:Sapphire amplifiers (Legend and Libra, Coherent, Santa Clara, California, USA). The two amplifiers are synchronized via synchronization and delay generator (SDG and SDG Elite, Coherent, Santa Clara, California, USA)[179–181].

The pump beam was tuned to desired wavelength via optical parametric amplifier (OPA) (OPerA Solo, Coherent, Santa Clara, California, USA). Depending on the measurement requirements, the pump beam was tuned to 400/ 520/ 530/ 610/ 620

nm with a laser power of ~100 – 200 nJ. Optical chopper (500 Hz) is placed in the beam path to regulate the frequency of the pump pulse[179–181].

Sample absorption changes are measured with white light laser pulse. The probe beam is focused onto CaF_2 plate to generate the supercontinuum white light. The probe beam is spectrally dispersed and projected onto photodiode array. The measured wavelength range was set to 360 - 720 nm. Both pulses are aligned to overlap on the sample. The pump beam diameter at the sample plain is 150 μm, and the sample beam diameter is ~50 μm[179–181].

Time delay between the pump and probe beams are produced by optical and electronic delay generation. The optical delay stage provides time delay from femtoseconds to nanoseconds. It is constructed from pair of mirrors and retroreflector placed on translational stage. The electronic delay provides time delay from nanoseconds to milliseconds. Electronic delay generation is realized via SDG[179–181].

The sample is filled in a custom-made holder, which is assembled from two 1-mm-thick round quartz windows with adjustable distance (set by a spacer at 400 μm) and placed on a moving Lissajous scanner. The circulating sample holder ensures exposure of a renewed sample after each laser shot with a time interval of 60 seconds[180–182].

According to the experimental requirements a backlight illumination LED was used to ensure recovery of the photoproduct of interest. The backlight illumination of red light (625 nm) LED (Luxeon Star LEDs, Alberta, Canada) was used to recover the P580/P400 species. Whereas, blue light (400 nm) LED (Luxeon Star LEDs, Alberta, Canada) was used to recover the dark-like D590' state.

To improve the SNR, the measurements are repeated over multiple runs and averaged. Data analyses were performed using MatLAB and Glotaran 1.5.1. The specified instrument response function (IRF) is ~80 fs.

For each time point the difference absorption spectra (ΔOD) can be expressed as: $\Delta OD = log_{10}\left(\frac{I_{unpumped} - I_{dark}}{I_{pumped} - I_{dark}}\right)$

In this equation $I_{unpumped}$ stands for probe beam signal of the molecule in the dark state, without pump pulse excitation. I_{pumped} stands for probe beam signal of the

excited molecule, after pump pulse triggered. Lastly, I_{dark} stands for background intensity, with no pump and probe pulses[177–179].

The pump-probe experiments were carried out together with Dr. Yusaku Hontani (QuasAr1 and QuasAr2) and Dr. Patrick E. Konold (Archon1, Archon2, Arch3) at Vrije Universiteit Amsterdam under supervision of Prof. Dr. John T.M. Kennis.

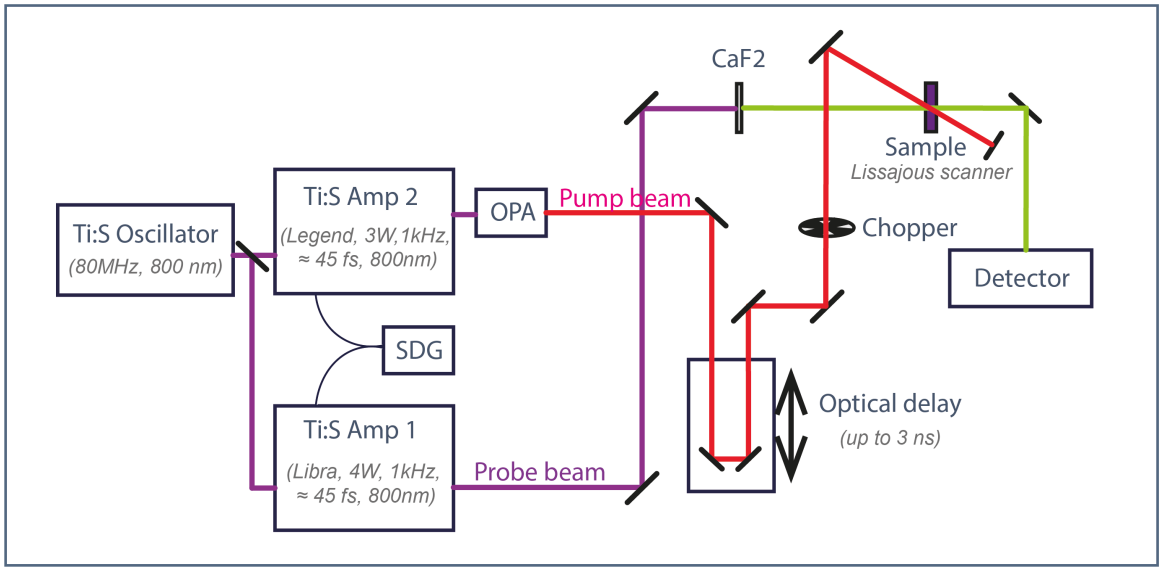

Figure 13. Schematic drawing of ultrafast pump-probe setup

The ultrafast photodynamics of the protein were monitored with femtosecond pump-probe setup. The scheme is adapted from[177–179]. Seed pulse from Ti:Sapphire oscillator is split in two – pump and probe pulse – and amplified by Ti:Sapphire amplifiers. The two amplifiers are electronically synchronized via synchronization and delay generator (SDG). OPA is used to tune the wavelength of the pump pulse and the chopper (500 Hz) modulates the frequency of pump pulse. The probe pulse is focused onto CaF_2 plate to generate supercontinuum as the monitoring light. The delay between pump and probe pulses is generated with (from -50 fs to 3 ns) and electronic delay (from 12.5 ns to1 μs). Both beams are aligned to overlap onto the sample. Sample is filled into Liassajous scanner holder. The probe pulse is spectrally dispersed by a grating and projects onto detector (photodiode array).

2. 3. 4. Global analysis methodology:

The transient absorption spectra were globally analysed using Glotaran 1.5.1 software (Joris Snellenburg, VU University Amsterdam)[183,184]. The data sets are three-dimensional – time, wavelength and intensity (optical density). To extract the spectral and kinetic information from the complex data sets, model-based analysis is required. With visual evaluation of the reconstructed 3D spectra and estimation of

photochemistry model is done to predict sufficient number *n* of decay components. The data are globally fitted over all wavelengths simultaneously with the *n* kinetic components. Two reaction model schemes can be applied: parallel scheme resulting in Decay-associated difference spectra (DADS); and sequential scheme resulting in Evolution Associated Difference Spectra (EADS). Both models are mathematically equivalent and result in identical time constants[184,185].

The sequential scheme model consists of evolution of spectral components (1 → 2 → 3 →...), where the spectral components transition can be fitted with mono-exponential decays (τ_1, τ_2, τ_3, etc.). These decays are referred to as the lifetime of each EADS. The parallel scheme model consists of DADS, where the transition between the spectral components can be fitted with parallel decay components[184].

The fitted models provide knowledge of the photointermediate states of the rhodopsin and their decay time constants[177,180,181,184]. The fitted time constants provided standard errors less than 5%.

2. 3. 5. Fluorescence spectroscopy

The fluorescence excitation and emission spectra of QuasArs were recorded with Fluoromax (Horiba Jobin Yvon, Kyoto, Japan) at room temperature (~22 °C), as reported previously[186]. To correct the recorded fluorescence intensity according to the fluctuations of the excitation light, the excitation photon flux was monitored with a photodiode. The slit openings were set as follows: excitation slit - 2 nm, detection slit -10 nm. For emission spectra recordings the acquisition time was set to 0.1 s with 5 nm increment steps. For excitation spectra recordings the acquisition time was set to 0.2 s with 3 nm increment step.

The sample concentration for the measurements was adjusted to $OD_{MAX} \lesssim 0.05$ to eliminate reabsorption. *Oxazine 1* laser dye (Φ_{FL} = 14.1 ± 0.8%[187]) prepared in ethanol solution, was chosen as a fluorescent standard for comparison. Fluorescence signal were recorded for both buffer (water based) and ethanol solutions to reassure no background fluorescence signal. The fluorescence quantum yield ($\Phi_{FL,QuasAr}$) of QuasArs were determined as follows[187]:

$$\Phi_{FL,QuasAr} = \Phi_{FL,dye} \times \frac{f_{dye}(\lambda_{ex})}{f_{QuasAr}(\lambda_{ex})} \times \frac{\int_{\lambda_{em}} F_{QuasAr}}{\int_{\lambda_{em}} F_{dye}} \times \frac{n^2_{water}}{n^2_{ethanol}}$$

Here *f* stands for 1−transmittance (1-T) and *F* stands for the fluorescence count. To determine the total fluorescence count, the fluorescence intensities were integrated over the entire wavelength region. And *n* stands for the refractive index.

2. 3. 6. Raman spectroscopy

Fourier transform - Raman spectrometer RFS100/S (Bruker, Massachusetts, USA) was used for pre-resonance Raman spectra recordings. The sample is excited with preresonant 1064 nm, 640 mW Nd:YAG laser light (DPY 301 II0.50 EM, Coherent, California, USA). Back-scattering geometry was used for detection of scattered light (Figure 14) The spectral resolution obtained was with 4 cm^{-1}.

Recordings of purified QuasAr Raman spectra were performed as described previously[188]. The purified protein samples were highly concentrated to reach optical density of $OD_{\lambda max}$~30 at the absorption peak maximum (580-590). A droplet (7 µL) of the sample was set on cryostat sample holder and the measuring temperature was set to −190°C to prevent thermal conversion. To reach high signal-to-noise ratio, the spectra were accumulated over 2000 scans.

Additionally, Raman spectra recordings of purified Archon1 were carried out also at room temperature (~22°C), for better comparison to *E .coli* cell assay measurements. To avoid artefacts, the spectra were accumulated over 300 scans (3 sets of 100 scans) and sufficient signal-to-noise was still remained.

E. coli cell assay was established to record Raman spectra of Archons under different membrane voltage conditions. The cells were prepared as described above. 1 mL of intact cell suspension (0.5 g/mL) with overexpressed Archon was used for measurements and exchanged after every 500 scans. A quartz cuvette with a reflecting side was used as sample holder. The measurements were carried out at room temperature (~22 °C). To insure that there is no drastic increase in the sample temperature over the measuring time, a digital thermometer with a sensor wire was immersed in the sample cuvette for real-time recordings. The resting potential of intact *E. coli* cells is roughly −140 mV[189], allowing to monitor the spectra at negative membrane voltage. To record Raman spectra of sample at depolarized membrane the cell suspension was supplemented with 1mM 1799 (2,6-dihydroxy-1,1,1,7,7,7-hexafluoro-2,6-bis(trifluoromethyl)heptane-4-one) protonophore[166]. The cells were incubated at room temperature for 15 min with additional protonophore to abolish

the membrane potential before commencing the measurement.

As the *E. coli* cell samples produce more noise compared to purified samples, multiple scans (10000) were needed to reach satisfactory signal-to-noise. The sample was exchanged every 500 scans (20 sets) to reduce artefacts.

The data was analysed with OPUS (Bruker) and Origin 9.0 (Origin Labs).

The Raman spectra were recorded at Technische Universität Berlin under supervision of Prof. Dr. Peter Hildebrandt and Dr. Francisco Velazquez Escobar.

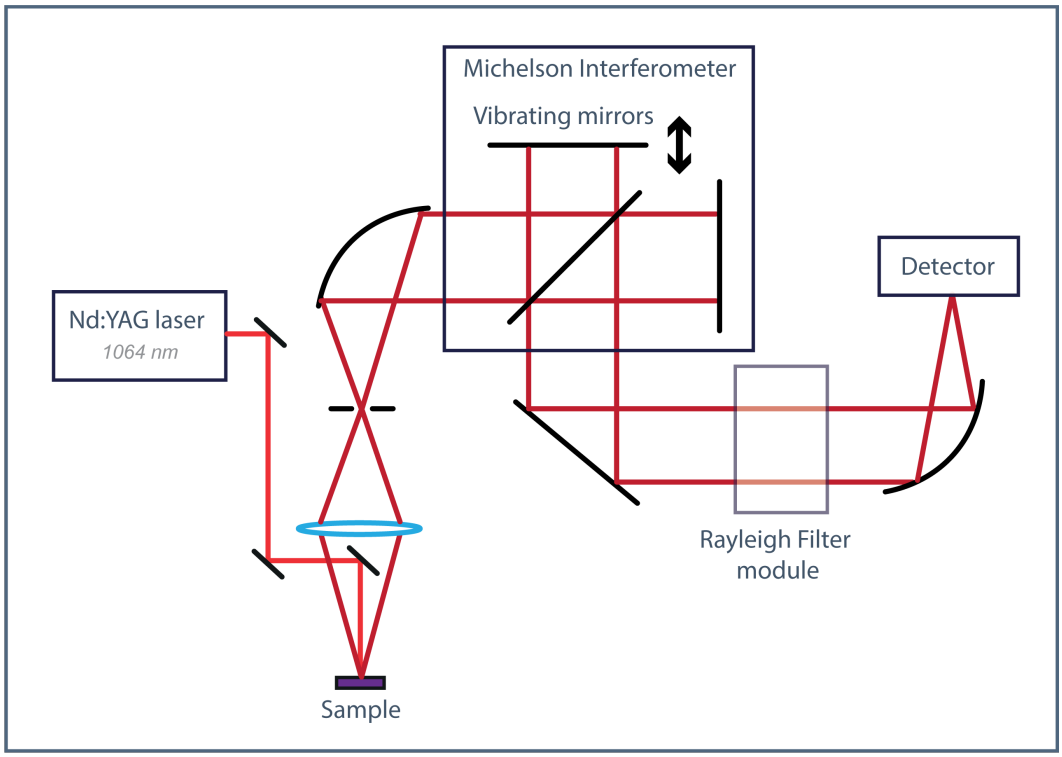

Figure 14. Schematic drawing of Fourier transform - Raman spectrometer

The scheme of FT-Raman spectrometer (Bruker RFS/100S FTR) is adapted from[190]*. Excitation pulse from Nd:YAG laser (1064nm, 640 mW) is focused on the sample. The scattered light is collected by a lens and directed to Michelson interferometer. The sample signal is passed through Rayleigh filter module and projected onto a detector. The interferogram is processed with Fourier transformation to produce the infrared Raman spectra.*

2. 3. 7. Two-photon excitation

The two-photon spectra were measured using a confocal setup as described previously[191]. The two-photon excitation was measured in spectroscopic range of 1020 to 1395 nm. To acquire the desired excitation wavelengths a pump laser (Chameleon Ultra II, APE Berlin & Coherent Inc., 800 nm, 4W, 80 MHz) was tuned

using an optical parametric oscillator (IR OPO, APE Berlin). To insure no spectral bleedthrough a long pass filter (FEL900, Thorlabs) was used. To keep the excitation power constant (1 mW) a linear variable neutral density filter (NDL-10C-2, Thorlabs) was implemented in the optical pathway. A telescope system widened and collimated the beam to illuminate the whole objective. The beam was coupled into an Olympus IX50 microscope equipped with dichroic mirror (T860spxrpt, AHF) and objective (UPlanApo/IR 60x 1.20W, Olympus). The dichroic mirror reflects the excitation light towards the objective, but filters it out for emission detection. Additional short pass filter (HC770/SP, AHF) is placed before the detector, to insure all excitation light is removed. The emission signal was recorded using electron multiplying charge coupled device camera (iXonEM+897 back illuminated, Andor Technology). The range was measured using increments of 5 nm. For each wavelength videos of 50 frames were recorded at 31.25 Hz.

The two photon excitation spectra was recorded by Rainer Matis at Technische Universität Braunschweig under supervision of Prof. Dr. Peter J. Walla.

2. 4. Imaging

2. 4. 1. Fluorescence lifetime imaging microscopy

A custom-built fluorescence lifetime imaging microscopy (FLIM) setup was used to measure the fluorescence lifetime of Archon1 (solubilised and overexpressed in *E.coli* cells). The system comprises time-correlated single photon counting (TCSPC) and confocal laser scanning microscopy as described before[192,193].

Pulsed supercontinuum laser source (19.5MHz) NKT SuperK Extreme EXU-3 (NKT Photonics, Birkerød, Denmark) is used as excitation beam. From the white-light spectrum a specific excitation wavelength (640 nm) is selected with acousto-optical tunable filter system (AOTF, UV/VIS Select, NKT Photonics, Birkerød, Denmark). The pulse width (FWHM – full width at half maximum) of the excitation pulse at 640 nm is ~60 ps. The excitation beam is coupled into inverted microscope (IX71, Olympus, Tokyo, Japan) and focused on the sample plane by objective (60× water immersion, UPSLAPO60XW, Olympus, Tokyo, Japan). The scanning of laser signal is obtained by Fast Galvanometer Mirrors (DCS-120, Becker & Hickl, Berlin, Germany). The emitted light from sample is filtered by a 665 nm long pass (HQ,

Chroma, Vermont, USA) and a Quad-Notch filter (405/488/532/635 nm) (StopLine, Semrock, New York, USA). The emitted light is then detected by hybrid PMT (Photomultiplier tube) detector (HPM-100-40, Becker & Hickl, Berlin, Germany) and recorded by multidimensional (1024 time channels with width of 19.5 ps) TCSPC (SPC-160, Becker & Hickl, Berlin, Germany). The instrument response function (IRF) is determined by the hybrid PMT detector with 120 picoseconds FWHM[193].

To record the fluorescence lifetime of Archon1 in intact cell assay, the subsequent protocol was established. The cells were prepared as described above. The cell volume used for measurements was 100 µL with concentration of 0.05g/mL. The fluorescence spectra were recorded at resting potential and upon depolarization (after addition of an ionophore, 10 µM of gramicidin[194]). The FLIM images were recorded in 15-20 continuous sets of 1 min measurements at room temperature (~20°C). To estimate the change in fluorescence intensity, the photon count was normalized by the number of image pixels, which captured *E. coli* cells.

The data were analyzed with a custom-made software (program written with C++ (Bjarne Stroustrup, ISO/IEC JTC)). Multivariate pattern recognition allowed grouping the fluorescence decay traces from individual pixels into clusters dependent on their characteristics[195,196]. After deconvolution and IRF, the fluorescence lifetime was fitted with the following equation[197,198]:

$$I(t) = \sum_{i}^{n} \propto_i e^{-t/\tau_i}$$

where n is the total number of decay components, τ_i is the fluorescence lifetime (ith component), α_i is the amplitude (i-th component).

The FLIM recordings were carried out together with Jens Balke at Freie Universität Berlin under supervision of Prof. Dr. Ulrike Alexiev. The spectral fits were provided by Jens Balke.

The FLIM recordings of Archon1 and its variants reconstituted in vesicles (presented in supplement Figure S28) were carried and analysed by Jens Balke at Freie Universität Berlin under supervision of Prof. Dr. Ulrike Alexiev.

2. 4. 2. Fluorescence recordings with patch-clamp in ND7/23 cells

The patch pipettes (micropipettes) were made from borosilicate capillaries with filament (Science Products GmbH, Hofheim, Germany) with outer diameter of 1.50

mm and inner diameter of 0.86 mm using a horizontal P1000 micropipette puller (Sutter Instrument, Novato, USA) as described previously[133].

The fluorescence intensity changes of Archon1 (and its variants) under clamped membrane voltage conditions of whole-cell recordings were performed with patch-clamp in mammalian cell line ND7/23 at room temperature (~22 °C). The resistances of the pipettes were 1.5-3 MΩ. During the patch-clamp recordings, the membrane resistance was >500 MΩ and access resistance was <10 MΩ. The intracellular buffer is comprised of: 110 mM NaCl, 1 mM KCl, 1 mM CsCl, 2 mM $MgCl_2$, 2 mM $CaCl_2$, 10 mM HEPES and 10 mM EDTA (Ethylenediaminetetraacetic acid). The pH is adjusted to pH 7.2. The extracellular buffer has the same composition, except the NaCl concentration was increased to 140 mM. The osmolarity is adjusted using osometer (OM 815, Vogel, Fernwald, Germany or Osmomat, Gonotec, Berlin, Germany) to 290 mOsm (intracellular)/ 320 mOsm (extracellular) using glucose.

A Xenon lamp (150 W, L.O.T.-Oriel GmbH Co. KG, Darmstadt) combined with a band-pass filter for wavelength selection (FB540-10 – FB620-10, FWHM 10nm, Thorlabs, New Jersey, United States) was used as the excitation light source. The measured intensity at the sample plane was ~0.26-0.28 mW/mm^2 over all applied λ_{ex}. The excitation light was coupled into inverted microscope Olympus ix70 (Tokyo, Japan) and focused on the sample plane with Olympus 40x water immersion objective (Tokyo, Japan). The emitted light was detected and recorded with pco.panda sCMOS camera (Kelheim, Germany). To remove the excitation light from the optical detection pathway a dichroic mirror (DMLP650R and FELH0650, Thorlabs, New Jersey, United States) was used. Ten image frames were recorded per voltage step (–80 mV to +40 mV in 20 mV steps) , and each frame was recorded with exposure time of 1.5 s.

For each of the constructs the fluorescence intensity change was measured in three to six cells. The recorded data were analysed separately for each cell and then averaged. The initial analyses of the recorded images were carried out with ImageJ to extract the intensity profile. The further data analyses were carried out using Origin 9.0 (Origin Labs).

The patch-clamp fluorescence intensity increase was recorded by Rodrigo Fernandez Lahore (Humboldt Universität zu Berlin, AG Hegemann).

2. 5. Chromatography

2. 5. 1. Retinal extraction and analyses by high-pressure liquid chromatography (HPLC)

To study the retinal isomer composition, retinal extraction and high-pressure liquid chromatography (HPLC) were performed as previously reported[199].

To extract the retinal the detergent-solubilized sample was mixed with cooled ethanol (–20°C). Within 2 min, the extracted chromophore was dissolved in a mixture of heptane and 7% (w/w) diethyl ether. After another 2 min the phase separation was achieved with a centrifugation step (1min, 2000 rpm). The steps subsequent to chromophore extraction with ethanol were carried out under dim red light.

To extract retinal isomers from different QuasAr photoproducts, different pre-illumination steps were carried out. To obtain mixture of P580/P400 photoproducts, the sample was illuminated for 30 s with red light LED (625 nm). To obtain the recovered dark state D590' the red light illumination was proceeded with illumination of 1 min with blue light LED (400nm).

To determine the retinal isomer composition, the dissolved chromophore in the heptane/diethyl ether mixture was analysed using HPLC device LC-20AD (Shimadzu, Kyoto, Japan) equipped with ReproSil 70 Si, 5 mm column (Dr. Maisch, Ammerbuch-Entringen, Germany).

The obtained chromatogram was evaluated in Origin 9.0 (Originlabs) and the ratio between the different isomers was determined by peak integration.

2. 6. Molecular dynamics simulations

2. 6. 1. Molecular dynamics simulations

The molecular dynamics (MD) simulations were performed with Gromacs 5.1.2 and 5.1.4[200]. Force field parameters were set by amber99sb[201] and the all-*trans* retinal was embedded according to[202,203].

Modeller 9.22[204] program was used to build homology models of Arch3 and Archon1 (and its variants) 3D structure. Arch2 shares 86% sequence identity to

Arch3 and 80% sequence identity to Archon1, enabling the use of Arch2 crystal structure (PDB entry 3WQJ; 1.8 Å-resolution,[205]) to create these homology models.

The 3D protein structure was embedded into a pre-equilibrated simulation box of a POPC (1-palmitoyl-2-oleoyl-sn-glycero-3-phosphocholine) bilayer, water, K^+, and Cl^- using the Gromacs tool *g_membed*. Ion strength was set to 270 mM. Water modelling was done using SPC/E potential[206]. The single membrane equilibration is described in more detail elsewhere[207]. The single membrane was doubled and used to create a double membrane, allowing to create closed system and to study the protein under opposite transmembrane voltage (TMV) simultaneously.

Ion gradient across the membrane was used to generate the TMV. Ion gradient was created from q = 0e^- to q = 6e^- with a step of 2e^-. The TMV range of Arch3 was from –790 mV to + 790 mV, whereas of Archon1 from –850 mV to +850 mV. The high TMV values are crucial to observe voltage dependent changes in protein structure in accelerated simulation time. Simulations were repeated six times for each TMV for statistical evaluation.

Short-range electrostatics and van der Waals interactions were abolished beyond 10 Å. Long-range electrostatic interactions were calculated with the Particle mesh Ewald (PME) summation. All bonds to hydrogen atoms were constrained using the LINCS algorithm[208].

MDAnalysis[209] and PropKa 3.1[210] were used to estimate the pK_a values of residues. MDAnalysis[209] were used to also calculate the hydrogen bond interactions.

For visual representation the images were prepared with PyMOL 2.1 and matplotlib, numpy, pandas, and seaborn[211].

The MD simulations were carried out by Songhwan Hwang at Leibniz-Institut für Molekulare Pharmakologie under supervision of Dr. Utesch Tillmann and Prof. Dr. Han Sun.

3. Results

3. 1. Photocycle

3. 1. 1. Steady-state absorption spectra investigation

In the first part of the Results, I will introduce the study of the photodynamics and photocycle of QuasArs. In this chapter QuasAr1 and QuasAr2[3] are in the focus. As described above, QuasArs are fluorescent voltage sensors based on Arch3. They carry five point mutations compared to the wild-type (Figure 8), but differ from one another with only one mutation (D95H/Q). The distinctive properties emerging from the single mutation makes QuasAr1 and QuasAr2 desirable constructs for photodynamic studies. The results of spectroscopic studies compared among the two constructs ease the correlation of the photodynamics and their properties.

Three-photon excitation is needed to trigger fluorescence of the wild-type Arch3 (Fig. I5). The first photon (550 nm) initiates the photocycle, the second photon (560 nm) initiates photo-branching and the third photon (570 nm) induces the fluorescence[116]. However, the ~10-fold increased fluorescence in QuasArs is achieved through one photon excitation[3,167]. To reveal the underlying differences in the photoresponse of QuasArs compared to the wild-type, a range of spectroscopic and chromatography studies will be introduced – steady-state UV/Vis spectroscopy, time-resolved pump-probe spectroscopy and Raman spectroscopy, complemented by high-performance liquid chromatography (HPLC).

The absorption spectra of QuasArs were determined with steady-state UV/Vis absorption spectroscopy. The absorption spectra maximum of QuasAr1 is 580 nm (D580) and of QuasAr2 590 nm (D590) (Figure 15 A). The different residues at the counterion position (D95H/Q) of the constructs results in 10 nm difference of the dark state spectra absorption maximum. The absorption maximum of the next generation, Archons, is λ_{MAX} = 585 nm and the spectra are introduced in the supplement Figure S1.

The changes in the steady-state UV/Vis absorption spectra were monitored after different LED illumination steps. Similar characteristics were observed in both constructs - QuasAr1[212] and QuasAr2. Here, QuasAr2 will be disrobed in more detail

(Figure 15 B). In the first step, the sample was illuminated for ~ 10 s with a red-light LED (625 nm). The absorption spectra showed 10 nm hypsochromic shift of the spectral maximum. The newly accumulated species is denoted P580. In the second step, the red-light (625 nm) illumination was prolonged (~1 min). The absorption of protonated $RSBH^+$ species decreased and accumulation of UV absorbing species (P400) emerges. Both photoproducts, P580 and P400, are thermally stable. Following the absorption spectra changes of the light adapted sample for 24h stored in darkness, indicates that the dark state is not fully recovered (Figure S2)[212,213]. In the third step, the P580/P400 photoproduct mixture was illuminated for 30 s with blue light (400 nm) and a dark state like (D590') spectra was recovered.

Results from the UV/Vis steady state absorption spectra recordings are summarized in Figure 15 C. QuasArs display three thermally stable, spectroscopically distinguishable photoproducts. The transition between the photoproducts occurs after light excitation.

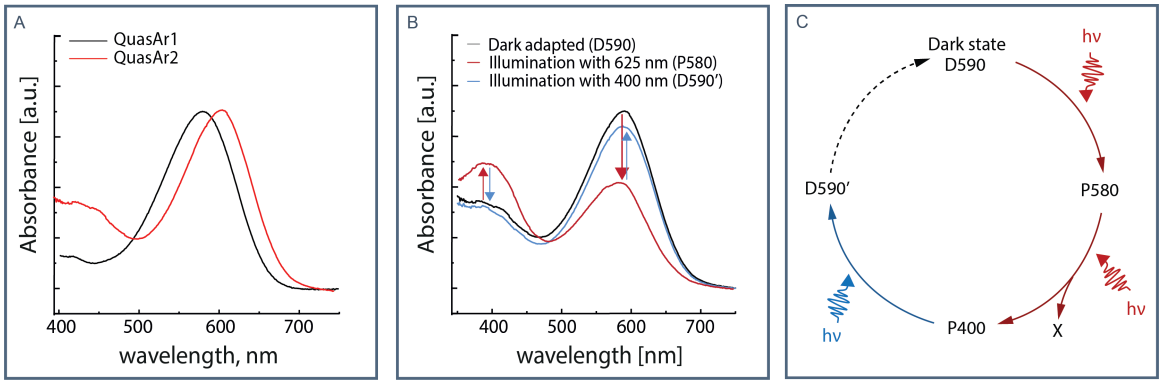

Figure 15. Study of photocycle of QuasArs

(A) Absorption spectra of QuasAr1 (580 nm) and QuasAr2 (590 nm) dark state. (B) Absorption spectra of QuasAr2 before (black curve) after 625 nm (red curve) LED and 400 (blue curve) LED illumination. (C) Preliminary photocycle comprising the identified three photoproducts.

3. 1. 2. Transient absorption spectra of QuasArs

To study the photo cycle of QuasArs, transient absorption spectra was recorded using flash photolysis spectroscopy. The sample was excited using 580 nm laser pulse and the spectra were recorded in the spectral region of 350 nm – 700 nm and in the time range between 10 ns up to 10 s. Changes in the retinal-binding pocket

would generate transient changes in the absorption spectra as seen for Arch3 (Figure 16 B, C). However, no spectral characteristics distinctive of photointermediates were observed in the reconstructed 3D plot (Figure 16 A). The results suggest that the formation of the photoproducts, presented above (Figure 15), is highly inefficient.

To specify, QuasArs do not go through a photocycle typical for microbial rhodopsins. Transient absorption spectra of the wild-type Arch3 is shown in Figure 16 B, C and the results are summarized in a photocycle in Figure 16 D. Upon excitation, the light energy triggers retinal isomerization from all-*trans* to 13-*cis* and results in population of K state with red-shifted absorption spectrum. K state decays with time component of 7,6 μs and leads to proton release from the extracellular side E204 and E214, deprotonation of RSB and population of blue-shifted M state. D95 is the counterion, which accepts the Schiff base proton. M state transitions to N state occurs within 4.7 ms. The $RSBH^+$ is reprotonated from proton donor D106, resulting in N state. The N state absorption spectra is similar to the dark state spectra. Upon dark state recovery within 481 ms, D106 is reprotonated from the intracellular side, and retinal reisomerization takes place, which is ~10-fold slower than previously reported by Maclaurin et al. 2013[116]. The dsicreptency likely arrises due to the chosen time range of the measurement. In the previous study the spectra were recorded up to 100ms, hindering precise exponential fit of the slowly recovering dark state.

As presented in the introduction (Figure 5), the highly fluorescent Q state is reached with photo-branching of the N state. The long-lived N state of Arch3, in comparison to BR, is a curious observation and might be a prerequisite of successful creation of fluorescent sensors.

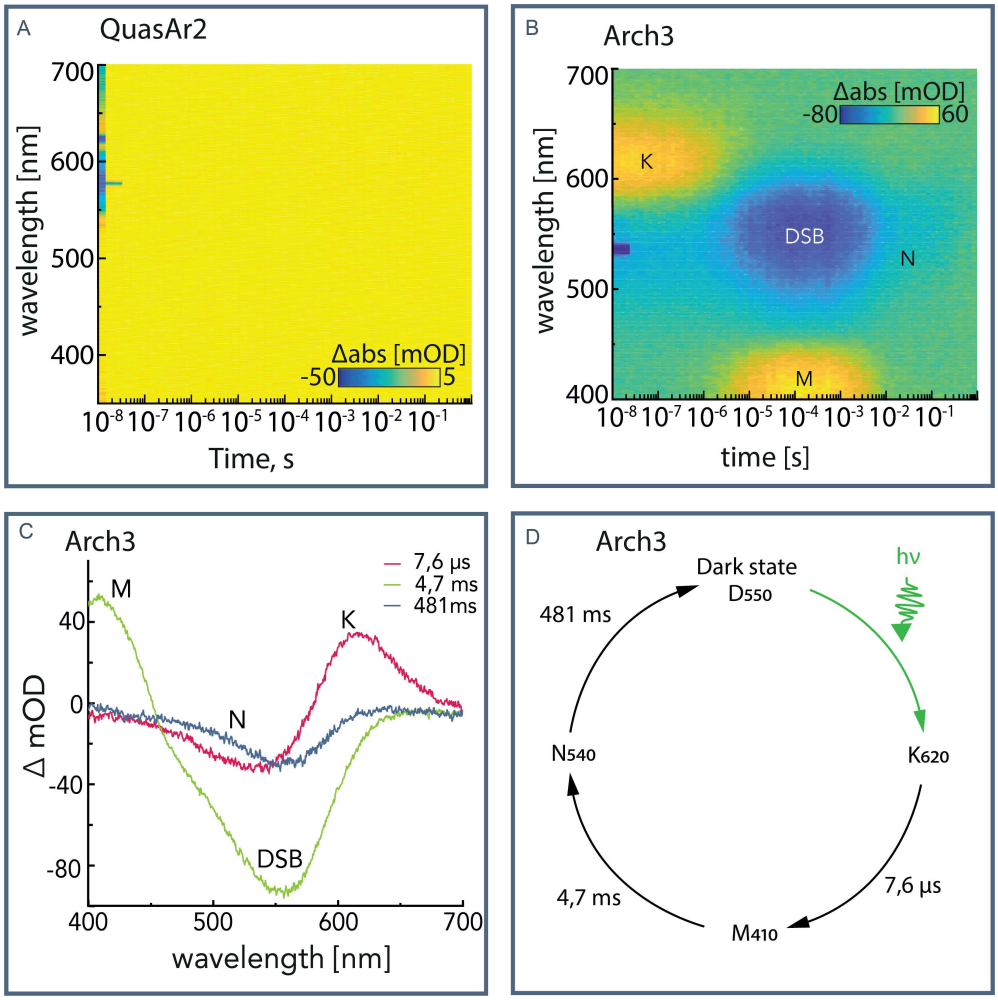

Figure 16. Transient absorption spectra of QuasAr2

Reconstructed 3D plot of transient absorption spectra in time range between 10 ns - 10s, and spectral range from 350 nm to 700 nm. (A) Transient absorption spectra of QuasAr2 with 580 nm excitation. In the reconstructed plot one can observe scattered light of laser (up to 100 ns) and stimulated emission (up to 20ns). (B,C) Transient absorption spectra of Arch3 recorded with excitation at 530 nm. The reconstructed 3D plot is shown in the panel (B). The resulting EADS spectra of the photointermediates are shown in panel (C). Global fit of the transient spectra provides the decay time constants of the photointermediates and are indicated in the upper right corner of the panel (C). The data are summarized in the photocycle (D).

The pump-probe spectroscopy gave further insights into the photodynamics of QuasArs. By tracing ultrafast changes in the absorption spectra, this technique allows to investigate the excited state and the early photointermediates. The transient absorption spectra (TAS) were recorded in a broad spectral window 360 nm – 720 nm and in time range from -50 fs to 1 µs (Figure 17, Figure S3, Figure S4). The excitation wavelengths were selected to excite the red shoulder of the

absorption spectra. QuasAr1 was excited with 610 nm and QuasAr2 was excited with 620 nm. The data were globally analyzed to resolve the decay time constants of spectral intermediates. The spectra were fitted with five exponential constants - τ_0 – τ_4, which are specified for each measurement in the panel upper right corner (Figure 17 B, E).

In addition to the dark state, also the photodynamics of the photoproducts were studied. The comparison of the QuasAr2 dark state D590 (QuasAr1 D580) and the photoproducts P580 (P570), D590' (D580') are shown in supplementary Figure S3, Figure S4. All of the photoproducts showed highly similar photodynamics and will not be introduced in detail.

Here, the case study of QuasAr2 dark state (D590) is described (Figure 17 A-C). Upon photon absorption, the molecule is excited to the S_1 state Franck–Condon region. Rapid Franck-Condon relaxation to the lowest vibrational level takes place in $\tau_0 \approx 180$ fs. A positive signal emerges with a peak at ~510 nm, assigned to excited state absorption (ESA) and two negative bands at ~590 nm and >670 nm, subsequently assigned to the ground state bleach (GSB) and the stimulated emission (SE). Compared to the ground state S_0, the excited state S_1 absorption is blue-shifted. The excited state decays with two time constants: $\tau_1 = 4$ ps and $\tau_2 = 40$ ps and is proceeded by a positive band ~640 nm. The band is assigned to the first photointermediate I640 in the ground state. A 20 nm hypsochromic shift is observed with time component $\tau_3 = 288$ ns, indicating new photointermediate I620. The decay of I620 is beyond the time resolution of the measurement (1 μs), therefore the fifth exponential τ_4 is set to infinity. Figure 18 A displays a schematic illustration of the reaction coordinate of QuasAr excited state dynamics and Figure 18 B summarizes the data in a preliminary photocycle.

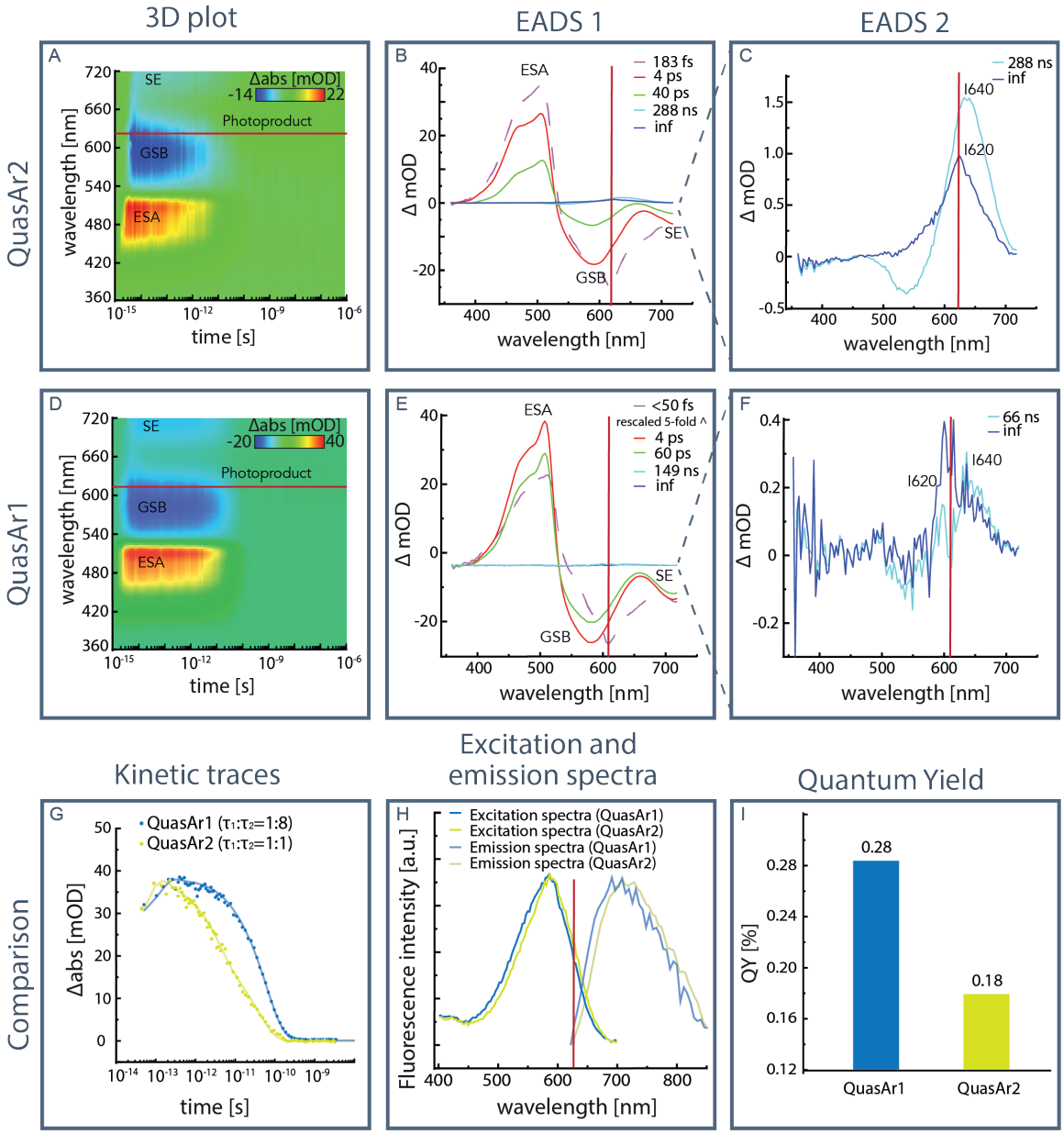

Figure 17. Ultrafast pump-probe spectra of QuasAr1 and QuasAr2

Excited state dynamics of QuasAr2 are shown in upper row (A-C), and excited state dynamics of QuasAr1 are shown in the middle row (D-F). (A,D) Reconstructed 3D plot of transient absorption spectra in time range between fs - µs and spectral range from 320 nm to 720nm are shown. (B,E) Evolution associated difference spectra (EADS) resulting from global analysis. (C,F) Close up of EADS to distinguish formed photointermediates. The laser excitation 610/620 nm is indicated with a red line. (G) Comparison of kinetic traces of QuasAr1 and QuasAr2 excited state decay. (H) Excitation and emission spectra of QuasAr1 and QuasAr2 (I) Measured quantum yield of QuasAr1 and QuasAr2 measured with excitation at 620 nm (610 nm).

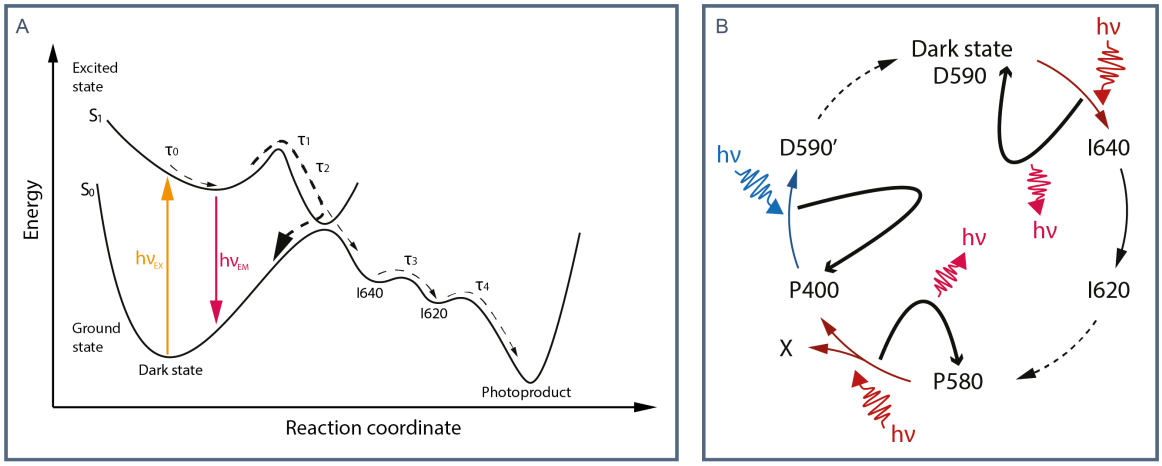

Figure 18. Excited state dynamics of QuasArs

The panel (A) shows the reaction coordinate upon photoexcitation of QuasArs. Upon absorption of a photon the molecule is promoted to the excited state S_1. Quick relaxation from Franck-Condon region to the excited state minimum is assigned to decay (τ_0). The excited state decay is fit with two time constants – τ_1 and τ_2. Both time constants are unusually slow, designating high energy barrier. Most of the molecules return back to the original ground state. A minor fraction of the excited molecules undergoes isomerization and forms a photointermediate I640, that transitions into photointermediate I620 with τ_3. The photointermediate I620 then decays with τ_4. (B) According to the data shown in Figure 15 and Figure 17 preliminary photocycle is proposed. The four stable photoproducts – D590, P580, P400 and D590', are proposed from Figure 15. After excitation most of the molecules return back to the original ground state, which is designated with the curved thick black arrows and release of a photon. A minor fraction (~4%) of the excited molecules undergo isomerisation and forms photointermediates I640 and I620 as seen in Figure 17. The intermediates are shown only following the dark state and are likely to result in population of the subsequent photoproduct.

The QuasAr2 (and QuasAr1) dynamics are atypical for microbial rhodopsins[57,58,111,214]. In comparison, the excited state decay of the wild-type Arch3 (Figure 19) is much faster with ~0.3 ps and it results in formation of J state (620 nm). Within 3 ps the retinal isomerization is completed and K state (610nm) is formed. The rise of the blue-shifted species of QuasAr2 I640 (τ_2 ~ 40 ps) and I620 (τ_3 ~ 290 ns) is too slow for vibrational relaxation, and consequently these photointermediates are not associated with J and K state.

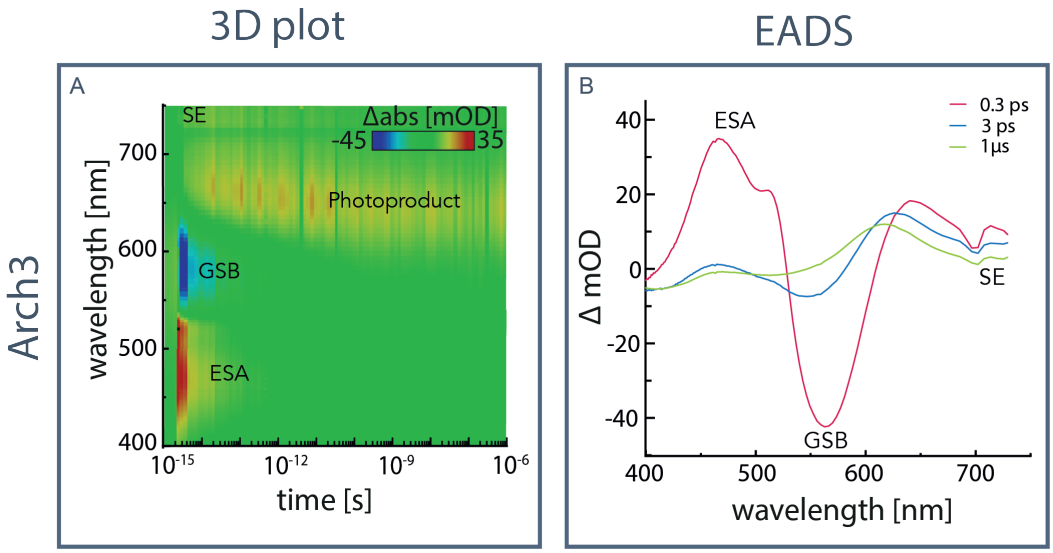

Figure 19. Transient absorption spectra of Arch3

The transient absorption spectra of Arch3 in time range between fs - µs after excitation with 560 nm. (A) The reconstructed 3D plot. (B) Globally fitted evolution associated difference spectra (EADS).

Additionally, the amplitudes of the formed photointermediates are unusually low. It can be suggested that high amount of molecules are excited owing to the strong signal of ESA and GSB. Estimated from EADS spectral amplitudes, 4% of the excited QuasAr2 form photointermediates and 1% of the excited QuasAr1 form photointermediates. These values are noticeably lower than 45 % efficiency of Arch3 (estimated from EADS). Only a minor fraction of the excited molecules undergo isomerization, most of the excited molecules return to the original excited state.

Although, the photodynamics are conserved also in QuasAr1 (Figure 17 D-F), the observed differences between the two constructs (Figure 17 A-G) provide critical insights in interrelation of the construct excited state dynamic and its properties. The comparison of the temporal profile of QuasAr1 and QuasAr2 (Figure 17 G) reveal different contribution of the two time components. QuasAr2 ESA and SE decay is comprised of equally contributing shorter-lived species (τ_1) and longer-lived species (τ_2). But the ESA and SE decay in QuasAr1 is mostly carried (~90%) by the longer-lived component (τ_2). Furthermore, the slow component (τ_2) in QuasAr1 is 1.5-fold slower (60ps vs. 40ps) resulting in 1.6-fold higher fluorescence QY of QuasAr1 (Figure 17 H, I).

As QuasArs are membrane voltage sensitive fluorescence sensors it is of high interest to study also the effect of proton concentration in the surrounding media on the photodynamics. For these experiments the pH of the buffer was exchanged from pH 8.0 to pH 11.0. The recorded spectra of dark species D590 (D580) at pH11 are shown in Figure 20.

The steady state UV/Vis spectra of QuasAr1 and QuasAr2 show shifts in equilibrium between protonated and deprotonated species upon pH exchange (Figure 20 A, D). QuasAr2 RSB deprotonation rate upon pH exchange is higher than in QuasAr1.

The reduced proton concentration causes change in the excited state dynamics, but does not change the spectral features of the ESA, GSB or SE. The excited state S_1 decay of QuasAr1 at pH 11 is fitted with two time constants τ_1 ≈ 11 ps, τ_2 ≈ 85 ps (Figure 20 B), which are noticeably slower than the excited state decay in pH8 (τ_1 ≈ 4 ps, τ_2 ≈ 60). The amplitude of the photointermediate is very small, and the decay of the photointermediate is beyond the measurement time resolution is set to infinity. In contrast, the kinetics of QuasAr2 (Figure 20 E) excited state decay are two-fold faster at pH 11.0 (τ_1 ≈ 2 ps, τ_2 ≈ 20) than at pH 8.0 (τ_1 ≈ 4 ps, τ_2 ≈ 40). The I640 photointermediate is formed with decay of excited state and experiences blue shift to I620 within τ_3 = 35 ns. The I620 photointermediate decays with $\tau_4 = \infty$.

Also the fluorescence QY exhibits dependency on the pH values. In alkaline conditions QuasAr1 shows 1.6-fold increase in the QY, but QuasAr2 displays 1.9-fold decrease in fluorescence QY. The variations in the QY are in agreement with the observed changes in the time constants of the excited state decay. The observed features could elucidate the higher voltage sensitivity of QuasAr2 compared to QuasAr1.

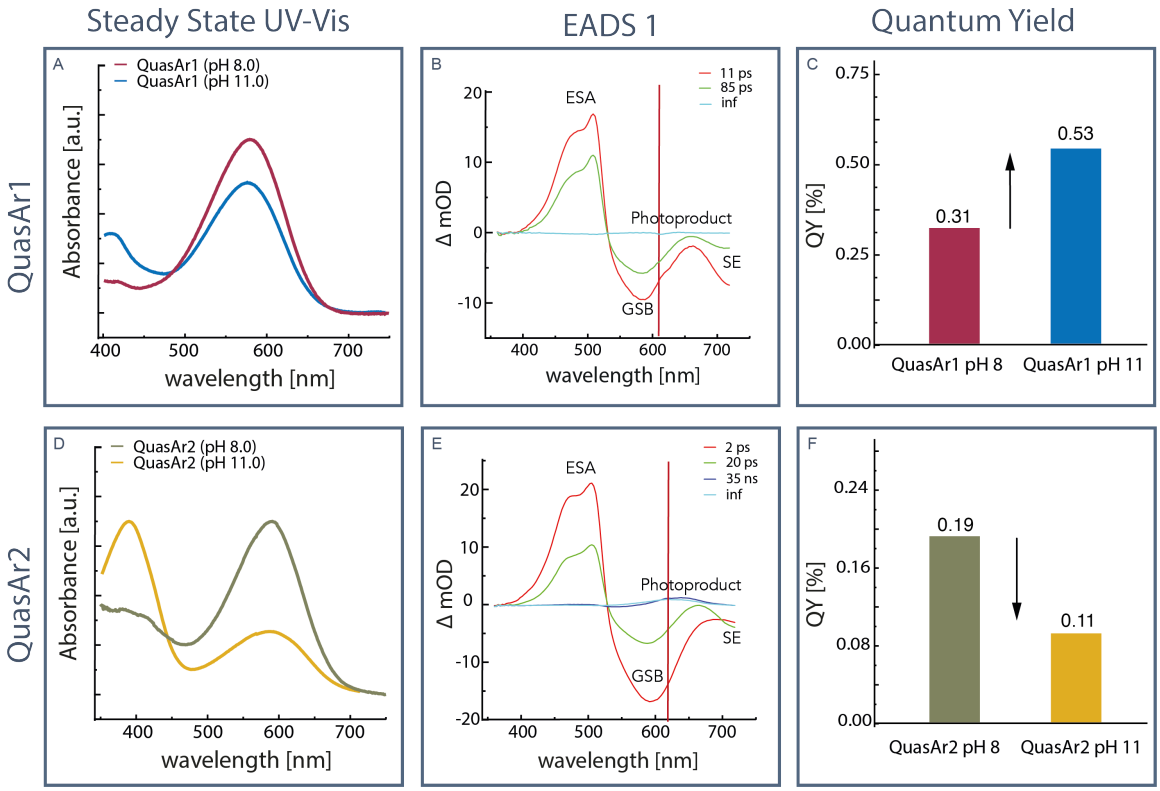

Figure 20. Transient absorption spectra of QuasAr1 and QuasAr2 at alkaline pH

(A,D) Steady-state absorption spectra of QuasAr1(A) and QuasAr2 (D) at pH8 and pH11. (B,E) Evolution-associated difference spectra (EADS) of QuasAr1 (B) and QuasAr2 (E) at alkaline pH. The laser excitation 610/620 nm is indicated with a red line. (C,F) Comparison of fluorescence quantum yield of QuasAr1 (C) and QuasAr2 (F) at pH8 and pH 11.

Further studies at reduced proton concentration were carried out on deprotonated species of QuasAr2 (D400) (Figure 21). The buffer exchange to alkaline conditions (pH 8.0 to pH 11.0) results in a rise of deprotonated species with absorption maxima at ~ 400 nm (Fig. 20D). Upon excitation with 400 nm light three positive bands emerge, which peak around 490 nm, 580nm, 630nm, and a negative band around 400 nm. The positive bands are assigned to the excited-state absorption (ESA) of S_1 and S_2. The negative band is assigned to the ground-state bleaching (GSB). Excited state absorption of deprotonated retinal differs from protonated excited state retinal, due to energy level inversion. Similar observations were done for HKR1[215]. For protonated retinal the lowest lying excited state S_1 is ^2B_u state, whereas for unprotonated retinal the lowest lying state S_1 is the optically forbidden ^2A_g state, resulting in excitation to S_2 state, which is ^2B_u state[216].

The TAS data of D400 at pH 11 were globally fitted with five time constants (τ_1 – τ_5). Once the molecule absorbs a photon, it is excited to S_2 state, which decays with time constant τ_1 ≈ 160 fs to the optically forbidden S_1 state. As only single fs-component could be resolved, it is likely that the time constant τ_1 is a mixture of S_2 to S_1 decay and the vibrational cooling of S_1. The S_1 state decays with two time constants τ_2 ≈ 4 ps, τ_3 ≈ 44 ps and only minor amount of photoproduct is formed. Figure 21 C shows schematic representation of deprotonated retinal photodynamics and assigned time constants.

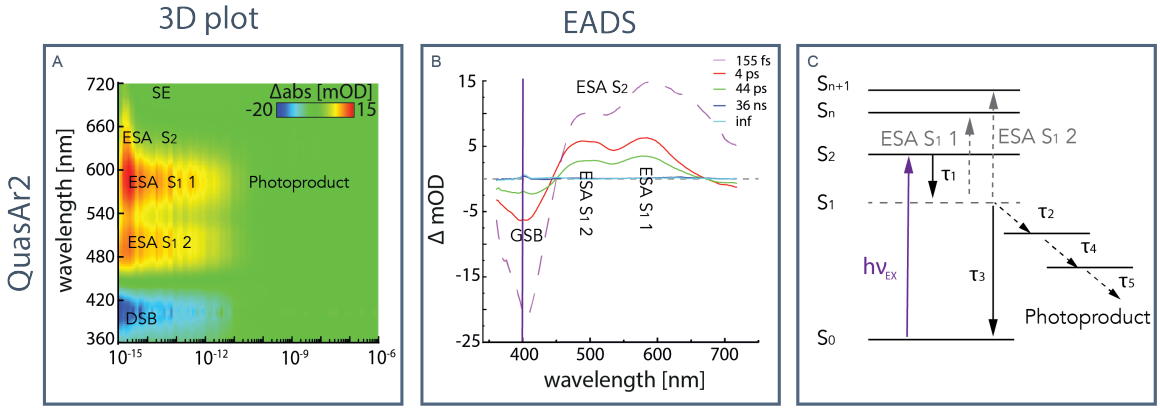

Figure 21. Transient absorption spectra of deprotonated species of QuasAr2 at alkaline pH

Reconstructed 3D plot of TAS of deprotonated species of QuasAr2 are shown in panel (A). The Evolution associated difference spectra (EADS) is shown in panel (B). The proposed Jablonski diagram of photodynamics with corresponding time components is shown in panel (C). Upon light excitation the molecule is brought to the excited state S_2, followed by decay τ_1 to optically forbidden S_1. The S_1 excited state decays with two time constants – τ_2 and τ_3. Most of the molecules return to the original ground state. The photoproducts decay with τ_4 and τ_5.

Also the new constructs Archon1 and Archon2[2] were studied using pump-probe spectroscopy (Figure 22). The overall dynamics resembled closely those reported for QuasArs, and schematic representation shown in Figure 18 A is in good agreement with excited state dynamics observed for Archons. The data were globally analyzed and fitted with five time constants τ_0 – τ_4, which are specified for each construct in the figures EADS panel upper right corner (Figure 22 A,B). Also here the observed S_1 excited state lifetime was long-lived, with a slow component of ~75 ps/~84 ps. The resolved spectra of Archons showed even further reduction of formed photoproduct (~0.05% as determined from EADS).

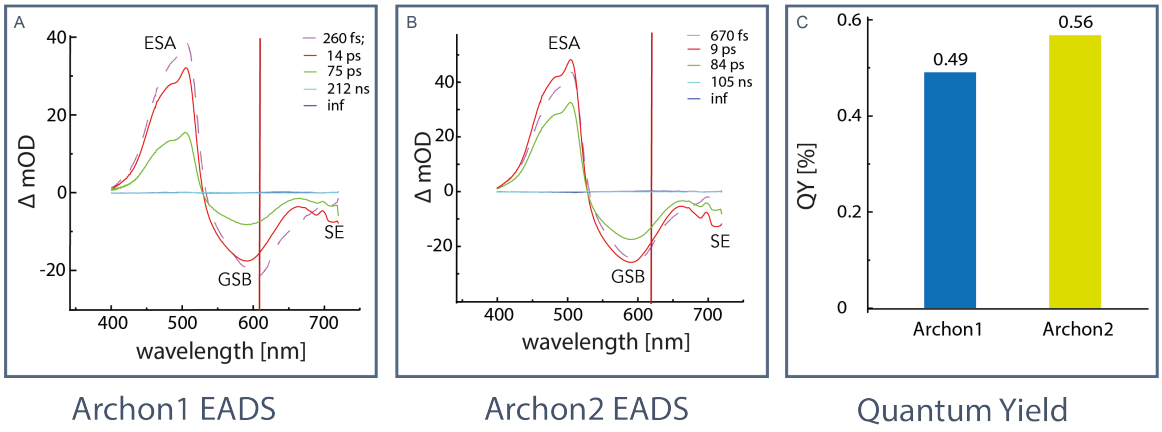

Figure 22. Ultrafast pump-probe spectra of Archon1 and Archon2

The samples were exited with 610 nm laser pulse as indicated with a red line. (A, B) Evolution associated difference spectra (EADS) resulting from global analysis. (C) Measured quantum yield of Archon1 and Archon2.

The study of excited state dynamics has supported tremendously understanding of the origin of fluorescence in QuasArs (Figure 17). The absorbed photon promotes the molecule to the excited state S_1. The excited state is extraordinarily long lived for microbial rhodopsins, consequently the stimulated emission is slowly decaying. Most of the excited molecules return to the original ground state. As estimated from EADS only <5% of the excited molecules undergo isomerization and form a photoproduct. Additionally, as observed in the spectral studies, the excited state lifetime correlates with the fluorescence QY (Figure 17, Figure 20, Figure 22).

3. 1. 3. Two-photon vs one-photon excitation of QuasArs

Two-photon excitation offers multiple advantages for applications in neuroscience research, such as, high spatial resolution, improved penetration depth of infrared light in tissue, and minimizes photodamage[217]. This denotes the importance of also characterizing the two-photon excitation properties of fluorescent constructs. The two-photon excitation spectrum of QuasAr2 was recorded in the spectral region of 1025-1400 nm and is shown in Figure 23 A. Interestingly, the two-photon excitation spectra overlaps with the one-photon excitation spectra (Figure 23 B).

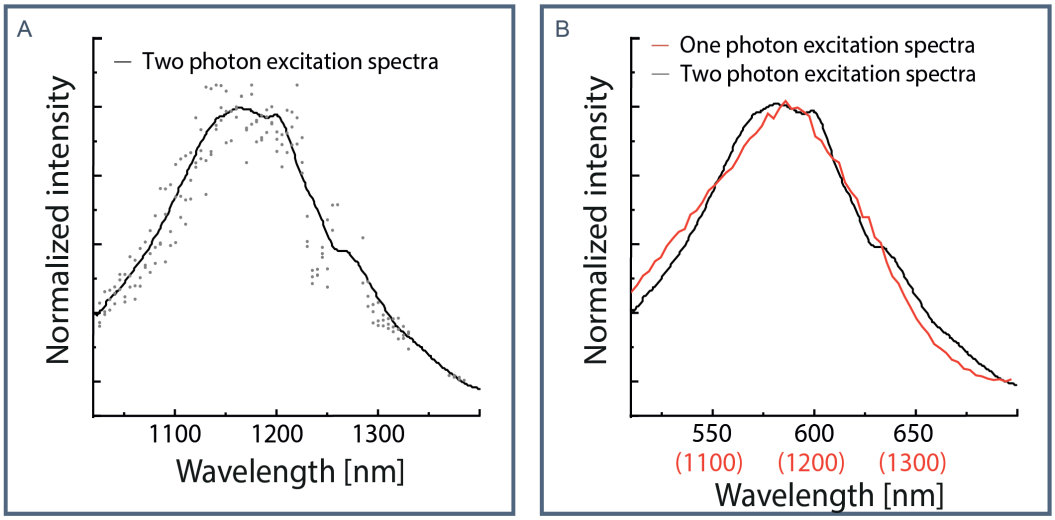

Figure 23. Two-photon study of QuasArs

(A) Two-photon excitation spectra of QuasAr2. The dip in the excitation spectra at 1235nm is most likely arising due to the absorption of water. (B) The excitation spectra recorded of QuasAr2 dark state D590 with one-photon (red) and two-photon (black) are compared. The two-photon excitation spectra values are divided by two for the evaluation.

3. 1. 4. Retinal isomer composition study using HPLC

To further elucidate the photodynamics of QuasArs, the chromophore was studied in more detail. Two methods were used for this study – High-performance liquid chromatography (HPLC) and Raman spectroscopy. Due to the unusual characteristics of QuasArs it was crucial to study the retinal isomer composition. To explore if a certain 'atypical' retinal isomer is responsible for prolongated excited state lifetime and increased fluorescence.

Hexane-extracted chromophores of QuasArs were analyzed with HPLC which separates the different isomeric forms by the retention time (Figure 24). From the calculated peak integral of the chromatogram retinal isomer composition was determined for QuasArs in the dark state and the photoproducts (Figure 15 B). Interestingly, the single counterion mutation of QuasArs (D95H/Q) result in different dark state retinal isomers. The dark state (D580) of QuasAr1 is comprised of 21% 13-*cis* and 79% all-*trans* retinal isomers (Figure 24 A). In contrast, QuasAr2 has much higher contribution of 13-*cis* retinal isomer, with composition of 47% 13-*cis* and 53% all-*trans* (Figure 24 D).

Even more astounding were retinal isomer composition in the photoproducts. With red illumination (30 s 625 nm LED) the mixture of blue-shifted (P570/ P580)

and deprotonated (P400/P380) photoproduct were generated (Figure 15 B). Despite the different retinal composition of the dark state, the photoproduct chromatograms appeared more alike (Figure 24 B,E). The QuasAr1 is comprised of 18% 13-*cis*, 14% 11-*cis*, 14% 9*cis* and 54% all-*trans* retinal. The QuasAr2 is comprised of 29% 13-*cis*, 16% 11-*cis*, 7% 9-*cis* and 48% all-*trans* retinal. In both constructs contribution of unusual isomers- 11-*cis* and 9-*cis* was observed. Both isomers are rarely found in microbial rhodopsins. In case of QuasAr1 all-*trans* contribution decreased and minor change was observed for 13-*cis* contribution. Whereas in QuasAr2 13-*cis* contribution decreased and minor change in all-*trans* was observed.

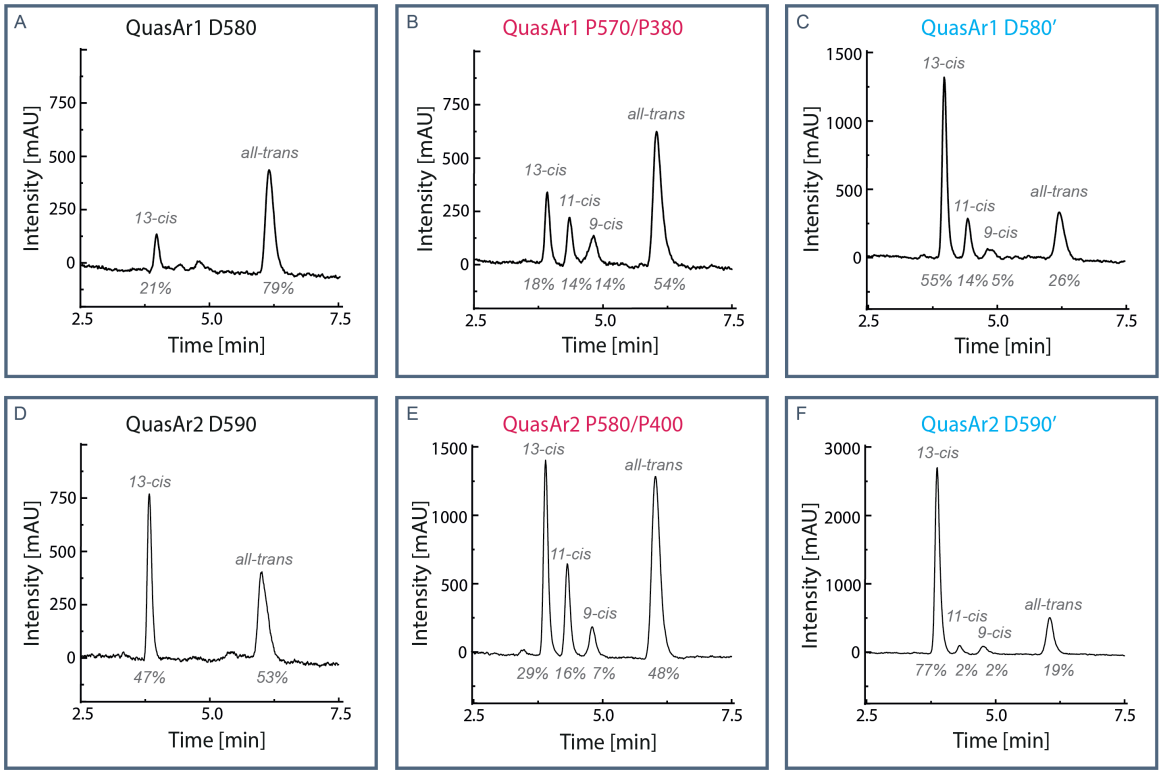

Figure 24. HPLC analysis of extracted retinal isomers

High-pressure liquid chromatography (HPLC) of extracted chromophore isolated from QuasArs. Dark state of QuasAr1(A) and QuasAr2 (D). Also the photoproduct retinal isomer composition was studied. Mixture of blue-shifted (P570 or P580) and deprotonated (P400 or P380) species were populated with 30s 625 nm LED and are depicted in panels (B) for Quasar1 and (E) for Quasar2. Recovered dark state like (D580' and D590') species were populated with subsequent 30 s 400 nm LED illumination and are shown in panels (C) QuasAr1 and (F) QuasAr2. Using peak integration the contribution of particular retinal isomer was determined and is indicated as a percentage below the chromatogram.

To recovere the dark state like photoproducts, the red illumination was followed with UV illumination (30 s 400 nm LED). The QuasAr1 D580' is comprised of 55% 13-*cis*, 14% 11-*cis*, 5% 9-*cis* and 26% all-*trans* retinal (Figure 24 C, Figure 15 C). The QuasAr2 D590' is comprised of 77% 13-*cis*, 2% 11-*cis*, 2% 9-*cis* and 19% all-*trans* retinal (Figure 24 F). In both constructs all-*trans* retinal isomer contribution decreased, whereas the 13-*cis* retinal isomer contribution increased, in particular for QuasAr2. Decrease in 11-*cis* and 9-*cis* retinal isomers are more pronounced in QuasAr2, suggests lower efficiency of backreaction. Despite the similar absorption spectra of dark state D590 (D580) and recovered dark state D590' (D580'), the retinal isomer composition is rather diverse. The observed diversity of retinal isomer composition, within the dark state and photoproducts, uncover the heterogeneous nature of the QuasArs.

3. 1. 5. Retinal isomer composition study using pre-resonance Raman spectroscopy

Additional qualitative studies of retinal conformation were carried out with preresonance Raman spectroscopy (Figure 25, Figure 26). Resonance and preresonance Raman spectroscopy allows to study the vibrational signals of the chromophore. The Raman spectroscopy is based on the inelastic light scattering. The energy loss (gain) corresponds to the frequencies of the normal modes. If the incident monochromatic light is in resonance or pre-resonance to an electronic transition of a part of a molecule (here, the retinal chromophore), those modes localized in the chromophore are selectively enhanced compared to the optically transparent matrix (here, the protein). These conditions are largely fulfilled in the present study even for 1064 nm excitation such that the corresponding (pre-)resonance Raman spectra predominantly display the modes of the retinal. The assignments of these modes of the retinal are depicted in Figure 25 C[218,219].

In the spectral region of interest (between 950 cm^{-1} and 1700 cm^{-1}) the retinal modes can be classified by their internal coordinates: C-H out of plane (HOOP) wagging, C-CH_3 rocking, C-C stretching, C-H rocking, C=C stretching and C=N (Schiff base) stretching (Figure 25). To characterize the retinal conformation, the C-C stretching (Figure 25, orange frame), the C=C stretching (Figure 25, green frame), the C=N stretching (Figure 25, blue frame) and HOOP coordiantes are of particular

interest. These corresponding spectral regions provide information of the retinal isomer composition, absorption maxima and retinal protonation state[220,221] and will be discussed in detail below.

Due to excitation with 1064 nm (640 mW), which is considerably red-shifted from the absorption maxima, no photoreactions are induced, such that the dark state retinal isomer composition is not altered[222].

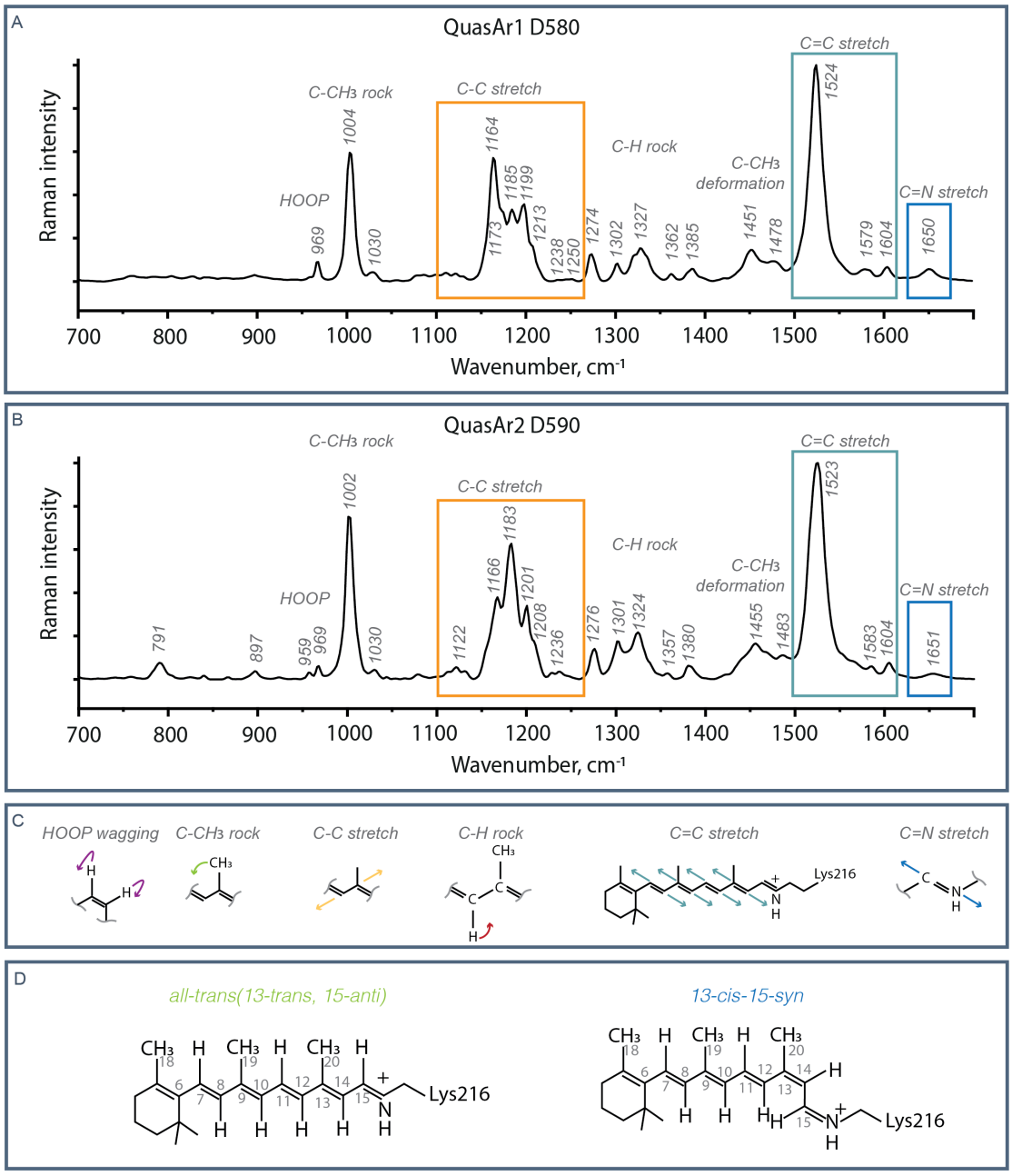

Figure 25. Recorded pre-resonance Raman spectra

Raman spectra were recorded with 1064 nm excitation (640 mW). The sample was purified in SMA nanodiscs. Panel(A) shows QuasAr1 Raman spectra and panel (B) shows QuasAr2

Raman spectra. Panel (C) designates the assignments of the retinal vibrational modes. The floating frames designate the regions of interest for spectral analysis – C-C stretch/ Fingerprint region (orange), C=C stretch (green), C=N stretch (blue). (D) Retinal conformation in all-trans and 13-cis/15-syn isomers.

In-depth study of Raman spectra of the BR dark- and light-adapted states, its photointermediates and the BR variants reconstituted with labeled retinal derivatives have supported the assignment of the retinal vibrational modes in rhodopsins[220,221,223]. The previous ground work done on BR is also used here to guide the assignment of the band frequencies observed in QuasArs.

Fingerprint region (1150-1300 cm^{-1}) provides insights into the retinal configuration. The observed peak frequencies in this region are highly sensitive to conjugation around the double and the single bonds of the polyene[220,221].

Similar to BR_{568}[220] and BR_{548}[221], also in QuasArs the bound protein introduced an upshift of ~10 cm^{-1} of the observed frequencies in the fingerprint region compared to the PSB all-*trans* and 13-*cis* chromophore[221,224]. The bound protein increases the electron delocalization, consequently, increasing the C-C stretch frequencies.

In the C-C stretching region of QuasAr1 pronounced peaks at 1164 cm^{-1}, 1173 cm^{-1} (merged with the 1165 cm^{-1} band), 1185, 1199 and 1213 cm^{-1} frequencies are observed. Additional minor signals can be observed at 1238 and 1250 cm^{-1} (Figure 25 A). QuasAr1 is comprised of mixture of all-*trans* and 13-*cis* retinal isomers.

According to high similarity to BR_{568} (all-*trans*)[220] the bands at 1173, 1199 and 1213 cm^{-1} are assigned to the all-*trans* retinal isomer. The 1199 cm^{-1} mode is assigned to C_{14}-C_{15} stretch (1201 cm^{-1} in BR_{568}). The 1173 cm^{-1} mode is assigned to the C_{10}-C_{11} stretch (1169 cm^{-1} in BR_{568}). The 1213 cm^{-1} frequency is assigned to the C_8-C_9 stretch (1214 cm^{-1} in BR_{568}). The C_{12}-C_{13} stretch is delocalized in BR_{568} and contributes to modes at 1169, 1248 and 1255 cm^{-1}, where the latter have very low intensities[220]. The intensity of signal at 1250 cm^{-1} is extremely low in QuasAr1, whereas the signal at 1164 cm^{-1} is very intense. It is suggested that the C_{12}-C_{13} stretch contributes more strongly to the observed band at 1164 cm^{-1}, and provides a minor contribution to the mode at 1250 cm^{-1} frequency.

In resemblance to BR_{548} (13-*cis*/15-*syn*)[221] the bands 1164, 1185, 1238, and 1199 cm^{-1} mode, are assigned to the 13-*cis* retinal isomer. In case of the 13-*cis*/ 15-*syn* retinal conformation the C_{14}-C_{15} stretch is assigned to the band at 1164 cm 1

(1167 cm^{-1} in BR_{548}), which is ~25 cm^{-1} downshifted compared to the all-*trans* counterpart. The C_{12}-C_{13} stretch is also delocalized in case of 13-*cis* isomer and contributes to the modes at 1164 and 1238 cm^{-1} (1165 and 1234 cm^{-1} in BR_{548}). The intensity of 1238 cm^{-1} band is very low due to antisymmetric combination with the C_{14}-C_{15} coordinate[221]. The C_{10}-C_{11} stretch gives rise to an intense band at 1185 cm^{-1} (1183 cm^{-1} in BR_{548}). This band is particularly characteristic of the 13-*cis* retinal isomer. In BR_{548} the C_8C_9 stretch is assigned to band at 1202 cm^{-1} frequency[221]. It is likely that this band is merged with that at 1199 cm^{-1} band in QuasAr1 spectra.

To investigate the C=N configuration of the retinal isomers present in QuasAr1, particular bands are taken in consideration. One of them is the C_{14}-C_{15} stretch. In case of the C=N (*syn*) configuration, the C=N stretch interacts symmetrically with C_{14}-C_{15}. Upon deuteration the C_{14}-C_{15} increases in frequency by ~40 cm^{-1}. However, in the C=N (*anti*) configuration there is no longer the symmetric interaction, and the C_{14}-C_{15} stretch frequency remains unaltered by deuteration[47]. A second marker band for the C=N (*syn*) configuration is specific for the conjugated C_{13}=C_{14} (*cis*) retinal. Due to the geometry of the retinal, a HOOP band emerges (~800 cm^{-1} in BR_{548}) originating from the uncoupled C_{14}H wag[221].

In case of QuasAr1, there is no pronounced band observed around ~800 cm^{-1}, which could be due to low 13-*cis* concentration. However, upon deuteration there is a strong shift in the 1165 cm^{-1} band, which is assigned to 13-*cis* C_{14}-C15 stretch (Figure 26 A). But there is no shift of the 1199 cm^{-1} band, which is assigned to the all-*trans* C_{14}-C_{15} stretch. Therefore, contributions of all-*trans* and 13-*cis*/15-*syn* retinal isomers can be resolved.

In the C-C stretching region of QuasAr2 pronounced peaks at 1166, 1183, and 1201 cm^{-1} are observed. An additional minor signal can be detected at 1236 cm^{-1} (Figure 25 B). QuasAr2 is comprised of mixture of all-*trans* and increased contribution of 13-*cis* retinal isomer, as also observed in HPLC study (Figure 24 A,D).

According to BR_{548} (13-*cis*/15-*syn*)[221] the bands 1166, 1183, and 1236 cm^{-1} are assigned to the 13-*cis* retinal isomer. The C_{14}-C_{15} stretch is assigned to the band at 1166 cm^{-1}. Also the C_{12}-C_{13} stretch contributes to the band at 1164 cm^{-1}. Additionally, the antisymmetric combination of the C_{12}-C_{13} and C_{14}-C_{15} stretches produces a minor signal at 1236 cm^{-1}. The characteristic high intensity band at

1183 cm^{-1} is assigned to the C_{10}-C_{11} stretch. The C_8-C_9 stretch is assigned to band at 1201 cm^{-1}.

Due to strong intensity of 13-*cis* modes, the all-*trans* retinal contributions are vaguely noticeable in the recorded pre-resonance Raman spectra of QuasAr2. According to BR_{568} (all-*trans*)[220] the C_{14}-C_{15} stretch contributes to the 1201 cm^{-1} mode, the C_{10}-C_{11} stretch would contribute to the 1166/1183 cm^{-1} modes, and the C_8C_9 stretch to the 1208 cm^{-1}.

In QuasAr2 the 13-*cis* isomer is likely to also carry the C=N (*syn*) configuration. The C_{14}H HOOP mode at 793 cm^{-1} is explicitly observed in double-conjugated isomers (Figure 25 B)[221]. Upon deuteriation (Figure 26 B) the signal at 1166 cm^{-1} diminishes. The contribution from C_{14}-C_{15} stretch is upshifted by 46 cm^{-1} and band at 1212 cm^{-1} emerges. An additional critical indicator is the 12 cm^{-1} shift of C_{14}H HOOP from 793 cm^{-1} to 803 cm^{-1} upon deuteriation[221].

The observed Raman spectra in the fingerprint region support the HPLC chromatograms, which show that both QuasArs comprise all-*trans* and 13-*cis* retinal isomer. QuasAr1 has a stronger signal from all-*trans* retinal, whereas QuasAr2 has a higher contribution from 13-*cis*/15-*syn* retinal.

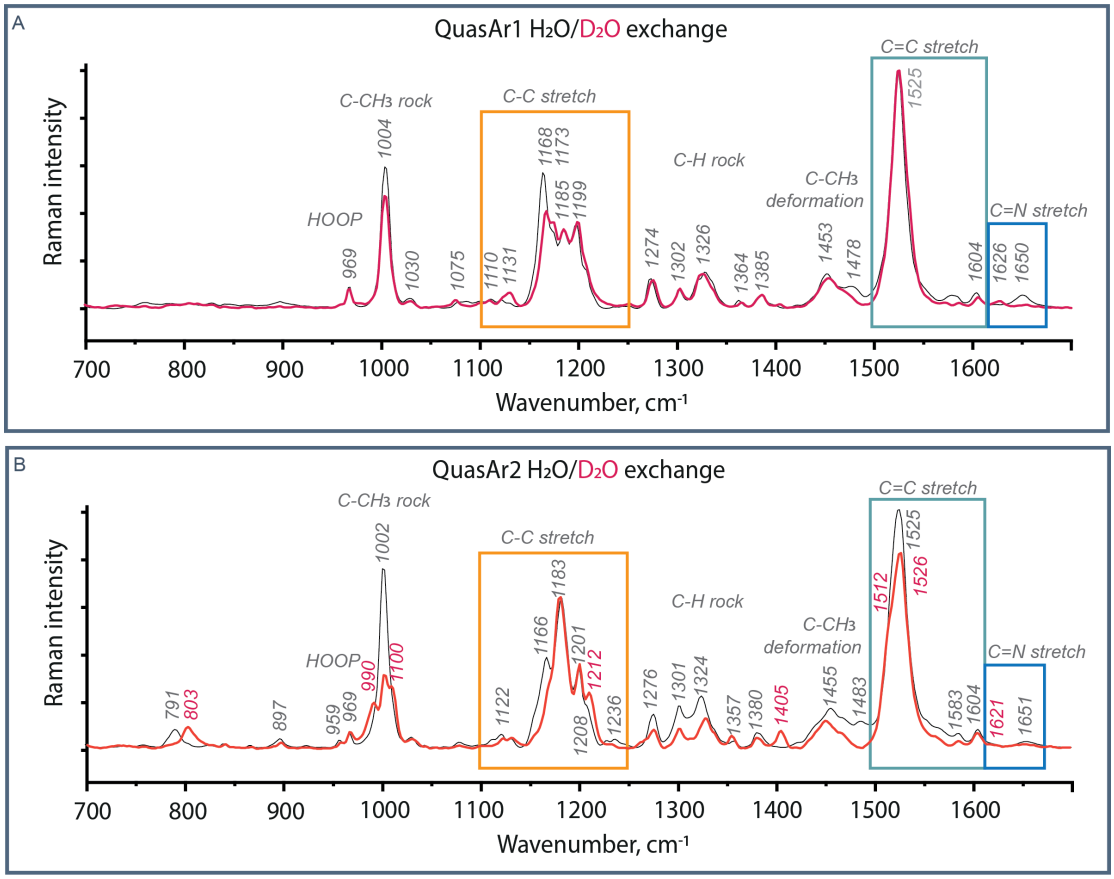

Figure 26 H_2O/D_2O exchange

Panel (A) shows Raman spectra of QuasAr1 in H_2O (black) and D_2O (red). Panel (B) shows Raman spectra of QuasAr2 in H_2O (black) and D_2O (red).

The C=C stretch (ethylenic stretch) is observed in spectral region from 1500 to 1600 cm^{-1} (Figure 25). The highest intensity in this region band is based on the combination of the C_{13}=C_{14}, C_{11}=C_{12}, C_9=C_{10}, C_7=C_8, and C_5=C_6 in phase stretching and is of particular interest for investigating the chromophore[220]. The frequency of the C=C stretch band is strongly inversely correlated to the absorption maximum (Figure S5, Table S2)[225]. Comparable to BR (1526 cm^{-1}, 568 nm) and Arch3 (1527 cm^{-1}, 565 nm)[117], both constructs follow the reported correlation (Figure S5, Table S2)[225]. However, despite their different absorption maxima (□□ = 10 nm), the ethylenic stretch frequency peaks for QuasAr1 and QuasAr2 are very similar. QuasAr1 C=C stretching is observed at 1524 cm^{-1} (Figure 25 A), and the absorption maximum in the visible spectral region is 580 nm (Figure 15 A). Whereas the QuasAr2 C=C stretching band is slightly downshifted and peaks at 1523 cm^{-1} (Figure 25 B), and the absorption maximum is red-shifted to 590 nm (Fig.1A). Additionally,

the peak of Quasar2 (FWHM - 19 cm^{-1}) is broader than the one of QuasAr1 (FWHM - 16 cm^{-1}) (Figure 25).

First attempts to disentangle the contributing peaks were done with by second-derivative transformation of the recorded spectra (Figure S6). Despite the promising method and observing sharper bands, the peaks of subspecies could not be resolved. Second attempt was to record cryo-UV/Vis spectra (Figure S7). Also with this method the subspecies were spectroscopically overlapping, and did not permit determination of their absorption peaks.

The C=N stretching band is observed above 1620 cm^{-1} (Figure 25). The strength of the N-H bond has a strong effect on the frequency of the C=N stretching band. Stronger hydrogen bond interactions yield higher frequencies[226]. QuasAr1 peak frequency appears at 1651 cm^{-1}. QuasAr2 peak frequency appears at 1652 cm^{-1}. Both frequencies are noticeably upshifted compared to BR_{568} (1639 cm^{-1}) and Arch3 (1641 cm^{-1})[117]. Upon deuteriation the C=N frequency undergoes a larger downshift (~25/30 cm^{-1}, Figure 26) compared to BR_{548} (17 cm^{-1}) and Arch3 (20 cm^{-1})[117]. Both observations are indicators of a strong N-H bonding.

Hydrogen-out-of-plane (HOOP) vibrations are found in spectral range from 700 to 1000 cm^{-1} (Figure 25)[223]. HOOP modes may provide additional information about the retinal conformation, in particular its planarity. Planar chromophore produces only weak intensity modes in HOOP region, whereas torsional deformation strongly enhances the intensities[220,223]. In QuasAr1 the chromophore appears to be highly planar, and only single mode with low intensity is observed at 969 cm^{-1}. This mode is assigned to $HC_7=C_8H$ HOOP vibration according to all-*trans* retinal and BR_{568} (972 cm^{-1})[220,223]. In QuasAr2 additional bands are observed, although in low intensity, likewise suggesting planar retinal conformation. Stronger band appears at 791 cm^{-1}, which is assigned to $C_{14}H$ HOOP mode and is characteristic for 13-*cis*/ 15-*syn* retinal (800 cm^{-1})[221]. Further bands are observed at 897 cm^{-1} and 959 cm^{-1} and are assigned to $C_{10}H$ (897 cm^{-1}) and $HC_{11}=C_{12}H$ (959 cm^{-1}) HOOP modes, correspondingly[220,221].

3. 2. Voltage sensing

Fundamental characteristic of QuasArs is their ability to change the fluorescence intensity upon changes in membrane voltage. However, the mechanism of this property is not yet understood. In the following chapter voltage sensing mechanism of QuasArs will be explored. Multiple factors that could contribute to the voltage sensitive fluorescence are hypothesized. Firstly, voltage modulated equilibrium of protonated and deprotonated RSB. This would affect population of red light absorbing species (QuasArs and Archons typically excited with 640 nm[3,8]). Alternatively the voltage might influence protonation or deprotonation of carboxyl group in the proximity of $RSBH^+$ (candidates D125, D222), which would result in a shift of the absorption spectra maximum. This again would result in change in the amount of photoactive species. Third, voltage modulated isomer composition, for instance, equilibrium shift between 13-*cis* and all-*trans* retinal isomers. Fourth, voltage regulated rearrangement of residues and hydrogen bonding network, resulting in changes in the electrostatic environment surrounding the $RSBH^+$. Fifth, membrane voltage affected changes in the fluorescence lifetime.

For this part of the study Archon1 was selected as the model construct (Figure 9), because Archon1 has higher expression and membrane targeting, increased brightness and high voltage sensitivity[8].

3. 2. 1. MD simulations on Archon1

To investigate the voltage sensing mechanism of Archon1 and study the voltage dependent reorientation of residues and hydrogen bonding we used molecular dynamic (MD) simulations. Additionally, the wild-type Arch3 was chosen as a model system. In order to accelerate the dynamics (the rearrangement of the residues and hydrogen bonding) as response to the membrane voltage, a high charge difference per membrane of $q=5e^-$ was used, and the consequent voltages are in the range of ± 800 mV. The wild-type Arch3 and Archon1 surprisingly displayed different key residues and voltage sensitive hydrogen bond networks. The comparison of results for Arch3 and Archon1 are provided below.

In Arch3, R92 played the central role in voltage sensing (Figure 27 A-C). At negative voltage conditions (negative inside and positive outside) R92 flips towards

the RSB and forms hydrogen bonds with the D95 and D222 from the counterion complex (Figure 27 A)[207]. At positive voltage conditions (positive inside and negative outside) R92 flips towards the extracellular side and forms hydrogen bonds with the E204 and E214 from the proton release complex (Figure 27 B). Observations of additional hydrogen bonds modulated by voltage are shown in Figure 27 C. The hydrogen bond between D95 and T99 was indicated to be the most essential (HB1-hydrogen bond 1) and is formed upon more positive membrane voltage.

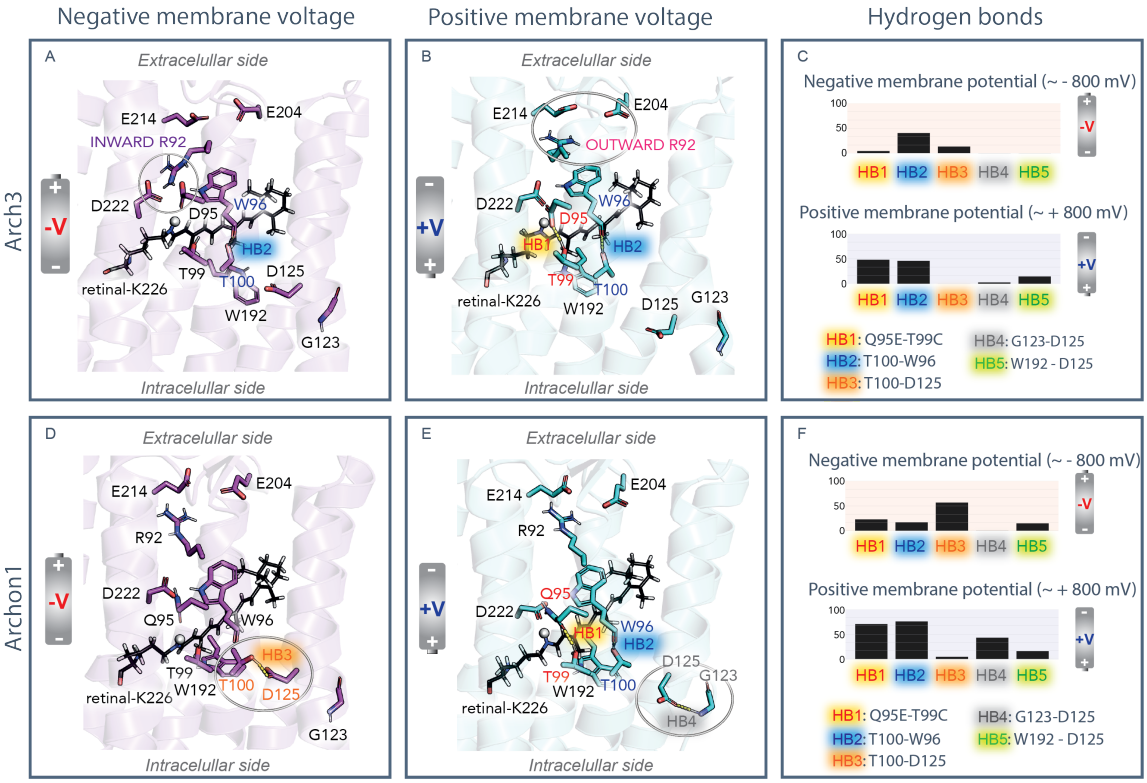

Figure 27. Voltage-sensing in Arch3 and Archon1

The structures are color coded for applied membrane voltage. Magenta is used for negative membrane voltage, whereas blue is used for positive membrane voltage. The Schiff base proton is designated as a white sphere. (A-C) Voltage modulated conformational changes in Arch3. The most pronounced changes are observed for R92. Upon negative membrane voltage (A) R92 orients towards the intracellular side and forms hydrogen bonds with D95 and D222. Upon positive membrane voltage (B) R92 orients towards the extracellular side and forms hydrogen bonds with E204 and E214. Change in other hydrogen bonds are shown in (C). Voltage modulates hydrogen bond between D95 and T99 (HB1). Whereas other hydrogen bonds, which are important for Archon1, do not show strong voltage-dependance. (D-F) Voltage-modulated changes in Archon1. The most pronounced changes are observed forD125. Upon negative membrane voltage (D) D125 orients towards the retinal binding pocket and forms a hydrogen bond with T100 (HB3). Upon positive voltage (E) D125 flips towards the intracellular side

disrupting HB2 and forming a new hydrogen bond with G123 (HB4). Additional two new hydrogen bonds are observed between Q95 and T99 (HB1) and between T100 and W96. Panel (F) shows the voltage dependance of the key hydrogen bonds observed in Archon1.

The data are described in more detail in dissertation of Hwang Songhwan[207].

The MD simulations revealed important differences in the voltage sensing mechanism of Archon1[207]. One may expect that R92 plays an essential role also in Archon1 as observed in Arch3 and suggested for other microbial rhodopsins[227,228]. However, R92 in Archon1 is always oriented towards the extracellular side, independent of the applied membrane voltage (Figure 27 D, E). This results also in maintained hydrogen bond to residues E204 and E214 on the extracellular side.

The MD simulations predicted D125 as the key residue involved in voltage sensing of Archon1. In Archon1, flipping of D125 has strong impact on the hydrogen bond rearrangement in the retinal binding pocket and conformational changes. At negative voltage D125 flips towards the retinal binding pocket (Figure 27 D). This orientation leads to hydrogen bond formation between D125 and T100 (HB3). At more positive membrane voltage, D125 flips away from the retinal binding pocket, towards the intracellular side (Figure 27 E). The new orientation of D125 disrupts HB3 (D125-T100), but new hydrogen bonds are observed. D125 forms a hydrogen bond with G123 (HB4). T100 forms a hydrogen bond with W96 (HB2). A fundamental hydrogen bond between Q95 and T99 (HB1) is formed (Figure 27 E, F). Under positive voltage, the loss of HB3 destabilizes the connection between helices C and D, and results in unwinding of helix D (Figure S8).

Interestingly, in Archon1 the distance distribution between D222- $RSBH^+$ is closer than between Q95- $RSBH^+$ (Figure S9 G, H). Additionally, the distance distribution shows dependency on the membrane voltage. At more positive membrane voltage, the observed distance distribution varies less, indicating higher rigidity of the retinal. The close relation between D222 and $RSBH^+$ permits a proton pathway from Schiff base to the counterion. Conversely, the calculated pK_a~3.5 of D222 is very low and insensitive to voltage change (Figure S9 E). However, the membrane voltage modulates the pK_a of D125 and possibly its protonation. At negative voltage the pK_a of D125 is ~5, which is much lower than one observed at positive voltage pK_a~7 (Figure S9 E).

3. 2. 2. Spectroscopy with intact cells

To further explore the mechanism of voltage sensing, spectroscopic assay using intact cells were established. *E. coli* cell suspension was prepared with overexpressed Archon1. The addition of an ionophore to the cell suspension increases membrane permeability allowing cations and/or protons to move across the membrane. The disruption of the ion gradient between intracellular and extracellular environment results in changes in the membrane potential[166,194]. The resting potential of *E. coli* is ~ –140 mV and after addition of ionophore the membrane potential reaches to the value ~ 0 mV[189]. Employing the *E. coli* cell assay, allowed investigating changes in fluorescence lifetime and retinal isomer composition upon membrane depolarization.

To investigate the fluorescence lifetime at resting potential and upon more positive membrane potential, fluorescence lifetime imaging microscopy (FLIM) was used. Initial fluorescence lifetime recordings were carried out on solubilized and purified Archon1 and compared to the excited state lifetime. The excited state lifetime decays with two time components τ_1 = 14ps and τ_2 = 75ps (Figure 22 A, Figure 28 A). The FLIM recordings revealed fluorescence decay that could be fitted with three time components. The fastest time component of the pump-probe experiments (τ_1 = 14ps) is beyond the time resolution of FLIM recordings, however Streak camera recordings provided faster time resolution (3ps) and revealed that this component is not present (Figure S10). Furthermore, FLIM allowed to determine two additional time components. The purified Archon1 fluorescence lifetime was fitted with τ_1 = 70ps (96.5%), τ_2 = 230ps (3%), τ_3 = 2700ps (0.5%), resulting in mean fluorescence lifetime τ_{mean} = 87,95 ps. The observed time component τ_1 = 70 ps (96.5%) with the highest amplitude is in good agreement with the observed slower component of the excited state decay (τ_2 = 75ps) (Fig.14).

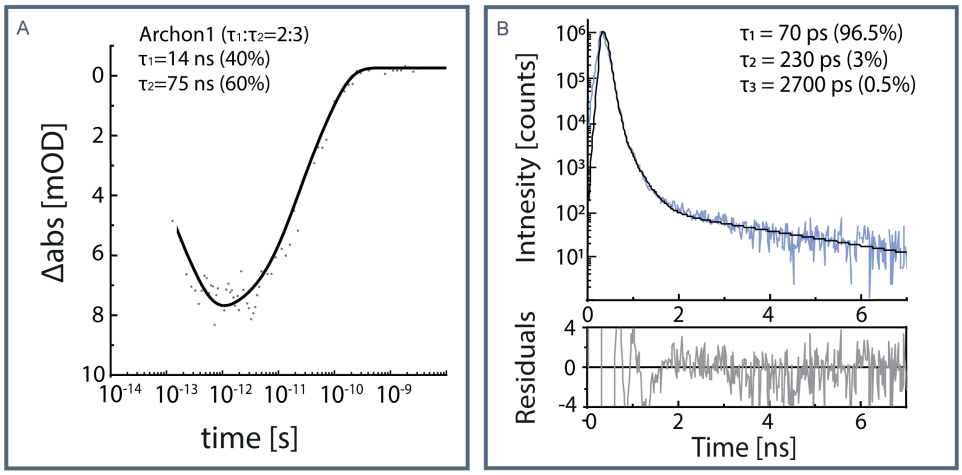

Figure 28. Fluorescence lifetime of Archon1

The comparison between (A) stimulated emission decay and (B) fluorescence lifetime of Archon1 - detergent solubilized (DDM&CHS micelles) and purified.

The measurements were followed up with recordings of Archon1 overexpressed in *E. coli* (C41(DE3)) cells. Figure 29 shows evolution of fluorescence after addition of ionophore (gramicidin[194]) over time period of 15 min. Each of the images (Figure 29 A) captures 1 min cumulative recording. The fluorescence intensity gradually increases upon membrane depolarization until membrane potential reaches ~0 mV (Figure 29 D). The fluorescence lifetime of 1st minute is shown in Figure 29 B, and after 15 min - Figure 29 C. Both traces can be exponentially fitted with four time components. The fluorescence lifetime of Archon1 overexpressed in *E. coli* cell was slower than that of purified protein. At resting membrane potential the values obtained were: τ_1 = 90ps (89.5%), τ_2 = 300ps (4%), τ_3 = 790ps (1%), τ_4 = 2850ps (5.5%) and the resulting mean value τ_{mean} = 260ps (Fig.14B). After depolarization the values obtained were: τ_1 = 100ps (94.5%), τ_2 = 460ps (2%), τ_3 = 2000ps (2%). and τ_4 = 5200ps (1.5%) and the resulting mean value τ_{mean} = 220 ps (Figure 29 C). Despite the increase of fluorescence intensity there was no increase observed in the mean fluorescence lifetime (with fitting error of 5-10%).

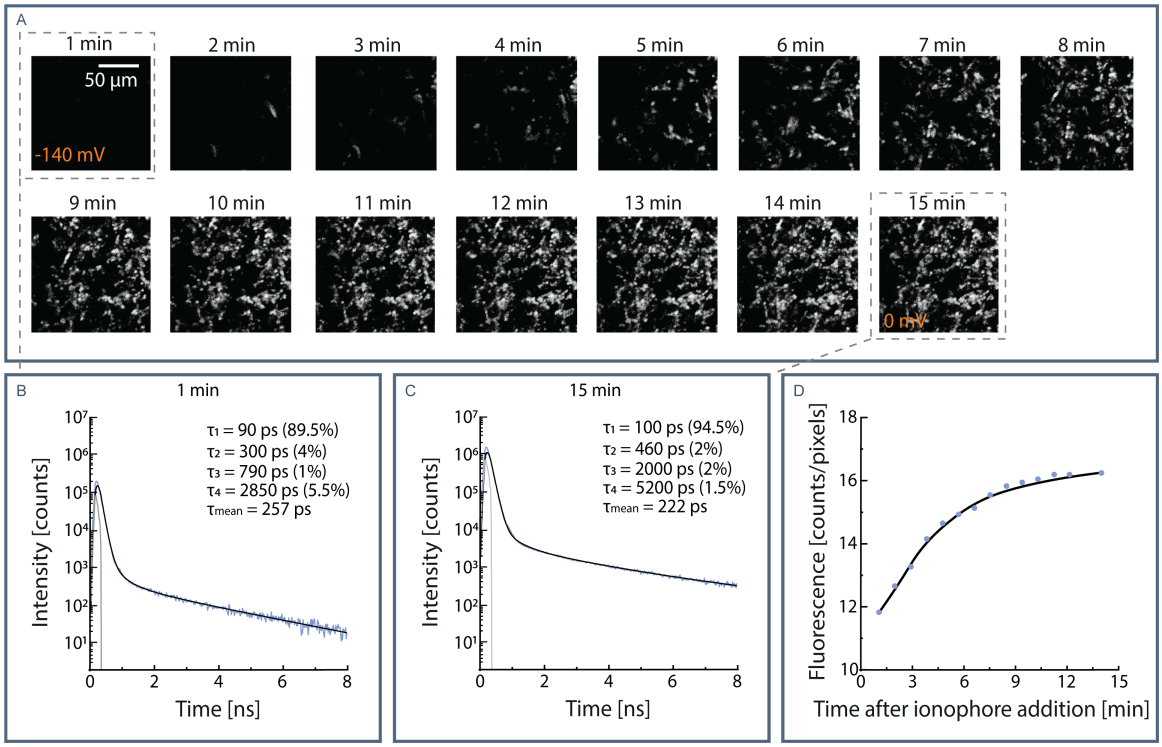

Figure 29. Fluorescent lifetime measured in cells

The recorded FLIM images and fluorescence kinetics of Archon1 overexpressed in E. coli *cells. Panel (A) shows images portraying the evolution of the fluorescence intensity increase during the first 15 min after addition of ionophore. The fluorescence intensity increases in response to a depolarization of the membrane potential (from ~ –140 mV to 0 mV). The fluorescence counts per pixel per time point are summarized in panel (D). The corresponding fluorescence lifetimes are shown for Archon1 at resting potential (B) and after abolishment of membrane potential (C).*

Comparison between different ionophores is included in the supplement (Figure S11). Also comparison between intensity increase of Archon1 and other fluorescent variants are shown in supplementary Figure S12.

The established cell assay was used also for Raman spectra recordings, to study the effect of depolarization on the retinal chromophore. The comparison of pre-resonance Raman spectra of solubilized Archon1 (room temperature) and Archon1 in intact cells are shown in Figure 30. Spectra of Archon1 in cells without subtraction of *E. coli* contribution is shown in Figure S13. Two regions of interest are conserved in *E. coli* recordings, and do not have a strong contributing signal from the cell. First, the fingerprint region (1150-1220 cm^{-1}, orange) that allows investigating the retinal isomer configuration. Second, the ethylenic stretch (1500-1550 cm^{-1}, green) that

allows investigating possible shifts in the absorption spectra maximum. Detailed spectra investigation of solubilized Archon1 in cryogenic temperatures is shown in Figure S14.

In the C-C stretch region three major peaks emerge – 1165, 1179, 1198, 1210 cm^{-1}. The bands 1198 cm^{-1} (C_{14}-C_{15} stretch), 1210 cm^{-1} (C_8-C_9) and contribution to signal 1165 cm^{-1} (C_{10}-C_{11}, C_{12}-C_{13}) are assigned to all-*trans* retinal[220]. Whereas the modes observed at 1165 cm^{-1} (C_{14}-C_{15}, C_{12}-C_{13}), 1179 cm^{-1} (C_{10}-C_{11}) and contribution to 1198 cm^{-1} (C_8-C_9) are typical to 13-*cis*/15-*syn*[221]. The C=N configuration is confirmed upon deuteriation (Figure S14), where the shift of C_{14}-C_{15} is observed. The observed peak of C=C stretch at 1522 cm^{-1} remain unchanged upon probing of Archon1 purified or overexpressed in *E. coli.*

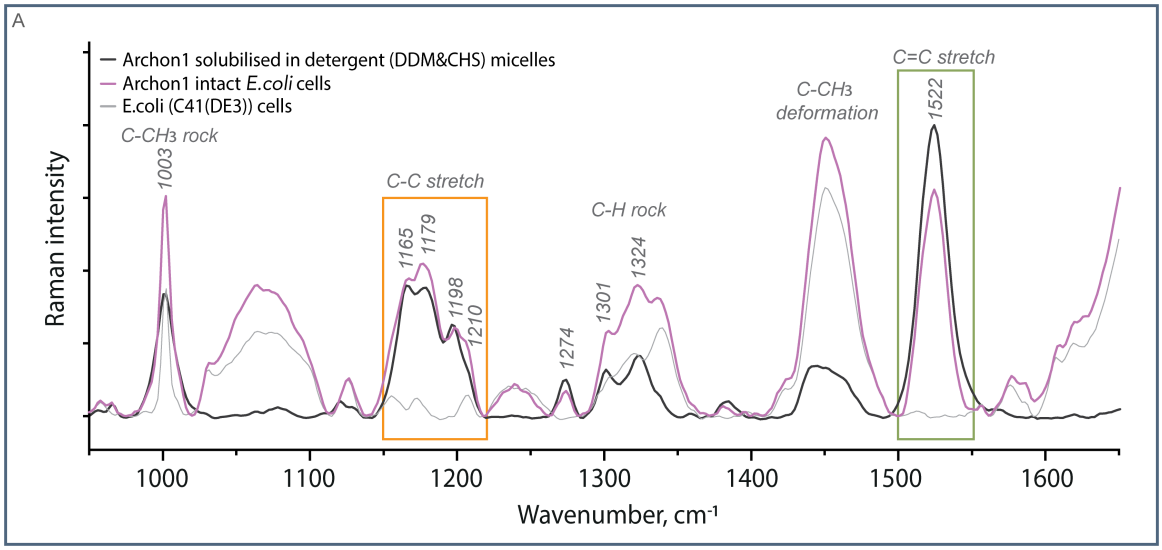

Figure 30. Raman spectra recordings

Comparison of solubilized Archon1 (black) and Archon1 overexpressed in E. coli (violet). The spectra are recorded with 1064 nm excitation, 640mW laser power and at RT (23°C). The regions of interest – C-C stretch and C=C stretch – are conserved between the different measurement conditions.

The comparison of the spectra at different membrane potentials are shown in Figure 31. The spectra of *E.coli* cells with overexpressed Archon1 were accumulated before addition of ionophore (~–140 mV, black) and 15 min after (0 mV, red) addition of ionophore (protonophore 1799 (2,6-dihydroxy-1,1,1,7,7,7-hexafluoro-2,6-bis(trifluoromethyl)heptane-4-one[166]). The alterations in spectral features upon membrane depolarization are minor. No change was observed in the

C=C stretch frequency (Figure 31 C). It can, therefore, be concluded that there is no shift in the absorption spectra maximum upon membrane depolarization, according to the reported correlation of C=C stretch and absorption maximum[225]. The intensities of fingerprint region modes have increased with more positive membrane potential. Moreover, the ratio between the strongest bands in the C-C stretch region has changed. The contribution of the 13-*cis* characteristics bands at 1165 and 1179 cm^{-1} is lower than the all-*trans* characteristic bands at 1198 and 1210 cm^{-1} (Figure 31 B). Upon more positive membrane potential contribution of all-*trans* retinal isomer increases, suggesting a slight shift in equilibrium of retinal isomers.

Spectral differences observed for Archon2 upon membrane depolarization were very minor and are shown in the supplementary Figure S15.

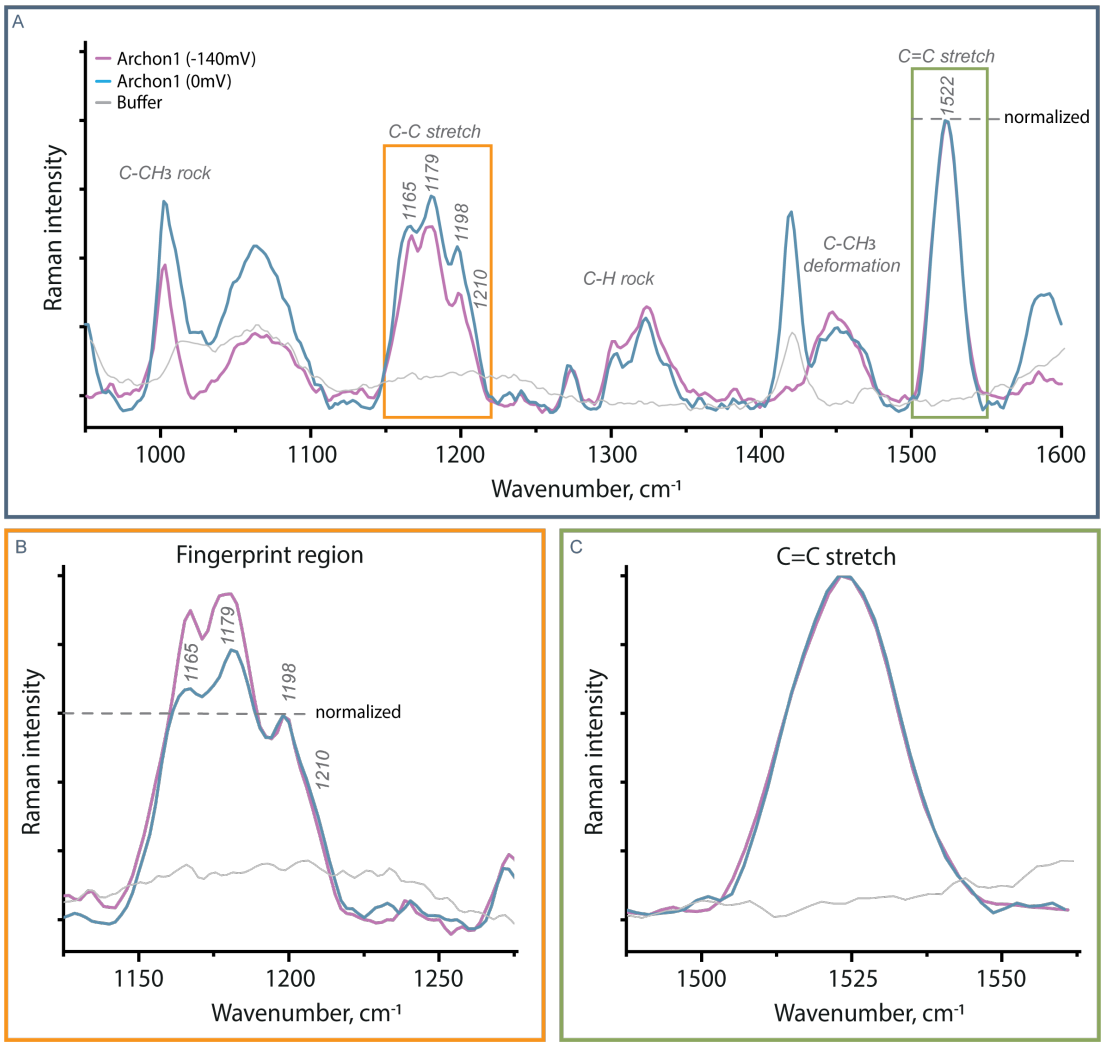

Figure 31. Raman spectra recordings

(A) The comparison between recorded spectra of Archon1 at resting membrane potential (~–140 mV) and abolished membrane potential (~0mV) normalized to C=C stretch peak. The

spectra recorded of Archon1 in intact E.coli cells (~–140 mV) is shown in violet and the spectra recorded after addition of ionophore (1mM 1799) with disrupted membrane potential (0 mV) is shown in blue. The spectra are corrected for E.coli contribution. The grey curve represents the spectral contribution of buffer (75 mM NaCl, 75 mM KCl, 50 mM Tris-HCl, pH 8.0) with addition of 1% DMSO and ionophore (1mM 1799). The close up to regions of interest are shown in lower panels – Fingerprint region (B) and C=C stretch (C). The fingerprint region (B) is normalized to 1198 cm^{-1} peak to highlight the difference between 13-cis and all-trans contributing bands.

3. 3. Archon1 variants

In the final chapter of the thesis I will introduce studies of Archon1 mutants. The first part will be dedicated to study of residues involved in the voltage sensing and the second part will be devoted to study of residues increasing the fluorescence QY. Summary of the absorption maximum and fluorescence QY are listed in Table S3.

3. 3. 1. Archon1-R92K

MD simulations proposed that residue R92, in particular its reorientation, plays a central role in Arch3 voltage sensing. However, there was no R92 reorientation observed in Archon1 (Figure 27). To experimentally investigate the significance of R92, Arginine was replaced with a shorter positively charged residue lysine (Figure 32). The purified construct of Archon1-R92K allowed investigating its absorption and spectral properties. The absorption spectra of R92K showed 10 nm blue-shift (λ_{MAX} = 575 nm) and increased ratio between $A_{280}/A_{chromophore}$ (Figure 32 B). The increased ratio might originate either from decreased extinction coefficient or destabilized chromophore. Interestingly, the fluorescence QY is increased 1.8-fold after arginine (0.49%) to lysine (0.74%) substitution (Figure 32 C).

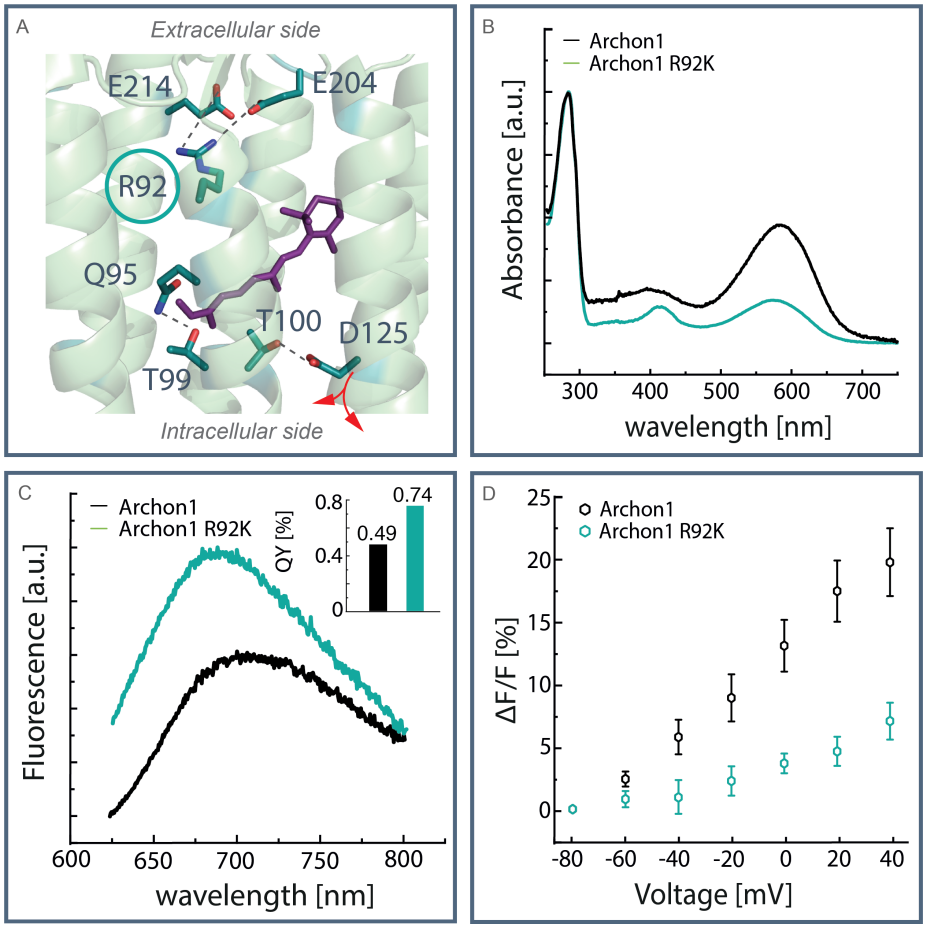

Figure 32. Study of Archon1-R92K

Panel (A) shows the retinal binding pocket with indicated R92, flipped towards the extracellular side and proton release group E204 and E214. Panel (B) shows comparison of the Archon1 and Archon1-R92K absorption spectra. Panel (C) shows comparison of Archon1 and Archon1-R92K emission spectra, with sub-panel indicating the increase of the fluorescence QY of the mutant.

To study the voltage dependent fluorescence, Archon1-R92K was expressed in ND7/23 cells. The fluorescence intensity change (ΔF/F, %) upon increase of patch-clamp-controlled membrane voltage (20 mV steps from –80 mV to 40 mV) of Archon1 and Archon1-R92K are shown in Figure 32 D. The fluorescence increase is measured with 620 nm excitation.

Archon1 shows excitation wavelength dependent voltage sensitivity (Figure S16). For applications, it is generally preferred to use red-shifted excitation (640 nm) of QuasArs[3,8]. This is due to higher voltage sensitivity at red excitation wavelengths and reduced spectral crosstalk with coupled ChRs (λ_{MAX}~ 470 nm). The setup used in

this study, generated negligible signal with excitation beyond 630 nm. Therefore, for characterization of Archon1 variants, excitation wavelength was set to 620 nm.

The fluorescence increase observed for Archon1 ($\Delta F/F_{max} \approx 20\%$) was higher than the fluorescence change of Archon-R92K ($\Delta F/F_{max} \approx 7\%$). Although R92 does not play a direct role in the voltage sensing of Archon1, it is essential for the hydrogen bond network of the retinal binding pocket. The replacement R92K maintains the positive charge, but due to lack of a guanidium group, lysine does not facilitate formation of the hydrogen bonds to other residues.

The pH dependent absorption changes allow to determine the pK_a values of titratable residues of the protein. The pH titration to alkaline (Figure 33 A, B) induced RSB deprotonation, which is indicated by a strong blue shift and rise of absorption at 410 nm. The RSB pK_a of Archon1 and Archon1-R92K are similar ~9 (Figure 33 A, B Figure S17, Figure S18). The pH titrations to acidic (Figure 33 C, D) displayed a blue-shift (13-15 nm) of the absorption spectra, indicating a titratable residue in the retinal chromophore proximity. The most likely candidate is D222, the only remaining counterion. Archon1 shows blue shift of the spectra, from 585 nm to 572 nm. The pK_{a1} is determined to be 3.5 (Figure 33 C, Figure S17). Archon1-R92K showed more complex absorption changes upon acidification. First, the absorption maximum is blue-shifted from 575 nm to 560 nm, which is then followed by even further blue shift to 455 nm, suggesting two titratable residues effecting the absorption spectra. The results specify two pK_a values pK_{a1} = 5.9, pK_{a2} = 3.2 (Figure 33 D, Figure S18).

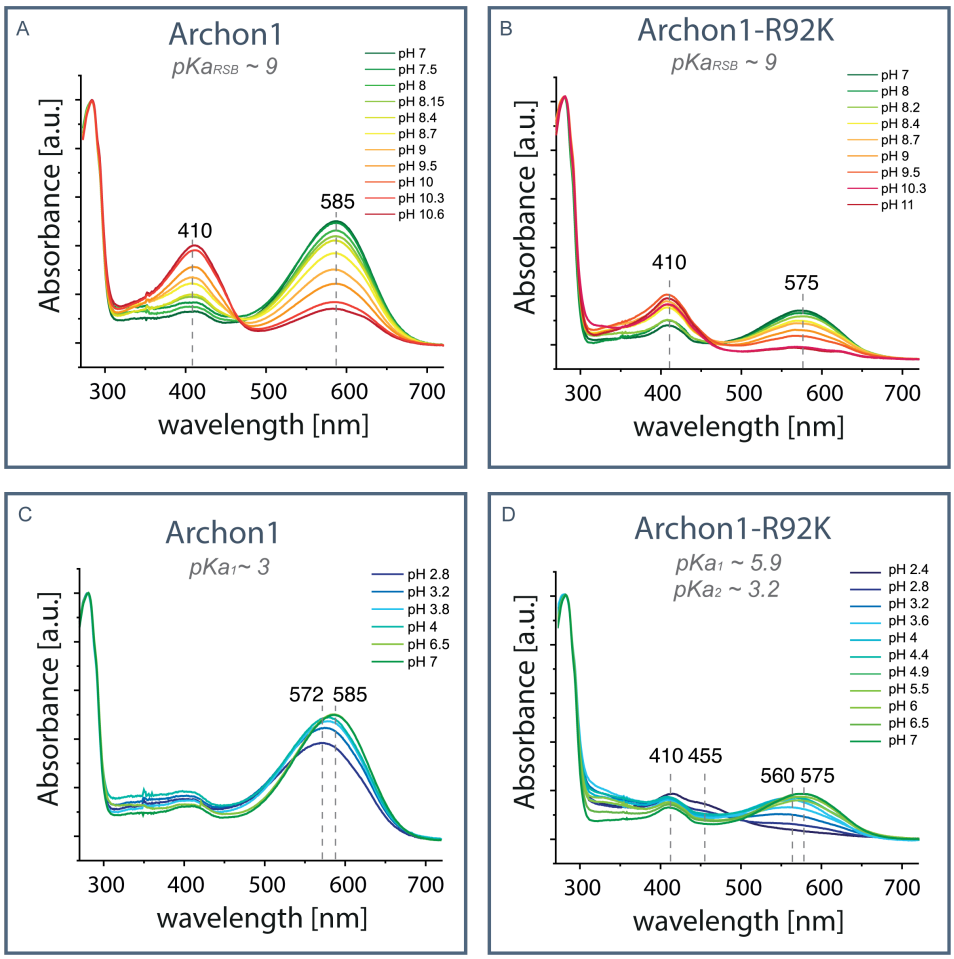

Figure 33. The pH titration of Archon1 and Archon1-R92K

Panels (A,B) shows the pH titration to alkaline for Archon1 (A) and its variant Archon1-R92K (B). Panels (C,D) shows the pH titration to acidic for Archon1 (C) and its variant Archon1-R92K (D).

3. 3. 2. Archon1-T100S/A and Archon1-D125N

The MD simulations identified D125 as the key residue involved in the voltage sensing of Archon1, which at negative membrane voltages forms a hydrogen bond with T100 (HB3), and at more positive membrane voltages forms a hydrogen bond with G123 (HB4) (Figure 27). To experimentally test the proposed mechanism, mutations were introduced at T100 and D125 positions.

The spectral properties of purified constructs of Archon1-T100S and Archon1-D125N are shown in Figure 34. The absorption maximum of T100S (575 nm) and D125N (580 nm) variants were blue-shifted compared to Archon1. Archon1-T100S showed spectral broadening of the peak, which is indicated in the sub-panel of

Figure 34 B. The two Archon1 variants showed increased fluorescence QY. Fluorescence QY of D125N is 0.6%, whereas QY of T100S is 0.67%.

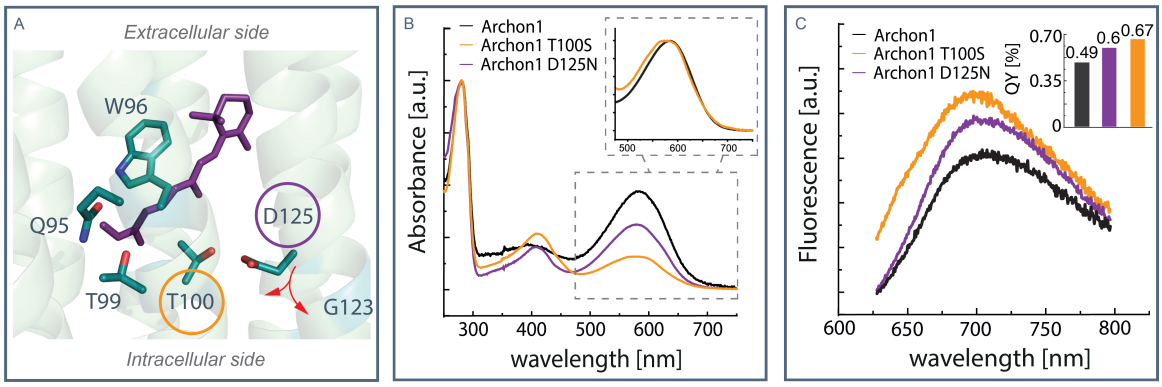

Figure 34. Study of purified Archon1-T100S and Archon1 D125N

Panel (A) shows the retinal binding pocket with indicated T100 and D125 residues. The panel (B) shows comparison of the Archon1 variant absorption spectra, where Archon1 is shown with black curve, Archon1-T100S is shown with orange curve and Archon1-D125N is shown with violet curve. The panel (C) shows comparison of Archon1 variant emission spectra, with sub-panel indicating the increase of the fluorescence QY of the mutant. The color code is preserved from panel B.

The pH titration to alkaline conditions revealed the pK_a values of RSB are similar for the mutants (Figure 35) and Archon1 (Figure 33). The Archon1-T100S pK_{aRSB} ~8.9 (Figure S19) is slightly lower than for parental Archon1 ($pK_{aRSB} \sim 9$). Whereas Archon1-D125N $pK_{aRSB} \sim 9.1$ has slightly increased (Figure S20). The pH titration to acidic conditions revealed a complex titration curve, similar to one observed in R92K construct. Suggesting the mutations introduced in the retinal binding pocket affect the interaction between titratable residues. The mutants first showed slight blue-shift of the absorption maxima, which is assigned as $pK_{a1} \sim 4.7$ for Archon1-T100S and $pK_{a1} \sim 5.6$ for Archon1-D125N. Second, the spectra showed strong blue shift to ~450 nm, which provided $pK_{a2} = 2.2$ for Archon1-T100S and $pK_{a2} = 2.7$ for Archon1-D125N.

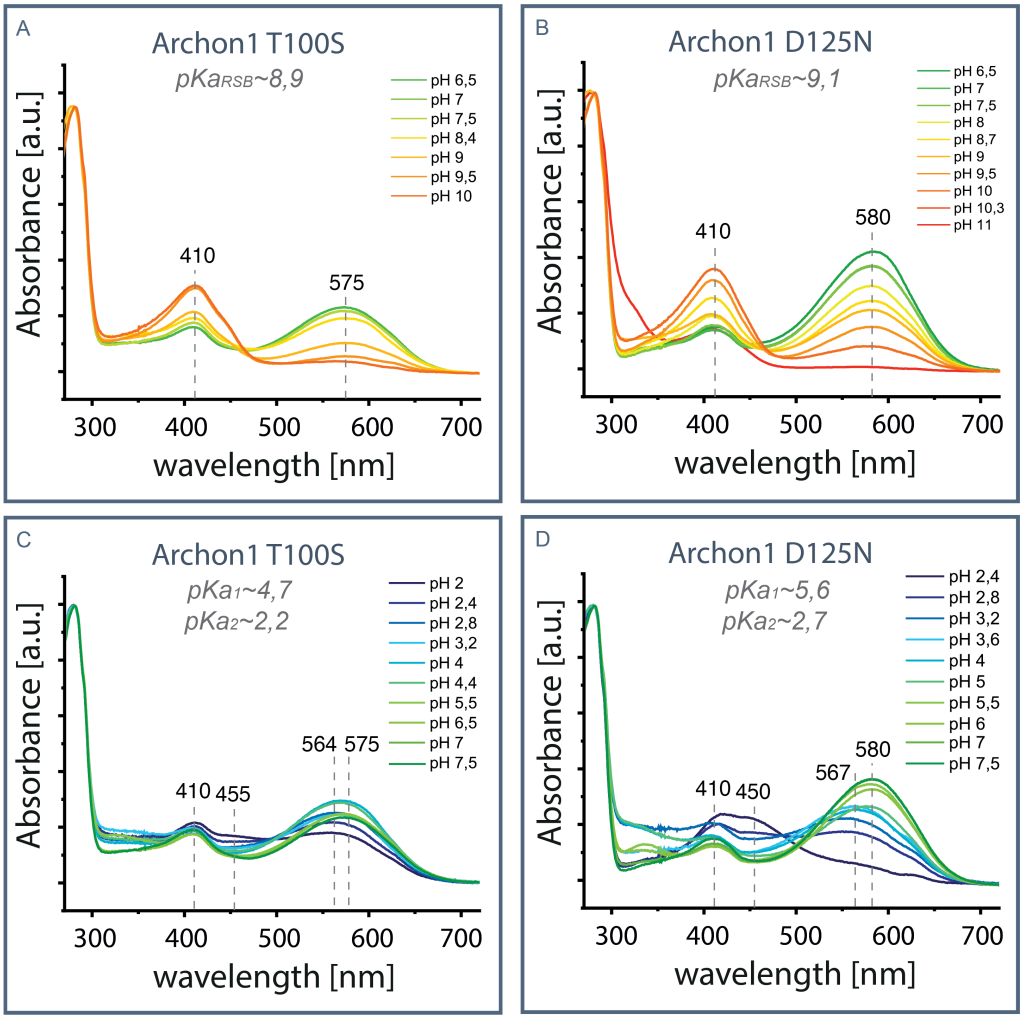

Figure 35. The pH titration of Archon1-T100S and Archon1-D125N

Panels (A,B) shows the pH titration to alkaline for Archon1-T100S (A) and Archon1-D125N (B). The determined pK_a values of RSB are 8.9 and 9.1, correspondingly. Panels (C,D) shows the pH titration to acidic for Archon1-T100S (C) and Archon1-D125N (D). The pH titration revealed two pK_a values for both constructs. The determined values are pK_{a1}=4.7 and pK_{a2}=2.2 for T100S mutation, and pK_{a1}=5.6 and pK_{a2}=2.7 for D125N mutation.

To test the fluorescence intensity dependence on membrane voltage (ΔF/F, %), the mutants were expressed in ND7/23 cells. Images were accumulated over membrane voltage range from –80 mV up to 40 mV with 20 mV step using patch-clamp. The resulting fluorescence intensity increase is shown in Figure 36 A. In addition to T100S mutant, also T100A mutant was studied. The Archon1-T100A variant, could not be characterized spectroscopically, due to lack of expression in *E. coli*, and was not introduced before. Archon1-T100A and Achon1-T100S mutants showed contrasting impact on the voltage sensitivity. Threonine to Alanine

replacement (T100A) results in residue with a shorter side chain and no –OH group. This mutation causes decrease in voltage sensitivity ($\Delta F/F_{max} \approx 12\%$; Figure 36 A). Archon1-T100A (Figure 36 C) showed small dependance on the excitation wavelength. The highest voltage sensitivity was observed at 580 nm excitation wavelength ($\Delta F/F_{max} \approx 14\%$). On the other hand, Threonine to Serine substitution (T100S) provides residue with displaced –OH group. This mutant showed increase in voltage sensitivity ($\Delta F/F_{max} \approx 24\%$; Figure 36 A). Further studies were carried out to compare the voltage sensitivity dependence on excitation wavelength (Figure 36 B). The Archon1-T100S variant showed improved voltage sensitivity, compared to Archon1 (Figure S16), also in response to blue-shifted excitation wavelengths (560 nm, 580nm; Figure 36 B).

The Archon1-D125N variant allowed investigating the proposed key residue involved in the voltage sensing. Aspartate to Asparagine substitution, results in improved voltage sensitivity ($\Delta F/F_{max} \approx 33\%$) compared to Archon1. Also for this construct, the voltage sensitivity showed dependency on the excitation wavelength (Figure 36 D). While Archon1-D125N variant showed improved voltage sensitivity, the expression of this variant in ND7/23 was decreased.

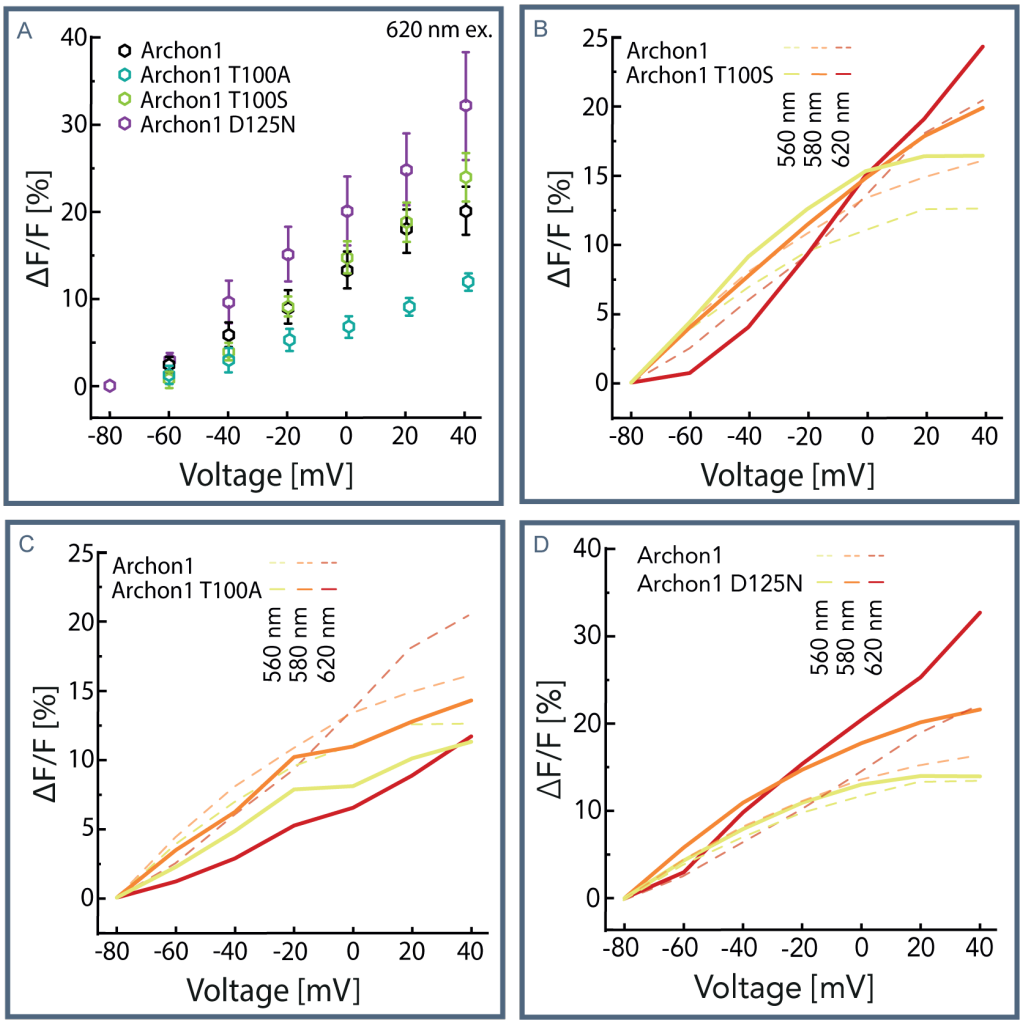

Figure 36. Voltage sensitivity of Archon1-T100S, Archon1-T100A and Archon1-D125N

Panel (A) shows voltage sensitivity of Archon1-T100A (blue), Archon1-T100S (green) and Archon1-D125N (purple) compared to Archon1 (black) at 620 nm excitation. Panels (B-D) show excitation wavelength dependent voltage sensitivity of the variants: Archon1-T100S (B), Archon1-T100A (C) and Archon1-D125N (D).

3. 3. 3. Archon1-D222E

Another interesting position, in the context of voltage sensing, is the remaining counterion D222 (Figure 37 A, D). Range of tested uncharged residues at this position resulted in low protein expression. The only possible substitution was Archon1-D222E that expressed well in *E. coli*, but not in ND7/23 cells. Only the spectroscopic characterization will be introduced below. Archon1-D222E showed 15 nm blue shift of the absorption maximum (λ_{MAX} = 573 nm; Figure 37 B). Also in this mutant, the chromophore stability is reduced, as indicated by increased A_{280} / $A_{chromophore}$ ratio. The fluorescence QY of Archon1-D222E is equivalent to the

one of Archon1 (Figure 37 C). Additionally, the pH titration of the D222E mutant allowed to investigate the mutations effect on the pK_a value of the RSB. The replacement of the anticipated proton acceptor D222E upshifts the value to pK_{aRSB} ~ 10.4 (Figure 37 E, Figure S21). Afterwards, the absorption spectra was recorded with gradual transition to more acidic pH values. The mutation of residue D222E disrupts the hydrogen-bonding network. The titration curve show significant difference to Archon1 (Figure 33 C). Archon1-D222E (Figure 37 F) absorption spectra displays a slight blue shift (~15nm) of the absorption maxima, which is followed by further blue shift to ~450 nm. According to the two-step absorption spectra change at acidic conditions, two pK_a values are assigned to Archon1-D222E: pK_{a1} ~ 6.1 and pK_{a2} ~3.6 (Figure S21).

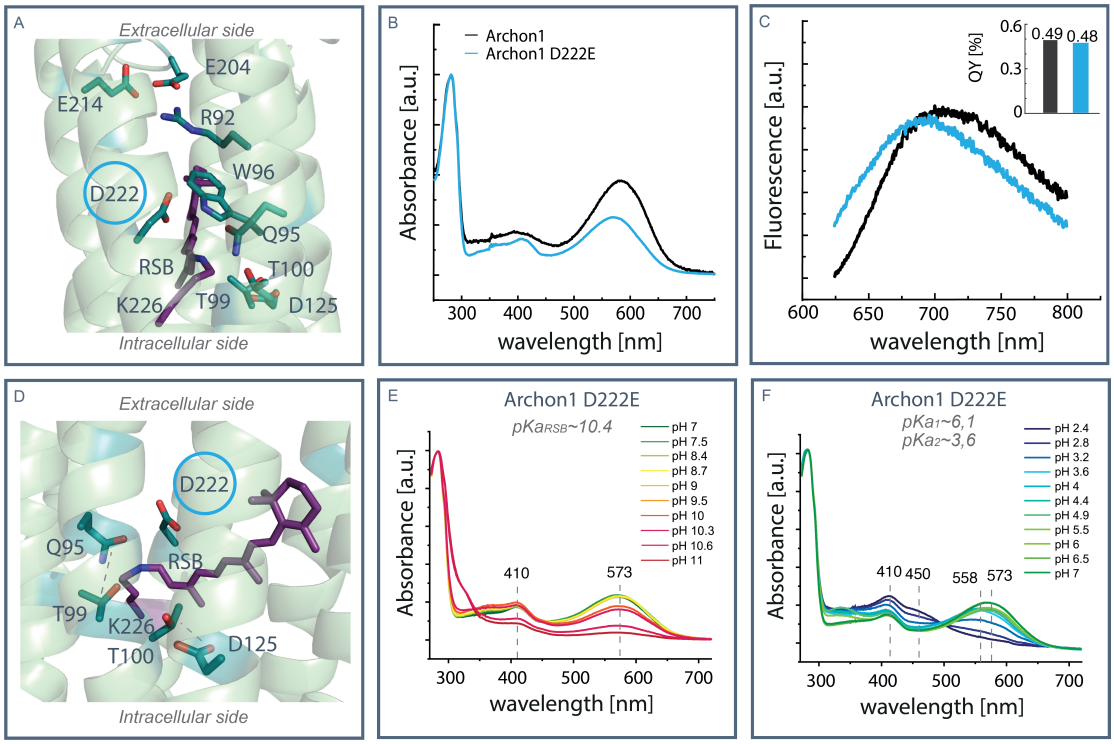

Figure 37. Study of purified Archon1-D222E

Panels (A,D) shows the retinal binding pocket with indicated D222 residue. The panel (B) shows the absorption spectra of Archon1 and Archon1-D222E. The panel (C) shows comparison of Archon1 and Archon1-D222E emission spectra, with sub-panel indicating the fluorescence QY. Lower panels show pH titration of Archon1-D222E to alkaline (E) and acidic (F) conditions.

3. 3. 4. Archon1-Q95X

It has been proposed that D95X (Figure 38 A) is the fundamental mutation needed to increase the fluorescence QY in Arch3 variants. The studies carried out previously[6,8,229] have already indicated the central role of this mutation. In particular, the counterion mutation D95H/Q present in QuasAr1/2 showed different voltage sensing and fluorescence QY properties[3]. To ascertain the role of H/Q substitution, the mutation was transferred to Archon1 and is shown in Figure 38. The Archon1-Q95H variant showed 10 nm blue-shifted absorption spectra (λ_{MAX} = 575 nm; Figure 38 B), 1.6-fold increase in fluorescence QY (Figure 38 D, E). Equivalent observations were made in QuasAr1/2 (Figure 15 A). Furthermore the Archon1-Q95H variant showed 1.8-fold decrease in voltage sensitivity ($\Delta F/ F_{max} \approx 11\%$; Figure 38 C).

Replacement of the counterion D95X, with various residues (Figure 38), allowed confirming the impact of the residues placed at this position on the absorption maxima, pK_a of RSB and the fluorescence QY. Besides the Q/H replacement, the strongest changes were observed in Q/G and Q/L mutations. Archon1-Q95G and Archon1-Q95L showed very similar absorption maximum (λ_{MAX} = 583 nm, Figure 38 A), but their pK_a values of RSB differ strongly (according to the ratio between protonated and deprotonated species). Furthermore, Archon1-Q95G substitution shows increase in fluorescence QY ~0.7%, whereas Archon1-Q95L showed strong decrease in fluorescence QY ~0.32% (Figure 38 D,E).

In contrast, the backmutation Q95D resulted in destabilized retinal binding pocket and abolished protein expression.

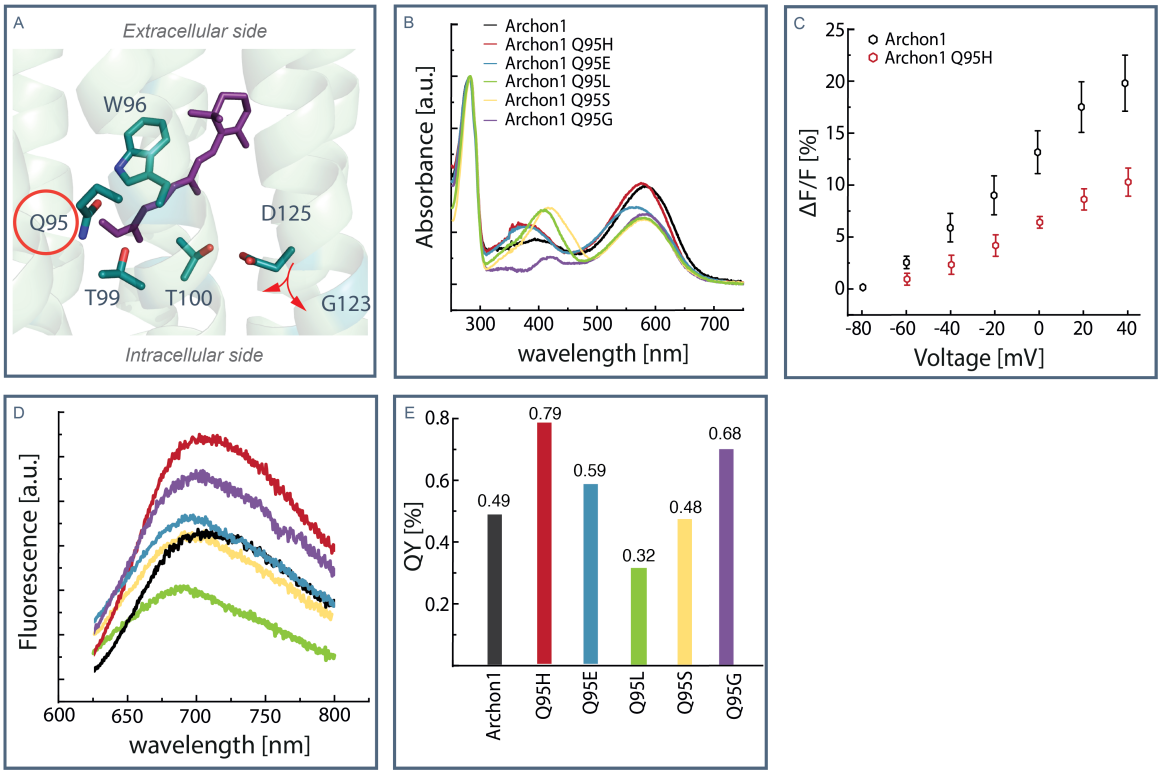

Figure 38. Study of Archon1-Q95X variants

Panel (A) shows the retinal binding pocket with indicated Q95 residue. The panel (B) shows the absorption spectra of Archon1 and its Q95X variants. Panel (C) shows the fluorescence intensity change of Archon1 and Archon1-Q95H upon 20 mV steps in membrane voltage (–80 mV to 40 mV). Panel (D) shows comparison of Archon1 and its Q95X variant emission spectra. The fluorescence QY comparison is provided in panel (E).

After verification of the essential role of Q95X in Archon1 fluorescence intensity, further investigation was carried out at this position in aim to improve the properties of Archon1 for applications (red-shifted absorption and increased fluorescence QY). The mutation pair D95E and T99C, in Archer1 and Arch5 (Table S1, Nr. 4 and Nr. 9)[1], have afforded red-shifted absorption maximum (626 nm - Archr1, 622 nm - Arch5) and increased fluorescence QY (0.33% - Archer1, 0.87% - Arch5). Despite the high fluorescence QY of Arch5, it has not been used in applications, likely, due to the strong bleaching observed in cell cultures (Figure S22). In analogy to Archer1 and Arch5, mutations at the counterion position Q95E and adjacent T99C were introduced in Archon1. Also Archon1-Q95E-T99C variant showed 18 nm red-shifted absorption maximum to 603 nm (Figure 39 A) and 1.4-fold increase in fluorescence QY (0.71%; Figure 39 B-C). These properties are highly

desirable for applications, where red light excitation is commonly used due to lower scattering in tissue.

The fluorescence intensity change upon voltage increase of Archon1-Q95E-T99C variant ($\Delta F/F_{max} \approx 11\%$) was lower than the one of Archon1 ($\Delta F/F_{max} \approx 20\%$). However, the voltage response was highly similar between the two constructs in the membrane voltage range between –80 mV and 0 mV (Figure 39 E). Due to the reduced voltage sensitivity of the construct, mutation combinations were investigated to improve the voltage sensitivity. The mutations - T100S and D125N - showed improved voltage sensing in the parental Archon1 (Figure 36). However, the two mutations, in addition to Q95E and T99C mutations, did not show improved voltage sensitivity (ΔF/F) (Figure 39 F). The construct Archon1-Q95E-T99C-D125N showed minor decrease in voltage sensing. Whereas, Archon1-Q95E-T99C-T100S showed complete abolishment of the voltage sensing.

Also in Archon1-Q95E-T99C, hydrogen bonding network, formed by T100 and D125 residues, is important for voltage sensing. However the replacement of this residues in Archon1-Q95E-T99C reduce the voltage sensitivity, indicating that the underlying voltage sensing mechanism differs from one observed in Archon1.

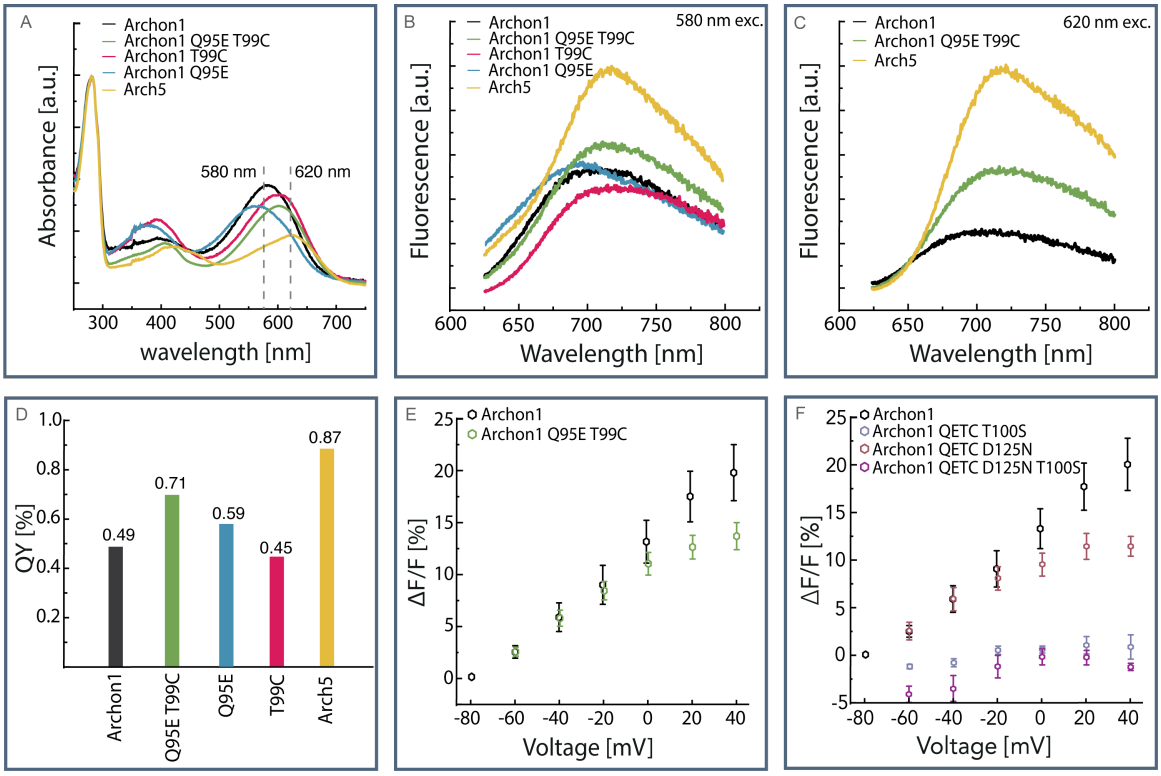

Figure 39. Study of Archon1-Q95E-T99C variant

Panel (A) shows absorption spectra comparison between Archon1(black) and its variants with Q95E (blue) and T99C (red) single mutations and Q95E-T99C (green) double mutation. Additionally, comparison with Arch5 (yellow) is provided. Panel (B) shows fluorescence emission comparison at 580 nm excitation of the constructs. Panel (C) shows fluorescence emission comparison at 620 nm excitation of Archon1, Archon1-Q95E-T99C and Arch5. Panel (D) shows comparison of the fluorescence QY of the different constructs. Panel (E) shows voltage dependent increase in fluorescence intensity of Archon1 and Archon1-Q95E-T99C at 620 nm excitation. Panel (F) shows voltage dependent increase in fluorescence intensity of Archon1and variants Archon1-Q95E-T99C-T100S (light blue), Archon1-Q95E-T99C-D125N (dark red) and Archon1-Q95E-T99C-D125N (purple).

3. 3. 5. Archon1 variants with mutations in the retinal binding pocket

Further mutations in the retinal binding pocket can be introduced to increase the fluorescence QY (Figure 40). The mutation A225C was introduced in analogy to Arch7. Arch7[1] has the highest fluorescence QY to date, among rhodopsin-based GEVIs reported so far, while no applications have been reported (Table S1, Nr. 10). The Archon1-A225C variant showed strong increase in the fluorescence QY (1.07%), while having no color-shifting properties (λ_{MAX}= 585 nm).

G132S, S151A were introduced close to the β-ionone ring. The G132S mutation replaces a hydrophobic residue with one bearing -OH group. The Archon1-G132S variant showed even higher increase in the fluorescence QY (1.17%). The mutation provided 2.4fold increase in the fluorescence, while having no color-tuning effect (λ_{MAX}= 585 nm). The S151A mutation removes the -OH group from the β-ionone ring proximity, while introducing a hydrophobic residue. This mutation resulted in a 25 nm blue shift of the absorption spectra (λ_{MAX}= 560 nm) and a minor effect on the fluorescence QY (0.6%).

From the mutations introduced, the G132S showed the highest fluorescence QY and was tested in combination with the QETC double mutant. The triple mutant showed heterogeneous chromophore absorption band with two peaks λ_{MAX1} = 588 nm and λ_{MAX2} = 615 nm (Figure 40 B insert). The fluorescence excitation spectra revealed higher fluorescence of the blue-shifted species compared to the red-shifted one (Figure S23). The determined QY showed only 1.1-fold increase compared to single mutant (1.32%). The variants studied in this chapter are summarized in Table S3.

The mutations serve as proof of principle that fluorescence QY can be further improved by modifications in the retinal binding pocket and further combinations can be explored. The most promising mutations from the listed is G132S.

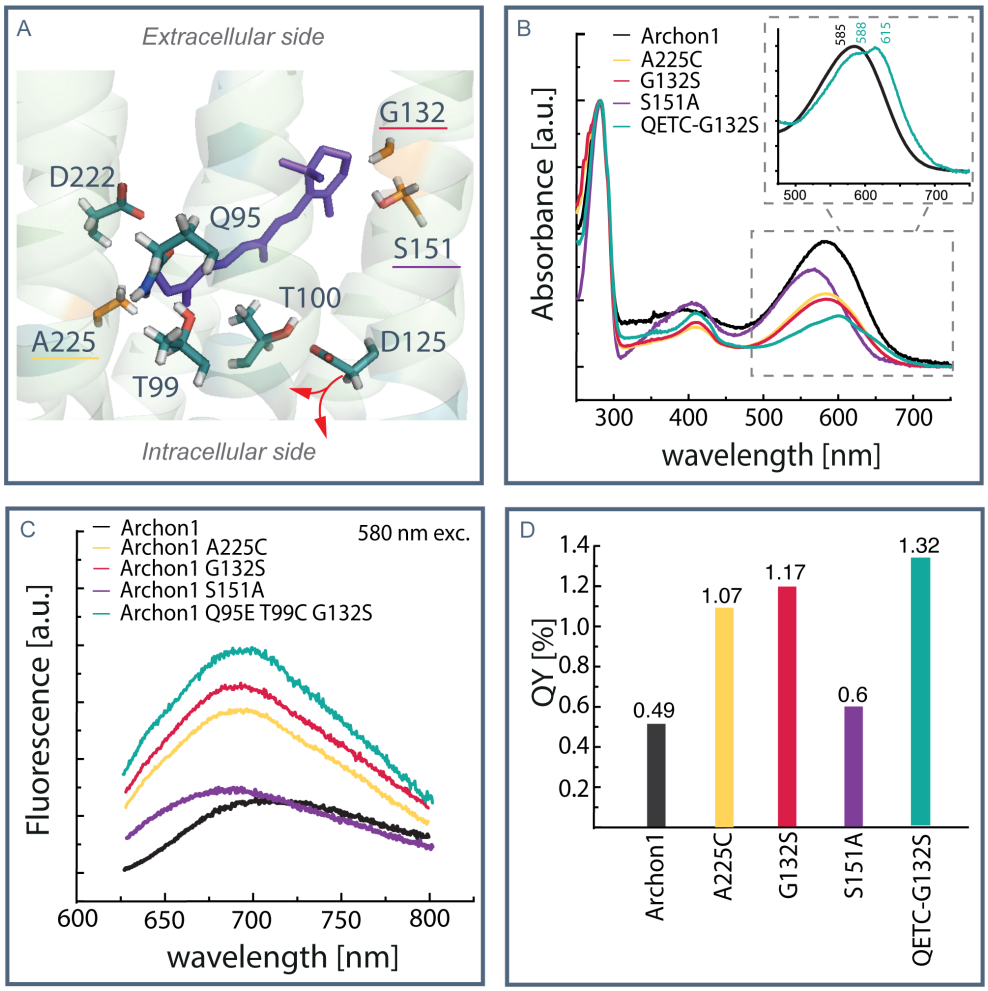

Figure 40. Study of Archon1 variant

Panel (A) shows the retinal binding pocket with indicated key residues (green) and positions chosen for further mutant studies (orange). Panel (B) shows absorption spectra comparison between Archon1(black) and its variants. Panel (C) shows comparison of fluorescence emission of variants at 580 nm excitation. Panel (D) shows comparison of the fluorescence QY of the different constructs.

4. Discussion

Within this research work three main questions have been studied: how the fluorescence arises in Arch3-based sensors, how the membrane voltage generates change in fluorescence intensity and whether it is possible to improve the properties of the currently available voltage sensors. In this section the photodynamics of QuasArs, retinal chromophore composition, origin of voltage sensing and outlook will be discussed.

4. 1. Photodynamics of QuasArs

4. 1. 1. Excited state dynamics

Study of QuasAr photodynamics allowed gaining insights into the QuasAr fluorescence origin. Transient absorption spectroscopy revealed that QuasArs do not undergo a photocycle typical for microbial rhodopsins. The studied constructs showed prominent excited state formation, but only minor (< 4%) amount of the molecules undergo retinal isomerization. Evidently, these differences are essential for the improved fluorescence QY compared to the wild-type Arch3.

Upon absorption of a photon, QuasArs are excited to their first singlet excited state S_1 (Figure 17, Figure 18). This excited state is extraordinary long-lived compared to that of the wild-type Arch3. The excited state of Arch3 decayed within 0.3 ps, forming the J state (Figure 19). However, the excited state of QuasArs decays biphasic and both time components are considerably slower ($\tau_1 \sim$ 4-15 and $\tau_2 \sim$ 4084 ps) than the one of Arch3. Furthermore, with the decay of the excited state, most of the molecules return back to the original ground state and only the minor fraction undergone isomerization, form a red-shifted photointermediates (I640 and I620). The long lived excited states make the fluorescence QY of QuarArs significantly larger than that of wild-type Arch3 (0.28% in QuasAr1 and 0.18% in QuasAr2 vs 0.01% in Arch3[1]).

These observations are in close agreement with a study carried out on retinal analog MMAR (3-methylamino-16-nor-1,2,3,4-didehydroretinal)-substituted proteorhodopsin (PR:MMAR) and recently found NeoR[230]. The fluorescent

proteorhodopsin variant showed fluorescence QY of 3.3% and extended excited state decay of ~ 310 ps[186]; and NeoR shows fluorescence QY of ~20% and the excited state lifetime of ~1.1 ns[230].

Comparison between constructs revealed further relationship between the excited state dynamics and fluorescence properties. In QuasAr1 and QuasAr2 the contributions of short-lived species (τ_1) and the longer-lived species (τ_2) are different (Figure 17 G). In QuasAr2 τ_1 and τ_2 contribute almost equally to the signal (1:1). Whereas in QuasAr1, the τ_1:τ_2 ratio was 1:8, indicating that most of the signal is carried by the long-lived component τ_2. Furthermore, the long-lived component τ_2 is notably slower in QuasAr1 than in QuasAr2 (60 ps vs. 40 ps). The major contribution and larger value of τ_2 explains the 1.6-fold higher fluorescence QY of QuasAr1 (Figure 17 I). Moreover, QuasAr1 showed 4-fold smaller photointermediate yield than QuasAr2 (~1% vs. ~4%). These observations imply that the faster component (τ_1) contributes mainly to the formation of the photoproduct (still with low efficiency), whereas the slower component (τ_2) contributes more significantly to the fluorescence.

QuasAr1 and QuasAr2 also showed different properties under reduced proton concentration (pH 11 vs pH 8). First, the two constructs have different pK_a of RSB (Figure 20 A, D). Second, the two constructs differ in the excited state lifetime and the resulting fluorescence QY. In alkaline conditions QuasAr1 showed increased fluorescence QY and slowed excited state kinetics, whereas QuasAr2 displayed decreased fluorescence QY and accelerated excited state kinetics (Figure 20).

If the voltage sensing mechanism would rely on the RSB protonation/ deprotonation, these observations might also apply for negative voltage conditions. Suggesting the increased voltage sensitivity of QuasAr2 could be attributed to lower pK_a of RSB, decrease in kinetics and resulting decrease in fluorescence QY. However, symmetric change in proton concentration are substantially different from voltage changes (ion and proton gradient across membrane) and can serve only as intuitive guess.

The key difference in QuasAr1 and QuasAr2 is the mutation introduced at the counterion position (D95H/Q). The different charges at this position in QuasAr1 (positive charge) and QuasAr2 (neutral) are linked to the different excited state dynamics and fluorescence QY (Figure 17).

4. 1. 2. Population of photoproducts

The steady-state UV/Vis measurements revealed that with prolonged illumination three stable and reversible photoproducts can be populated – P580, P400, D590' (Figure 15). The transition between the photoproducts is highly inefficient and requires a photon to overcome energy barrier of the transition. All of the protonated species showed similar excited state dynamics and are fluorescent with slight differences in their fluorescence QY (Figure S4, Figure S24, Table S4).

The observed photoswitching between photoproducts has also been reported recently for Arch3-D95Q, QuasAr2 and NovArch by an independent study[231]. The study demonstrated that alternating extended red (660 nm) and blue (405 nm) illumination, allows reversible optical switching between thermally stable protonated and deprotonated species. NovArch[232] (Table S1, Nr. 36) displays curious property for voltage sensor, where the fluorescence intensity could be enhanced up to 8-fold with blue (488 nm) illumination in addition to typically used red (640 nm). These reports, in agreement to findings of this study (Figure 15 B, C), suggest that photodesensitization of the fluorescent tools could be recovered with additional blue light illumination. The photoinduced reprotonation of the RSB results in absorption maxima shift from ~400 nm to ~590 nm, yielding increased population of the photoactive species.

In a collaborative work with Penzkofer et al., extensive studies of highly fluorescent QuasAr1[213,233] and Archon2[234,235] confirmed the high energy barriers for isomerization. Within the studies the gradual changes in the absorption spectra, and resulting emission spectra, were recorded in response to illumination (590 nm LED) or thermal activation (2.5 °C or 23 °C). The studies demonstrate the heterogeneous nature of the constructs and the complex isomerization pathways.

Interestingly, the thermally activated isomerization was observed in QuasAr1[213], whereas the next generation Archon2[235] appeared thermally stable in the observed time frame (22 days). The observations indicated that further improved fluorescence QY (1.6-fold[235]) in addition to high potential energy energy barrier of S_1 state also causes increase in the energy barrier along the ground state S_0, designating it too high to overcome thermally.

Photoinduced absorption changes were observed in both constructs; also in these experiments the isomerization yield was lower in Archon2[234] than QuasAr1[212]. The

calculated weighted photoconversion quantum yield were Φ_{iso} ~ 1.7% for Archon2 vs. Φ_{iso} ~ 2.4% for QuasAr1. Despite the slight differences between the two constructs, the photoconversion quantum yield is exceptionally low in both variants. For example, the photoconversion quantum yield of BR_{568} has been estimated to be Φ_{iso} ~ 65%[236].

In a collaborative work with Penzkofer et al.[212,234], the observed gradual changes in the absorption spectra, induced by 590 nm LED illumination, allowed disentangling of the isomerization pathways of the different retinal isomers present already in the dark state. The dark state consists of two spectrally overlapping isomers- I and II. It was proposed that isomer I results in formation of blue-shifted species (λ_{MAX} ~ 540 nm) and isomer II results in red-shifted species (λ_{MAX} ~ 600/640 nm). The photoconversion quantum yield is much lower for isomer II (<0.1%), resulting in smaller contribution of subsequent red-shifted species. However, with persistent illumination both isomers result in deprotonation of the RSB (λ_{MAX} ~ 370 nm).

These observations allow explaining the observed blue-shift (10 nm) of the absorption spectra maximum observed in this study (Figure 15 B). The more likely formation of blue-shifted subpopulation (~540 nm) superimposed with remaining absorption curves of isomer I and isomer II (~590 nm) would likely result in a blue-shifted absorption maximum (~ 580 nm).

The photoconversion quantum yields estimated from EADS of the femtosecond pump-probe experiments were ~ 1% for QuasAr1 (Figure 17 E, F) and ~0.4% for Archon2 (Figure 22 B). Both of these values are lower than the estimated values in Penzkofer et al. studies[212,234]. The discrepancy could be arising from the heterogeneous nature of the constructs. In time-resolved absorption spectroscopy the spectral changes were monitored after excitation of the red absorption shoulder (610 nm), which might result in higher probability of excitation of isomer II, yielding lower isomerization quantum yield than estimated from the weighted average value.

In Penzkofer et al. studies[212,234] the calculated average Strickler-Berg-based radiative lifetimes were $\tau_{QuasAr1}$ = 61.5 ps and $\tau_{Archon2}$ = 106 ps. The calculated value of QuasAr1 is in close agreement to experimentally determined slow component of the excited state decay τ_2 = 60 ps, whereas the experimentally determined value for Archon2 is slightly (1.3-fold) slower τ_2 = 84 ps. However, for both constructs these

values are in good agreement, designating, once more, the excited state as the fluorescent state.

4. 1. 3. High energy barrier for isomerization

QM/MM (quantum mechanics/molecular mechanics) study on fluorescent mutant of *Anabaena* Sensory Rhodopsin (ASR-W76S/Y179F) proposed that fluorescence increase originates from coupling between the two excited singlet states S_1 (^1B_u) and S_2 (^2A_g)[237]. The mutations change the steric and electrostatic properties of the chromophore and its surroundings. These changes result in increased ^2A_g character along the S_1 potential energy surface, temporarily trapping the excited molecules in the S_1 state and extending the excited state lifetime. The coupling of the states also increase the energy barrier for isomerization[237].

The observed close overlap between one- and two-photon excitation spectra (Figure 23) would support mechanism proposed by the QM/MM simulations. Previous observations in protonated retinal chromophore showed blue-shifted two-photon excitation spectra, placing S_2 state (^2A_g) above S_1 state (^1B_u)[216,238], designating the spectral overlap of S_1 and S_2 states of QuasAr2 unusual. However, the chromophore-binding pocket of the protein may affect the energy levels of the excited singlet state of the bound chromophore. Therefore, it is not possible to exclude that one- and two-photon excitation promotes QuasAr to the same singlet state (S_1). To elucidate this further, it would be necessary to perform two-photon femtosecond transient absorption spectroscopy. The additional spectroscopic data would allow comparing the excited state dynamics between the different excitation protocols, clarifying which states are populated by two-photon excitation.

4. 1. 4. One-photon vs three-photon generated fluorescence

It has been shown that in wild-type Arch 3 and BR_{568} the O and Q states are fluorescent (Figure 4, Figure 5)[107,108,110,229,239]. The O state (part of typical photocycle), upon excitation with a second photon, shows increased fluorescence compared to the dark state. The Q state shows even higher fluorescence, and is reached through photo-branching from the N state (three-photon triggered fluorescence). The fluorescence decay of the O and Q states are reported to be ~9 ps and ~62 ps, respectively[107]. Their fluorescence QY (0.1% and 0.7%, in the O and Q

states, respectively) are considerably higher than that of the dark state (from 0.0025% to 0.027%)[104–106,110]. Remarkably, the fluorescence decay (τ_1 ~ 4-15 ps and τ_2 ~ 40-84 ps) and the QY (from 0.18% to 0.56%) are comparable between QuasArs and the fluorescent O and Q states of BR_{568}. However, in QuasArs the fluorescence arises already with one photon excitation of the dark state, populating the long-lived excited state. Therefore, in QuasArs, a second photon is not required to reach the fluorescent state. Despite the similarities of the fluorescence properties, it is uncertain if QuasArs are trapped in one of these states (O-like and Q-like states in BR), as little is known about their structural properties. However, the O state, possesses uncharged counterion (protonated D95), as also observed in QuasArs. As described above the charged counterion in the O state results in 40-fold higher fluorescence QY compared to the dark state[110,239]. Further arguments, that would support trapping of these states arise, firstly, from Raman studies on QuasAr1, substituted with a retinal analog (MMAR), which proposed it is trapped in an O-like state[240]. Secondly, previous study of the BR-D85N counterion mutant demonstrated that pH dependent equilibrium of M/N/O-like states present already before photoexcitation[241].

4. 2. Retinal isomer composition of QuasArs

4. 2. 1. Dark state retinal isomer composition

Investigation of QuasAr retinal isomer composition is a crucial aspect to understand their functionality. The HPLC study of the extracted chromophore (Figure 24) revealed the dark state of QuasArs consists of mixture of all-*trans* and 13-*cis* retinal isomers. Pre-resonance Raman spectroscopy (Figure 25, Figure 26), in addition to validation of C_{13}=C_{14} bond conformation, allowed further specification of C=N bond conformation, determining contribution of 13-*trans*/15-*anti* and 13-*cis*/ 15-*syn* retinal isomers.

The C=N conformation is confirmed by isotopic shifts of C_{14}-C_{15} stretch mode upon H/D exchange (Figure 26). The C_{14}-C_{15} stretch mode (1199 cm^{-1}) of 13-*trans* isomer remain unchaineg upon deuteriation, indicating weak coupling of C_{14}-C_{15} to the N-H rock[47], and specifying 13-*trans*/15-*anti* isomer. The C_{14}-C_{15} frequency (1164 cm^{-1}) of 13-*cis* isomer displayed a strong upshift (1212 cm^{-1}), indicating

coupling between the C_{14}-C_{15} stretch and the N-H rock[47], and identifying 13-*cis*/15-*syn* isomer.

The assignment of the Raman bands in the fingerprint region for BR and QuasArs, observed in Raman spectra, according to the retinal isomers present is shown in Figure 41. QuasAr1 has a higher contribution from 13-*trans*/15-*anti* retinal isomer (~80%), whereas QuasAr2 has a higher contribution from 13-*cis*/15-*syn* (~50%). Despite the electrostatic changes introduced in QuasArs by elimination of the counterion negative charge (D95Q/H), the retinal maintains the isomer conformation as found in light adapted BR_{568} (all-*trans*) and dark state BR_{548} (13-*cis*/15-*syn*). In agreement with these observations, in analogous counterion mutants BRD85N and BR-D85A, Raman spectroscopy and NMR studies confirmed contributions from the all-*trans* and 13-*cis*/15-*syn* retinal isomers[242].

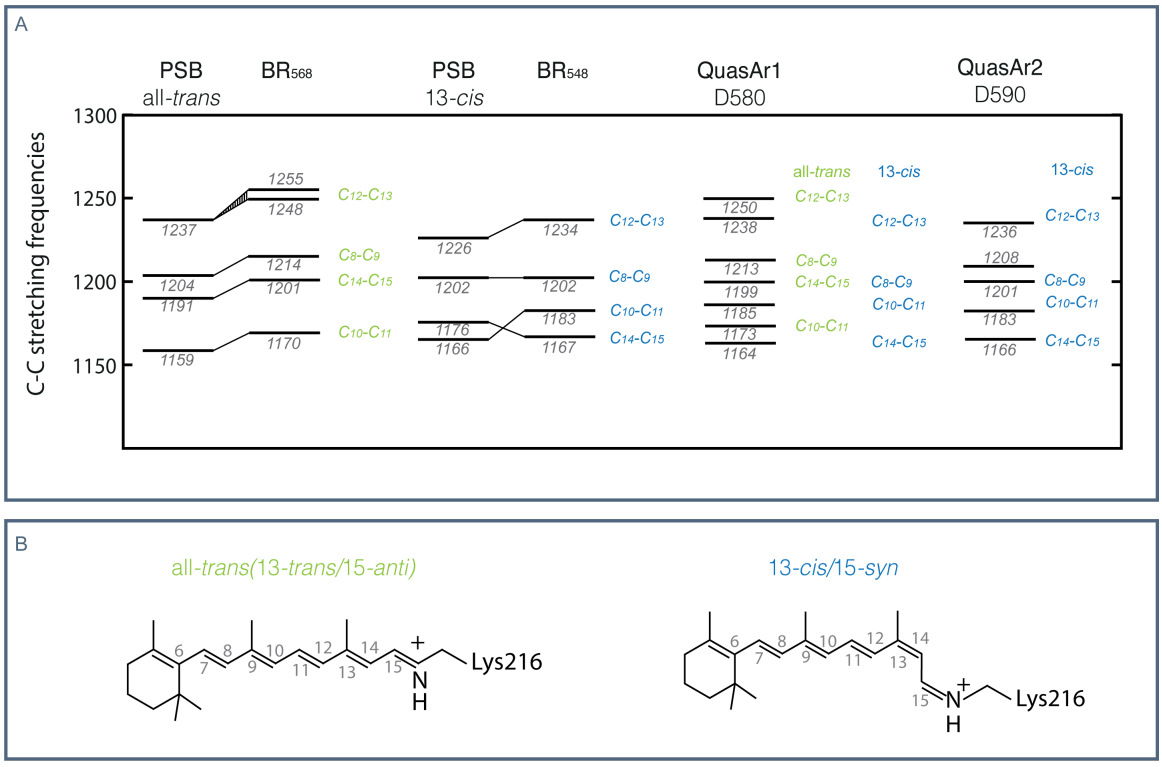

Figure 41. Correlation diagram of the C-C single bond stretches

The C-C stretching frequencies for PSB all-trans retinal and BR_{568} (all-trans) are adapted from[220]. The C-C stretching frequencies for PSB 13-cis/15-anti retinal and BR_{548} (13-cis/15-syn) are adapted from[221]. These frequencies are used to assign the bands observed in QuasAr1 and QuasAr2.

4. 2. 2. Protonated retinal Schiff base

Despite the replacement of the negative counterion to histidine (likely uncharged) (QuasAr1-D95H) or neutral glutamine (QuasAr2-D95Q), the retinal Schiff base remains protonated. Moreover, the Raman spectra (Figure 25, Figure 26) indicate strong hydrogen bonding interactions of the Schiff base proton, as indicated by the (i) upshift of the C=N frequency (~1650 cm^{-1}) compared to the wild-type Arch3 (1641 cm^{-1})[117], and (ii) the larger H/D-downshift (~25 cm^{-1}) compared to the wild-type Arch3 (20 cm^{-1})[117].

Also, in BR-D85N/A, despite the elimination of the negative charge at the counterion position, the hydrogen bond of the Schiff base proton was preserved[242]. However, the pK_a of the RSB was decreased from ~13 (wild-type BR) to ~8.2 (BR-D85A) and ~9 (BRD85N)[243,244]. It was proposed that in D85N mutant, the neutrally charged asparagine interacts directly with the Schiff base (C=O…NH$^+$ bond). Whereas the alanine, in D85A, is too small for direct interaction, but allows access of a water molecule, which interacts with the RSB[242].

Correspondingly, in QuasAr1 the histidine (uncharged) or in QuasAr2 the glutamine could interact directly with the RSB, insuring the strong bond between the Schiff base and its proton. Both of the residues have long side chains, hindering water access in the RSBH$^+$ proximity. Thus, in QuasArs, the interaction between RSBH$^+$ and a water molecule is unlikely. But we expect that D222 still acts as a single counterion.

The role of D222 is supported by additional studies carried out on Archon1. Similar to QuasAr1 and QuasAr2, also Archon1 maintains the strong interaction between RSBH$^+$ and its proton as shown by pre-resonance Raman spectroscopy (Figure S14). The MD simulations on Archon1 showed D222 is in close proximity to the Schiff base (Figure S9 G, H). In fact, D222 is closer to the RSBH$^+$ than Q95. Furthermore, the Archon1-D222E mutant showed strong effect on the pK_a of the Schiff base, increasing it from ~9 to ~10.4 due to the close proximity of the negative charge (Figure 37 E).

4. 2. 3. Retinal chromophore planarity

Further essential information of the chromophore is obtained from the HOOP bands of the Raman spectra. The small intensities of HOOP bands observed for

QuasArs indicate highly planar chromophore conformation[220,223]. In QuasAr1, a single HOOP band is observed at 969 cm^{-1}, which is assigned to $HC_7=C_8H$ HOOP vibration, suggesting a slight twist of the chromophore at $C_7=C_8$ position. In QuasAr2, additional band at 959 cm^{-1} ($HC_{11}=C_{12}H$) is observed, which most likely corresponds to the 13-*cis*/15-*syn* isomer. The 13-*cis* retinal isomer has additional twist of the chromophore at $C_{11}=C_{12}$ position.

4. 2. 4. Ethylenic stretch mode

The C=C stretch of the QuasArs (Figure 25) allowed to elucidate further understanding of the constructs. The relation between the absorption maximum of the chromophore (λ_{MAX}) and C=C stretch frequency is depicted in Figure S6 (Table S2). The ethylenic frequency shift between BR_{548} (13-*cis*/15-*syn*) and BR_{568} (all-*trans*) showed a 10 cm^{-1} downshift. The shift is attributed to a reduced conjugation length in the 13-*cis* compared to the all-*trans* retinal[221]. Furthermore, in BR-D85A and Arch3-D95N mutants, two well separated C=C stretching modes are observed, dependent on the retinal isomer composition. In Arch3-D95N, the 13-*cis* retinal isomer is correlated with C=C stretch frequency at 1527 cm^{-1}, and the all-*trans* isomer is associated with the 1518 cm^{-1} mode[117]. In BR-D85A, the 13-*cis* isomer is associated with the 1525 cm^{-1} band and the all-*trans* isomer is associated with the 1515 cm^{-1} band[242].

However, despite the 10 nm difference in absorption maxima of QuasAr1 and QuasAr2 (Figure 15 A), the C=C stretch modes peaks of QuasArs differ only by 1 cm^{-1} (Figure 25). QuasAr1 shows a peak at 1524 cm^{-1} (FWHM of 16 cm^{-1}), whereas in QuasAr2 the peak is observed at 1523 cm^{-1} (FWHM of 19 cm^{-1}). This observation is astounding since QuasAr2 has much higher contribution of 13-*cis* retinal (Figure 24, Figure 25). These observations indicate that the heterogeneous dark state consists of subspiecies that are spectroscopically strongly overlapping.

4. 2. 5. Are QuasArs populating an O-like state in the dark?

As previously mentioned, due to the lack of counterion, and increased excited state lifetime, it is likely that QuasArs are trapped in O-like and Q-like states. Moreover, the Raman spectral features of QuasAr all-*trans* isomer in C=C and C-C would be consistent with those of the O state of BR[245,246]. However, one pronounced

difference is the O state displays intense HOOP modes, indicating a distorted chromophore[246], whereas QuasArs display a rigid and planar chromophore.

Nevertheless, one needs to consider the possible large conformational changes of the protein introduced in the constructs after removal of the proton donor (D95H/Q) and acceptor (D106H), which would not be resolved by identifying retinal isomers. For example, the analogous BR double mutant D85N/D96N also holds mixture of all-*trans* and 13-*cis*/15-*syn* retinal isomers (with ratio of ~1:1), as confirmed by HPLC and Raman spectroscopy[247]. But the elimination of both proton donor and acceptor negative charges triggers electrostatic changes leading up to large-scale protein conformational changes[247,248]. The crystal structure of the double-mutant resembles the one of the M state, with a strongly distorted helix C, demonstrating, that the structural changes do not directly correlate with the retinal isomers present, but depend on the charge distribution within the protein[247,249]. These previous findings are signifying the need for structural investigation of QuasArs.

4. 2. 6. Retinal isomers and photodynamics

After in-depth study of the chromophore in the dark state, the retinal isomer composition is correlated to the photoynamics. Here, the results form HPLC study (Figure 24) are in focus, due to the direct estimation of isomer contribution.

Interestingly, in QuasAr1, where equilibrium between retinal isomers is shifted towards all-*trans* (80%, Figure 24), also the contribution of the longer-lived species (τ_2) of the excited state is considerably higher (~90%, Figure 17). Furthermore, in both constructs, QuasAr1 and Quasar2, we observe that higher concentration of all-*trans* retinal chromophore correlates with the higher fluorescence QY, whereas higher concentration of 13-cis retinal chromophore yields lower fluorescence QY (Figure S24, Table S4). We can conclude that fluorescence QY of all-*trans* isomer is higher than 13-*cis* retinal isomer. This is in good agreement with previous reports of BR_{605}, where it has been shown that fluorescence QY of the 13-*cis* retinal is 2.5-fold lower than one of the all-*trans*[106].

Another observation made in QuasArs, corresponds to retinal contribution and isomerization percentage. In QuasAr2 the 4-fold increase of 13-*cis* retinal (Figure 24 A, D) isomer contribution, compared to QuasAr1, correlates with 4-fold increase of

the fraction of the excited molecules, which undergo isomerization (4% vs 1%, Figure 17). This suggest that 13-*cis* retinal in QuasArs is more likely to undergo isomerization. However, the energy barrier for isomerization is expected to be particularly high for both retinal isomers: all-*trans* as well as 13-*cis.*

Sample illumination with red LED (625 nm) produced mixture of 13-*cis*, 11-*cis*, 9-*cis* and all-*trans* retinal isomers (Figure 24). The isomerization along the different C=C double bonds is likely arising due to mutation D95X and the resulting absence of the negative charge in the counterion position. It has been shown in BR_{568} that counterion complex, in particular D85, plays a crucial role in the retinal isomerization. Upon excitation, ultrafast collective motion of counterion complex and temporal rearrangement of hydrogen bonds lowers the energy barrier for particular isomerization about the C_{13}=C_{14} bond[48]. Sample illumination with blue LED (400 nm) produced mixture of 13-*cis* and all-*trans* retinal isomers, with stronger preference of backisomerization towards 13-*cis* (Figure 24).

As noted above, the efficiency of isomerization is very low, and it is possible to interpret only the data of the photoproducts formed with prolonged illumination. Focusing on the observations of retinal isomer changes of QuasAr2 (Figure 24) a retinal isomer equilibrium scheme is proposed as shown in Figure 42.

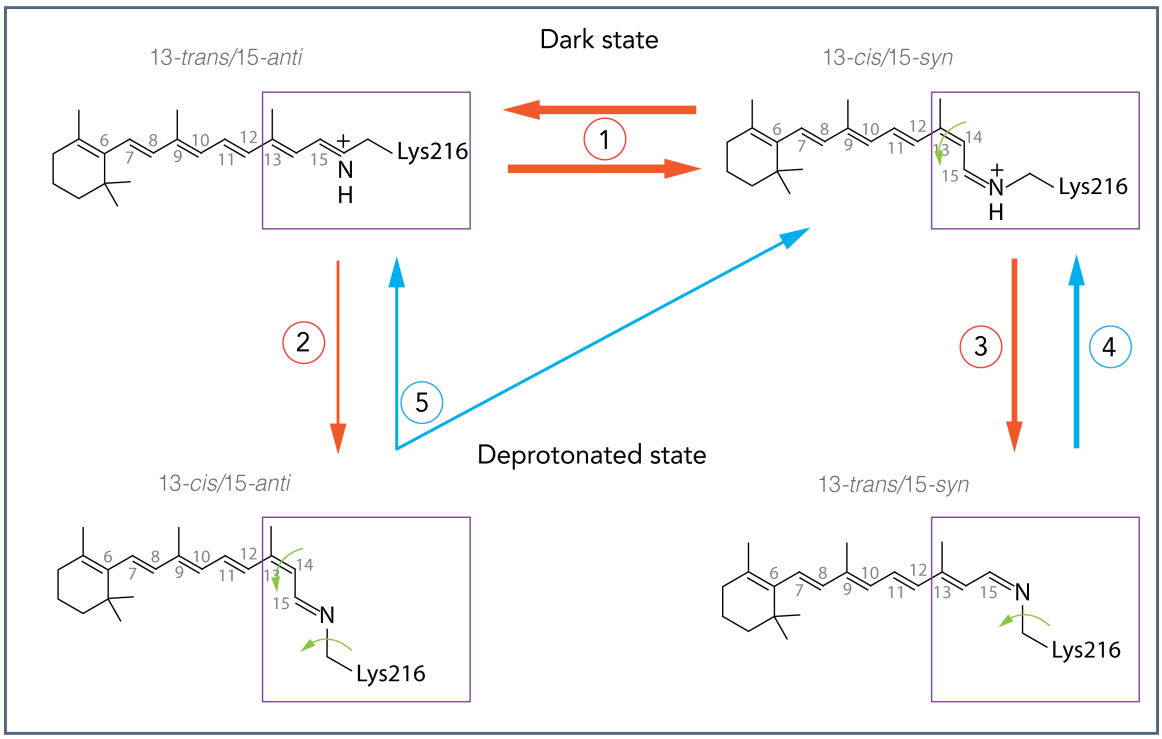

Figure 42. Illumination-induced equilibrium of retinal isomers

Proposed isomerization pathways and resulting equilibrium between retinal isomers. Isomerization induced with red LED (620 nm) is designated with orange arrows and isomerization induced with blue LED (400 nm) is designated with blue arrows. The width of the arrows designates the probability of the isomerization. All of the reactions have very low efficiency. It is proposed that red light induces single and double isomerization. Double isomerization is proposed to have higher efficiency than the single isomerization. Double isomerization would shift the equilibrium between protonated 13-trans/15-anti and 13-cis/15-syn (upper row). Single isomerization would likely result in an inefficient photocycle and deprotonation (shift from upper to lower row isomers). Blue light (400 nm) induces backisomerization and reprotonation of the retinal with a stronger preference towards 13-cis/15-syn isomer (shift from lower to upper row isomers).

The observations suggest that illumination can trigger both double (1) and single (2,3) isomerization. The double isomerization (1), around C_{13}=C_{14} and C_{15}=N bonds, would produce a photoproduct with a similar geometry and charge distribution, resulting in two species, with similar absorption spectra. Thus, the red illumination is expected to produce a photo-equilibrium between 13-*trans*/15-*anti* and 13-*cis*/15-*syn* (Figure 42, isomerization 1).

The single isomerization (2,3) would likely result in deprotonation of RSB, leading to blue-shifted absorption spectra (Figure 42, isomerization 2 and 3). Furthermore,

the single isomerization-driven low-efficiency photocycle would produce a mixture of 13-*cis*/15-*anti,* 11-*cis*/15-*anti,* 9-*cis*/15-*anti* and 13-*trans*/15-*syn* as observed in the HPLC experiment (Figure 24). Comparison of chromatograms of QuasAr2 dark state and red light adapted state (Figure 24 D, E) reveal greater change in 13-*cis*/15-*syn* concentration compared to 13-*trans*/15-*anti*, indicating that the efficiency of 13-*cis*/15-*syn* isomerization (3) is higher than 13-*trans*/15-*anti* (2).

Mutations introduced in QuasAr1 and QuasAr2 (D95H/Q) result in different charges at the counterion position, leading to different energy barriers for retinal isomerization. Consequently, it is expected that the efficiency of 13-*cis* and all-*trans* isomerization between the two constructs is different. The HPLC data of the retinal isomer composition of photoproducts is inconclusive to determine the isomerization efficiency, and further spectroscopic studies would be needed.

The blue illumination (400 nm) triggers backreaction (Figure 15 B, Figure 24 F) and is also expected to drive both single and double isomerization with preference towards 13-*cis*/15-*syn* (Figure 42, isomerization 4 and 5). It is likely that the double isomerization is more prominent for 13-*trans*/15-*syn* isomer (5) as observed in HPLC chromatogram (Figure 24). The 11-*cis*/15-*anti* and 9-*cis*/15-*anti* are expected to backisomerize to 13*trans*/15-*anti.*

Also in HKR1 a complex isomerization pathway was observed for UV-excited deprotonated species (Figure S25)[215,250]. The recorded spectra of ultrafast UV/Vis absorption and Raman spectra allowed correlating the excited state dynamics with retinal isomerization. Compared to protonated species, deprotonated species exhibit an excited state inversion, resulting in higher-lying optically allowed S_2 state with ^1B_u symmetry, and lower-lying optically forbidden S_1 state with ^2A_g symmetry[215,216]. The inversion of the states results in excitation of the chromophore to the S_2 state, fast decay to S_1 state and recovery to the ground state S_0[215,216]. The retinal isomerization takes place in two phases as demonstrated for HKR1. First, the S_2 to S_1 state decay may results in retinal isomerization around the C_{13}=C_{14} band. Second, the S_1 to S_0 decay may results in retinal isomerization around the C=N band (Figure S25)[215].

In QuasArs, similar excited state inversion was observed for the deprotonated species (Figure 21). The molecule was excited to the S_2 state with a fast (~ 155 fs) decay to S_1 state and slow bi-expoential decays to the ground state S_0 (~4 ps and ~44 ps). In difference to HKR1, only one femtosecond component was revolved,

suggesting that the ~155 fs component has likely contribution from the S_2 to S_1 transition, and vibrational cooling on the S_1 state. It can be speculated that a similar two-step isomerization takes place in QuasArs after UV-excitation of the deprotonated species as observed in HKR1.

Additional recordings with femtosecond Raman spectroscopy would be needed to further elucidate the isomerization mechanism of QuasArs. This would allow correlating the excited state dynamics with the ultrafast isomerization.

4. 3. Essential residues to aid increase in fluorescence intensity

4. 3. 1. The role of D95X mutation

Previous reports had already indicated the central role of D95X mutation to construct microbial rhodopsin-based fluorescent voltage sensors[3,167]. The additional experiments carried out in this study have confirmed the significance of removing the counterion (Figure 38, Figure 39). As observed by Q95H replacement in QuasArs, the mutation influences the fluorescence QY, the absorption maximum, the excited state dynamics, the retinal isomer composition and the voltage sensitivity (Figure 15, Figure 17, Figure 24, Figure 38). Further study of alternative residue substitutions reconfirmed, that the residue placed at D95X position determines the properties of the fluorescent voltage sensors, like fluorescence QY, pK_a of RSB and the absorption maximum (Figure 38).

The mutations D95Q/H remove the negative charge of the counterion. Interestingly, several of the properties observed in QuasArs resemble those of BRD85N mutant and acidified BR_{605}, with also neutralized proton acceptor D85.

Firstly, the strong red-shift of the QuasArs is attributed to lack of negative charge at D95 position. The changes in the electrostatic interaction between the Schiff base and removed counterion, destabilizes the S_0 ground state and reduces the energy gap between the ground state S_0 and the excited state S_1 [251]. Similar red-shift was observed in BR_{605}. The extensive studies of BR_{605} show further correlations. Upon excitation of BR_{605}, the excited state is populated and decays in ~20 ps. The long-lasting excited state results in 10-fold rise to the fluorescence QY compared to BR_{568}. In addition, efficiency of the K-state formation is decreased, suggesting that most excited molecules return back to the original dark state[252]. The dark state of BR_{605} is

composed of approximately equal mixture of 13-*trans*/15-*anti* and 13-*cis*/15-*syn* retinal isomers, where the 13-*trans*/15-*anti* possesses 2.5-fold higher fluorescence QY[252,253]. Another consistent finding between BR_{605} and QuasArs, was 11-*cis* and 9-*cis* retinal isomer formation upon irradiation[113]. Correspondingly, similar observations in QuasArs are attributed to the replacement of the counterion.

In addition, replacement of aspartate to a larger, negatively charged glutamate (D95E), in combination with mutation of the adjacent threonine (T99C), have also been reported as promising substitutions. Arch3-D95E-T99C double mutant (Archer1[1], Table S1 Nr. 4) and Arch5[1] (Figure 10, Table S1 Nr. 9) have been reported as red-shifted (λ_{MAX} ~625 nm) fluorescent voltage sensors.

It has been shown in BR-D85E that the aspartate to glutamate replacement, at the counterion position, shifts the pK_a of the purple-to-blue (λ_{MAX} shift from 569 nm to 605 nm) transition from 3.6 to 6.5[254], that is the counterion protonation takes place at higher pH. Therefore the strongly red-shifted absorption maximum in Arch3-D95E-T99C and Arch5 is also interpreted as uncharged D95E residue.

Due to the desirable properties of Arch5 (QY~0.87% and λ_{MAX} ~625 nm)[1], the proposed central mutation pair (D95E and T99C) was also tested in Archon1 (Figure 39). The Archon1-Q95E-T99C showed improved properties: 18 nm red-shifted absorption maximum and 1.4-fold increase in fluorescence QY. These characteristics denote the construct promising for applications in membrane voltage imaging, and further studies need to be carried out for testing applications in neuron cell cultures.

4. 3. 2. The role of D106H mutation

The mutation of the proton donor D106H (Figure 8) has not been studied in detail in this work, but other works have demonstrated that it aids further increase of the fluorescence QY[3] and plays role in the voltage sensing mechanism[160]. Removal of the negative charge of the proton donor (D106H), in addition to the first counterion mutation (D95H), has been reported to increase the fluorescence QY 5-fold from 0.04% to 0.2%[3] (Table S1, Nr. 1 and Nr. 13). The recovery of the negative charge of the primary counterion (D95) and replacement H106N at the proton donor position has been shown to reverse the voltage sensitivity in QuasAr-based FRET sensors[160], and will be introduced in more detail below.

Despite the distant position of the proton donor D106 from the chromophore

(Figure 8, ~ 11 Å), it affects the properties of the fluorescent voltage sensors and should be studied in more detail.

4. 3. 3. The role of proline mutations

In addition to the fundamental D95X mutation, other mutations can further increase the fluorescence QY. Prolines in transmembrane helices are highly conserved in microbial rhodopsins and it has been proposed that prolines contribute to the conformation changes of the rhodopsin after light-activation[255,256]. It is likely that mutation of prolines, such as P60S in QuasArs (Figure 8), and additional P196S in Arch5 (Figure 10), confines the protein and the chromophore. Reduced flexibility of the protein has been shown to increase the excited state lifetime. A study of BR_{568} carried out by Gillbro and Sundström[257] showed that increasing the rigidity of protein by lowering temperature to 77K, extends the excited state lifetime up to ~60ps. Implying that proline mutations could contribute to longer excited state lifetime by introducing rigidity to the protein matrix. In fact, it has been shown that in an addition to the two counterion mutations D95H/D106H, the substitution P60S yields 2.5-fold increase in fluorescence QY (Table S1, Nr. 13 and Nr. 14[3]). Also in NeoR (QY~20%) the analogous position of Arch3-P196 is replaced by threonine (T238)[230].

4. 3. 4. Mutations in the retinal binding pocket

To further improve the fluorescence QY of these constructs, it is essential to consider further mutations in the retinal binding pocket, which would modify the polarity and polarizability of the chromophore environment. As shown in this study, mutations close to the retinal Schiff base (A225C) and β-ionone ring, (G132S), show notable increase in the fluorescence QY (Figure 40, Table S3). In both cases a nonpolar residue is replaced by polar residue. To understand the role of these mutations, and the possible change in electrostatic environment, further MD simulations should be carried out.

Another interesting construct presented in this study is Archon1-S151A. The mutation replaced an -OH bearing residue by hydrophobic residue with shorter side chain in the proximity of β-ionone ring. The elimination of polar residue results in slight increase in the fluorescence QY, and 25 nm blue-shift of the excitation spectra

(Figure 40, Table S3). The role of the highly conserved Serine in color-tuning had been already presented in context of BR and Arch3[258,259]. The previous studies have shown that S151A mutation result in tilting of the β-ionone ring. The reduced planarity of the chromophore results in decreased coupling between the polyene chain and the β-ionone ring, yielding a blueshift of absorption maxima. Even further rotation of β-ionone ring (~140°) and isomerization around the C_6-C_7 (6-s-*cis* form) was achieved in mutants Arch3-M128A/S151A/A225T (~50 nm blue shift) and Arch3-M128A/G132V/A225T (~100 nm blue shift)[258,259].

For application in tissue, it is of high interest to use far-red or infrared excitation. In addition to the red shift of the absorption maximum previously discussed, the blue-shifted maximum could broaden the application range, and allow two-photon imaging. Two-photon imaging provides high spatial and temporal resolution and allows higher penetration depth of light and lower photobleaching in tissue (living animals). In two-photon laser scanning microscopy typically near-infrared wavelength range (700–1000 nm) is used[260]. As revealed by fluorescence recordings, fluorescence of QuasArs can be acquired by two-photon-excitation. Furthermore, the one and two photon excitation spectra are overlapping (Figure 23). To obtain desired signal it would be necessary to blue-shift the chromophore absorption maxima to ~500 nm.

Exploring additional mutations and their combinations in the retinal binding pocket, would aid the development of the next generation of voltage sensors.

4. 4. Voltage sensing of QuasArs

A highly challenging aim of this study was to understand the voltage sensing mechanism of the fluorescent microbial rhodopsins. The multiple pathways, in which the voltage may alter the fluorescence intensity, have been already introduced in the result section. The voltage may modulate equilibrium of RSB/$RSBH^+$, it may affect the electrostatic environment of retinal binding pocket, it may alter the retinal isomer composition or modulate the fluorescence lifetime (and QY). To address the complex voltage sensing mechanisms in microbial rhodopsins, it was important to employ different experimental and theoretical methods to understand the mechanism.

4. 4. 1. Voltage sensing mechanism as proposed from MD simulations

MD simulations of the wild-type Arch3 indicated R92 flipping as the key event in the voltage sensing mechanism (Figure 27)[207]. Under negative voltage it oriented towards the $RSBH^+$ and D95 and D222. Whereas, upon positive voltage the hydrogen bonding to the counterion complex is broken and R92 flips towards the extracellular side forming hydrogen bond to the proton release complex E204 and E214.

Indeed, it has been proposed previously, that reorientation of highly conserved arginine (R82 in BR) is crucial for the function of microbial rhodopsins. In bacteriorhodopsin, upon proton transfer from Schiff base to the counterion, the arginine flips (small energy barrier for movement 1.5 kcal/mol) towards the extracellular side triggering the proton release from the proton release complex (E194 and E204)[227,261]. Whereas it has been shown in pumps like CsR (R83)[228] and KR2 (R109)[134] the mobile arginine serves as extracellular barrier, preventing passive ion transport. The arginine replacement to glutamine resulted in formation of proton or ion channel, respectively.

Additionally, the MD simulations of Arch3 indicated that hydrogen bond between the proton acceptor D95 and close by T99 (HB1) is formed only under positive voltage conditions. Interestingly, also in Archon1 the hydrogen bond between Q95 and T99 (HB1) showed high voltage sensitivity. The hydrogen bond plays crucial role in proton pumps for proton transfer from RSB to the counterion complex. The QM/MM simulations in bacteriorhodopsin have shown that T89, in particular its hydrogen bonding to RSB and D85, aids the proton transfer from RSB to the counterion D85[86]. It can be presumed that similar process takes place also in the proton pump Arch3.

The MD simulations revealed that voltage sensing mechanism of Archon1 is quite different than one observed in wild-type Arch3[207]. R92 remained oriented towards the extracellular side, independent on the membrane voltage. This is in agreement with acidic crystal structure of BR (with protonated D85), which demonstrated the R82 sidechain orientation towards the extracellular side[89]. The MD simulations have identified D125 as the key residue involved in the voltage sensing in Archon1, governing the formation of HB1 (Figure 43).

In Archon1 the sidechain of D125 showed voltage dependent reorientation, triggering alterations of the hydrogen bonding network (Figure 27). Under negative

voltage, D125 forms hydrogen bond with T100 (HB3). However, under positive voltage this bond is broken and D125 interacts with G123 (HB4), T100 interacts with W96 (HB2) and allows the formation of the essential hydrogen bond between Q95 and T99 (HB1). Furthermore, the disruption of HB3, results in loss of hydrogen bonding between helices C and D, destabilizing the helix D (Figure S8).

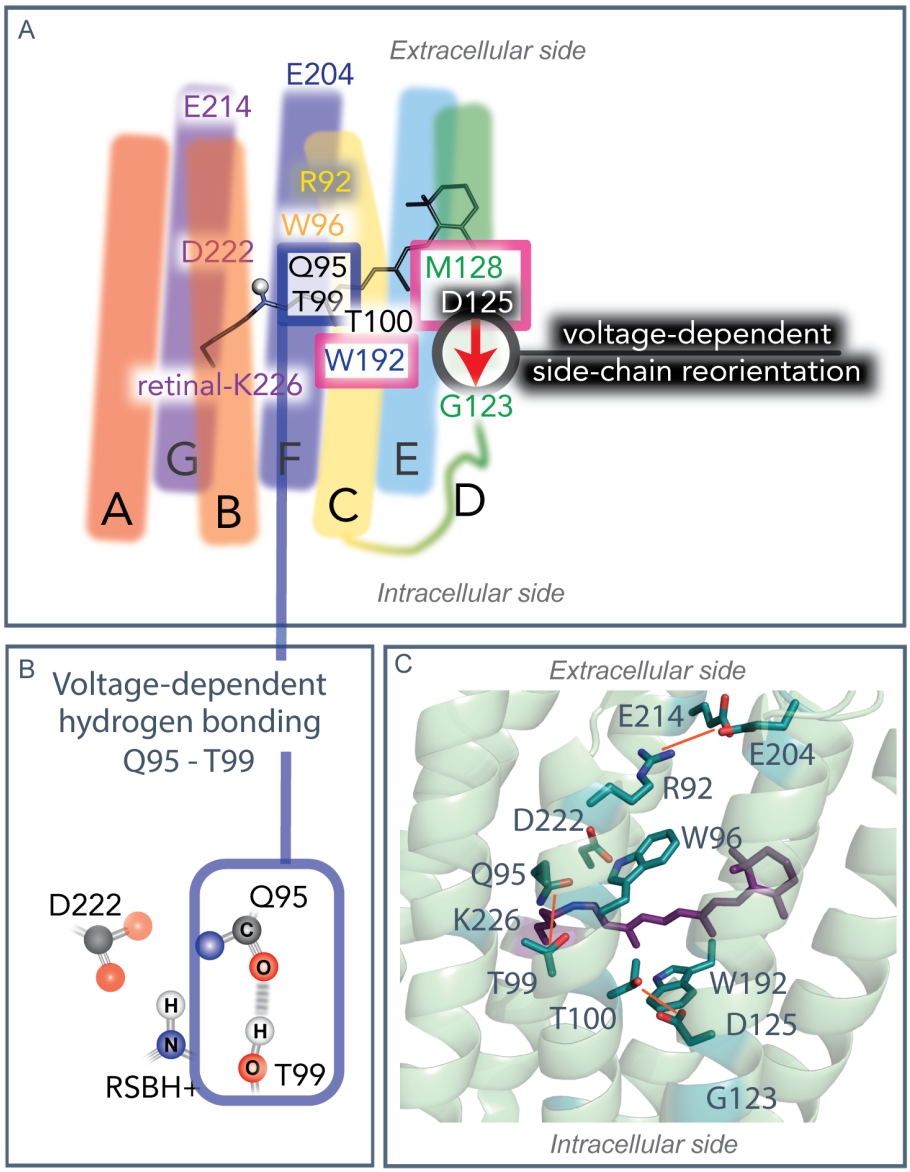

Figure 43 Voltage sensing mechanism of Archon1

(A) The key residues involved in the voltage sensing. Upon negative voltage D125 orients towards the RSB and forms a hydrogen bond with T100 (HB3). However, upon positive voltage D125 flips towards the intracellular side (downwards in the image) and forms a hydrogen bond with G123 (HB4). This allows two new hydrogen bonds to form between T100 and W96 (HB2) and, most importantly, between Q95 and T99 (HB1), which is indicated in (B). The panel (C) indicates the essential residues – Q95, T99, T100, D125, W96, W192, D222, R92, E204 and

E214. The important interactions between Q95-T99, T100-D125 and R92-E204/E214 are indicated with orange lines.

The intra-helical connections introduced by threonine and aspartate hydrogen bonding have been recognized in other rhodopsins already. In BR the T46-D96 and T90-D115 facilitate connection between helices C and B and helices C and D, correspondingly[262]. The hydrogen bonding between T90 and D115 has been shown to be highly rigid, which is attributed to hydrophobic residues (L94, L87, M118) in their vicinity[262]. For future investigation of the role of T100-D125N hydrogen bond in Archon1, it would be interesting to explore mutations in the hydrophobic positions (L104, L97, M128), possibly allowing higher flexibility of D125 and increasing the voltage sensitivity. Furthermore, as mentioned previously M128A mutation in Arch3 was associated with rotation of β-ionone ring and strong blue-shift of the absorption[258,259]. The M128A mutation, might yield blue-shifted voltage sensor with further improved voltage sensitivity and should be studied experimentally.

The intra-helical connections introduced by threonine and aspartate (Arch3: T100-D125; BR: T90-D115) is conserved in proton pumps, but not in channelrhodopsins[262]. Instead, threonine (position T100 in Arch3) is replaced by cysteine (C128 in ChR2). In ChR2 the C128-D156 pair forms an intra-helical hydrogen bonding between helices C and D. Cysteine at this position insures structural plasticity of channelrhodopsin during the photocycle and allows protonation and deprotonation of D156 to take place[262]. The introduction of threonine in this position Chr2-C128T, resulted in long-lived cation-conducting state[263]. However, cysteine introduction into proton pump BR-T90C did not strongly affect the proton-pumping activity, but resulted in rearrangement of the hydrogen bonding network, with T90C and D115 forming dynamic hydrogen bonds to W86[262]. It would be interesting to study further the role of threonine and aspartate interaction in Archon1 by substitution T100C. In analagoy to observations in BR, Archon1-T100C variant might result in increase in voltage sensitivity of hydrogen bond T100C-D125 and flexibility of helices C and D.

4. 4. 2. Mutation studies of the key residues involved in the voltage sensing

Extensive studies of the mutants confirmed the key residues involved in voltage sensing in Archon1.

R92 showed voltage dependent reorientation in the wild-type Arch3, but not in Archon1. To test the role of arginine, it was replaced by lysine. Other residues tested at this position, abolished protein expression, designating the significance of the positive charge in the protein stability. Archon1-R92K variant maintains the positive charge, but lacks guanidium group, which might disrupt the hydrogen bonds to other residues (E204 and E214). The R92K mutant showed decrease in retinal stability, but increased the fluorescence QY of the construct (Figure 32). No effect was observed on the pK_a of the RSB. However, substantial difference was observed in the pK_a titration curve at acidic conditions (Figure 33). Surprisingly, the voltage modulated fluorescence intensity changes were decreased in Archon1-R92K variant, despite the lack of direct involvement of arginine in the voltage sensing mechanism in Archon1 (Figure 32). The experimental observations are supported by MD simulations. Results of MD simulations indicate, that the hydrogen bonding network is independent on the voltage (Figure S26). The HB3 (T100-D125) is always formed and HB1 (Q95-T99) is not established.

As reported, in light-driven pumps CsR (R83)[228] and KR2 (R109)[134], the mobile arginine serves as extracellular barrier. In correspondence, this role can be suggested also in Archon1. Moreover, in Archon1-R92K the lack of arginine and the associated hydrogen bond to the proton release complex E214 and E204, permits interaction with the extracellular bulk. This is confirmed by MD simulations, where substitution R92K shows increased water density in the retinal binding pocket in contrast to Archon1 (Figure S26).

The study was proceeded with investigation of the key residue – D125. Only the variant Archon1-D125N could be obtained, whereas other mutations at this position destabilized the retinal binding pocket and prohibited protein expression. The mutant showed only slight blue-shift (~5 nm) and 1,4-fold increase in fluorescence QY (Figure 34). The aspartate to asparagine replacement did not result in change in the pK_a of the Schiff base ~9 (Figure 35). However, the Archon1-D125N showed the highest voltage sensitivity observed in this study ($\Delta F/F_{max} \approx 33\%$), which showed 1.65fold increase compared to parental Archon1 (Figure 36).

As introduced previously, hydrogen bond between helices C and D (T100-D125) in unmodified proton pumps shows high rigidity, whereas in Archon1 the hydrogen bonding appears voltage sensitive (Figure 27). Mutations at analog position D115 in BR showed increased flexibility in the hydrogen bonding and resulted in changes in the functionality of the rhodopsin. The residue D115 in BR is expected to stay protonated throughout the photocycle, however the conservative mutant BR-D115N showed slowed kinetics of reprotonation and dark state recovery[262]. In analogy, it could be speculated that also in Archon1 replacement of aspartate to asparagine further increases the flexibility of the hydrogen bond T100-D125. The improved plasticity of the conformational changes would aid higher voltage sensitivity of the construct. However, the MD simulations showed no voltage dependent changes in the hydrogen bonding network (Figure S27). Furthermore, N125 did not show formation of hydrogen bonds as observed for D125 (HB2, HB3). Only, voltage independent hydrogen bond between T100-W96 (HB2) and essential Q95-T99 (HB1) were observed. Due to the lack of the voltage sensitivity in hydrogen bond network, but increased voltage sensitivity of the fluorescence intensity, further investigation of Archon1-D125N was carried out using MD simulations (Figure S27 F). Interestingly, in comparison to Archon1 (Figure S27 E), Archon1-D125N showed higher rigidity of the chromophore and the retinal binding pocket, suggesting Archon1-D125N populates the fluorescent conformational states more efficiently than Archon1.

The determined pK_a of D125 by MD simulations at positive voltage was ~7, whereas at negative - slightly lower ~ 5 (Figure S9). If D125 would change its protonation under different voltage conditions, a shift in absorption maxima of the chromophore would be expected. However, pre-resonance Raman recordings of Archon1 in cell suspension, did not show any shift in C=C frequency, which would correspond to color tuning (Figure 31 C). Furthermore, mutation D125N showed only slight absorption shift and no loss in voltage sensitivity, in contrary, it further increased the voltage sensitivity. Suggesting, D125 in Archon1 remains protonated, independent on membrane voltage.

To investigate the hydrogen bond partner T100, threonine was replaced by alternative polar residue serine (T100S) and hydrophobic residue alanine (T100A). Only T100S could be purified for spectroscopic studies, and it showed spectral

broadening with blue-shifted absorption maximum (10 nm) and slightly increased fluorescence QY (Figure 34). The pK_a of RSB, remained unaffected (Figure 35). Archon1-T100S, with conserved hydroxymethyl group, showed slightly increased voltage sensitivity. However, Archon1-T100A, with side chain reduced to a methyl group, showed decreased voltage sensitivity.

The experimental studies have shown that mutations at positions T100 and D125 affect the voltage sensitivity of Archon1, verifying the voltage sensitive nature of T100-D125 hydrogen bond. The experimental observations were supported by MD simulations, where voltage dependent formation of the essential HB1 (Q95-T99) was observed in Archon1-T100S, and not in Archon1-T100A (Figure S27).

Analog mutation in BR-T90A showed loss of T90-D115 hydrogen bond and reduction in proton-pumping. Whereas double mutant BR-T90A/D115A resulted in absence of structural changes during the photocycle and complete loss of proton pumping[262]. Indicating once more, the hydrogen bond between helices C and D (Arch3-T100-D125/BR-T90-D115) is important for proton-pumping in unmodified proton pump, and remains essential for voltage sensing in Archon1.

4. 4. 3. The determined pK_a values

Recordings of absorption spectra at different pH values revealed additional comparable feature between Archon1 and its mutants. The pK_a of the RSB, in Archon1 and its variants Archon1-R92K, Archon1-T100S and Archon1-D125N, was conserved pK_a ~9 (Figure 33, Figure 35). Despite the central role of T100 and D125 residues in voltage sensing, mutations at these positions did not affect the pK_a of the RSB. However, as expected, a strong shift, in the pK_a of the RSB, was observed upon mutation of the remaining counterion in Archon1-D222E variant (pK_a ~10.4, Figure 37 E).

Pronounced differences could be observed between Archon1 and the four mutants in the recorded titration of the absorption spectra at acidic conditions. The parental Archon1 showed ~13 nm blue-shift of the absorption maxima (Figure 33 C) with assigned pK_{a1} ~ 3 of the protonation of adjacent D222. The experimentally determined pK_a value is in good agreement with the calculated value by MD simulations (Figure S9 E). However, the mutants (Archon1-R92K, Archon1-T100S, Archon1-D125N and Archon1-D222E) showed complex titration curve (Figure 33 D,

Figure 35 C, D, Figure 37 F). In each of the variants, first, similar to Archon1, pH dependent ~15 nm blue-shift of the absorption maxima was observed, assigned to pK_{a1}. Second, upon further acidification, even further blue-shift (~120-130 nm) of the absorption maximum was observed.

As suggested, the pK_{a1}, which corresponds to ~15 nm blue shift of the absorption maxima, is assigned to protonation of the remaining counterion D222 according to BR. In BR upon acidification, the protonation of primary counterion D85 results in purple-to-blue transition (568 to 605 nm) with assigned pK_a ~3.6, and additionally protonation of the secondary counterion D212 results in ~20 nm blue shift (from 605 nm to 585 nm)[241,264]. The corresponding pK_a values are pK_a ~3.6 of D85 and pK_a~ 1.5 of 212[241,264]. In BR-D85N the negative charge of the primary counterion is removed, leading to upshift of the pK_a of the secondary counterion from 1.5 to 4[241]. The reported pK_a~4 of D212 in BR-D85N is in close agreement with the value observed in Archon1 (pK_a~3 of D222).

The observed strong blue shift (λ_{MAX} ~ 450/455 nm) upon acidification in Archon1 mutants is unusual for microbial rhodopsins and this transition is assigned to pK_{a2} of titratable residue X_2. The reoccurring strong blue shift in all the mutants (Archon1-R92K, Archon1-T100S, Archon1-D125N and Archon1-D222E) suggest that the residues – R92, T100, D125 and D222 - play an important role in the formation of the hydrogen bonding network in the retinal proximity. The absorption maxima at 450 nm could be assigned either to destabilization of the chromophore or formation of a 9-*cis* retinal isomer.

The absorption maximum at 440 nm has been previously assigned to free protonated retinylidene Schiff bases in denatured bacteriorhodopsin[19,265]. According to previous reports, the blue-shifted absorption maxima (λ_{MAX} ~ 450/455 nm) observed in mutants could be resulted from destabilization of the chromophore under acidic conditions (pH < 3.6). However, the observed absorption maximum is slightly red-shifted by 10 to 15 nm (λ_{MAX} = 450 nm - 455 nm) in Archon1 variants.

The rise of absorption maximum at 450 nm has been previously assigned also to 9-*cis* retinal isomer containing bacteriorhodopsin BR_{450}[113,266]. However, this photoproduct was obtained in two steps from the wild-type BR. First, red light illumination of BR at acidic conditions yield BR_{500}, which comprised 9-*cis* isomer. Second, pH exchange to alkaline resulted in blue shift and population of BR_{450}.

Additionally, photobranching of O-state yields a photoproduct with a 9-*cis* retinal and displays absorption maximum of 490 nm[114]. However, formation of 9-*cis* retinal in Archon1 variants upon acidification without illumination is unlikely.

4. 4. 4. Spectroscopic observations of fluorescent kinetics and retinal isomer composition upon membrane depolarization

Further experimental studies were aimed to elucidate the voltage sensing mechanism in QuasArs. To study the consequences of the discussed rearrangement of hydrogen bond network, an *E. coli* cell assay was established for voltage dependent spectroscopic studies. FLIM allowed investigating the changes in the fluorescent lifetime, whereas Raman spectra allowed investigating changes in the retinal isomer composition and shifts in the absorption maximum. However, upon membrane depolarization the increase in the fluorescence intensity did not result neither in change in the fluorescence lifetime (Figure 29), nor in substantial change in the retinal isomer composition (Figure 31).

The lack of the changes detected spectroscopically, could be explained with the voltage modulated population of the fluorescent species.

One of the proposed mechanisms is voltage modulated RSB/$RSBH^+$ equilibrium. Upon RSB deprotonation, the absorption maximum is strongly blue-shifted ($\Delta\lambda \sim$ 175 nm, Figure 33 A), consequently changing the population of the photoactive species. The most likely proton acceptor would be the remaining D222 from the counterion complex. First, the distance distribution estimated from MD simulations (Figure S9 G, H) showed that D222 is in close proximity to RSB. Second, the observed Raman spectra recordings indicated that hydrogen bonding between the Schiff base and its counterion is very strong, where likely D222 is counterbalancing the positive charge and substituting the primary counterion D95Q (Figure S14). Third, the pK_a of the RSB was increased from ~9 to ~10.4, upon D222E substitution (Figure 33 C , Figure 37 E). However, another pathway of proton transfer may be through the the voltage dependent HB1 (Q95-T99), as already described for BR[86].

Electric-field-induced UV/Vis absorption spectra changes of purple membrane (BR_{568}) and BR-D85N are one of the few reported experimental data of microbial rhodopsin voltage dependency. The wild-type BR_{568} showed voltage dependent shift in the absorption spectra maximum of the protonated species. The difference

spectra showed decrease at ~530 nm and increase at ~620 nm. Whereas, BR-D85N showed very strong blue-shift, indicating deprotonation of RSB. The difference spectra showed decrease at ~600 nm and increase at ~410 nm. The pK_a of the RSB in BRD85N has decreases from ~13 to ~9[244], however it is far from neutral ~7. Despite the high pK_a~9 of the RSB, the voltage dependent deprotonation of RSB was observed.

Similar to BRD85N, also in Archon1 the pK_a of the Schiff base is ~9 (Figure 33 A), suggesting similar voltage dependent deprotonation might take place. Furthermore voltage dependent deprotonation of the RSB would alter the concentration of photoactive species and would explain the decrease in fluorescence without changing the kinetics or the retinal isomer composition.

Interestingly, pre-resonance Raman recordings of a single counterion mutant Arch3-D95N overexpressed in *E. coli* showed voltage dependent change in 13-*cis* retinal isomer, whereas no change was observed for all-*trans* retinal isomer[117]. Saint Clair et al. proposed that the 13-*cis* retinal isomer protonation is voltage sensitive, hence changing the contribution to the spectra upon voltage change[117]. In BR-D85A, it was possible to resolve stronger hydrogen bonding in all-*trans* compared to 13-*cis* retinal. The all-*trans* isomer was associated with higher frequency of the C=N band (1630 cm^{-1}) compared to 13-*cis* (1616 cm^{-1}). Additionally, upon deuteriation, all-*trans* isomer showed a stronger downshift (14 cm^{-1}) compared to 13-*cis* isomer (6 cm^{-1}). But, only single C=N band at ~1650 cm^{-1} is observed in QuasArs (Figure 25) and Archon1 (Figure S14).

The constructs with D95Q mutation (Archon1, QuasAr2) consequently have also higher contribution of 13-*cis* retinal compared to ones with D95H mutation (Archon2, QuasAr1[3,8]) (Figure 24, Figure 25, Figure S14, Figure S15 A). Correspondingly, the constructs with D95Q mutations also showed higher voltage sensitivity. From the previous reports[117,242] it could be suggested that 13-*cis* retinal isomer shows stronger voltage sensitivity due to higher probability of proton transfer between RSB and D222. This could also aid explaining excitation wavelength dependent voltage sensitivity (Figure S16). If excitation of the population with 13-*cis* is increased, the higher voltage response is observed. However, further studies should be carried out in QuasArs.

Further elucidation of isomer specific voltage sensitivity is hindered by strong

spectral overlap between the two isomers. And retinal isomer composition dependent C=N stretching frequency was not observed (Figure 25). Furthermore, *E. coli* cell assay recordings of pre-resonance Raman spectra of Archon1 showed more voltage sensitive contribution of all-*trans* retinal isomer compared to 13-*cis* (Figure 31 B).

Additional experimental evidence on proposed voltage controlled equilibrium of RSB/RSBH$^+$ is presented in work by Abdelfattah et al. 2020[267]. Microbial rhodopsin based fluorescent voltage sensors benefit from fast response and high voltage sensitivity, however they have low fluorescence QY ($\leq 1\%$). This has initiated development of eFRET pairs, such as Voltron[160]. Voltron comprises rhodopsin (Ace2-D81N) as a voltage sensing domain and a HaloTag-linked fluorescent molecule. Upon depolarization, fluorescence decreases, suggesting that upon depolarization the rhodopsin absorption increases and quenches the fluorescence. This would suggest similar process taking place as in QuasArs, but opposite outcome of the fluorescence intensity due to FRET. Ace2 rhodopsin with a single analogous counterion mutation D81N showed transient inward photocurrent, suggesting RSB proton exchange with intracellular side (D92 – proton donor). Ace2 rhodopsin with a single proton donor D92N mutation showed transient outward photocurrent, suggesting RSB proton exchange with extracellular side. In fact, the Ace2-D92N variant showed reversed - positively sloped fluorescence voltage relationship. The transfer of the mutations (Q95D-H106N) into QuasAr3[267] (QuasAr2 with additional mutation K171R, Table S1, Nr. 34, Nr. 37) showed also inverted voltage sensitivity. The performance was further enhanced with additional mutation at the proton release complex E214V[267].

The reported observations of RSB protonation role in the fluorescence intensity, supports also similar mechanism could take place in QuasArs. In case of QuasArs, the negatively charged proton acceptor (D95Q/H) and proton donor (D106H), are removed. The most likely proton exchange would take place between the RSB and D222. However, it cannot be excluded that water molecules, in the proximity of the RSB, could take place in proton exchange (yet MD simulations showed no water present in the RSB sproximity, Figure S26 D). Moreover, transfer of single mutations Q95D and E204V or E214V resulted in abolition of Archon1 expression, suggesting the retinal binding pocket and its surrounding hydrogen bond network is altered between the different constructs.

The second mechanism that can be proposed for voltage modulated population of fluorescent species is static quenching. In the cell assay, the mean fluorescence lifetime did not change between the negative (–140 mV) and ~ 0 mV membrane voltage, despite the 1.3-fold increase in fluorescence intensity (Figure 29). Similar observations, as in *E. coli* assay, could be reproduced for Archon1, Archon1-T100S and Archon1-D125N reconstituted in lipid vesicles (Figure S28 A-D). Also in this experiment the voltage dependent increase in fluorescence intensity did not result in increased mean fluorescence lifetime. These observations could be explained with static quenching: at negative voltage, fluorescence is quenched, whereas it is released upon membrane depolarization. Static quenching takes place already in the dark state when the fluorescent molecule collides with a quencher molecule. The formation of the non-radiative complex results in abolishment of the fluorescence and does not affect the fluorescence kinetics[197].

It has been shown previously that tryptophans can form, in the ground state, a non-fluorescent complexes with an organic dyes[197,268]. Static quenching could be also observed in all-*trans* retinal/BSA and tryptophan assay (Figure S28 E). The Stern-Volmer plot displays decrease in fluorescence intensity of all-*trans* retinal (increase in F_0/F) upon increase in tryptophan concentration, whereas the fluorescence lifetime remains unaffected ($\tau_0/\tau - const$). Two tryptophans (W96 and W192) are located in the proximity of the chromophore (Figure S29), which may serve as static quenchers via electron transfer. Moreover, the MD simulations of Archon1 and Archon1-D125 showed that W196 orientation is important for voltage sensing (Figure S27 E, F).

However, the fluorescence quenching of Archon1 bound chromophore via tryptophans is unlikely considering the following observations. First, the MD simulations did not show voltage depedent distance changes between chromophore and the two tryptophans (Figure S29 D, E). Also there was no correlation between the distance distribution and resulting fluorescence QY (Figure S29 C-E). Also in recently reported highly fluorescent (QY~20%) rhodopsin NeoR, the two tryptophans are conserved (W137 and W234)[230], suggesting fluorescence quenching does not take place.

Interestingly, the studies of tryptophan mutations in BR (BR-W86F, BR-W182F) preserved functional protein and confirmed the dipole-dipole interaction between

the chromophore and the two tryptophans[52,269]. The recorded ultrafast absorption spectra displayed that the charge redistribution in the chromophore upon excitation, results in a Stark shift of the tryptophan absorption band[52,269]. But no electron transfer was reported. This is in agreement with work by Kovacs et al. 2019[270], which reported the charge transfer (CT) state of retinal chromophore to lay above the excited state (0.3 eV).

However, we cannot exclude possible effects of counterion mutation D95Q and voltage on the excited state and the CT state, which should be investigated using QM/MM simulations.

4. 5. Conclusions

In this work three questions have been studied: how the fluorescence arises in Arch3-based sensors; how the membrane voltage generates change in fluorescence intensity and whether it is possible to improve the properties of the currently available voltage sensors.

QuasArs in the dark state comprise 13-*trans*/15-*anti* and 13-*cis*/15-*syn* retinal isomers. Both isomers show fluorescence, increased excited state lifetime and inefficient photoisomerization. The high fluorescence QY originates from the slow decaying stimulated emission. The increase in energy barrier of the excited state S_1 is likely the cause for the extended lifetime of the excited state and decrease in the isomerisation yield.

The counterion mutation D95X, and resulting elimination of the negative charge, is crucial to increase the fluorescence QY. Furthermore, the active site residue D95Q interaction with $RSBH^+$, is also important for the voltage sensing.

It has been shown in Arch3, the flipping of R92 results in voltage dependent hydrogen bond (HB1, D95-T99). Although in Archon1, the voltage sensitive flipping was observed for D125, the voltage dependent hydrogen bond (HB1, Q95-T99) was conserved. Under positive voltage, D125 flips towards the intracellular side, breaking the HB3 (T100-D125) and forming HB2 (T100-W96), which then allows the formation of the key hydrogen bond HB1 (T99-Q95). Moreover, the higher probability of formation of HB1, the higher voltage sensitivity of the construct observed. The MD simulations and experimental studies allowed to identify and confirm the key residues involved in the voltage sensing – Q95, T99, T100, D125 and

D222. The changes in the hydrogen bonding network correlated with increased fluorescence intensity, however no changes in fluorescence kinetics or retinal isomer composition was observed. The experimental observations suggest voltage modulated population of fluorescent species, where the equilibrium between RSB/ $RSBH^+$ is the most likely.

Within this study we have shown that fluorescence QY of current sensors can be improved with mutations introduced at the counterion position (Archon1-Q95H and Archon1-Q95E-T99C) and the retinal binding pocket (Archon1-A225C, Archon1-G132S). Additionally, we have shown that voltage sensitivity can also be further improved, as shown in variants Archon1-T100S and Archon1-D125N.

4. 6. Outlook

For a better understanding of the system, it would be important to gain structural information of QuasArs. Resolved 3D structure of the protein could provide detailed information of the conformational changes of the apoprotein triggered by the mutations. This could allow to identify the similarity to proposed O-like and Q-like states. Furthermore, this would provide information of the retinal chromophore and its binding pocket, indicating the hydrogen bonding network. This would also allow to perform MD and QM/MM simulations with higher precision.

The developed variants Archon1-T100S, Archon1-D125N are interesting for possible applications in neuroscience research. These variants offered increased fluorescence (1.2 -1.4 fold) and increased voltage sensitivity (1.2 - 1.65-fold). These properties are in high demand to improve the current systems. Besides also Archon1-Q95E T99C show increased fluorescence 1.4-fold and ~20 nm red-shifted absorption. This would increase the overall signal in the setups currently actively used with 633/640 nm excitation of the voltage sensor. While this was beyond the scope of the current work, these tools show promising properties and should be further investigated in neuronal cell cultures and in transgenic animal systems.

Another intriguing future prospect could be to apply the findings of this research work in recently published neorhodopsin RGC3 (NeoR)[230]. NeoR found in fungus *Rhizoclosmatium globosum* has a far-red-shifted absorption maximum at 690 nm, with a shoulder at 640 nm, and a fluorescence QY of ~20%. However, the fluorescence is not voltage sensitive. Using the naturally found high fluorescence QY,

the voltage sensitivity may be introduced by transfer of the mutations to the retinal binding pocket. Transfer of the key residues found in Archon1 could lead to similar hydrogen bonding network and voltage sensing mechanism. As for example, the key hydrogen bond T100-D125 is not conserved in NeoR, where T99-T100 motive is replaced by D140-E141 and D125 is replaced by S166. By introducing a charged residue at position S166D one may allow voltage sensitive flipping of the side chain. Further mutations could be introduced to allow formation of the key hydrogen bonds E141T/C and L171G/S. Although the negatively charged residues (E136, D140, E262) in the $RSBH^+$ proximity are essential for the rigidity of the chromophore and the red shift of the NeoR absorption spectra, mutations at position E141 should be applicable. The E141C mutation has been presented in NeoR previously[230], where it did not affect the fluorescence QY, but further red-shifted absorption maximum to 697 nm. However, as discussed in the current work, even a single residue change in the retinal proximity can have large effect on the stability and hydrogen bonding network and properties of the construct. For further development and investigation of voltage sensors, it is crucial to maintain the collaboration between experimental studies and MD simulations.

5. Bibliography

1. McIsaac, R. S. *et al.* Directed evolution of a far-red fluorescent rhodopsin. *Proc. Natl. Acad. Sci. U. S. A.* **111**, 13034–13039 (2014).
2. Piatkevich, K. D. *et al.* A robotic multidimensional directed evolution approach applied to fluorescent voltage reporters article. *Nat. Chem. Biol.* **14**, 352–360 (2018).
3. Hochbaum, D. R. *et al.* All-optical electrophysiology in mammalian neurons using engineered microbial rhodopsins. *Nat. Methods* **11**, 825–833 (2014).
4. Mathes, T. Natural Resources for Optogenetic Tools. in *Optogenetics. Methods in Molecular Biology* (ed. Kianianmomeni, A.) 19–36 (Humana Press, 2016). doi:10.1007/978-1-4939-3512-3_2
5. Karl Deisseroth. Optogenetics: 10 years of microbial opsins in neuroscience. *Nat. Neurosci.* **18**, 1213–1225 (2015).
6. Kralj, J. M., Douglass, A. D., Hochbaum, D. R., Maclaurin, D. & Cohen, A. E. Optical recording of action potentials in mammalian neurons using a microbial rhodopsin. *Nat. Methods* **9**, 90–95 (2011).
7. Patterson, G. H., Knobel, S. M., Sharif, W. D., Kain, S. R. & Piston, D. W. Use of the green fluorescent protein and its mutants in quantitative fluorescence microscopy. *Biophys. J.* **73**, 2782–2790 (1997).
8. Piatkevich, K. D. *et al.* A robotic multidimensional directed evolution approach applied to fluorescent voltage reporters article. *Nat. Chem. Biol.* **14**, 352–360 (2018).
9. Jenkins, G. I. The UV-B Photoreceptor UVR8: From Structure to Physiology. *Plant Cell* **26**, 21–37 (2014).
10. Losi, A. & Gärtner, W. The Evolution of Flavin-Binding Photoreceptors: An Ancient Chromophore Serving Trendy Blue-Light Sensors. *Annu. Rev. Plant Biol.* **63**, 49–72 (2012).
11. Meyer, T. E. *et al.* The growing family of photoactive yellow proteins and their presumed functional roles. *Photochem. Photobiol. Sci.* **11**, 1495 (2012).
12. Ortiz-Guerrero, J. M., Polanco, M. C., Murillo, F. J., Padmanabhan, S. & Elias-Arnanz, M. Light-dependent gene regulation by a coenzyme B12-based photoreceptor. *Proc. Natl. Acad. Sci.* **108**, 7565–7570 (2011).
13. Hauser, F. E., van Hazel, I. & Chang, B. S. W. Spectral tuning in vertebrate short wavelength-sensitive 1 (SWS1) visual pigments: Can wavelength sensitivity be inferred from sequence data? *J. Exp. Zool. Part B Mol. Dev. Evol.* **322**, 529–539 (2014).
14. Thoen, H. H., How, M. J., Chiou, T.-H. & Marshall, J. A Different Form of Color Vision in Mantis Shrimp. *Science (80-.).* **343**, 411–413 (2014).
15. Rockwell, N. C. *et al.* Eukaryotic algal phytochromes span the visible spectrum. *Proc. Natl. Acad. Sci.* **111**, 3871–3876 (2014).
16. Spudich, J. L., Yang, C.-S., Jung, K.-H. & Spudich, E. N. Retinylidene Proteins: Structures and Functions from Archaea to Humans. *Annu. Rev. Cell Dev. Biol.* **16**, 365–392 (2000).
17. Ernst, O. P. *et al.* Microbial and animal rhodopsins: Structures, functions, and molecular mechanisms. *Chem. Rev.* **114**, 126–163 (2014).
18. Govorunova, E. G., Sineshchekov, O. A., Li, H. & Spudich, J. L. Microbial Rhodopsins: Diversity, Mechanisms, and Optogenetic Applications. *Annu. Rev. Biochem.* **86**, 845–872 (2017).
19. OESTERHELT, D. & STOECKENIUS, W. Rhodopsin-like Protein from the Purple Membrane of Halobacterium halobium. *Nat. New Biol.* **233**, 149–152 (1971).
20. Kolbe, M. Structure of the Light-Driven Chloride Pump Halorhodopsin at 1.8 Å Resolution. *Science (80-.).* **288**, 1390–1396

(2000).
21. Avelar, G. M. *et al.* A Rhodopsin-Guanylyl cyclase gene fusion functions in visual perception in a fungus. *Curr. Biol.* **24**, 1234–1240 (2014).
22. Tomioka, H., Takahashi, T., Kamo, N. & Kobatake, Y. Flash spectrophotometric identification of a fourth rhodopsin-like pigment in Halobacterium halobium. *Biochem. Biophys. Res. Commun.* **139**, 389–395 (1986).
23. Luck, M. *et al.* A photochromic histidine kinase rhodopsin (HKR1) that is bimodally switched by ultraviolet and blue light. *J. Biol. Chem.* **287**, 40083–40090 (2012).
24. Jung, K.-H., Trivedi, V. D. & Spudich, J. L. Demonstration of a sensory rhodopsin in eubacteria. *Mol. Microbiol.* **47**, 1513–1522 (2003).
25. Yoshida, K., Tsunoda, S. P., Brown, L. S. & Kandori, H. A unique choanoflagellate enzyme rhodopsin exhibits light-dependent cyclic nucleotide phosphodiesterase activity. *J. Biol. Chem.* **292**, 7531–7541 (2017).
26. Kato, H. E., Inoue, K., Kandori, H. & Nureki, O. The light-driven sodium ion pump: A new player in rhodopsin research. *BioEssays* **38**, 1274–1282 (2016).
27. Mukherjee, S., Hegemann, P. & Broser, M. Enzymerhodopsins: novel photoregulated catalysts for optogenetics. *Curr. Opin. Struct. Biol.* **57**, 118–126 (2019).
28. Schobert, B. & Lanyi, J. K. Halorhodopsin is a light-driven chloride pump. *J. Biol. Chem.* **257**, 10306–13 (1982).
29. Oesterhelt, D. & Stoeckenius, W. Functions of a New Photoreceptor Membrane. *Proc. Natl. Acad. Sci.* **70**, 2853–2857 (1973).
30. Matsuno-Yagi, A. & Mukohata, Y. Two possible roles of bacteriorhodopsin; a comparative study of strains of Halobacterium halobium differing in pigmentation. *Biochem. Biophys. Res. Commun.* **78**, 237–243 (1977).
31. Ihara, K. *et al.* Evolution of the Archaeal Rhodopsins: Evolution Rate Changes by Gene Duplication and Functional Differentiation. *J. Mol. Biol* **285**, 163–174 (1999).
32. Chow, B. Y. *et al.* High-performance genetically targetable optical neural silencing by light-driven proton pumps. *Nature* **463**, 98–102 (2010).
33. Inoue, K. *et al.* A light-driven sodium ion pump in marine bacteria. *Nat. Commun.* **4**, 1678 (2013).
34. Inoue, K. *et al.* A natural light-driven inward proton pump. *Nat. Commun.* **7**, 1–10 (2016).
35. Nagel, G. *et al.* Channelrhodopsin-2, a directly light-gated cation-selective membrane channel. *Proc. Natl. Acad. Sci.* **100**, 13940–13945 (2003).
36. Govorunova, E. G., Sineshchekov, O. A., Janz, R., Liu, X. & Spudich, J. L. Natural light-gated anion channels: A family of microbial rhodopsins for advanced optogenetics. *Science (80-.).* **349**, 647–650 (2015).
37. Stoeckenius, W. The rhodopsin-like pigments of halobacteria: light-energy and signal transducers in an archaebacterium. *Trends Biochem. Sci.* **10**, 483–486 (1985).
38. Spudich, J. L. Variations on a molecular switch: transport and sensory signalling by archaeal rhodopsins. *Mol. Microbiol.* **28**, 1051–1058 (1998).
39. Hoff, W. D., Jung, K. & Spudich, J. L. MOLECULAR MECHANISM OF PHOTOSIGNALING BY ARCHAEAL SENSORY RHODOPSINS. (1997).
40. Brunet, T. *et al.* Light-regulated collective contractility in a multicellular choanoflagellate. *Science (80-.).* **366**, 326–334 (2019).
41. Avelar, G. M. *et al.* A Rhodopsin-Guanylyl Cyclase Gene Fusion Functions in Visual Perception in a Fungus. *Curr. Biol.* **24**, 1234–1240 (2014).
42. Scheib, U. *et al.* The rhodopsin-guanylyl cyclase of the aquatic fungus Blastocladiella emersonii enables fast optical control of cGMP signaling. *Sci. Signal.* **8**, 1–8 (2015).
43. Henderson, R. & Unwin, P. N. T. Three-dimensional model of purple membrane obtained by electron microscopy. *Nature* **257**, 28–32 (1975).

44. Henderson, R. *et al.* Model for the structure of bacteriorhodopsin based on high-resolution electron cryo-microscopy. *J. Mol. Biol.* **213**, 899–929 (1990).
45. Lanyi, J. K. Proton transfers in the bacteriorhodopsin photocycle. *Biochim. Biophys. Acta - Bioenerg.* **1757**, 1012–1018 (2006).
46. Luecke, H. Proton Transfer Pathways in Bacteriorhodopsin at 2.3 Angstrom Resolution. *Science (80-.).* **280**, 1934–1937 (1998).
47. Smith, S. O., Myers, A. B. & Pardoen, J. A. Determination of retinal Schiff base configuration in bacteriorhodopsin. *Proc. Natl. Acad. Sci. U. S. A.* **81**, 2055–2059 (1984).
48. Nogly, P. *et al.* Retinal isomerization in bacteriorhodopsin captured by a femtosecond x-ray laser. *Science (80-.).* **361**, (2018).
49. Braiman, M. & Mathies, R. Resonance Raman evidence for an all-trans to 13-cis isomerization in the proton-pumping cycle of bacteriorhodopsin. *Biochemistry* **19**, 5421–5428 (1980).
50. Mathies, R. A., Lin, S. W., Ames, J. B. & Pollard, W. T. From Femtoseconds to Biology: Mechanism of Bacteriorhodopsin's Light-Driven Proton Pump. *Annu. Rev. Biophys. Biophys. Chem.* **20**, 491–518 (1991).
51. Rothschild, K. J. FTIR difference spectroscopy of bacteriorhodopsin: Toward a molecular model. *J. Bioenerg. Biomembr.* **24**, 147–167 (1992).
52. Schenkl, S., Van Mourik, F., Van Der Zwan, G., Haacke, S. & Chergui, M. Chemistry: Probing the ultrafast charge translocation of photoexcited retinal in bacteriorhodopsin. *Science (80-.).* **309**, 917–920 (2005).
53. Kobayashi, T., Saito, T. & Ohtani, H. Real-time spectroscopy of transition states in bacteriorhodopsin during retinal isomerization. *Nature* **414**, 531–534 (2001).
54. Herbst, J. Femtosecond Infrared Spectroscopy of Bacteriorhodopsin Chromophore Isomerization. *Science (80-.).* **297**, 822–825 (2002).
55. Atkinson, G. H., Brack, T. L., Blanchard, D. & Rumbles, G. Picosecond time-resolved resonance Raman spectroscopy of the initial trans to cis isomerization in the bacteriorhodopsin photocycle. *Chem. Phys.* **131**, 1–15 (1989).
56. McCamant, D. W., Kukura, P. & Mathies, R. A. Femtosecond Stimulated Raman Study of Excited-State Evolution in Bacteriorhodopsin. *J. Phys. Chem. B* **109**, 10449–10457 (2005).
57. Mathies, R., Brito Cruz, C., Pollard, W. & Shank, C. Direct observation of the femtosecond excited-state cis-trans isomerization in bacteriorhodopsin. *Science (80-.).* **240**, 777–779 (1988).
58. Hasson, K. C., Gai, F. & Anfinrud, P. A. The photoisomerization of retinal in bacteriorhodopsin: Experimental evidence for a three-state model. *Proc. Natl. Acad. Sci. U. S. A.* **93**, 15124–15129 (1996).
59. Sharkov, A. V., Pakulev, A. V., Chekalin, S. V. & Matveetz, Y. A. Primary events in bacteriorhodopsin probed by subpicosecond spectroscopy. *Biochim. Biophys. Acta - Bioenerg.* **808**, 94–102 (1985).
60. Hamm, P. *et al.* Femtosecond spectroscopy of the photoisomerisation of the protonated Schiff base of all-trans retinal. *Chem. Phys. Lett.* **263**, 613–621 (1996).
61. Ruhman, S., Hou, B., Friedman, N., Ottolenghi, M. & Sheves, M. Following Evolution of Bacteriorhodopsin in Its Reactive Excited State via Stimulated Emission Pumping. *J. Am. Chem. Soc.* **124**, 8854–8858 (2002).
62. Altoè, P., Cembran, A., Olivucci, M. & Garavelli, M. Aborted double bicycle-pedal isomerization with hydrogen bond breaking is the primary event of bacteriorhodopsin proton pumping. *Proc. Natl. Acad. Sci. U. S. A.* **107**, 20172–20177 (2010).
63. Gozem, S. *et al.* Excited-State Vibronic Dynamics of Bacteriorhodopsin from Two-Dimensional Electronic Photon Echo Spectroscopy and Multiconfigurational Quantum Chemistry. *J. Phys. Chem. Lett.* **11**, 3889–3896 (2020).

64. Zgrablić, G., Novello, A. M. & Parmigiani, F. Population Branching in the Conical Intersection of the Retinal Chromophore Revealed by Multipulse Ultrafast Optical Spectroscopy. *J. Am. Chem. Soc.* **134**, 955–961 (2012).
65. Yabushita, A. & Kobayashi, T. Primary Conformation Change in Bacteriorhodopsin on Photoexcitation. *Biophys. J.* **96**, 1447–1461 (2009).
66. Gai, F. Chemical Dynamics in Proteins: The Photoisomerization of Retinal in Bacteriorhodopsin. *Science (80-.).* **279**, 1886–1891 (1998).
67. Song, L., El-Sayed, M. A. & Lanyi, J. K. Protein catalysis of the retinal subpicosecond photoisomerization in the primary process of bacteriorhodopsin photosynthesis. *Science (80-.).* **261**, 891–894 (1993).
68. Tavan, P., Schulten, K., Gärtner, W. & Oesterhelt, D. Substituents at the C13 Position of Retinal and Their Influence on the Function of Bacteriorhodopsin. *Biophys. J.* **47**, 349–355 (1985).
69. Lanyi, J. K. Proton transfers in the bacteriorhodopsin photocycle. *Biochim. Biophys. Acta - Bioenerg.* **1757**, 1012–1018 (2006).
70. Heberle, J., Fitter, J., Sass, H. J. & Büldt, G. Bacteriorhodopsin: the functional details of a molecular machine are being resolved. *Biophys. Chem.* **85**, 229–248 (2000).
71. Brown, L. S., Bonet, L., Needleman, R. & Lanyi, J. K. Estimated acid dissociation constants of the Schiff base, Asp-85, and Arg-82 during the bacteriorhodopsin photocycle. *Biophys. J.* **65**, 124–130 (1993).
72. Birge, R. R. *et al.* Revised assignment of energy storage in the primary photochemical event in bacteriorhodopsin. *J. Am. Chem. Soc.* **113**, 4327–4328 (1991).
73. E, N. *et al.* A three-dimensional movie of structural changes in bacteriorhodopsin. *Science (80-.).* **354**, (2016).
74. Lanyi, J. K. & Schobert, B. Structural Changes in the L Photointermediate of Bacteriorhodopsin. *J. Mol. Biol.* **365**, 1379–1392 (2007).
75. Maeda, A., Sasaki, J., Pfefferlé, J.-M., Shichida, Y. & Yoshizawa, T. FOURIER TRANSFORM INFRARED SPECTRAL STUDIES ON THE SCHIFF BASE MODE OF ALL-trans BACTERIORHODOPSIN and ITS PHOTOINTERMEDIATES, K and L. *Photochem. Photobiol.* **54**, 911–921 (1991).
76. Gerwert, K., Souvignier, G. & Hess, B. Simultaneous monitoring of light-induced changes in protein side-group protonation, chromophore isomerization, and backbone motion of bacteriorhodopsin by time-resolved Fourier-transform infrared spectroscopy. *Proc. Natl. Acad. Sci.* **87**, 9774–9778 (1990).
77. Sheves, M., Albeck, A., Friedman, N. & Ottolenghi, M. Controlling the pKa of the bacteriorhodopsin Schiff base by use of artificial retinal analogues. *Proc. Natl. Acad. Sci.* **83**, 3262–3266 (1986).
78. Lewis, A., Spoonhower, J., Bogomolni, R. A., Lozier, R. H. & Stoeckenius, W. Tunable Laser Resonance Raman Spectroscopy of Bacteriorhodopsin. *Proc. Natl. Acad. Sci.* **71**, 4462–4466 (1974).
79. Doukas, A. G., Aton, B., Callender, R. H. & Ebrey, T. G. Resonance Raman Studies of Bovine Metarhodopsin I and Metarhodopsin II. *Biochemistry* **17**, 2430–2435 (1978).
80. Hessling, B., Herbst, J., Rammelsberg, R. & Gerwert, K. Fourier transform infrared double-flash experiments resolve bacteriorhodopsin's M1 to M2 transition. *Biophys. J.* **73**, 2071–2080 (1997).
81. Hu, J. G. *et al.* Early and Late M Intermediates in the Bacteriorhodopsin Photocycle: A Solid-State NMR Study †. *Biochemistry* **37**, 8088–8096 (1998).
82. Lanyi, J. K. & Schobert, B. Crystallographic Structure of the Retinal and the Protein after Deprotonation of the Schiff Base: The Switch in the Bacteriorhodopsin Photocycle. *J. Mol. Biol.* **321**, 727–737 (2002).

83. Nagel, G., Kelety, B., Möckel, B., Büldt, G. & Bamberg, E. Voltage Dependence of Proton Pumping by Bacteriorhodopsin Is Regulated by the Voltage-Sensitive Ratio of M1 to M2. *Biophys. J.* **74**, 403–412 (1998).
84. Sass, H. J. The tertiary structural changes in bacteriorhodopsin occur between M states: X-ray diffraction and Fourier transform infrared spectroscopy. *EMBO J.* **16**, 1484–1491 (1997).
85. Varo, G. & Lanyi, J. K. Kinetic and spectroscopic evidence for an irreversible step between deprotonation and reprotonation of the Schiff base in the bacteriorhodopsin photocycle. *Biochemistry* **30**, 5008–5015 (1991).
86. Bondar, A. N., Elstner, M., Suhai, S., Smith, J. C. & Fischer, S. Mechanism of primary proton transfer in bacteriorhodopsin. *Structure* **12**, 1281–1288 (2004).
87. Garczarek, F., Brown, L. S., Lanyi, J. K. & Gerwert, K. Proton binding within a membrane protein by a protonated water cluster. *Proc. Natl. Acad. Sci.* **102**, 3633–3638 (2005).
88. Luecke, H., Schobert, B., Richter, H. T., Cartailler, J. P. & Lanyi, J. K. Structural changes in bacteriorhodopsin during ion transport at 2 angstrom resolution. *Science (80-.).* **286**, 255–260 (1999).
89. Sass, H. J. *et al.* Structural alterations for proton translocation in the M state of wild-type bacteriorhodopsin. *Nature* **406**, 649–653 (2000).
90. Luecke, H. *et al.* Coupling photoisomerization of retinal to directional transport in bacteriorhodopsin11Edited by D. C. Rees. *J. Mol. Biol.* **300**, 1237–1255 (2000).
91. Gerwert, K., Hess, B., Soppa, J. & Oesterhelt, D. Role of aspartate-96 in proton translocation by bacteriorhodopsin. *Proc. Natl. Acad. Sci.* **86**, 4943–4947 (1989).
92. Schobert, B., Brown, L. S. & Lanyi, J. K. Crystallographic Structures of the M and N Intermediates of Bacteriorhodopsin: Assembly of a Hydrogen-bonded Chain of Water Molecules Between Asp-96 and the Retinal Schiff Base. *J. Mol. Biol.* **330**, 553–570 (2003).
93. Száraz, S., Oesterhelt, D. & Ormos, P. pH-induced structural changes in bacteriorhodopsin studied by Fourier transform infrared spectroscopy. *Biophys. J.* **67**, 1706–1712 (1994).
94. Zscherp, C., Schlesinger, R., Tittor, J., Oesterhelt, D. & Heberle, J. In situ determination of transient pKa changes of internal amino acids of bacteriorhodopsin by using time-resolved attenuated total reflection Fourier-transform infrared spectroscopy. *Proc. Natl. Acad. Sci.* **96**, 5498–5503 (1999).
95. Checover, S., Nachliel, E., Dencher, N. A. & Gutman, M. Mechanism of Proton Entry into the Cytoplasmic Section of the Proton-Conducting Channel of Bacteriorhodopsin †. *Biochemistry* **36**, 13919–13928 (1997).
96. Marantz, Y., Nachliel, E., Aagaard, A., Brzezinski, P. & Gutman, M. The proton collecting function of the inner surface of cytochrome c oxidase from Rhodobacter sphaeroides. *Proc. Natl. Acad. Sci.* **95**, 8590–8595 (1998).
97. Checover, S. *et al.* Dynamics of the Proton Transfer Reaction on the Cytoplasmic Surface of Bacteriorhodopsin †. *Biochemistry* **40**, 4281–4292 (2001).
98. Wang, T. *et al.* Deprotonation of D96 in Bacteriorhodopsin Opens the Proton Uptake Pathway. *Structure* **21**, 290–297 (2013).
99. Lozier, R. H., Bogomolni, R. A. & Stoeckenius, W. Bacteriorhodopsin: a light-driven proton pump in Halobacterium Halobium. *Biophys. J.* **15**, 955–962 (1975).
100. Ludmann, K., Gergely, C. & Váró, G. Kinetic and Thermodynamic Study of the Bacteriorhodopsin Photocycle over a Wide pH Range. *Biophys. J.* **75**, 3110–3119 (1998).
101. Zimanyi, L. *et al.* Pathways of proton release in the bacteriorhodopsin photocycle. *Biochemistry* **31**, 8535–8543 (1992).
102. Balashov, S. P. *et al.* The Proton Release Group of Bacteriorhodopsin Controls the Rate of the Final Step of Its Photocycle at Low pH †. *Biochemistry* **38**, 2026–2039 (1999).
103. Hasegawa, N., Jonotsuka, H., Miki, K. & Takeda, K. X-ray structure analysis of

bacteriorhodopsin at 1.3 Å resolution. *Sci. Rep.* **8**, 13123 (2018).
104. Govindjee, R., Becher, B. & Ebrey, T. G. The fluorescence from the chromophore of the purple membrane protein. *Biophys. J.* **22**, 67–77 (1978).
105. Lewis, A., Spoonhower, J. P. & Perreault, G. J. Observation of light emission from a rhodopsin. *Nature* **260**, 675–678 (1976).
106. Kouyama, T., Kinosita, K. & Ikegami, A. Excited-state dynamics of bacteriorhodopsin. *Biophys. J.* **47**, 43–54 (1985).
107. Kamiya, N. *et al.* Picosecond fluorescence spectroscopy of the purple membrane of Halobacterium halobium in alkaline suspension. *Chem. Phys. Lett.* **265**, 595–599 (1997).
108. Ohtani, H., Itoh, H. & Shinmura, T. Time-resolved fluorometry of purple membrane of Halobacterium halobium O640 and an O-like red-shifted intermediate Q. *FEBS Lett.* **305**, 6–8 (1992).
109. Ohtani, H., Tsukamoto, Y., Sakoda, Y. & Hamaguchi, H. o. Fluorescence spectra of bacteriorhodopsin and the intermediates O and Q at room temperature. *FEBS Lett.* **359**, 65–68 (1995).
110. Ohtani, H., Kaneko, M., Ishikawa, M., Kamiya, N. & Yamamoto, N. Picosecond-millisecond dual-time-base spectroscopy of fluorescent photointermediates formed in the purple membrane of Halobacterium halobium. *Chem. Phys. Lett.* **299**, 571–575 (1999).
111. Polland, H.-J. *et al.* Early Picosecond Events in the Photocycle of Bacteriorhodopsin. *Biophys. J.* **49**, 651–662 (1986).
112. Matveetz, Y. A., Chekalin, S. V. & Sharkov, A. V. Molecular dynamics of primary photoprocesses in bacteriorhodopsin: subpicosecond study of absorption and luminescence kinetics. *J. Opt. Soc. Am. B* **2**, 634 (1985).
113. Maeda, A., Iwasa, T. & Yoshizawa, T. Formation of 9-cis- and 11-cis-Retinal Pigments from Bacteriorhodopsin by Irradiating Purple Membrane in Acid. *Biochemistry* **19**, 3825–3831 (1980).
114. Popp, A., Wolperdinger, M., Hampp, N., Brüchle, C. & Oesterhelt, D. Photochemical conversion of the O-intermediate to 9-cis-retinal-containing products in bacteriorhodopsin films. *Biophys. J.* **65**, 1449–1459 (1993).
115. Clair, E. C. S., Ogren, J. I., Mamaev, S., Kralj, J. M. & Rothschild, K. J. Conformational changes in the archaerhodopsin-3 proton pump: Detection of conserved strongly hydrogen bonded water networks. *J. Biol. Phys.* **38**, 153–168 (2012).
116. Maclaurin, D., Venkatachalam, V., Lee, H. & Cohen, A. E. Mechanism of voltage-sensitive fluorescence in a microbial rhodopsin. *Proc. Natl. Acad. Sci. U. S. A.* **110**, 5939–5944 (2013).
117. Saint Clair, E. C. *et al.* Near-IR resonance Raman spectroscopy of archaerhodopsin 3: Effects of transmembrane potential. *J. Phys. Chem. B* **116**, 14592–14601 (2012).
118. Enami, N. *et al.* Crystal Structures of Archaerhodopsin-1 and -2: Common Structural Motif in Archaeal Light-driven Proton Pumps. *J. Mol. Biol.* **358**, 675–685 (2006).
119. Bada Juarez, J.F., Judge, P.J., Vinals, J., Axford, D., Birch, J., Aller, P., Butryn, A., Sherrell, D.A., Beale, J.H., Orville, A.M., Watts, A., Moraes, I. Structure of Archaerhodopsin-3 obtained from LCP crystals.
120. Deisseroth, K. Optogenetics: 10 years of microbial opsins in neuroscience. *Nat. Neurosci.* **18**, 1213–1225 (2015).
121. Kim, C. K., Adhikari, A. & Deisseroth, K. Integration of optogenetics with complementary methodologies in systems neuroscience. *Nat. Rev. Neurosci.* **18**, 222–235 (2017).
122. Deisseroth, K. Optogenetics. *Nat. Methods* **8**, 26–29 (2011).
123. Boyden, E. S., Zhang, F., Bamberg, E., Nagel, G. & Deisseroth, K. Millisecond-timescale, genetically targeted optical control of neural activity. *Nat. Neurosci.* **8**, 1263–1268 (2005).
124. Deisseroth, K. *et al.* Next-Generation Optical Technologies for Illuminating Genetically

Targeted Brain Circuits. *J. Neurosci.* **26**, 10380–10386 (2006).
125. Crick, F. H. C. Thinking about the Brain. *Sci. Am.* **241**, 219–232 (1979).
126. Crick, F. The impact of molecular biology on neuroscience. *Philos. Trans. R. Soc. London. Ser. B Biol. Sci.* **354**, 2021–2025 (1999).
127. Nagel, G. Channelrhodopsin-1: A Light-Gated Proton Channel in Green Algae. *Science (80-.).* **296**, 2395–2398 (2002).
128. Li, X. *et al.* Fast noninvasive activation and inhibition of neural and network activity by vertebrate rhodopsin and green algae channelrhodopsin. *Proc. Natl. Acad. Sci.* **102**, 17816–17821 (2005).
129. Ishizuka, T., Kakuda, M., Araki, R. & Yawo, H. Kinetic evaluation of photosensitivity in genetically engineered neurons expressing green algae light-gated channels. *Neurosci. Res.* **54**, 85–94 (2006).
130. Cho, Y. K. & Li, D. Optogenetics: Basic Concepts and Their Development. in *Optogenetics. Methods in Molecular Biology* (ed. A., K.) 1–17 (Humana Press, 2016). doi:10.1007/978-1-4939-3512-3_1
131. Gunaydin, L. A. *et al.* Ultrafast optogenetic control. *Nat. Neurosci.* **13**, 387–392 (2010).
132. Yizhar, O. *et al.* Neocortical excitation/inhibition balance in information processing and social dysfunction. *Nature* **477**, 171–178 (2011).
133. Grimm, C. *et al.* Electrical properties , substrate specificity and optogenetic potential of the engineered light- driven sodium pump eKR2. *Sci. Rep.* 1–12 (2018). doi:10.1038/s41598-018-27690-w
134. Vogt, A. *et al.* Engineered Passive Potassium Conductance in the KR2 Sodium Pump. *Biophys. J.* **116**, 1941–1951 (2019).
135. Yizhar, O., Fenno, L. E., Davidson, T. J., Mogri, M. & Deisseroth, K. Optogenetics in Neural Systems. *Neuron* **71**, 9–34 (2011).
136. Gradinaru, V. *et al.* Molecular and Cellular Approaches for Diversifying and Extending Optogenetics. *Cell* **141**, 154–165 (2010).
137. Gunaydin, L. A. *et al.* Natural Neural Projection Dynamics Underlying Social Behavior. *Cell* **157**, 1535–1551 (2014).
138. Fenno, L. E. *et al.* Targeting cells with single vectors using multiple-feature Boolean logic. *Nat. Methods* **11**, 763–772 (2014).
139. Aravanis, A. M. *et al.* An optical neural interface: in vivo control of rodent motor cortex with integrated fiberoptic and optogenetic technology. *J. Neural Eng.* **4**, S143–S156 (2007).
140. Prakash, R. *et al.* Two-photon optogenetic toolbox for fast inhibition, excitation and bistable modulation. *Nat. Methods* **9**, 1171–1179 (2012).
141. Lauterbach, M. A. *et al.* Superresolving dendritic spine morphology with STED microscopy under holographic photostimulation. *Neurophotonics* **3**, 041806 (2016).
142. Kiritani, T., Wickersham, I. R., Seung, H. S. & Shepherd, G. M. G. Hierarchical Connectivity and Connection-Specific Dynamics in the Corticospinal-Corticostriatal Microcircuit in Mouse Motor Cortex. *J. Neurosci.* **32**, 4992–5001 (2012).
143. Kim, S.-Y. *et al.* Diverging neural pathways assemble a behavioural state from separable features in anxiety. *Nature* **496**, 219–223 (2013).
144. Stuber, G. D. *et al.* Excitatory transmission from the amygdala to nucleus accumbens facilitates reward seeking. *Nature* **475**, 377–380 (2011).
145. McCombs, J. E. & Palmer, A. E. Measuring calcium dynamics in living cells with genetically encodable calcium indicators. *Methods* **46**, 152–159 (2008).
146. Tian, L. *et al.* Imaging neural activity in worms, flies and mice with improved GCaMP calcium indicators. *Nat. Methods* **6**, 875–881 (2009).
147. St-Pierre, F. *et al.* High-fidelity optical reporting of neuronal electrical activity with an

ultrafast fluorescent voltage sensor. *Nat. Neurosci.* **17**, 884–889 (2014).
148. Gong, Y. *et al.* High-speed recording of neural spikes in awake mice and flies with a fluorescent voltage sensor. *Science (80-.).* **350**, 1361–1366 (2015).
149. Yamamoto, K. *et al.* Chronic Optogenetic Activation Augments Aβ Pathology in a Mouse Model of Alzheimer Disease. *Cell Rep.* **11**, 859–865 (2015).
150. Bi, A. *et al.* Ectopic Expression of a Microbial-Type Rhodopsin Restores Visual Responses in Mice with Photoreceptor Degeneration. *Neuron* **50**, 23–33 (2006).
151. Sahel, J.-A. *et al.* Partial recovery of visual function in a blind patient after optogenetic therapy. *Nat. Med.* (2021). doi:10.1038/s41591-021-01351-4
152. Lodish, H. F. Nerve cells. in *Molecular cell biology* 1019–1059 (W.H. Freeman and Co., 2013).
153. Knöpfel, T. & Song, C. Optical voltage imaging in neurons: moving from technology development to practical tool. *Nat. Rev. Neurosci.* **20**, 719–727 (2019).
154. Siegel, M. S. & Isacoff, E. Y. A Genetically Encoded Optical Probe of Membrane Voltage. *Neuron* **19**, 735–741 (1997).
155. Dimitrov, D. *et al.* Engineering and Characterization of an Enhanced Fluorescent Protein Voltage Sensor. *PLoS One* **2**, e440 (2007).
156. Akemann, W., Mutoh, H., Perron, A., Rossier, J. & Knöpfel, T. Imaging brain electric signals with genetically targeted voltage-sensitive fluorescent proteins. *Nat. Methods* **7**, 643–649 (2010).
157. Kang, B. E., Lee, S. & Baker, B. J. Optical consequences of a genetically-encoded voltage indicator with a pH sensitive fluorescent protein. *Neurosci. Res.* **146**, 13–21 (2019).
158. Gautam, S. G. Exploration of fluorescent protein voltage probes based on circularly permuted fluorescent proteins. *Front. Neuroeng.* **2**, (2009).
159. Zou, P. *et al.* Bright and fast multicoloured voltage reporters via electrochromic FRET. *Nat. Commun.* **5**, 4625 (2014).
160. Abdelfattah, A. S. *et al.* Bright and photostable chemigenetic indicators for extended in vivo voltage imaging. *Science (80-.).* **365**, 699–704 (2019).
161. Tang, Q. *et al.* In Vivo Voltage-Sensitive Dye Imaging of Subcortical Brain Function. *Sci. Rep.* **5**, 17325 (2015).
162. Marshall, J. D. *et al.* Cell-Type-Specific Optical Recording of Membrane Voltage Dynamics in Freely Moving Mice. *Cell* **167**, 1650-1662.e15 (2016).
163. Meng, G. *et al.* High-throughput synapse-resolving two-photon fluorescence microendoscopy for deep-brain volumetric imaging in vivo. *Elife* **8**, (2019).
164. Werley, C. A. *et al.* All-Optical Electrophysiology for Disease Modeling and Pharmacological Characterization of Neurons. *Curr. Protoc. Pharmacol.* **78**, (2017).
165. Kralj, J. M., Hochbaum, D. R., Douglass, A. D. & Cohen, A. E. Electrical spiking in Escherichia coli probed with a fluorescent voltage-indicating protein. *Science* **333**, 345–8 (2011).
166. Tittor, J., Schweiger, U., Oesterhelt, D. & Bamberg, E. Inversion of proton translocation in bacteriorhodopsin mutants D85N, D85T, and D85,96N. *Biophys. J.* **67**, 1682–1690 (1994).
167. Kralj, J. M., Douglass, A. D., Hochbaum, D. R., Maclaurin, D. & Cohen, A. E. Optical recording of action potentials in mammalian neurons using a microbial rhodopsin. *Nat Methods* **9**, 90–95 (2012).
168. Grimm, C. Electrophysiological characterization of the microbial rhodopsins ReaChR and KR2 and their optogenetic potential. 102 (2018).
169. Rajasethupathy, P. *et al.* Projections from neocortex mediate top-down control of memory retrieval. *Nature* **526**, 653–659 (2015).
170. Gradinaru, V., Thompson, K. R. & Deisseroth, K. eNpHR: a Natronomonas halorhodopsin enhanced for optogenetic applications. *Brain Cell Biol.* **36**, 129–139 (2008).
171. Mullis, K. B. & Faloona, F. A. [21] Specific synthesis of DNA in vitro via a polymerase-

catalyzed chain reaction. in 335–350 (1987). doi:10.1016/0076-6879(87)55023-6
172. Slater, G. W. & Noolandi, J. The biased reptation model of DNA gel electrophoresis: Mobility vs molecular size and gel concentration. *Biopolymers* **28**, 1781–1791 (1989).
173. Stellwagen, N. C. Electrophoresis of DNA in agarose gels, polyacrylamide gels and in free solution. *Electrophoresis* **30**, S188–S195 (2009).
174. Wood, E. Molecular Cloning. A Laboratory Manual. *Biochem. Educ.* **11**, 82 (1983).
175. Gibson, D. G. *et al.* Enzymatic assembly of DNA molecules up to several hundred kilobases. *Nat. Methods* **6**, 343–345 (2009).
176. Novel cell lines display properties of nociceptive sensory neurons. *Proc. R. Soc. London. Ser. B Biol. Sci.* **241**, 187–194 (1990).
177. Hontani, Y. *Photoreaction dynamics of functional photoreceptor proteins*. *Dissertation* (2018).
178. Berera, R., van Grondelle, R. & Kennis, J. T. M. Ultrafast transient absorption spectroscopy: Principles and application to photosynthetic systems. *Photosynth. Res.* **101**, 105–118 (2009).
179. Ravensbergen, J. *et al.* Unraveling the Carrier Dynamics of BiVO 4 : A Femtosecond to Microsecond Transient Absorption Study. *J. Phys. Chem. C* **118**, 27793–27800 (2014).
180. Hontani, Y. *et al.* The femtosecond-to-second photochemistry of red-shifted fast-closing anion channelrhodopsin PsACR1. *Phys. Chem. Chem. Phys.* **19**, (2017).
181. Hontani, Y. *et al.* Reaction dynamics of the chimeric channelrhodopsin C1C2. *Sci. Rep.* **7**, 7217 (2017).
182. Alexandre, M. T. A. *et al.* Primary reactions of the LOV2 domain of phototropin studied with ultrafast mid-infrared spectroscopy and quantum chemistry. *Biophys. J.* **97**, 227–237 (2009).
183. Snellenburg, J. J., Laptenok, S., Seger, R., Mullen, K. M. & van Stokkum, I. H. M. Glotaran: A Java-based graphical user interface for the R package TIMP. *J. Stat. Softw.* **49**, 1–22 (2012).
184. Van Stokkum, I. H. M., Larsen, D. S. & Van Grondelle, R. Global and target analysis of time-resolved spectra. *Biochim. Biophys. Acta - Bioenerg.* **1657**, 82–104 (2004).
185. Kennis, J. T. & Groot, M.-L. Ultrafast spectroscopy of biological photoreceptors. *Curr. Opin. Struct. Biol.* **17**, 623–630 (2007).
186. Hontani, Y. *et al.* Strong pH-Dependent Near-Infrared Fluorescence in a Microbial Rhodopsin Reconstituted with a Red-Shifting Retinal Analogue. *J. Phys. Chem. Lett.* **9**, 6469–6474 (2018).
187. Rurack, K. & Spieles, M. Fluorescence quantum yields of a series of red and near-infrared dyes emitting at 600-1000 nm. *Anal. Chem.* **83**, 1232–1242 (2011).
188. Velázquez Escobar, F. J. Vibrational spectroscopy of phytochromes and phytochrome-related photoreceptors. *Dissertation* 1–365 (2015). doi:10.14279/depositonce-4431
189. Felle, H., Porter, J. S., Slayman, C. L. & Kaback, H. R. Quantitative measurements of membrane potential in Escherichia coli. *Biochemistry* **19**, 3585–3590 (1980).
190. Buhrke, D. Spectroscopic investigation of phytochromes and NIR fluorescent variants. (2019).
191. Gacek, D. A., Moore, A. L., Moore, T. A. & Walla, P. J. Two-Photon Spectra of Chlorophylls and Carotenoid–Tetrapyrrole Dyads. *J. Phys. Chem. B* **121**, 10055–10063 (2017).
192. Balke, J. *et al.* Visualizing Oxidative Cellular Stress Induced by Nanoparticles in the Subcytotoxic Range Using Fluorescence Lifetime Imaging. *Small* **14**, 1–11 (2018).
193. Volz, P. *et al.* White-Light Supercontinuum Laser-Based Multiple Wavelength Excitation for TCSPC-FLIM of Cutaneous Nanocarrier Uptake. *Zeitschrift für Phys. Chemie* **232**, 671–688 (2018).
194. Winkel, J. D., Gray, D. A., Seistrup, K. H., Hamoen, L. W. & Denham, E. Analysis of Antimicrobial-Triggered Membrane Depolarization Using Voltage Sensitive Dyes. **4**, 1–10

(2016).
195. Volz, P. *et al.* Pitfalls in using fluorescence tagging of nanomaterials: tecto-dendrimers in skin tissue as investigated by Cluster-FLIM. *Ann. N. Y. Acad. Sci.* **1405**, 202–214 (2017).
196. Brodwolf, R. *et al.* Faster, sharper, more precise: Automated Cluster-FLIM in preclinical testing directly identifies the intracellular fate of theranostics in live cells and tissue. *Theranostics* **10**, 6322–6336 (2020).
197. Alexiev, U. & Farrens, D. L. Fluorescence spectroscopy of rhodopsins: Insights and approaches. *Biochim. Biophys. Acta - Bioenerg.* **1837**, 694–709 (2014).
198. Kim, T.-Y., Winkler, K. & Alexiev, U. Picosecond Multidimensional Fluorescence Spectroscopy: A Tool to Measure Real-time Protein Dynamics During Function†. *Photochem. Photobiol.* **83**, 378–385 (2007).
199. Krause, B. S. *et al.* Complex Photochemistry within the Green-Absorbing Channelrhodopsin ReaChR. *Biophys. J.* **112**, 1166–1175 (2017).
200. Hess, B., Kutzner, C., van der Spoel, D. & Lindahl, E. GROMACS 4: Algorithms for Highly Efficient, Load-Balanced, and Scalable Molecular Simulation. *J. Chem. Theory Comput.* **4**, 435–447 (2008).
201. Hornak, V. *et al.* Comparison of multiple Amber force fields and development of improved protein backbone parameters. *Proteins Struct. Funct. Bioinforma.* **65**, 712–725 (2006).
202. Hayashi, S., Tajkhorshid, E. & Schulten, K. Structural Changes during the Formation of Early Intermediates in the Bacteriorhodopsin Photocycle. *Biophys. J.* **83**, 1281–1297 (2002).
203. Malmerberg, E. *et al.* Time-Resolved WAXS Reveals Accelerated Conformational Changes in Iodoretinal-Substituted Proteorhodopsin. *Biophys. J.* **101**, 1345–1353 (2011).
204. Eswar, N. *et al.* Comparative Protein Structure Modeling Using Modeller. *Curr. Protoc. Bioinforma.* **15**, (2006).
205. Kouyama, T. *et al.* Structure of archaerhodopsin-2 at 1.8Å resolution. *Acta Crystallogr. Sect. D Biol. Crystallogr.* **70**, 2692–2701 (2014).
206. Berendsen, H. J. C., Grigera, J. R. & Straatsma, T. P. The missing term in effective pair potentials. *J. Phys. Chem.* **91**, 6269–6271 (1987).
207. Hwang, S. Structures and Dynamics of Supramolecular Assemblies AND Voltage Sensitivities of Archaerhodopsin and Its Variants. (Humboldt-Universität zu Berlin, 2021).
208. Berk Hess , Henk Bekker , Herman J.C. Berendsen, J. G. E. M. F. LINCS: A linear constraint solver for molecular simulations. *J. Comput. Chem* **18**, 1463–1472 (1997).
209. Michaud-Agrawal, N., Denning, E. J., Woolf, T. B. & Beckstein, O. MDAnalysis: A toolkit for the analysis of molecular dynamics simulations. *J. Comput. Chem.* **32**, 2319–2327 (2011).
210. Olsson, M. H. M., Søndergaard, C. R., Rostkowski, M. & Jensen, J. H. PROPKA3: Consistent Treatment of Internal and Surface Residues in Empirical p K a Predictions. *J. Chem. Theory Comput.* **7**, 525–537 (2011).
211. Hunter, J. D. Matplotlib: A 2D Graphics Environment. *Comput. Sci. Eng.* **9**, 90–95 (2007).
212. Penzkofer, A., Silapetere, A. & Hegemann, P. Photocycle dynamics of the archaerhodopsin 3 based fluorescent voltage sensor QuasAr1. *Int. J. Mol. Sci.* **21**, (2020).
213. Penzkofer, A., Silapetere, A. & Hegemann, P. Absorption and emission spectroscopic investigation of the thermal dynamics of the archaerhodopsin 3 based fluorescent voltage sensor quasar1. *Int. J. Mol. Sci.* **20**, (2019).
214. Nuss, M. C., Zinth, W., Kaiser, W., Kólling, E., Oesterhelt, D. Femtosecond Spectroscopy of the First Events of the Photochemical Cycle in Bacteriorhodopsin. *Chem. Phys. Lett.* **117**, 1–7 (1985).
215. Hontani, Y. *et al.* Dual Photoisomerization on Distinct Potential Energy Surfaces in a UV-Absorbing Rhodopsin. *J. Am. Chem. Soc.* **142**, 11464–11473 (2020).
216. Birge, R. R. Two-Photon Spectroscopy of Protein-Bound Chromophores. *Acc. Chem. Res.*

19, 138–146 (1986).
217. Mostany, R., Miquelajauregui, A., Shtrahman, M. & Portera-Cailliau, C. Two-Photon Excitation Microscopy and Its Applications in Neuroscience. in 25–42 (2015). doi:10.1007/978-1-4939-2080-8_2
218. Kochendoerfer, G. G., Lin, S. W., Sakmar, T. P. & Mathies, R. A. How color visual pigments are tuned. *Trends Biochem. Sci.* **24**, 300–305 (1999).
219. B. Curry, I. Palings, A.D. Broek, J.A. Pardoen, J. Lugtenburg, R. M. Chapter 3 Vibrational analysis of the retinal isomers, in: Advances in Infrared and Raman Spectroscopy. **12**, 115–178 (1985).
220. Smith, S. O. *et al.* Vibrational Analysis of the all-trans-Retinal Chromophore in Light-Adapted Bacteriorhodopsin. *J. Am. Chem. Soc.* **109**, 3108–3125 (1987).
221. Smith, S. O., Pardoen, J. A., Lugtenburg, J. & Mathies, R. A. Vibrational Analysis of the 13-c / s-Retinal Chromophore in Dark-Adapted Bacteriorhodopsin. 804–819 (1987). doi:10.1021/j100288a011
222. Rath, P., Krebs, M. P., He, Y., Khorana, H. G. & Rothschild, K. J. Fourier Transform Raman Spectroscopy of the Bacteriorhodopsin Mutant Tyr-185→Phe: Formation of a Stable O-like Species during Light Adaptation and Detection of Its Transient N-like Photoproduct. *Biochemistry* **32**, 2272–2281 (1993).
223. Curry, B., Broek, A., Lugtenburg, J. & Mathies, R. Vibrational Analysis of all-trans-Retinal. 5274–5286 (1982).
224. Smith, S. O. *et al.* Vibrational analysis of the all-trans retinal protonated Schiff base. *Biophys. J.* **47**, 653–664 (1985).
225. Aton, B., Doukas, A. G., Callender, R. H., Becher, B. & Ebrey, T. G. Resonance Raman Studies of the Purple Membrane. *Biochemistry* **16**, 2995–2999 (1977).
226. Fodor, S. P. A., Gebhard, R., Lugtenburg, J., Bogomolni, R. A. & Mathies, R. A. Structure of the retinal chromophore in sensory rhodopsin I from resonance Raman spectroscopy. *J. Biol. Chem.* **264**, 18280–18283 (1989).
227. Clemens, M., Phatak, P., Cui, Q., Bondar, A. N. & Elstner, M. Role of Arg82 in the early steps of the bacteriorhodopsin proton-pumping cycle. *J. Phys. Chem. B* **115**, 7129–7135 (2011).
228. Fudim, R. *et al.* Design of a light-gated proton channel based on the crystal structure of Coccomyxa rhodopsin. *Sci. Signal.* **12**, eaav4203 (2019).
229. Maclaurin, D., Venkatachalam, V., Lee, H. & Cohen, A. E. Mechanism of voltage-sensitive fluorescence in a microbial rhodopsin. *Proc. Natl. Acad. Sci.* **110**, 5939–5944 (2013).
230. Broser, M. *et al.* NeoR, a near-infrared absorbing rhodopsin. *Nat. Commun.* **11**, 2–11 (2020).
231. Mei, G. *et al.* Optical Switching Between Long-lived States of Opsin Transmembrane Voltage Sensors. *Photochem. Photobiol.* 0–2 (2021). doi:10.1111/php.13428
232. Brinks*, D. *et al.* Two-photon photoactivated voltage imaging in tissue with an Archaerhodopsin-derived reporter. *Submitted* 1–33 (2017). doi:10.1101/211946
233. Penzkofer, A., Silapetere, A. & Hegemann, P. Photocycle dynamics of the archaerhodopsin 3 based fluorescent voltage sensor QuasAr1. *Int. J. Mol. Sci.* **21**, (2020).
234. Penzkofer, A., Silapetere, A., Hegemann, P. Photocycle Dynamics of the Archaerhodopsin 3 Based Fluorescent Voltage Sensor Archon2. *Int. J. Mol. Sci.* **To be publ**, (2021).
235. Penzkofer, A., Silapetere, A. & Hegemann, P. Absorption and emission spectroscopic investigation of the thermal dynamics of the archaerhodopsin 3 based fluorescent voltage sensor archon2. *Int. J. Mol. Sci.* **21**, 1–19 (2020).
236. Tittor, J. & Oesterhelt, D. The quantum yield of bacteriorhodopsin. *FEBS Lett.* **263**, 269–273 (1990).
237. Marín, M. D. C. *et al.* Fluorescence Enhancement of a Microbial Rhodopsin via Electronic Reprogramming. *J. Am. Chem. Soc.* **141**, 262–271 (2019).

238. Birge, R. R. & Zhang, C. F. Two-photon double resonance spectroscopy of bacteriorhodopsin. Assignment of the electronic and dipolar properties of the low-lying 1A g*--like and 1Bu* +-like π, π* states. *J. Chem. Phys.* **92**, 7178–7195 (1990).
239. Ohtani, H., Tsukamoto, Y., Sakoda, Y. & Hamaguchi, H. Fluorescence spectra of bacteriorhodopsin and the intermediates O and Q at room temperature. *FEBS Lett.* **359**, 65–68 (1995).
240. Mei, G. *et al.* Analog Retinal Redshifts Visible Absorption of QuasAr Transmembrane Voltage Sensors into Near-infrared. *Photochem. Photobiol.* **96**, 55–66 (2020).
241. Turner, G. J. *et al.* Bacteriorhodopsin D85N: Three Spectroscopic Species in Equilibrium. *Biochemistry* **32**, 1332–1337 (1993).
242. Rath, P., Marti, T., Sonar, S., Khorana, H. G. & Rothschild, K. J. Hydrogen bonding interactions with the Schiff base of bacteriorhodopsin. Resonance Raman spectroscopy of the mutants D85N and D85A. *J. Biol. Chem.* **268**, 17742–17749 (1993).
243. Otto, H. *et al.* Substitution of amino acids Asp-85, Asp-212, and Arg-82 in bacteriorhodopsin affects the proton release phase of the pump and the pK of the Schiff base. *Proc. Natl. Acad. Sci. U. S. A.* **87**, 1018–1022 (1990).
244. Kolodner, P., Lukashev, E. P., Ching, Y. C. & Rousseau, D. L. Electric-field-induced Schiff-base deprotonation in D85N mutant bacteriorhodopsin. *Proc. Natl. Acad. Sci. U. S. A.* **93**, 11618–11621 (1996).
245. Smith, S. O., Lugtenburg, J. & Mathies, R. A. Determination of retinal chromophore structure in bacteriorhodopsin with resonance Raman spectroscopy. *J. Membr. Biol.* **85**, 95–109 (1985).
246. Smith, S. O. *et al.* Chromophore Structure in Bacteriorhodopsin's O640 Photointermediate. *Biochemistry* **22**, 6141–6148 (1983).
247. Brown, L. S. *et al.* A local electrostatic change is the cause of the large-scale protein conformation shift in bacteriorhodopsin. *Proc. Natl. Acad. Sci. U. S. A.* **94**, 5040–5044 (1997).
248. Lindahl, M. & Henderson, R. Structure of the bacteriorhodopsin D85N/D96N double mutant showing substantial structural changes and a highly twinned, disordered lattice. *Ultramicroscopy* **70**, 95–106 (1997).
249. Okumura, H., Murakami, M. & Kouyama, T. Crystal structures of acid blue and alkaline purple forms of bacteriorhodopsin. *J. Mol. Biol.* **351**, 481–495 (2005).
250. Luck, M. & Hegemann, P. The two parallel photocycles of the Chlamydomonas sensory photoreceptor histidine kinase rhodopsin 1. *J. Plant Physiol.* **217**, 77–84 (2017).
251. Katayama, K., Sekharan, S. & Sudo, Y. Color Tuning in Retinylidene Proteins. in *Optogenetics* 89–107 (Springer Japan, 2015). doi:10.1007/978-4-431-55516-2_7
252. Ohtani, H., Kobayashi, T., Iwai, J. I. & Ikegami, A. Picosecond and Nanosecond Spectroscopies of the Photochemical Cycles of Acidified Bacteriorhodopsin. *Biochemistry* **25**, 3356–3363 (1986).
253. Smith, S. O. & Mathies, R. A. Resonance Raman spectra of the acidified and deionized forms of bacteriorhodopsin. *Biophys. J.* **47**, 251–254 (1985).
254. Subramaniam, S., Marti, T. & Khorana, H. G. Protonation state of Asp (Glu)-85 regulates the purple-to-blue transition in bacteriorhodopsin mutants Arg-82----Ala and Asp-85----Glu: the blue form is inactive in proton translocation. *Proc. Natl. Acad. Sci.* **87**, 1013–1017 (1990).
255. Perálvarez-Marín, A., Bourdelande, J. L., Querol, E. & Padrós, E. The role of proline residues in the dynamics of transmembrane helices: The case of bacteriorhodopsin. *Mol. Membr. Biol.* **23**, 127–135 (2006).
256. Mogi, T., Stern, L. J., Chao, B. H. & Khorana, H. G. Structure-function studies on bacteriorhodopsin. VIII. Substitutions of the membrane-embedded prolines 50, 91, and

186: the effects are determined by the substituting amino acids. *J. Biol. Chem.* **264**, 14192–14196 (1989).
257. Gillbro, T. & Sundström, V. PICOSECOND KINETICS and A MODEL FOR THE PRIMARY EVENTS OF BACTERIORHODOPSIN. *Photochem. Photobiol.* **37**, 445–455 (1983).
258. Kato, H. E. *et al.* Atomistic design of microbial opsin-based blue-shifted optogenetics tools. *Nat. Commun.* **6**, (2015).
259. Sudo, Y. *et al.* A blue-shifted light-driven proton pump for neural silencing. *J. Biol. Chem.* **288**, 20624–20632 (2013).
260. Helmchen, F. *Two-Photon Functional Imaging of Neuronal Activity*. *In Vivo Optical Imaging of Brain Function* (2009).
261. Hutson, M. S., Alexiev, U., Shilov, S. V, Wise, K. J. & Braiman, M. S. Evidence for a Perturbation of Arginine-82 in the Bacteriorhodopsin Photocycle from Time-Resolved Infrared Spectra †. **5**, 13189–13200 (2000).
262. Del Val, C., Bondar, L. & Bondar, A. N. Coupling between inter-helical hydrogen bonding and water dynamics in a proton transporter. *J. Struct. Biol.* **186**, 95–111 (2014).
263. Bruun, S. *et al.* The chromophore structure of the long-lived intermediate of the C128T channelrhodopsin-2 variant. *FEBS Lett.* **585**, 3998–4001 (2011).
264. Balashov, S. P. *et al.* The Two PKa‘s of Aspartate-85 and Control of Thermal Isomerization and Proton Release in the Arginine-82 to Lysine Mutant of Bacteriorhodopsin. *Biochemistry* **34**, 8820–8834 (1995).
265. Subramaniam, S., Greenhalgh, D. A. & Khorana, H. G. Aspartic acid 85 in bacteriorhodopsin functions both as proton acceptor and negative counterion to the Schiff base. *J. Biol. Chem.* **267**, 25730–25733 (1992).
266. Fischer, U. C., Towner, P. & Oesterhelt, D. LIGHT INDUCED ISOMERISATION, AT ACIDIC pH, INITIATES HYDROLYSIS OF BACTERIORHODOPSIN TO BACTERIO-OPSIN AND 9-CIS-RETINAL. *Photochem. Photobiol.* **33**, 529–537 (1981).
267. Abdelfattah, A. S. *et al.* A general approach to engineer positive-going eFRET voltage indicators. *Nat. Commun.* **11**, 3444 (2020).
268. Marmé, N., Knemeyer, J.-P., Sauer, M. & Wolfrum, J. Inter- and Intramolecular Fluorescence Quenching of Organic Dyes by Tryptophan. *Bioconjug. Chem.* **14**, 1133–1139 (2003).
269. Léonard, J. *et al.* Functional electric field changes in photoactivated proteins revealed by ultrafast Stark spectroscopy of the Trp residues. *Proc. Natl. Acad. Sci. U. S. A.* **106**, 7718–7723 (2009).
270. Nass Kovacs, G. *et al.* Three-dimensional view of ultrafast dynamics in photoexcited bacteriorhodopsin. *Nat. Commun.* **10**, (2019).
271. Gong, Y., Li, J. Z. & Schnitzer, M. J. Enhanced Archaerhodopsin Fluorescent Protein Voltage Indicators. *PLoS One* **8**, 1–10 (2013).
272. Althaus, T., Eisfeld, W., Lohrmann, R. & Stockburger, M. Application of Raman Spectroscopy to Retinal Proteins. *Isr. J. Chem.* **35**, 227–251 (1995).
273. Mei, G. *et al.* Raman spectroscopy of a near infrared absorbing proteorhodopsin: Similarities to the bacteriorhodopsin O photointermediate. *PLoS One* **13**, 1–24 (2018).
274. Ogren, J. I. *et al.* Retinal Chromophore Structure and Schiff Base Interactions in Red-Shifted Channelrhodopsin-1 from Chlamydomonas augustae. *Biochemistry* **53**, 3961–3970 (2014).
275. Kralj, J. M., Spudich, E. N., Spudich, J. L. & Rothschild, K. J. Raman Spectroscopy Reveals Direct Chromophore Interactions in the Leu/Gln105 Spectral Tuning Switch of Proteorhodopsins. *J. Phys. Chem. B* **112**, 11770–11776 (2008).
276. Liguori, N., Novoderezhkin, V., Roy, L. M., van Grondelle, R. & Croce, R. Excitation dynamics and structural implication of the stress-related complex LHCSR3 from the green alga Chlamydomonas reinhardtii. *Biochim. Biophys. Acta - Bioenerg.* **1857**,

1514–1523 (2016).
277. Rigaud, J.-L., Pitard, B. & Levy, D. Reconstitution of membrane proteins into liposomes: application to energy-transducing membrane proteins. *Biochimica et Biophysica Acta (BBA) - Bioenergetics* **1231**, 223-246 (1995).

6. Supplement

Table S1. Table summarizing the reported fluorescent Arch3 variants

Nr.	Construct name	Mutations	Fluorescence	Voltage sensitivity	Special remarks
1	**Arch3 D95N**[167]	Arch3 D95N	QY~0.04%	~60% per 100 mV	
2	Arch EEN[271]	Arch3 D95N-D106E		~20% per 100 mV	
3	Arch EEQ[271]	Arch3 D95Q-D106E		~60% per 100 mV	
4	**Archer1**[271]	Arch3 D95E-T99C	QY~0.33%	~ 85% per 100 mV	
5	Archer 2[271]	Arch3 D95E- T99C-A225M	Brightness ~ 0.6x Archer1	~ 60% per 100 mV	Red-shifted absorption: λ_{MAX}~626 nm
6	Arch PLDETC[1]	Arch3 P60L-D95E-T99C	QY~0.4%	*E.coli* assay, pH sensitive	Red-shifted absorption: λ_{MAX}~624 nm
7	Arch DETCPS[1]	Arch3 D95E-T99C-P196S	QY~0.57%	*E.coli* assay, pH sensitive	Red-shifted absorption: λ_{MAX}~628 nm
8	Arch VADETC[1]	Arch3 V59A-D95E-T99C	QY~0.62%	*E.coli* assay, pH sensitive	Red-shifted absorption: λ_{MAX}~622 nm
9	**Arch5**[1]	Arch3 V59A-P60L-D95E-T99C-P196S	QY~0.87%	*E.coli* assay, pH sensitive	Red-shifted absorption: λ_{MAX}~622 nm
10	**Arch7**[1]	Arch3 V59A-P60L-D95E-T99C-P196S-D222S-A225C	QY~1,2%	*E.coli* assay, not pH sensitive	Red-shifted absorption: λ_{MAX}~616 nm
11	**QuasAr1**[3]	Arch3 P60S-T80S-D95H-D106H-F161V	QY~0.8%	~ 30% per 100 mV	
12	**QuasAr2**[3]	Arch3 P60S-T80S-D95H-D106Q-F161V	QY~0.4%	~ 90% per 100 mV	
13	Arch DHDH[3]	Arch3 D95H-D106H	QY~0.2%		
14	Arch DHDHPS[3]	Arch3 P60S-D95H-D106H	QY~0.5%		
15	Arch DHDHFV[3]	Arch3 D95H-D106H-F161V	QY~0.5%		
16	**Archon1**[2]	Arch3 T20S-G41A-V44E-P60S-T80P-D86N-D95Q-D106H-A136T-F161V-T183I-L197I-G241Q	Brightness ~2x QuasAr2	~ 80% per 100 mV	High expression, high membrane localization, fast kinetics

17	**Archon2** [2]	Arch3 T56P-P60S-T80P-D95H-T99S-T116I-F161V-T183I-L197I-A225C	Brightness ~7x QuasAr2	~ 20% per 100 mV	High brightness, high expression, fast kinetics
18	QuasAr2 – I[2]	QuasAr2 T20S-G41A-V44E-D88N-A137T-G242Q	Brightness ~1.4x QuasAr2	~ 47% per 100 mV	
19	QuasAr2 – II[2]	QuasAr2 T20S-G41A-V44E-S80P-D88N-A137T-G242Q	Brightness ~1.7x QuasAr2	~ 66% per 100 mV	
20	QuasAr2 – IV[2]	QuasAr2 T20S-G41A-V44E-T56P-S80P-D88N-A137T-T184I-L199I-G242Q	Brightness ~2.3x QuasAr2	~ 90% per 100 mV	
21	QuasAr2 – V[2]	QuasAr2 T20S-G41A-V44E-T56P-S80P-D88N-T118I-A137T-T184I-L199I-G242Q	Brightness ~2.5x QuasAr2	~ 84% per 100 mV	
22	QuasAr2 – VI[2]	QuasAr2 T20S-G41A-V44E-T56P-S80P-D88N- A137T-T184I-L199I-A226C-G242Q		~ 76% per 100 mV	
23	QuasAr2 – VII[2]	QuasAr2 T20S-G41A-V44E-T56P-S60C-S80P-D88N- A137T-T184I-L199I- G242Q	Brightness ~2.5x QuasAr2	~ 63% per 100 mV	
24	QuasAr2 – VIII[2]	QuasAr2 T20S-G41A-V44E-S60C-S80P-D88N- A137T-T184I-L199I- G242Q	Brightness ~2.1x QuasAr2	~ 74% per 100 mV	
25	QuasAr2 – IX[2]	QuasAr2 T20S-G41A-V44E-S60C-S80P-D88N- T118I-A137T-T184I-L199I- G242Q	Brightness ~1.9x QuasAr2		
26	QuasAr2 – X[2]	QuasAr2 T20S-G41A-V44E-S80P-D88N- T118I-A137T-T184I-P196S-L199I- G242Q	Brightness ~1.9x QuasAr2		
27	QuasAr2 – XI[2]	QuasAr2 T20I-G41A-V44E-S80P-D88N-A137T-T184I-L199I- G242Q	Brightness ~1.4x QuasAr2		
28	QuasAr2 – XII [2]	QuasAr2 T20I-G41A-V44E-S80P-D88N-T118I-A137T-T184I-L199I- G242Q	Brightness ~1.2x QuasAr2		
29	Variant 3[2]	Arch3 T20I- P60S-T80S- D95E-T99C-T118I-F161V- T184I-L199I	Brightness ~6x Archon1	~ 40% per 100 mV	
30	Variant 4[2]	Arch3 T20I- P60S-T80S- D95E-T99C-T118I-F161V- T184I-L199I-A225G	Brightness ~3.5x Archon1	~ 55% per 100 mV	
31	Variant 5[2]	Arch3 T56P- P60S-T80P-D95H-D106H- T118I-F161V- T184I-L199I	Brightness ~2x Archon1	~ 20% per 100 mV	
32	Variant 6[2]	Arch3 L38V-T56P-P60C-T80P-D95H- F161V- L199I-A225C	Brightness ~2.5x Archon1	~ 20% per 100 mV	
33	Variant 7[2]	Arch3 K47R-T56P-P60S-T80S-D95H-H140P-F161V-T184I-L199I- A225G-I232V	Brightness ~1.5x Archon1	~ 20% per 100 mV	

34	QuasAr3[232]	QuasAr2 K171R		~ 50% per 100 mV	Imrpoved expression
35	paQuasAr3[232]	QuasAr2 V59A-K171R		~ 25% per 100 mV	Simultaneous blue (470 nm) and red (620 nm) light illumination increases fluorescence intensity
36	NovArch[232]	QuasAr1 V59A -K171R-V209I-I213T		~ 40% per 100 mV	Blue and red light illumination yields fluorescence intensity
37	QuasAr3 QDHNEV[267]	QuasAr2 Q95D-H106N-K171R-E214V			Reversed voltage sensing

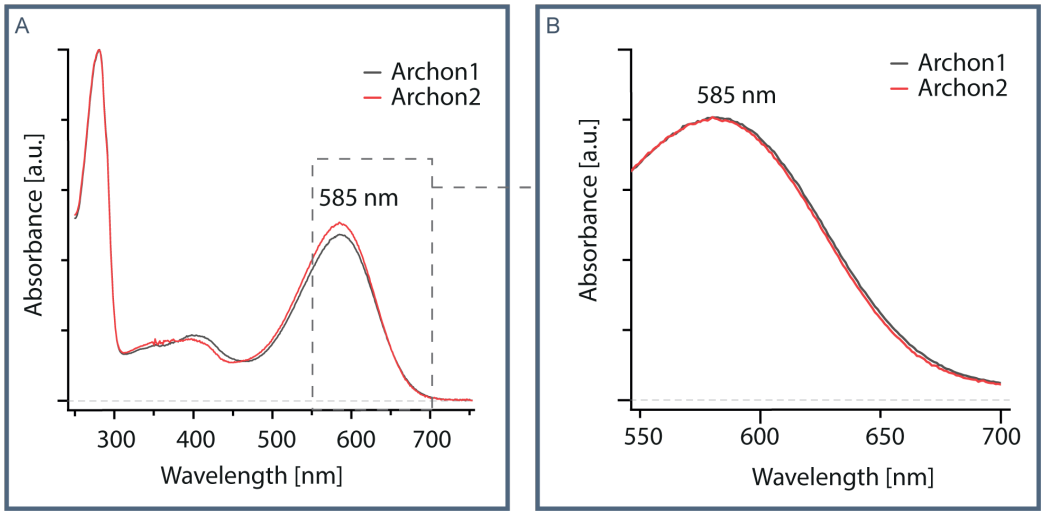

Figure S1. Absorption spectra of Archons

(A) Absorption spectra of dark state Archon1 (585 nm, black) and Archon2 (585 nm, red). Zoomed and normalized absorption spectra are shown in panel (B). Despite the various different mutations in the two constructs (Fig.I9) the absorption spectra are strongly overlaping.

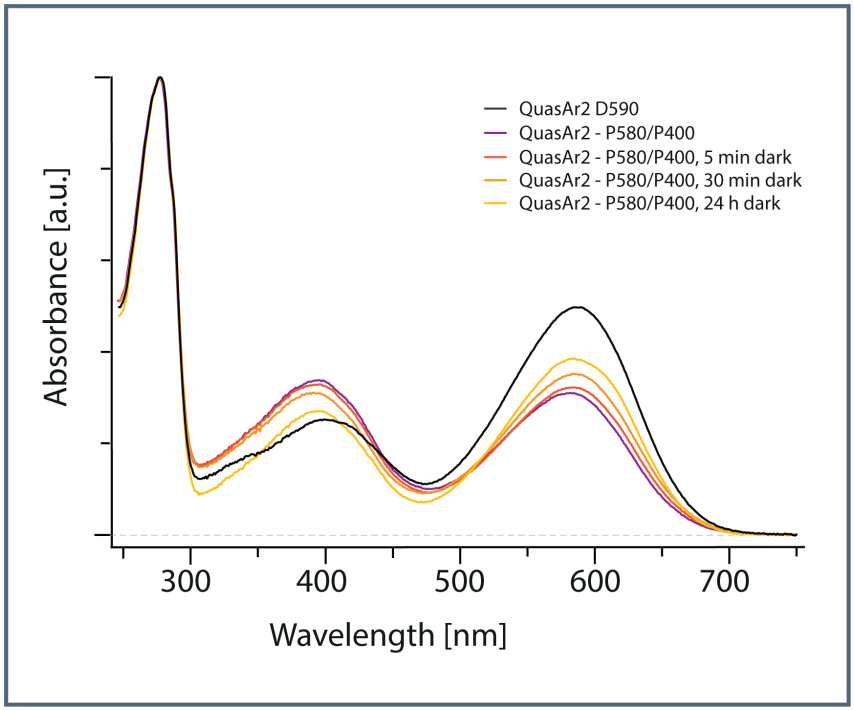

Figure S2. Steady state absorption of thermal recovery of QuasAr2 dark state (D590)

Dark state QuasAr2 (D590) absorption is shown with black curve. After 1 min illumination of the sample with 625nm LED a mixture of P400 and P580 photoproducts appears (purple curve). The sample is kept in darkness over 24h to monitor the thermal stability of the sample. The absorption spectra is recorded after 5 min (red), 30 min (dark orange), 24 h (light orange).

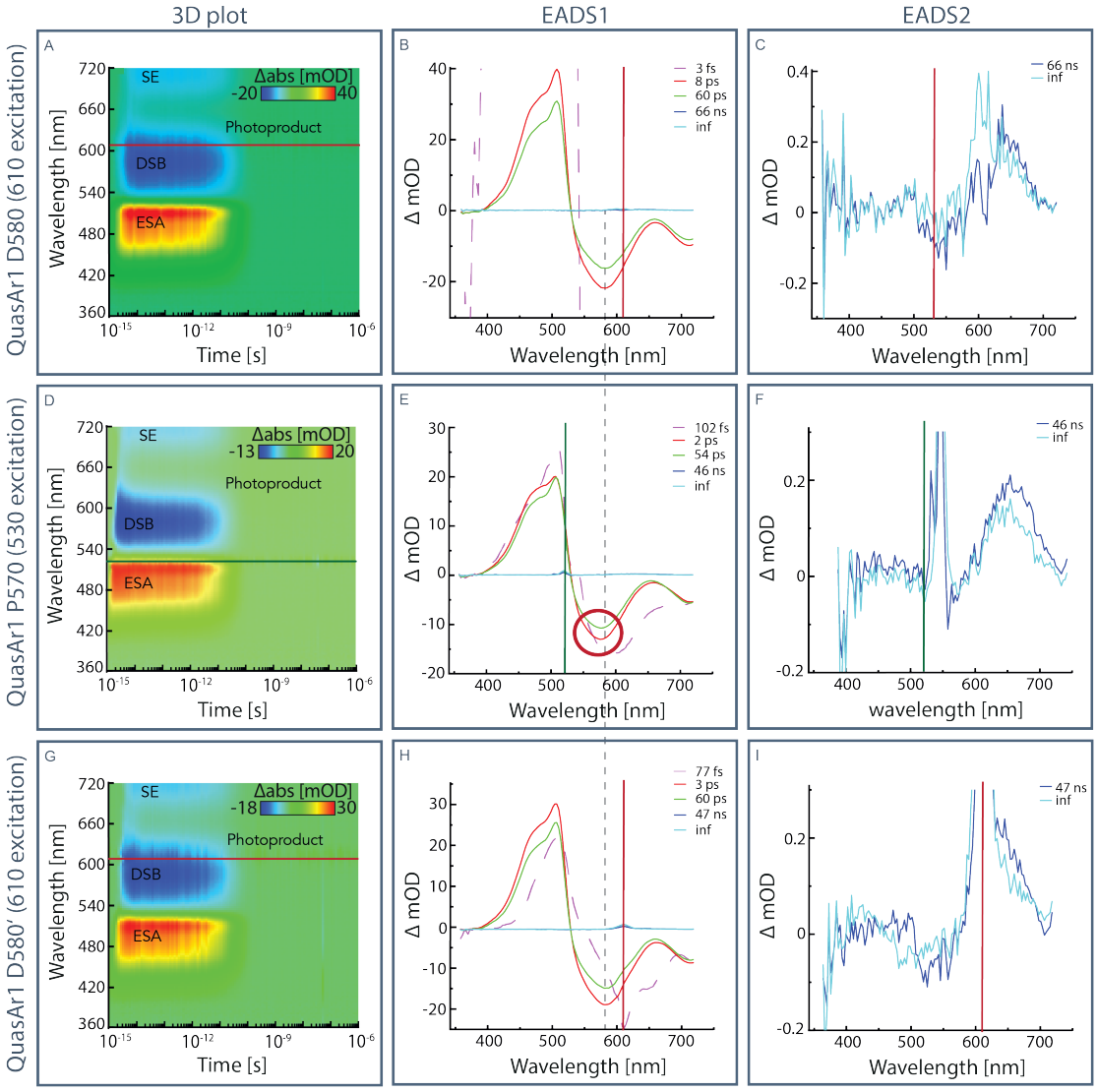

Figure S3. Transient absorption spectra of QuasAr1

The TAS of QuasAr1. The first column displays the reconstructed 3D plot. The second column shows the EADS of the recorded spectra. The third column is a close up of the photointermediates from the second column. The sample was excited with laser tuned to 610nm (or 530nm). The first row shows excited state dynamics of QuasAr1 in the initial dark state D580 (A-C). The second row shows the excited state dynamics of QuasAr1 in the P570 state (D-F). Here the red circle indicates the shift in the dark state bleach from 580nm to 570nm. The third row shows excited state dynamics of the D580' state (G-I).

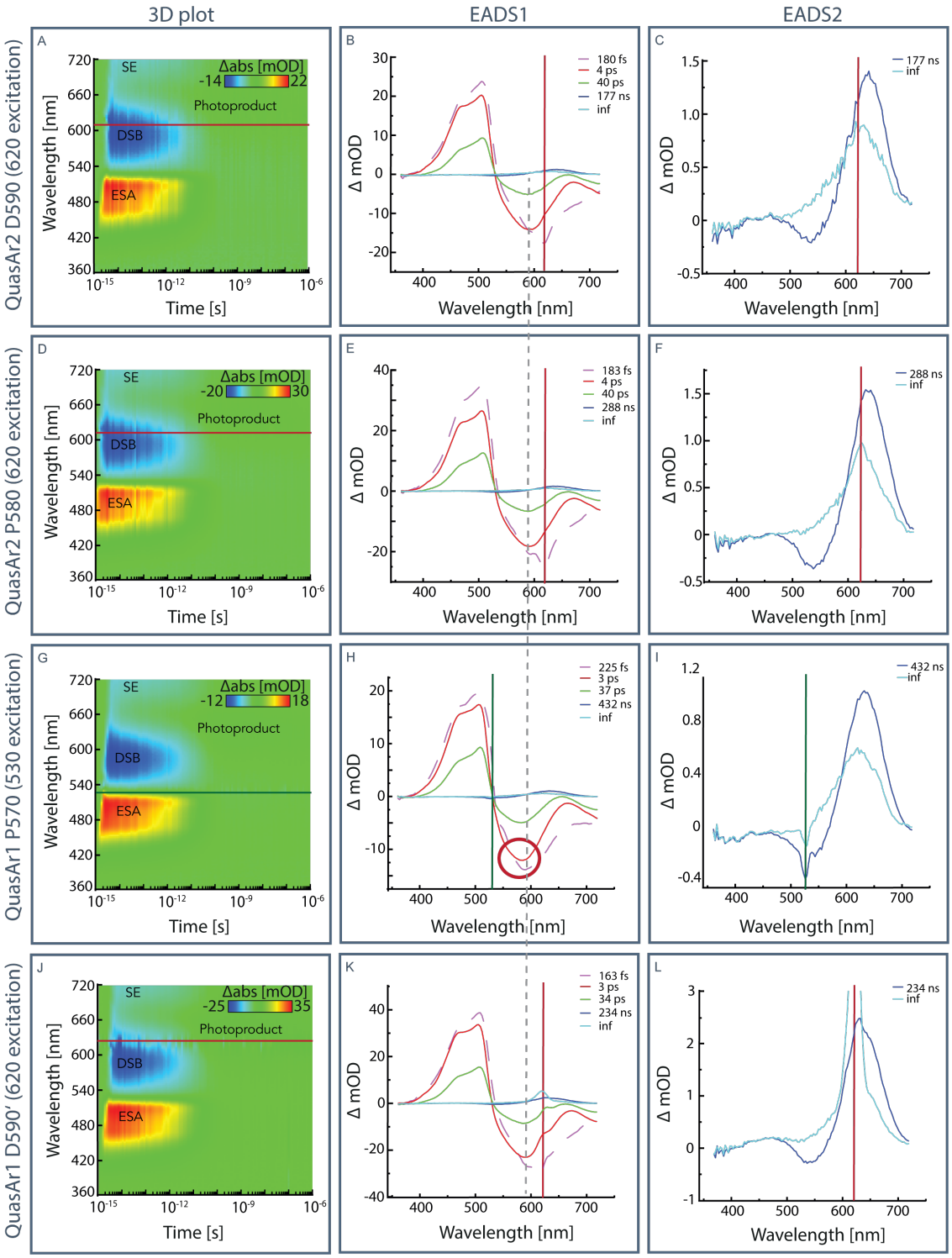

Figure S4. Transient absorption spectra of QuasAr2

The TAS of QuasAr2. The first column displays the reconstructed 3D plot. The second and third column shows the EADS. The sample was excited with laser tuned to 620nm (530nm). The first row shows excited state dynamics of QuasAr2 in it the initial dark state D590. The second and third row shows the excited state dynamics of QuasAr2 in the P580 state and the fourth row shows excited state dynamics of the D590' state. The red circle in the third row points to the shift in the dark state bleach from 590nm to 580nm.

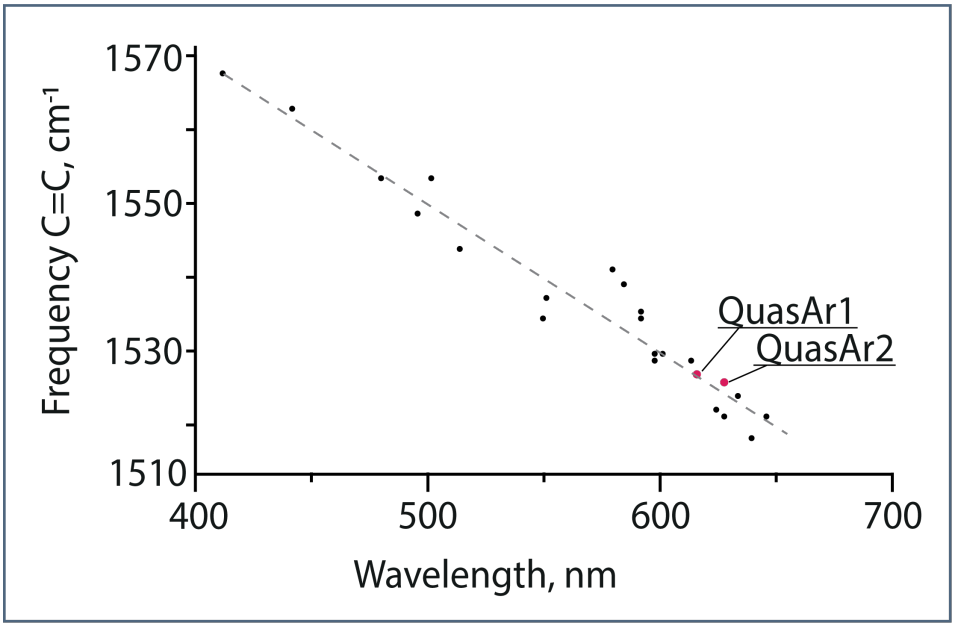

Figure S5. Correlation between C=C stretch band frequency and absorption maxima

The reported values of rhodopsin absorption spectra maxima and their corresponding frequencies of the C=C stretching band are plotted with black dots (Table S2 displays the data table). These values are used to determine the linear correlation trend line (dashed line). The QuasAr1 and Quasar2 values are depicted with red dots.

Table S2. Absorption and C=C stretch frequency values of rhodopsins depicted in Figure S5

Rhodopsin	**λ_{MAX}, nm**	**$\nu_{C=C}$, cm^{-1}**
Arch3 [117]	565	1527
Arch3 D95N [117]	590	1518
BR DA [253]	560	1533
BR LA [253]	568	1527
BR 605 [253]	605	1518
BR D85N [242]	595	1521
BR D85A [242]	600	1515
BR M state [272]	410	1567
PsChR [273]	435	1562
CrChR [274]	467	1553
BPR [275]	485	1552
NpSRII [274]	480	1547

GtACR1 [273]	495	1542
GPR [275]	526	1535
CaChR1 [274]	525	1532
BR L [272]	550	1539
BR 565 [253]	565	1526
BR 554 [272]	554	1537
BR N [272]	560	1532
HR [226]	578	1526
SRI [226]	587	1519

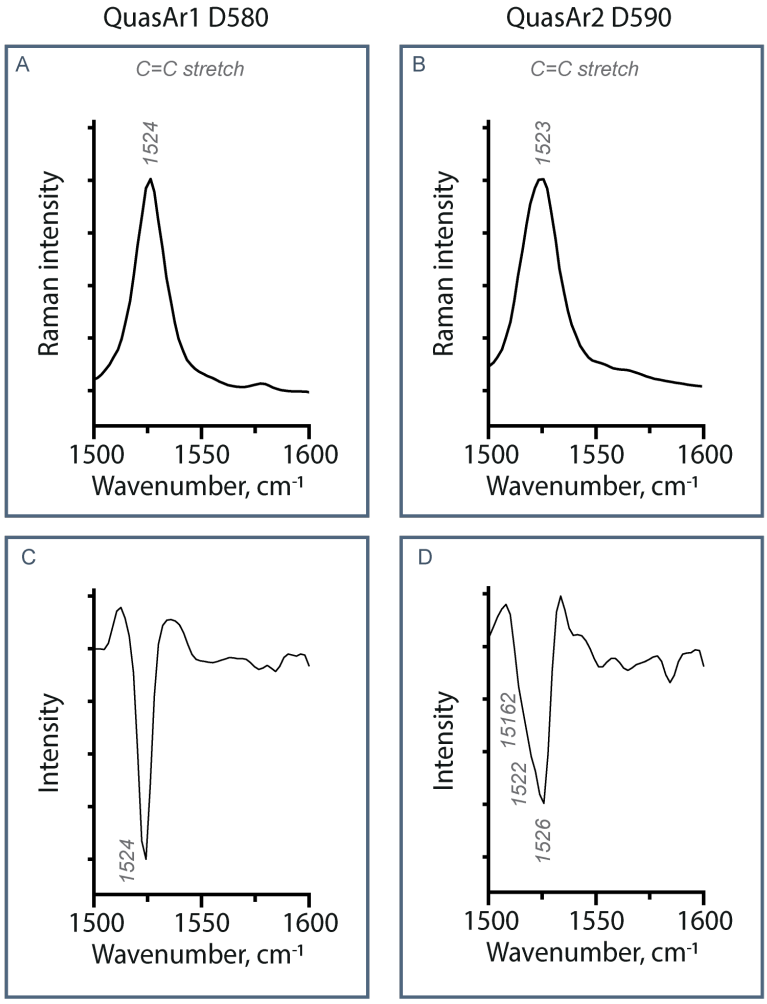

Figure S6. C=C stretch and the resulting 2nd derivative

Recorded Pre-resonance Raman C=C stretch of QuasAr1(A) and QuasAr2 (B) and 2nd derivative to investigate the heterogeneity of the peak and its subspecies.

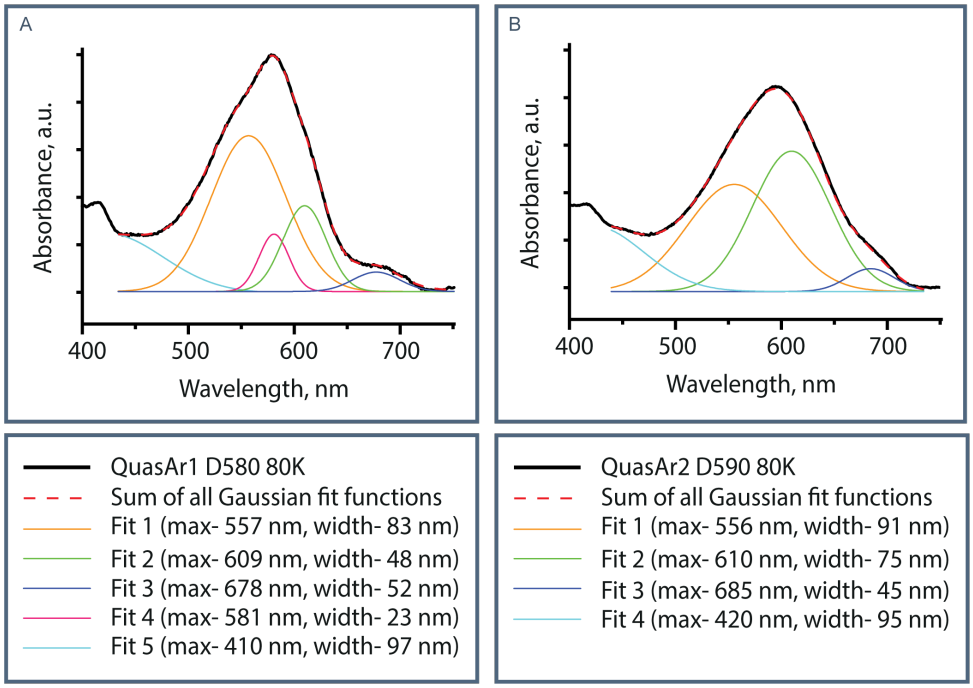

Figure S7. Cryo-UV/Vis spectra

Recorded UV/Vis spectra recorded at 80K. The Gaussian fit reveal the possible subspecies contributing to the spectra. The absorption maximum and FWHM of subspecies are listed in the panels below.

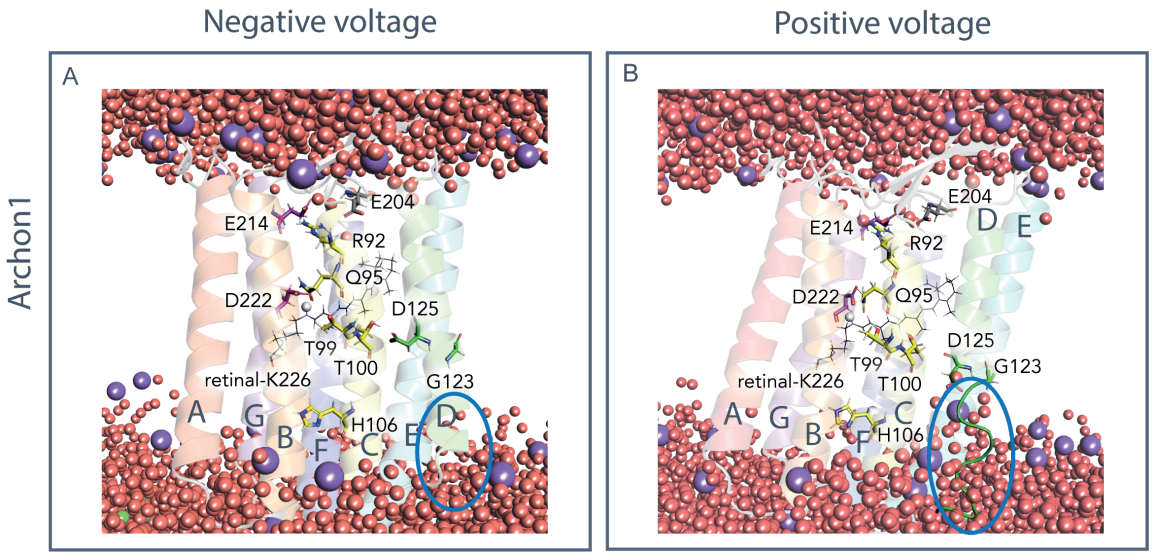

Figure S8 Movement of helices C and D in Archon1 at different membrane voltages

Voltage-dependent sidechain reorientations of D125 in Archon1 at negative voltage (A) and at positive voltage (B). MS simulations indicate voltage dependent closure and an opening of the helix D. Deformation of helix D and water and cation influx at positive voltage are highlighted by a blue ellipse. Key residues are represented by stick and line models. Oxygen atoms of water, potassium ions, chloride ions, and the proton of the Schiff base are depicted by

red, purple, green spheres, and a white sphere respectively. Lipid models are omitted for the sake of clarity.

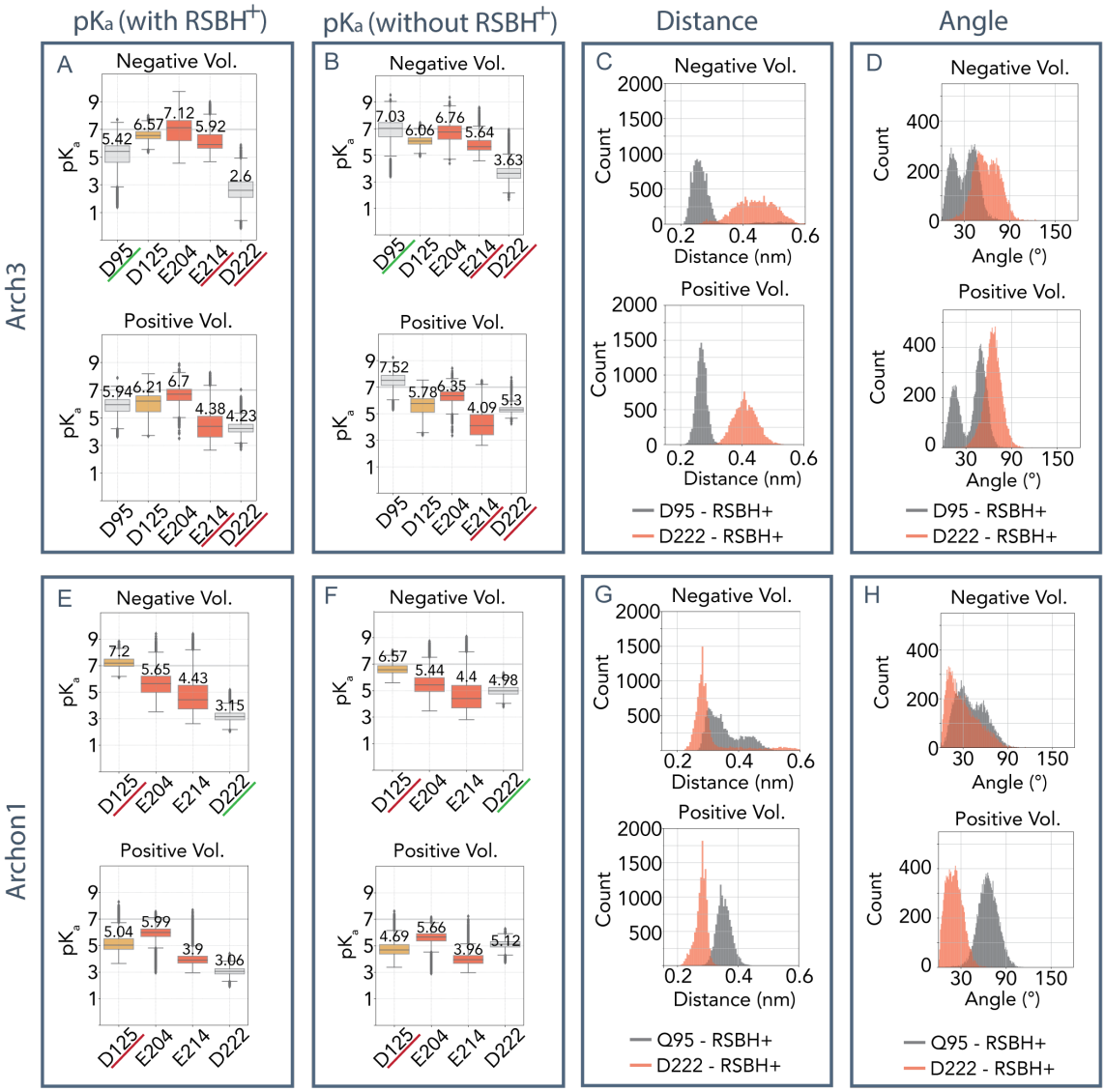

Figure S9. Calculated pKa values and distance distribution between RSBH+ and active site residues.

(A, B, E, F) Calculated pKa values of the key titratable residues at different membrane voltages for Arch3 (A,B) and Archon1 (E,F). The upper row shows the values calculated at negative voltage, the lower row shows values calculated at positive voltage. The pKa values are compared between calculations including RSBH+ (A,E) and disregarding RSBH+ (B,F). (C,G) Distance distributions between RSBH+ and its counter ions at different membrane voltages for Arch3 (C) and Archon1 (G). (D,H) Angle distributions between RSBH+ and its counter ions at different membrane voltages for Arch3 (D) and Archon1 (H).Distance (and angle) distribution between RSBH+ and D(Q)95 and D222 are coloured in black and red, respectively.

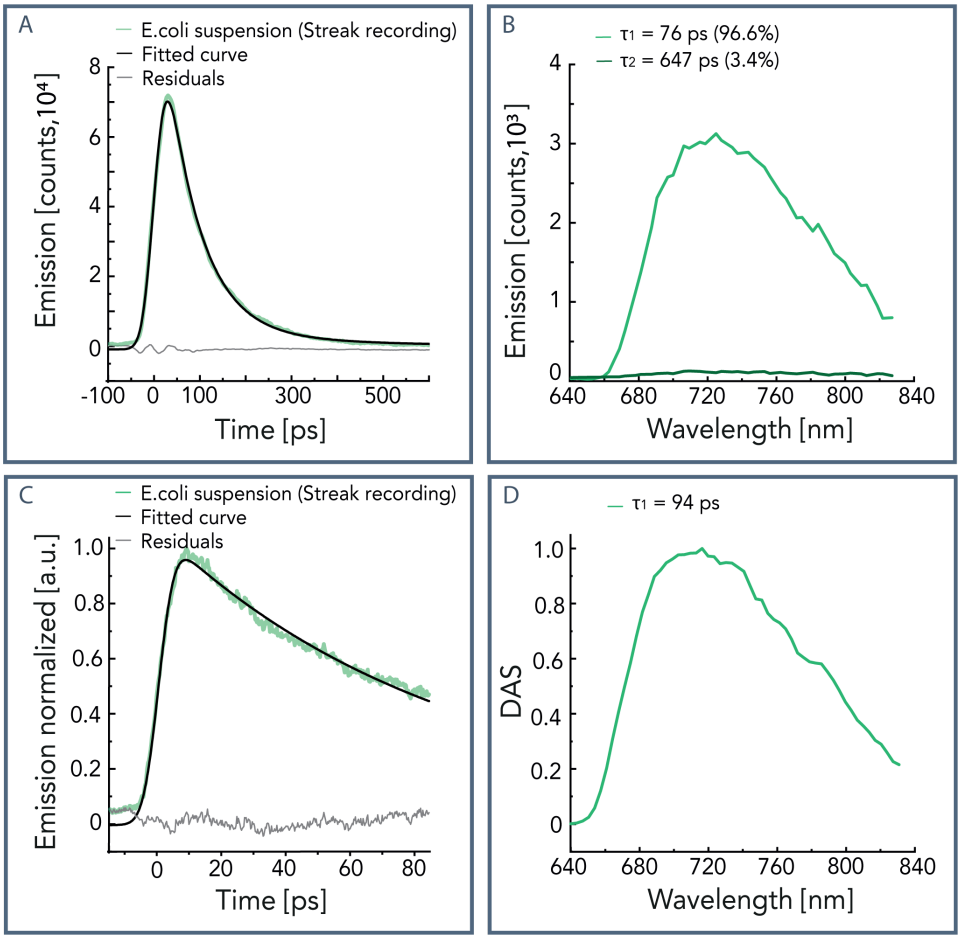

Figure S10. Streak camera recording of Archon1

The FLIM technique provides fluorescence kinetics with time resolution of 50ps, however ultrafast pump-probe experiments showed that Archon1 stimulated emission decays with two time components τ_1 = 14ps and τ_2 = 75ps. To confirm if the faster time component is present in Archon1 overexpressed in E.coli cells, the fluorescence lifetime was recorded with synchroscan streak camera system (625 nm excitation). Streak camera recordings were carried out in two time ranges: (1) up to 600 ps with 14ps time resolution (A,B); (2) up to 80 ps with 3 ps time resolution (C,D). The recorded fluorescence kinetic traces are shown in panels (A, 14 ps resolution) and (C, 3 ps resolution). And the recorded broad fluorescence spectra are shown in panel (B, 14 ps resolution) and (D, 3 ps resolution) and the resulting time components are indicated above. The results are in good agreement with those of FLIM. Furthermore, the results confirm there is no fast time component (14 ps) in Archon1(overexpressed in E.coli) fluorescence.

The time-resolved fluorescence measurement were recorded by Dr. Martijn Tros at Vrije Universiteit Amsterdam under supervision of Prof. Dr. John T.M. Kennis.

The measurements were carried out at RT with a streak camera (Hamamatsu C5680 synchroscan, Hamamatsu-city, Japan), combined with a Chromex 250IS spectrograph (Bruker, Massachusetts, United States). The sample was excited with 625 nm using fs-pump pulse

generated by Ti:Sapphire laser system as described previously in Liguori et al. 2016[276]. The laser repetition rate was set at 40 kHz with laser power of ~3 mW. The fluorescence emission was recorded in spectral range from 640 nm to 834 nm. The time-resolved fluorescence data were analyzed using Glotaran[183, 184]. The global analysis were carried out using parallel exponential model to obtain the decay associated spectra (DAS). Average decay lifetimes τ_{avg} could be calculated from the sum of all lifetimes weighed by the relative amplitudes of each of the DASs: $\tau_{avg} = \frac{\sum(\tau_n A_n)}{\sum A_n}$.

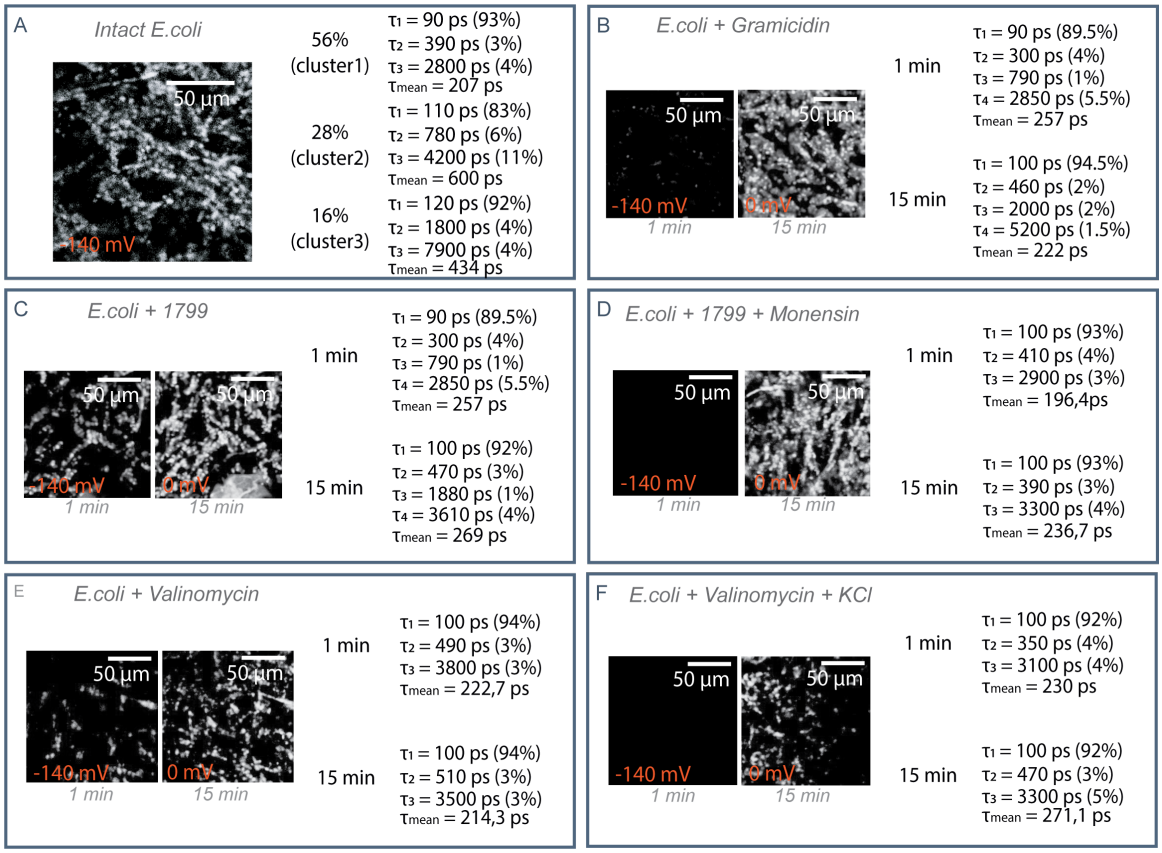

Figure S11. Comparison between FLIM recordings after addition of different ionophores.

The FLIM images and the resulting kinetics of Archon1 overexpressed in E.coli in varied conditions. The panel (A) shows Archon1 overexpressed in E.coli in buffer (50 mM Tris-HCl, pH 8, 75 mM NaCl, 75mM KCl). The kinetics of the fluorescence could be group in three clusters, and the following time components and their contributions are shown on the right side of the panel. However, only the first major cluster was observed in cell suspension with additional ionophore. The panels (B-F) show the FLIM images and the resulting kinetics of Archon1 overexpressed in E.coli with ionophore (indicated on the upper layer of the panel) added to the buffer. The kinetics are compared between the first minute and 15 min after addition of the ionophore.

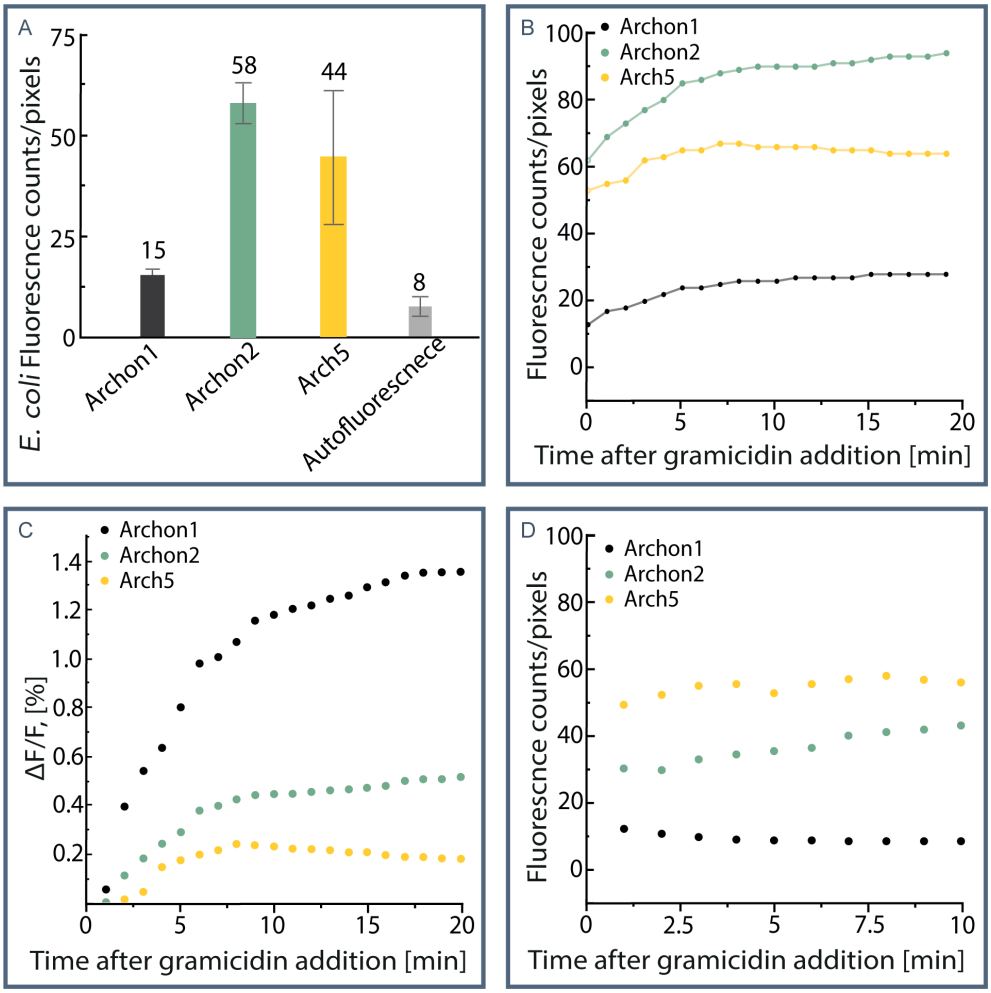

Figure S12. FLIM recordings of different constructs

Comparison between FLIM recordings after addition of gramicidin of different constructs – Archon1 (black), Archon2 (green) and Arch5 (yellow) – overexpressed in E.coli. The comparison between the initial fluorescence counts/pixel of constructs is shown in panel (A). The fluorescence intensity in counts/ pixel as determined from the FLIM images is normalized to the number of fluorescent pixels in the image. The mean of three independent samples is shown for each construct. The increase in intensity after addition of gramicidin to cell suspension over period of 20 min is shown in panel (B). The resulting fluorescence change expressed as ΔF/F of the constructs upon membrane depolarization is presented in panel (C). To account for possible bleaching of the constructs, 10 min recordings of the variants and the resulting fluorescence intensity per pixel is shown in panel (D).

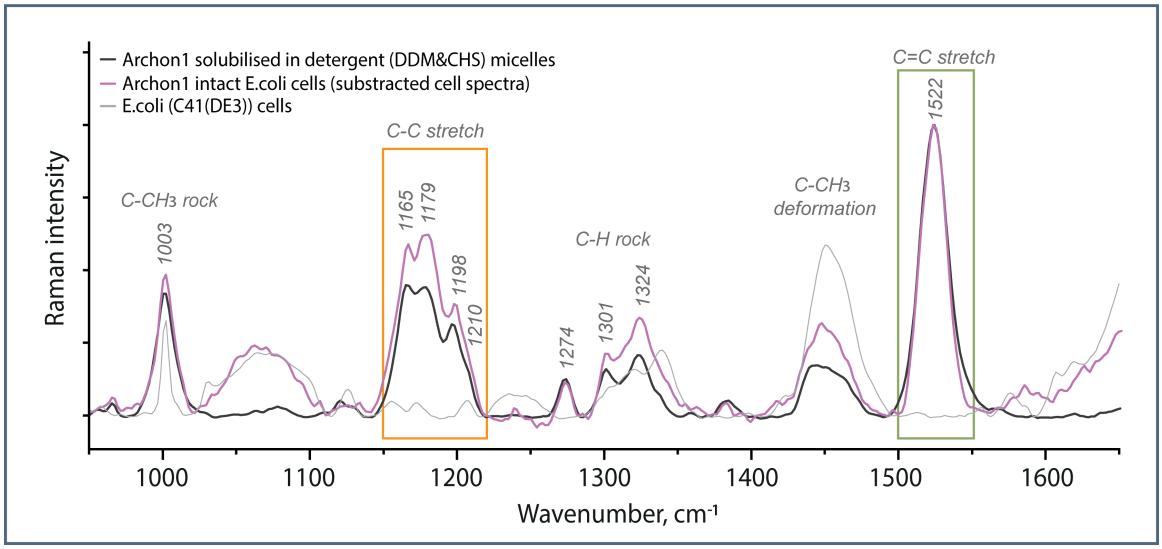

Figure S13. Pre-resonance Raman of Archon1

Pre-resonance Raman of Archon1 recorded with 1064 nm excitation. Spectra of solubilized Archon1 (black) is compared to spectra of Archon1 in intact cells (violet) without correction of E.coli contribution.

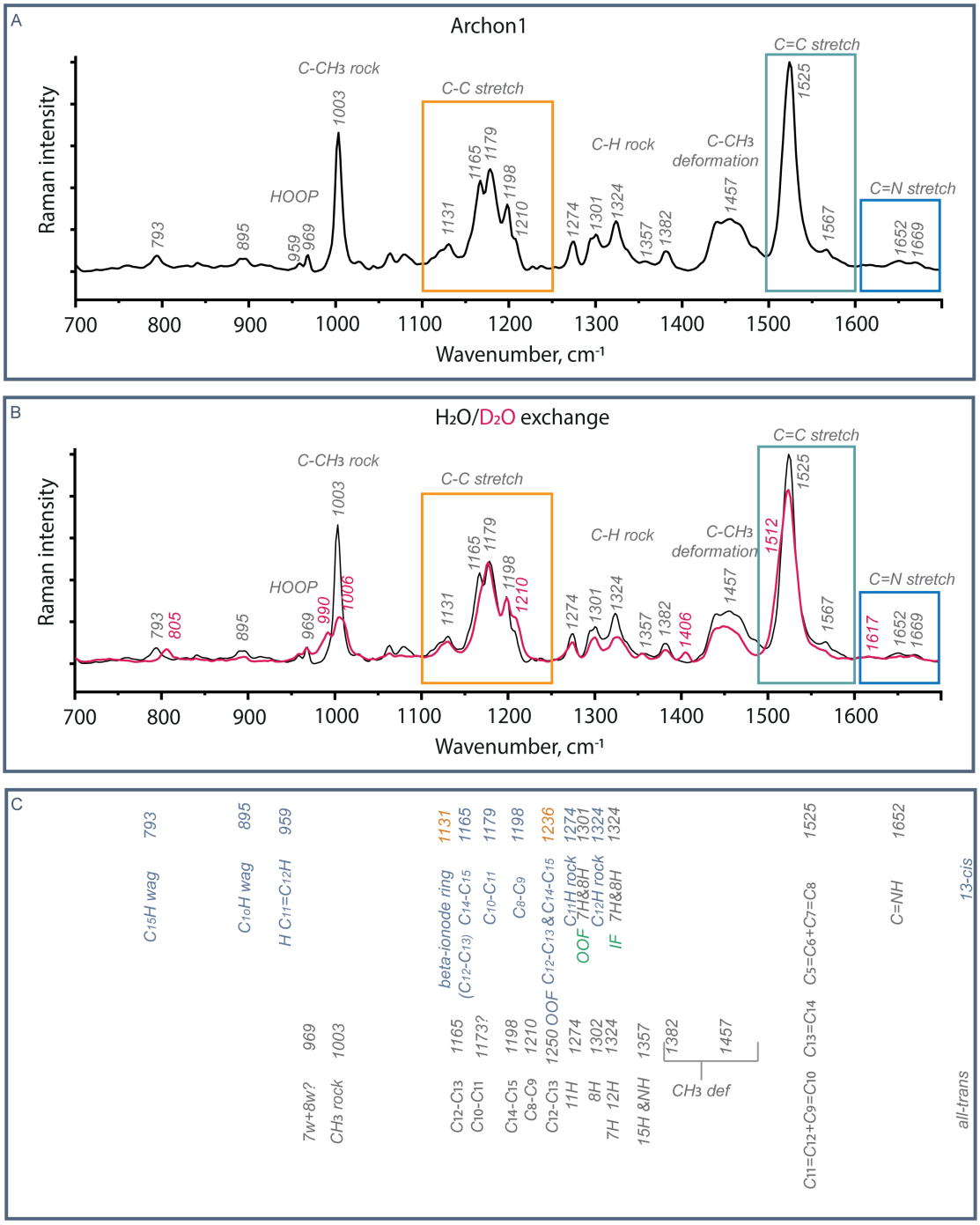

Figure S14. Pre-resonance Raman of Archon1

Pre-resonance Raman of Archon1 recorded with 1064 nm excitation at cryogenic temperatures (-190°C). (A)Spectra recorded in H_2O buffer (150mM NaCl, 50mM Tris-HCL, pH8). (B) Comparison of spectral changed upon deuteriation. (C) Assignment of observed bands.

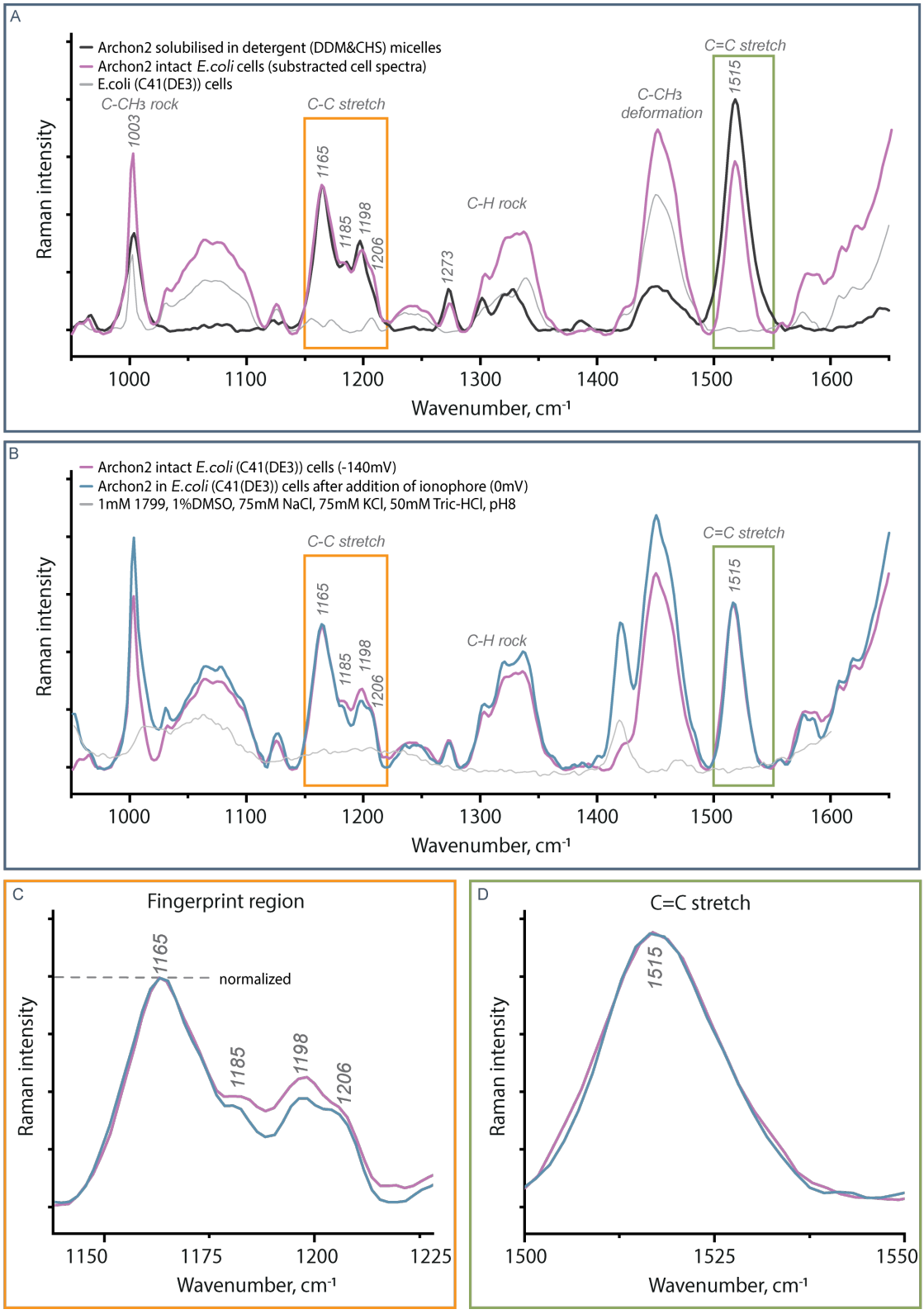

Figure S15. Pre-resonance Raman of Archon2

Pre-resonance Raman of Archon1 recorded with 1064 nm excitation. Spectra of solubilized Archon1 (black) is compared to spectra of Archon1 in intact cells (violet) without correction of E.coli contribution. (A) The comparison between recorded spectra of Archon1 at resting membrane potential (~-140 mV) and abolished membrane potential (~0mV) normalized to

C=C stretch peak. The spectra recorded of Archon1 in intact e.coli cells (~-140 mV) is shown in violet and the spectra recorded after addition of ionophore (1mM 1799) with disrupted of membrane potential (0 mV) is shown in blue. The spectra are corrected for E.coli contribution. The grey curve presents the spectral contribution of buffer with addition of 1% DMSO and ionophore (1mM 1799). The close up to regions of interest are shown in lower panels – Fingerprint region (B) and C=C stretch (C). The fingerprint region (B) is normalized to 1198 cm-1 peak to highlight the difference between 13-cis and all-trans contributing bands.

Table S3. Archon1 variants

Construct	**λ_{MAX}, nm**	**QY, %**
QuasAr1[3]	590	0.18 (reported- 0.4% [3])
QuasAr2[3]	580	0.28 (reported- 0.8% [3])
Archon1[2]	585	0.49
Archon1 – R92K	575	0.74
Archon1 – T100S	575	0.67
Archon1 – D125N	580	0.62
Archon1 – D222E	573	0.48
Archon1 – Q95H	575	0.79
Archon1 – Q95E	567	0.59
Archon1 – Q95L	585	0.32
Archon1 – Q95S	581	0.48
Archon1 – Q95G	585	0.68
Archon1 – T99C	604	0.45
Archon1 – Q95E T99C	603	0.71
Arch5[1]	626	0.87
Archon1 – A225C	583	1.07
Archon1 – S151A	560	0.6
Archon1 – G132S	584	1.17
Archon1 – Q95E T99C G132S	588 /615	1.32

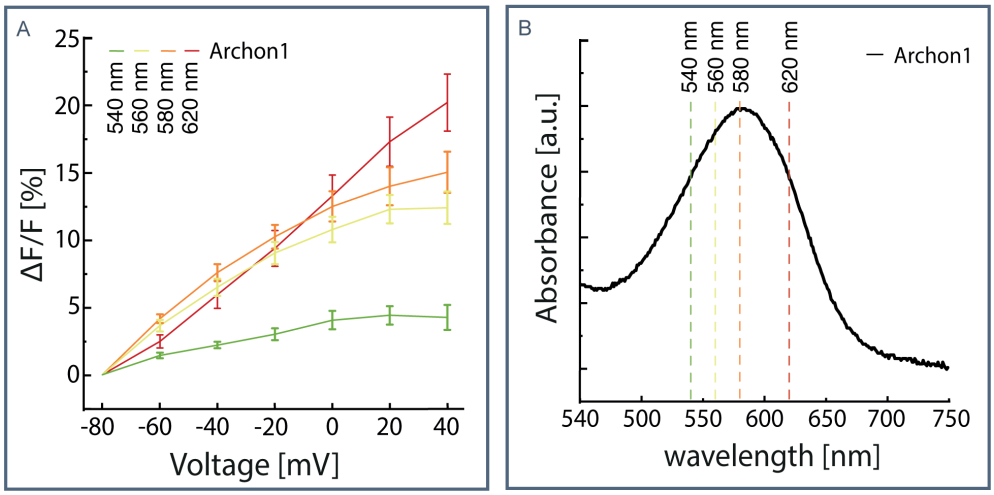

Figure S16. Archon1 voltage sensitivity

Archon1 wavelength dependant voltage modulated fluorescence increase (ΔF/F). Four excitation wavelengths are tested with step of 20 nm – 540 nm (green), 560 nm (yellow), 580 nm (orange) and 620 nm (red). The excitation wavelengths selected are designated on the absorption spectra curve in panel (B). The lowest voltage response ΔF/Fmax ≈ 4% was observed for 540 nm excitation on the blue shoulder of the absorption peak. The highest voltage response ΔF/Fmax ≈ 20% was observed for 620 nm excitation on the blue shoulder of the absorption peak.

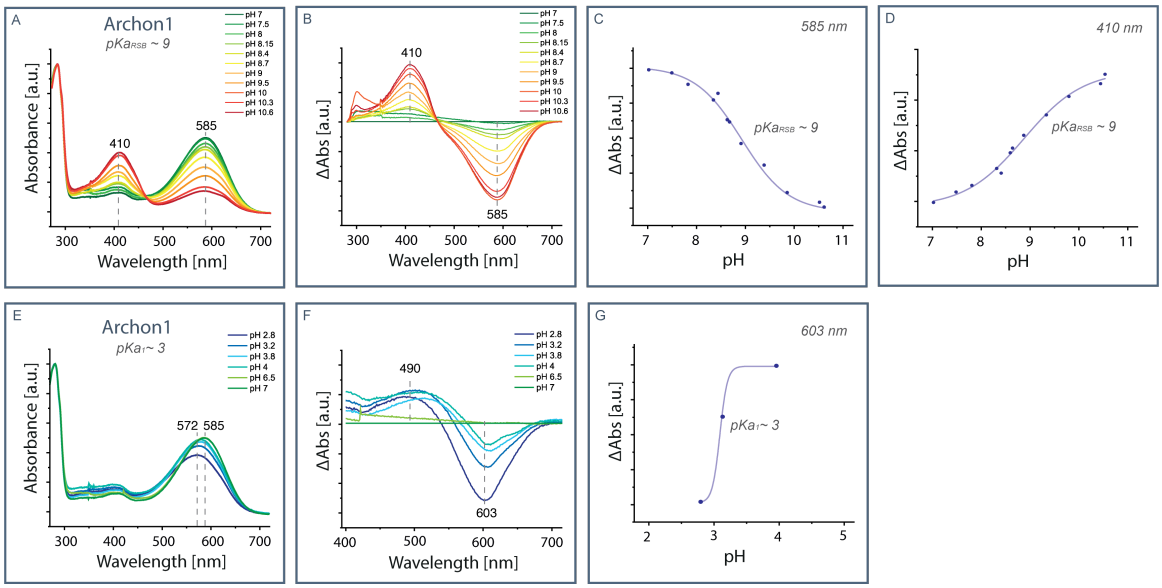

Figure S17. The pH titration of Archon1

Archon1 pH titration to alkaline is shown in the upper row. The absolute spectra are shown in panel (A) and the difference spectra is shown in panel (B). Panels (C,D) show the spectral amplitude changes versus the pH at selected wavelengths – 585 nm (C) and 410 nm (D). The pK_a values are determined with Boltzmann function shown as the fitted curves in panels (C) and (D). The lower row shows pH titration to acidic. Panel (E) shows the absolute spectra and

panel (F) shows the difference spectra. The Panel (G) shows spectral amplitude change at 603 nm versus the pH, only the latter data points are used for the fit with Boltzmann function and pK_a determination.

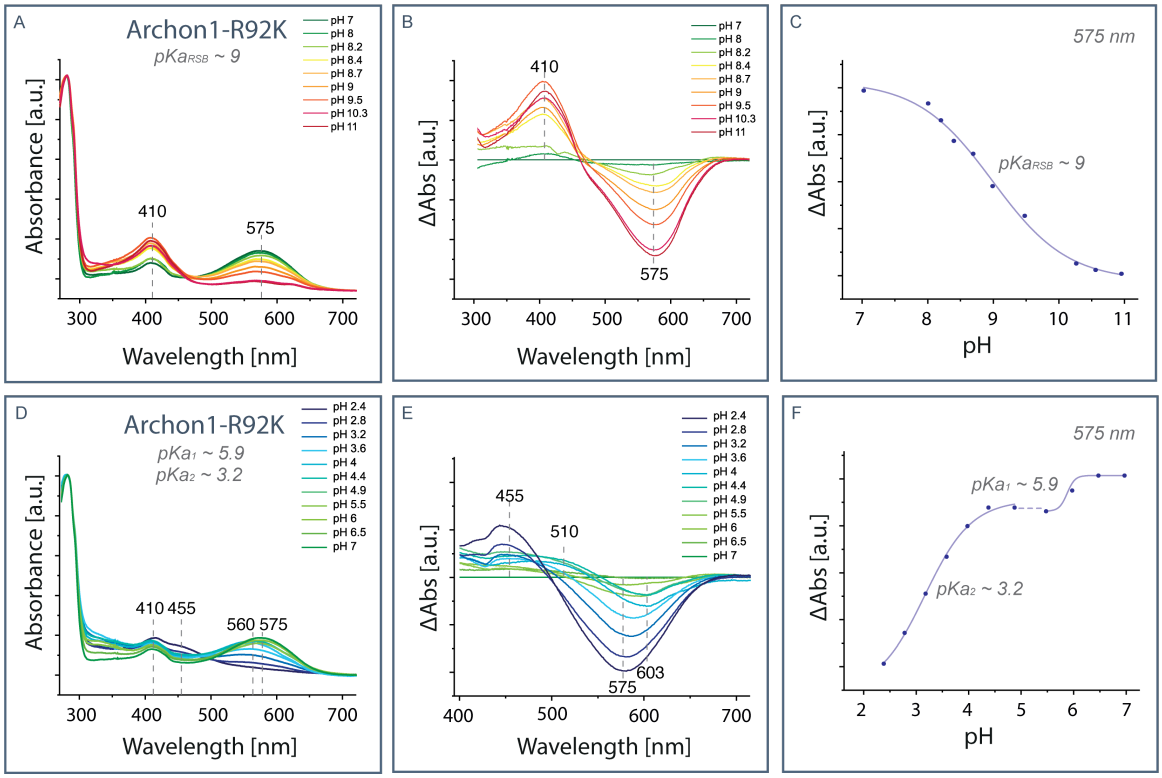

Figure S18. The pH titration of Archon1-R92K

Archon1-R92K pH titration to alkaline is shown in the upper row. The absolute spectra is shown in panel (A) and the difference spectra is shown in panel (B). Panel (C) show the spectral amplitude change at 575 nm versus the pH. The pK_a is determined using Boltzmann function. The lower row shows pH titration to acidic. Panel (D) shows the absolute spectra and panel (E) shows the difference spectra. The Panel (F) shows the spectral amplitude change at 575 nm versus the pH. The complex titration curve is fitted with Boltzmann function in two sets, to determine the two pK_a values.

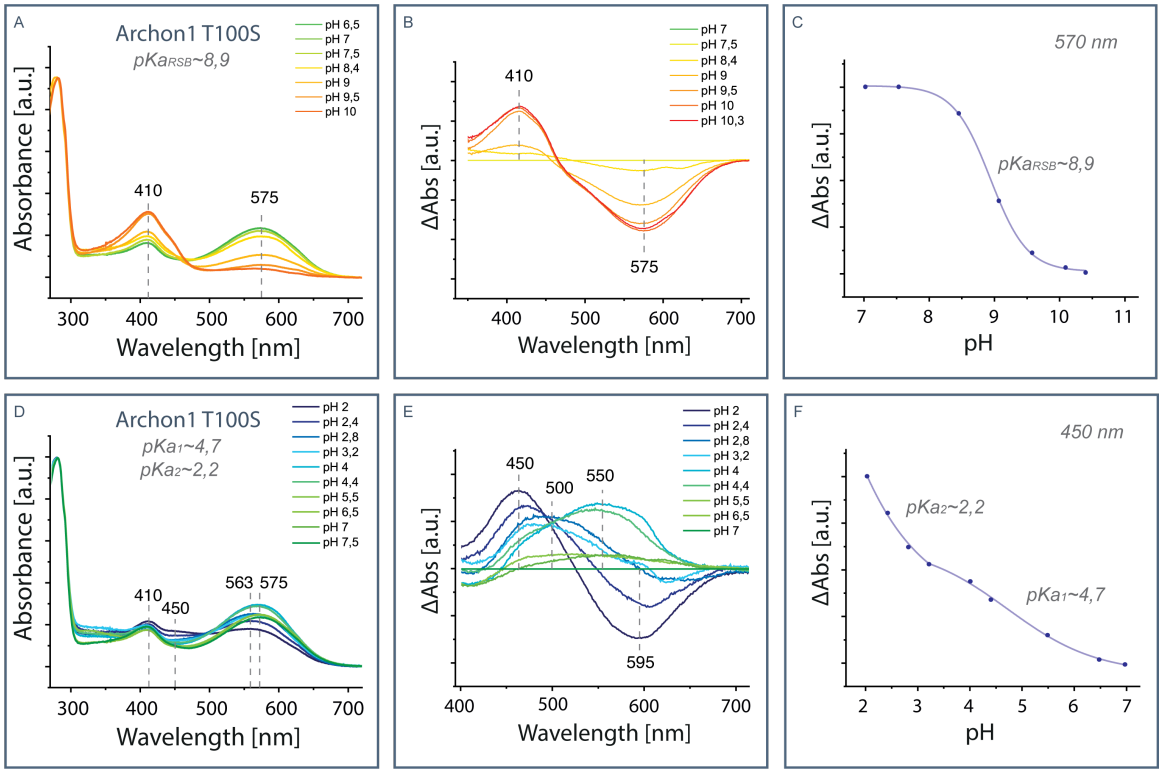

Figure S19. The pH titration of Archon1-T100S

Archon1-T100S absorption changes in alkaline conditions are shown in the upper row. The absolute spectra is shown in panel (A) and the difference spectra is shown in panel (B). Panel (C) show the spectral amplitude change at 575 nm versus the pH. The lower row shows absorption changes in acidic conditions. Panel (D) shows the absolute spectra and panel (E) shows the difference spectra. The Panel (F) shows the spectral amplitude change at 450 nm versus the pH. The pK_a values are determined with Boltzmann function shown as the fitted curves in panels (C) and (F).

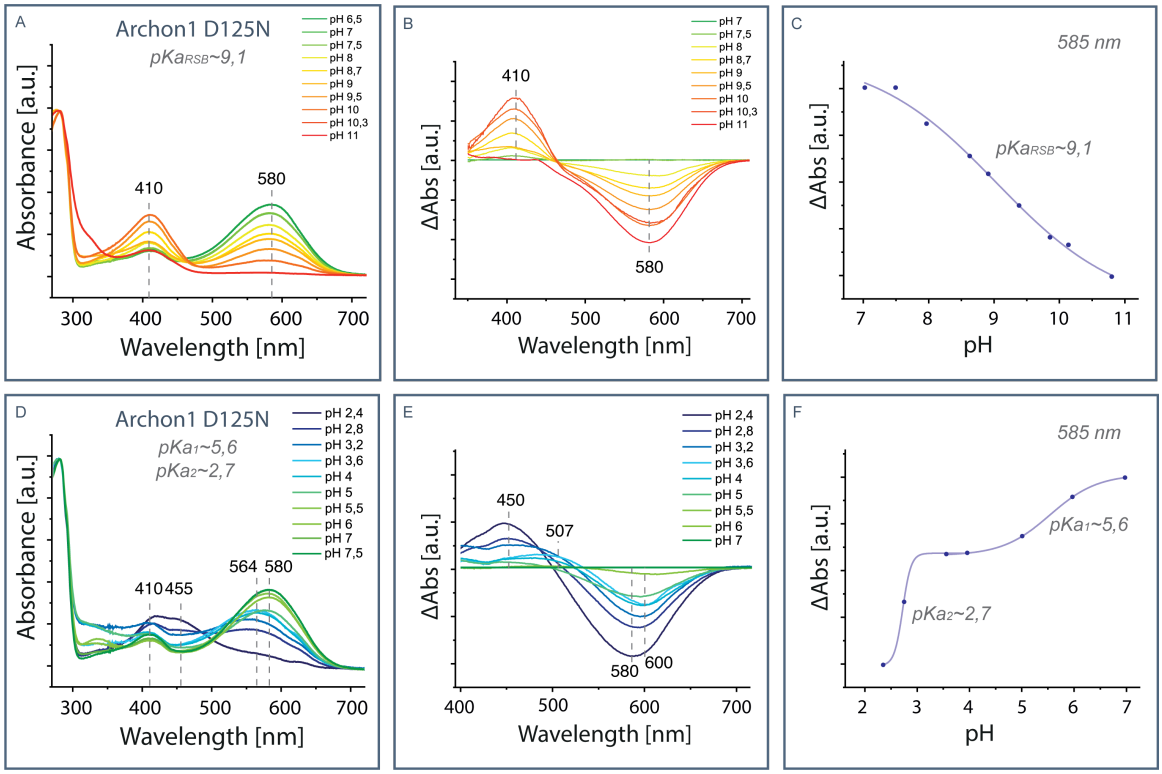

Figure S20. The pH titration of Archon1-D125N

Archon1-D125N absorption changes in alkaline conditions are shown in the upper row. The absolute spectra is shown in panel (A) and the difference spectra is shown in panel (B). Panel (C) show the spectral amplitude change at 580 nm versus the pH. The lower row shows absorption changes in acidic conditions. Panel (D) shows the absolute spectra and panel (E) shows the difference spectra. The Panel (F) shows the spectral amplitude change at 580 nm versus the pH. The pK$_a$ values are determined with Boltzmann function shown as the fitted curves in panels (C) and (F).

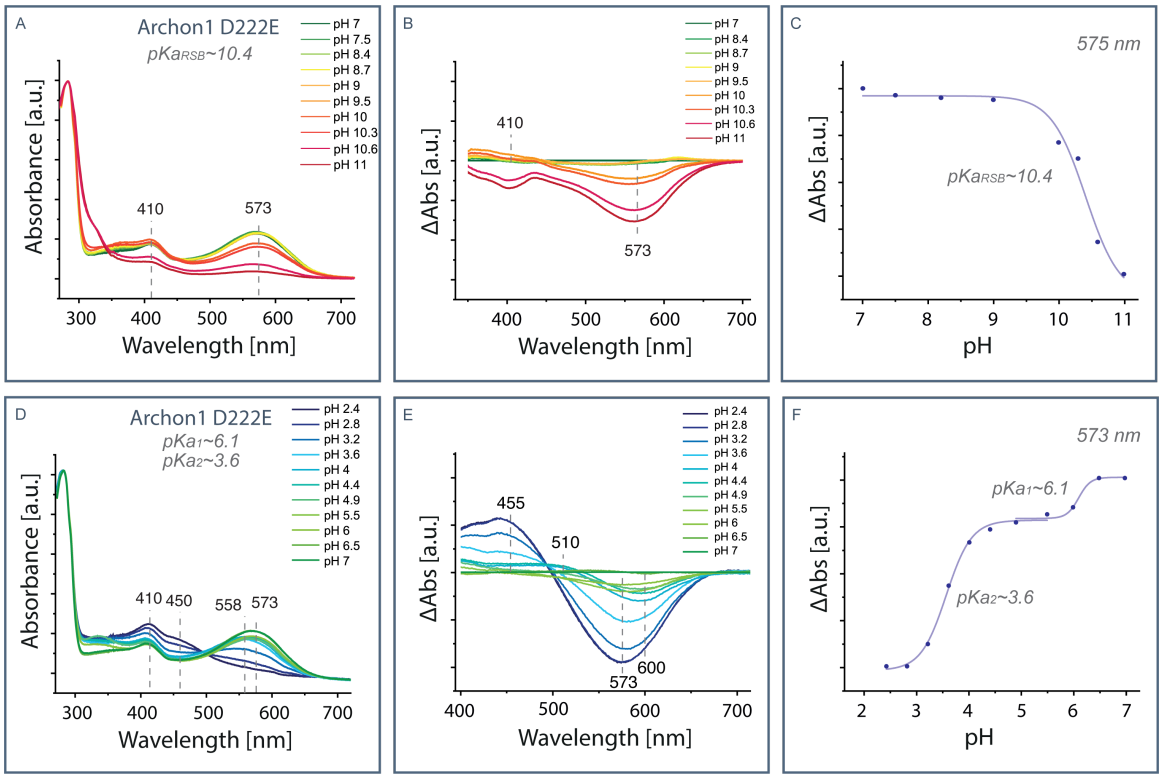

Figure S21. The pH titration of Archon1-D222E

Archon1-D222E absorption changes in alkaline conditions are shown in the upper row. The absolute spectra is shown in panel (A) and the difference spectra is shown in panel (B). Panel (C) show the spectral amplitude change at 573 nm versus the pH. The lower row shows absorption changes in acidic conditions. Panel (D) shows the absolute spectra and panel (E) shows the difference spectra. The Panel (F) shows the spectral amplitude change at 573 nm versus the pH. The pK_a values are determined with Boltzmann function shown as the fitted curves in panels (C) and (F).

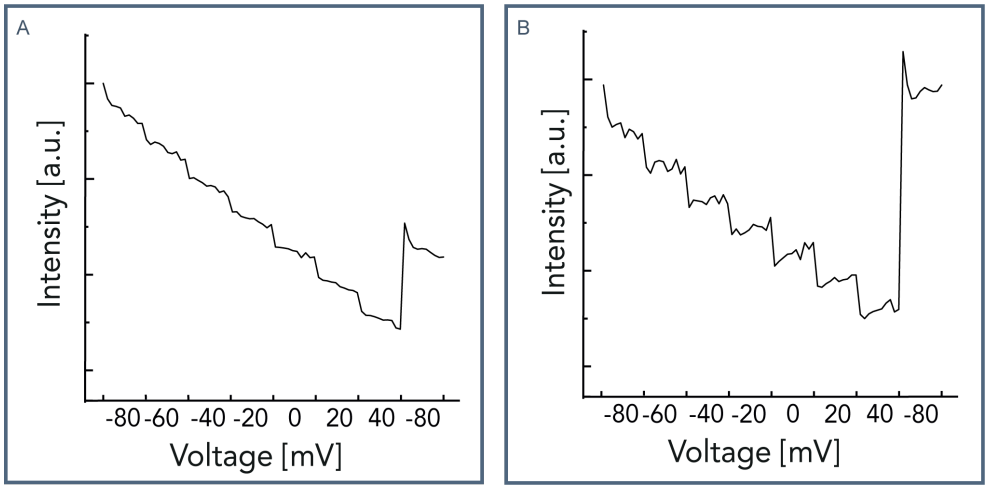

Figure S22. Arch5 fluorescence intensity change upon changes in membrane potential

(A) Recorded fluorescence intensity change (ΔF,%) upon stepwise (20 mV) increase of membrane potential (from -80 mV to 40 mV). Ten data points (150 ms exposure) are recorded per voltage step. Correction of the bleach is shown in panel (B).

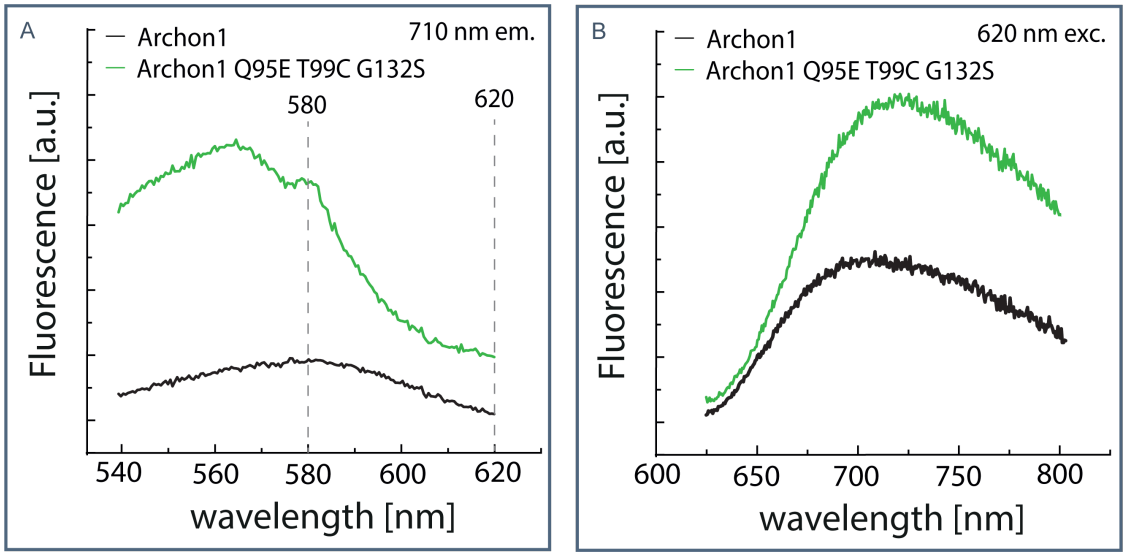

Figure S23. Archon1 Q95E T99C G132S fluorescence

Recorded excitation spectra (A) of Archon1 (black) and Archon1-Q95E-T99C-G132S (green) with emission detection set to 710 nm. Recorded emission spectra (B) of Archon1 and Archon1-Q95E-T99C-G132S with excitation at 620 nm.

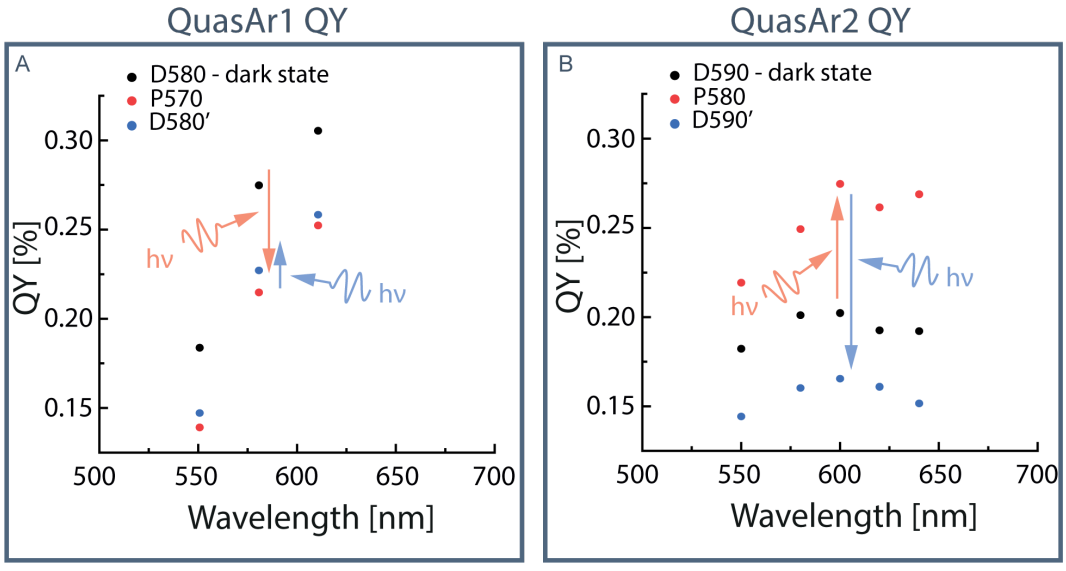

Figure S24. QuasAr1 and QuasAr2 fluorescence quantum yield

The fluorescence QY of QuasAr1 and QuasAr2 compared between dark state (D580/D590 -black dots), red illuminated (625 nm, 30s) state (P570/P580 – red dots) and blue illuminated (400 nm, 30s) state (D580'/D590' -blue dots). (A) In case of QuasAr1 the dark state shows the highest fluorescence QY, after red illumination it decreases, and slightly increases after blue

illumination. Furthermore for QuasAr1 we observe excitation wavelength dependent fluorescence QY, where more red-shifted excitation yield higher fluorescence. (B) In case of QuasAr2 the fluorescence QY increases after red illumination (625 nm, 30s). But after blue illumination (400 nm, 30s) the fluorescence QY decreases below the one observed in the dark state. In case of QuasAr2 the fluorescence QY does not strongly depend on excitation wavelength. In both constructs, higher all-trans retinal contribution correlated with increased fluorescence QY, but increased 13-cis retinal contribution correlated with lower fluorescence QY (Table S4).

Table S4. Fluorescence QY of QuasAr photoproducts

Construct	Retinal isomer composition	Fluorescence QY_{580}, %
QuasAr1-D580	**21% 13-*cis*, 79% all-*trans***	0.28
QuasAr1-P570	**18% 13-*cis*,** 14% 11-*cis*, 14% 9-*cis*, **54% all-*trans***	0.23
QuasAr1-D580'	**55% 13-*cis***, 14% 11-*cis*, 5% 9-*cis*, **26% all-*trans***	0.24
QuasAr2-D590	**47% 13-*cis*, 53% all-*trans***	0.20
QuasAr2-P580	**29% 13-*cis***, 16% 11-*cis*, 7% 9-*cis*, **48% all-*trans***	0.25
QuasAr2-D590'	**72% 13-*cis***, 3% 11-*cis*, 4% 9-*cis*, **21% all-*trans***	0.16

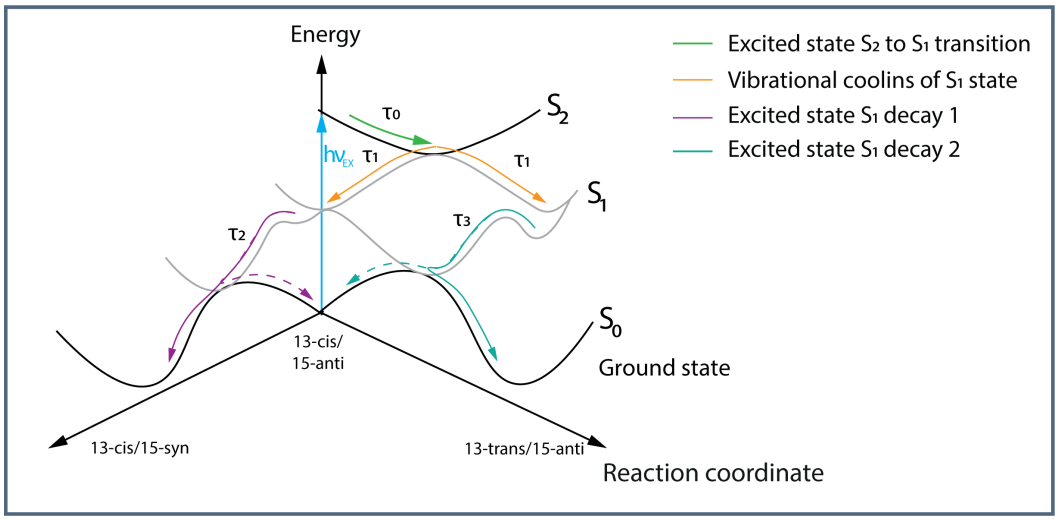

Figure S25. Reaction coordinate

Proposed reaction coordinated for retinal isomerization pathways of deprotonated species, adapted from study of HKR1 [258] [215]*. The green arrow represents transition from excited state S_2 to S_1. The transition is composed of reactive fraction, undergoing isomerization to 13-trans/15-anti (all-trans) and a nonreactive fraction maintaining the 13-cis/15-anti isomer. The orange arrow (370 fs) represents the vibrational cooling on the S_1 potential energy*

surface. The purple arrow indicates one of the isomerization pathways on the S_1–S_0 transition. Along this transition isomerization from 13-cis/15-anti to 13-cis/15-syn takes place. The turquoise arrow indicates internal conversion from the S_1 to the S_0 state, where the 13-trans/ 15-anti isomer is conserved.

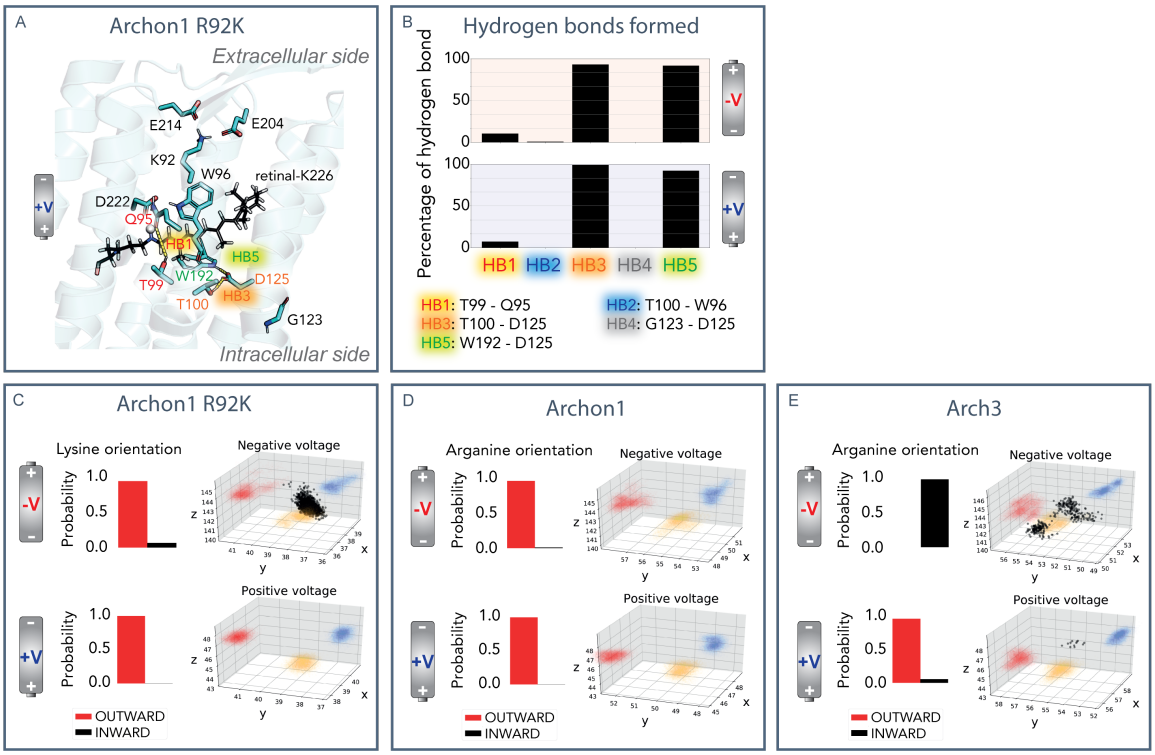

Figure S26. MD simulations of voltage modulated changes in Archon1-R92K

(A) Hydrogen bond network in proximity of RSBH⁺ in R92K . (B) Key hydrogen bond dependence on voltage. Independent of voltage HB3 (T100-D125) and HB5 (W192-D125) is always formed. Chances of HB1 (Q95-T99) formation are very low. (C) Voltage dependent orientation of lysine in Archon1-R92K is shown on the left, and voltage dependent water density at the RSBH⁺ proximity is shown on the right. Water molecules are represented with black sphere, the proton of the Schiff base is represented with yellow dots, D95/Q95 is represented with red dots, and D222 is represented with blue dots. (D) Voltage dependent orientation of arginine in Archon1 is shown on the left, and voltage dependent water density at the RSBH⁺ proximity is shown on the right. (E) Voltage deponent orientation of arginine in Arch3 is shown on the left, and voltage dependent water density at the RSBH⁺ proximity is shown on the right.

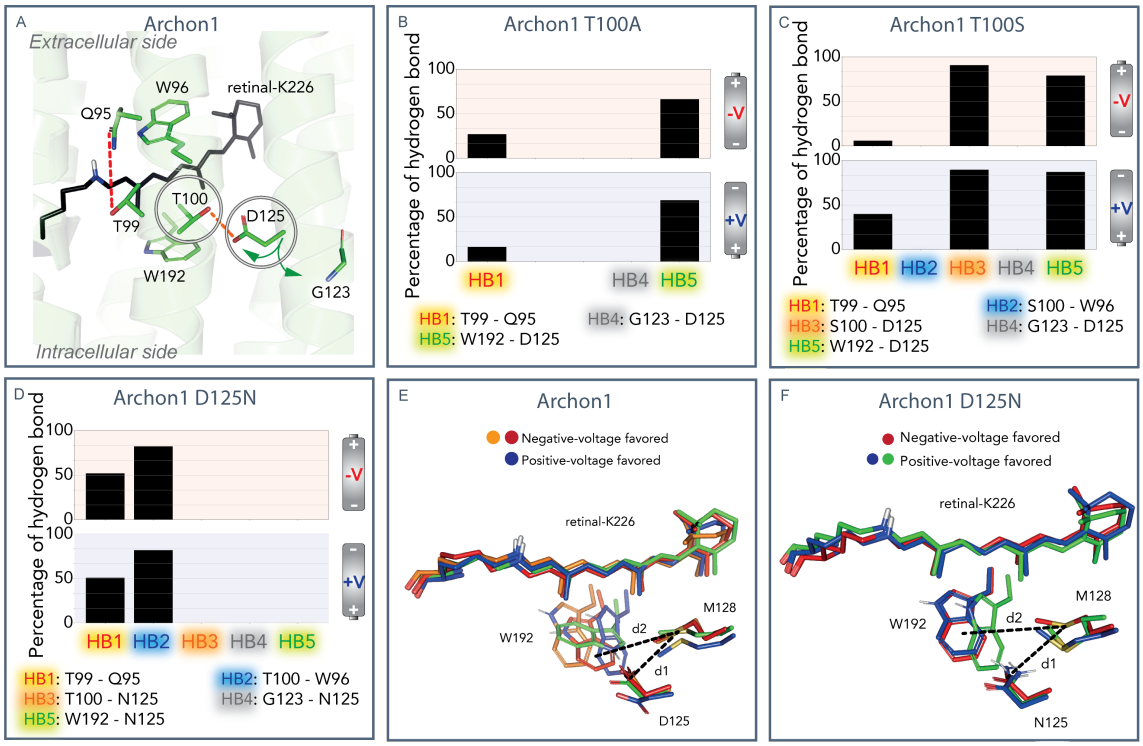

Figure S27. MD simulations of voltage modulated changes in Archon1-D125N

(A) retinal binding pocket with indicated residues T100 and D125. (B) Voltage dependent hydrogen bond rearrangement in Archon1-T100A. Independent of voltage HB5 (D125-W192) is formed. With low probability, voltage independent formation of HB1 (Q95-T99) was observed. (C) Voltage dependent hydrogen bond rearrangement in Archon1-T100S. HB3 (D125-S100) and HB5 (W192-D125) are observed, independent on voltage. The HB1 (Q95-T99) is formed only under positive voltage. (D) Voltage dependent hydrogen bond rearrangement in Archon1-D125N. Independent on voltage HB1 (Q95-T99) and HB2 (T100-W96) are observed. (E,F) Further investigation on voltage dependent structural changes were carried out on Archon1 and Archon1-D125N. (E) Archon1 shows high flexibility of W192. (F) Archon1-D125N shows more distinct voltage dependent orientations of W196.

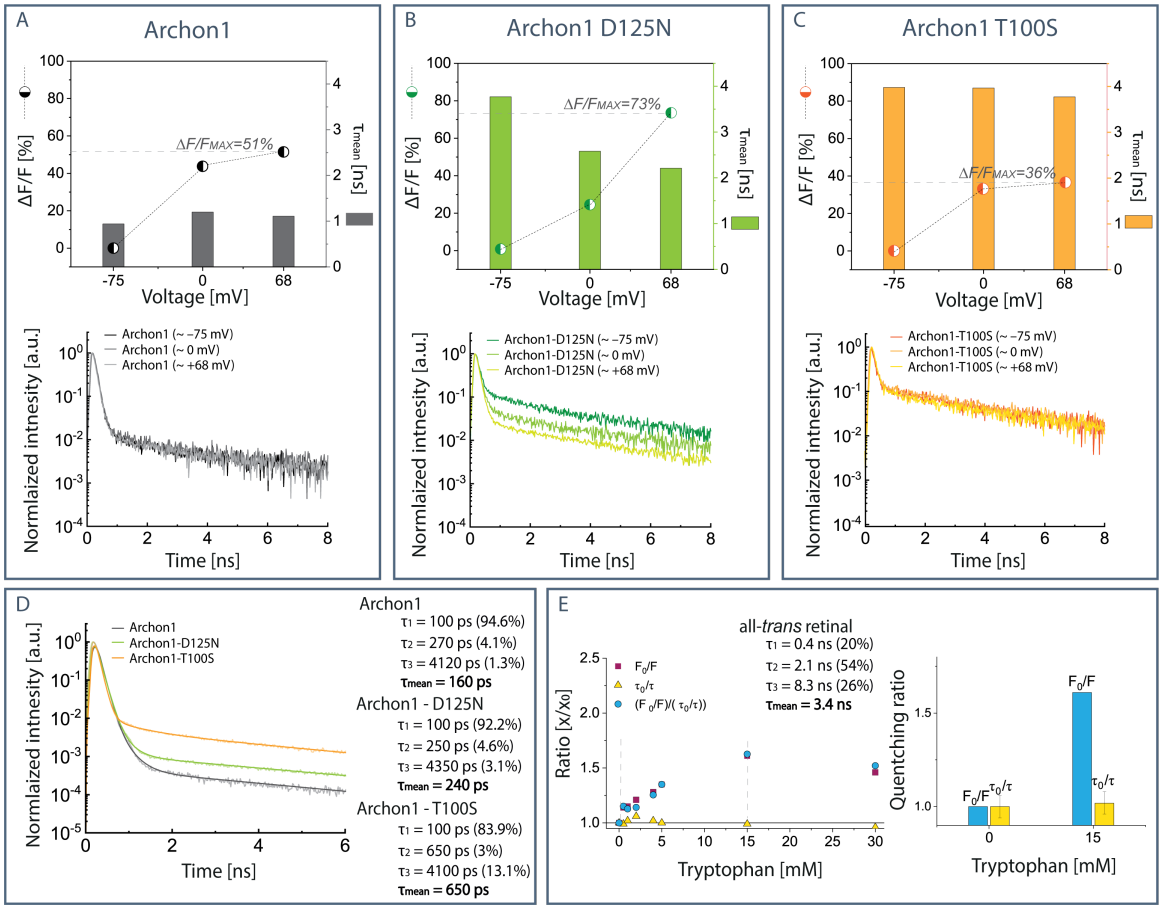

Figure S28. Fluorescence decay kinetics of Archon1 constructs reconstituted in lipid vesicles

Comparison between Archon1 (A), Archon1-D125N (B) and Archon1-T100S(C) is shown in the upper row. The purified protein is reconstituted in lipid vesicles, and upon external buffer exchange the ion gradient across the lipid bilayer is changed. The resulting voltage is calculated using Nernst equation. The upper part of the frame include overlay of fluorescence intensity change and mean fluorescence decay lifetime at the corresponding voltage. The lower part of the frame compares the normalized fluorescence decay curves at the three voltage conditions (−75 mV, 0 mV, +68 mV). The panel (D) shows direct comparison of the fluorescence lifetimes of the three constructs (19°C, 640 nm excitation). On the left side of the the panel (E) a Stern-Volmer plot of all-trans retinal/BSA complex and tryptophan is shown. On the right side of the panel (E) quenching ratio is compared between conditions of 0 mM tryptophan and 15 mM tryptophan.

The fluorescence lifetime recordings of Archon1 and its variants, reconstituted in vesicles, were carried and analysed by Jens Balke at Freie Universität Berlin under supervision of Prof. Dr. Ulrike Alexiev. The detergent-mediated reconstitution of solubilized Archon1, Archon1-D125N and Archon1-T100S in large unilamellar vesicles (LUVs, d = 100 nm) was performed by Jens Balke according to established procedures for membrane proteins as described Rigaud et al. 1995[277].

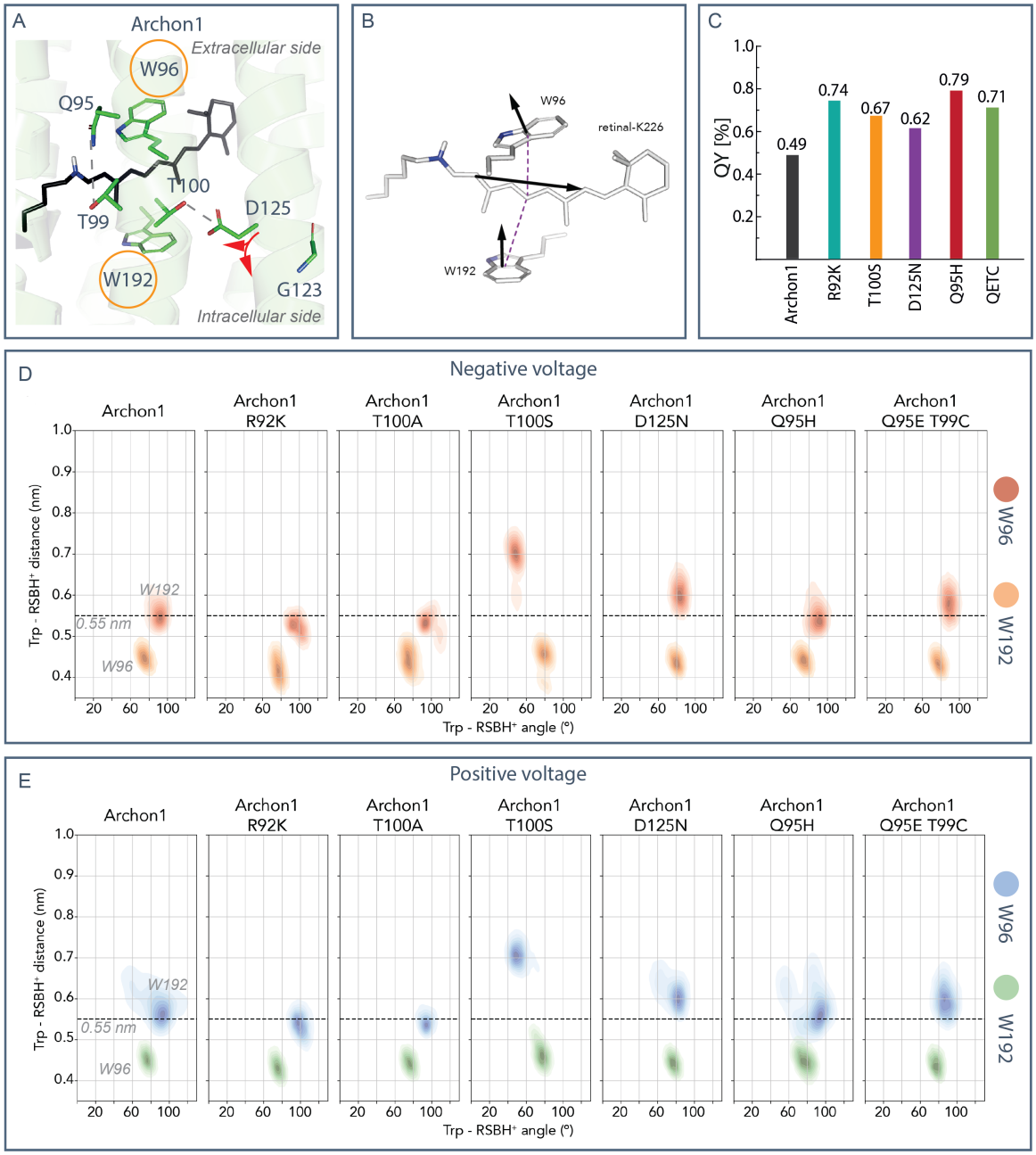

Figure S29. Tryptophan role in Archon1 and its variants

(A) The retinal binding pocket with indicated tryptophan residues W96 and W192. (B) Distances between tryptophans and chromophore which have been tracked in the MD simulations (shown in panel D, E). (C) Comparison between the fluorescence QY of Archon1 and its variants. (D) Distance and angle distribution between tryptophans (W96, W192) and retinal chromophore as observed by MD simulations at negative voltage. (E) Distance and angle distribution between tryptophans (W96, W192) and retinal chromophore as observed by MD simulations at positive voltage.

Eigenständigkeitserklärung

Hiermit, versichere ich, dass ich die vorliegende Dissertation mit dem Titel „Origin of fluorescence and voltage sensitivity in microbial rhodopsin-based voltage sensors“ eigenständig verfasst und keine weiteren als die angegeben Hilfmittel und Quellen verwendet habe.

Berlin, den 20.09.2022

Arita Silapetere